NASA Technical Memorandum 4296

Flow Field Over the Wing of a Delta-Wing Fighter Model With Vortex Control Devices at Mach 0.6 to 1.2

E. Ann Bare, David E. Reubush,
and Raymond C. Haddad

APRIL 1992

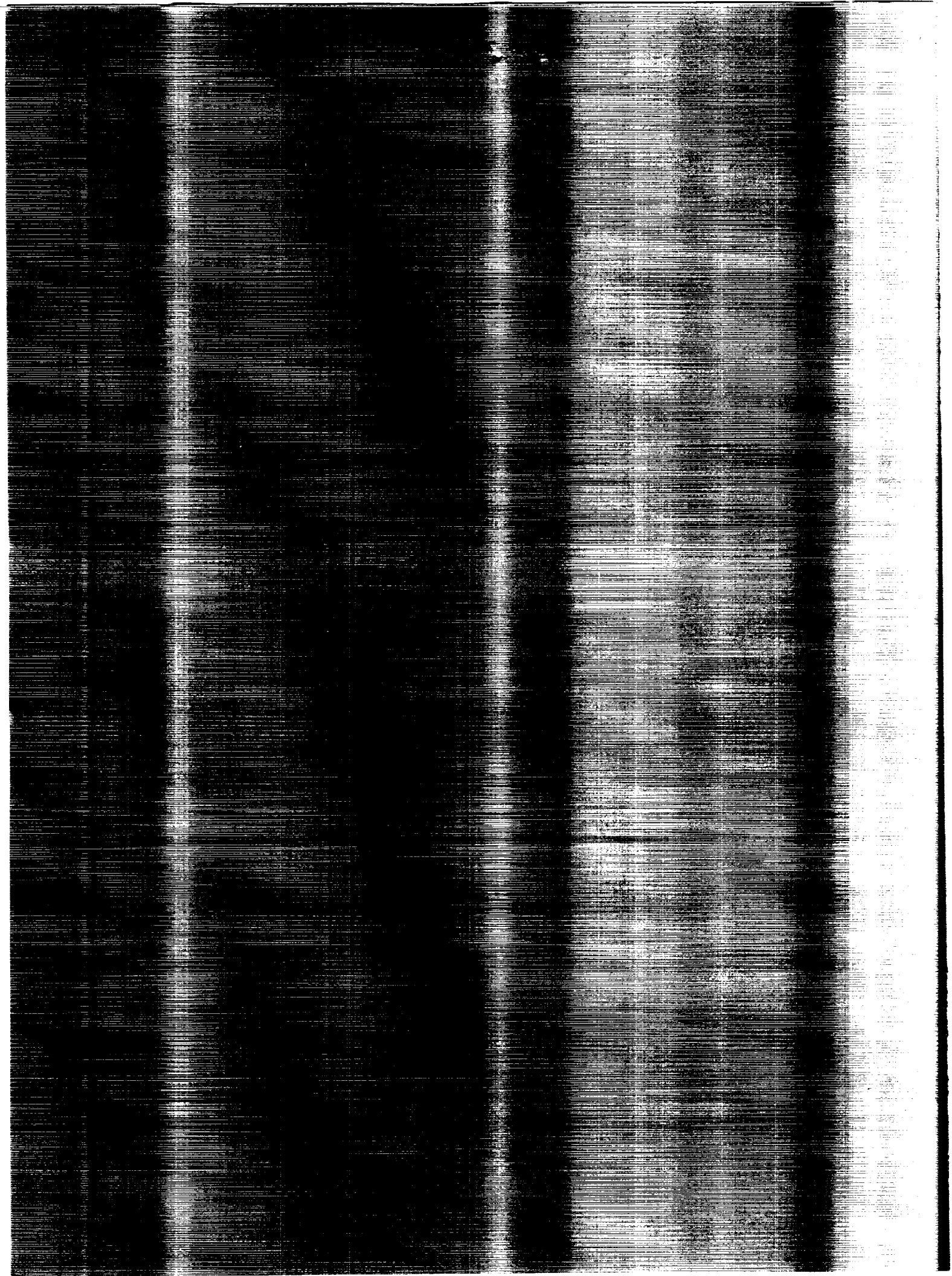

NASA Technical Memorandum 4296

Flow Field Over the Wing of a Delta-Wing Fighter Model With Vortex Control Devices at Mach 0.6 to 1.2

E. Ann Bare and David E. Reubush
Langley Research Center
Hampton, Virginia

Raymond C. Haddad
McDonnell Douglas Corporation
St. Louis, Missouri

National Aeronautics and
Space Administration

Office of Management

Scientific and Technical
Information Program

1992

Symbols and Abbreviations

BL	butt line
CF	pressure correction factor due to local angle of attack and local angle of sideslip
CFA	ratio of cone-probe side pressure to tip pressure ratio at $\alpha'_L = 0$ and $\Psi'_L = 0$ to cone-probe side pressure to tip pressure ratio at $\alpha'_L = \alpha'_L$ and $\Psi'_L = 0$
CFS	ratio of cone-probe side pressure to tip pressure ratio at $\alpha'_L = 0$ and $\Psi'_L = 0$ to cone-probe side pressure to tip pressure ratio at $\alpha'_L = 0$ and $\Psi'_L = \Psi'_L$
DPSHQL	local angle-of-sideslip calibration factor
DPSVQL	local angle-of-attack calibration factor
FS	fuselage station
LE	leading edge
M_∞	free-stream Mach number
M_L	local Mach number
PR	measured cone-probe tip pressure divided by tunnel total pressure
PR1	measured cone-probe 1 tip pressure divided by tunnel total pressure (see fig. A1)
PR2	measured cone-probe 2 tip pressure divided by tunnel total pressure (see fig. A1)
PR3	measured cone-probe 3 tip pressure divided by tunnel total pressure (see fig. A1)
PR4	measured cone-probe 4 tip pressure divided by tunnel total pressure (see fig. A1)
PR5	measured cone-probe 5 tip pressure divided by tunnel total pressure (see fig. A1)
PR6	measured cone-probe 6 tip pressure divided by tunnel total pressure (see fig. A1)
PSACP	average of cone-probe side pressures, $\frac{\text{PSCP1} + \text{PSCP2} + \text{PSCP3} + \text{PSCP4}}{4.0}$
PSCP1	measured cone-probe pressure at top of cone (see fig. A1)
PSCP2	measured cone-probe pressure at right side of cone (see fig. A1)
PSCP3	measured cone-probe pressure at bottom of cone (see fig. A1)
PSCP4	measured cone-probe pressure at left side of cone (see fig. A1)
PSPTCP	average of four cone-probe side pressures divided by tunnel total pressure
PTCP	measured cone-probe tip pressure (see fig. A1)
PTLCP	local total pressure
PTO	measured tunnel total pressure

Q_L	dynamic pressure used to nondimensionalize cone-probe side pressures for computation of local flow angles
q_L	local dynamic pressure
Re	Reynolds number
TPC	local static-to-total pressure ratio total pressure recovery correction factor
U, V, W	velocity component along Z, Y, and X model axis, respectively (see fig. A1)
U', V', W'	velocity component along Z', Y', and X' cone-probe axis, respectively (see fig. A1)
U'', V'', W''	velocity component along Z'', Y'', and X'' stationary rake axis, respectively (see fig. A1)
X, Y, Z	model axis system (see fig. A1)
X', Y', Z'	cone-probe axis system (see fig. A1)
X'', Y'', Z''	stationary rake axis system (see fig. A1)
α	model angle of attack (ALPHA in computer-generated figures)
α_L	local angle of attack in model axis system
α_L^1	local angle of attack in model axis system as computed at cone probe 1
α_L^2	local angle of attack in model axis system as computed at cone probe 2
α_L^3	local angle of attack in model axis system as computed at cone probe 3
α_L^4	local angle of attack in model axis system as computed at cone probe 4
α_L^5	local angle of attack in model axis system as computed at cone probe 5
α_L^6	local angle of attack in model axis system as computed at cone probe 6
α'_L	local angle of attack in cone-probe axis system
β	model angle of sideslip
β_L	local angle of yaw in model axis system
δ	angle between X' cone-probe axis and X model axes (see fig. A1)
ε	angle between X'' cone-probe axis and resultant free-stream velocity vector (see fig. A1)
γ	angle between Y' cone-probe axis and velocity vector in Y'-Z' plane (see fig. A1)
Ψ'_L	local angle of sideslip in cone-probe axis system
Θ	orientation angle between Z' cone-probe axis and Z model axis (see fig. A1)
θ	rake rotation angle (see fig. 10)

Introduction

Increased sophistication of ground-to-air and air-to-air weaponry requires that new tactical fighter aircraft be designed with a wider range of capabilities than is available on current aircraft. These new designs will include increased maneuverability and enhanced signature control to assure survivability. One of the most important decisions in designing future aircraft for these criteria will be the placement of the inlets. Increased maneuverability makes it essential that the inlets provide proper airflow to the engines at higher angles of attack and sideslip. However, airflow requirements must be balanced with survivability, since inlets are often a major contributor to high aircraft signature.

The location of vortices is particularly important to inlet placement because of the debilitating effect vortex ingestion can have on inlet operation. Experimental data usually used to determine the location of a vortex and to track its movement have been surface static pressures, which give local surface properties of the vortices but do little to indicate their formation and path. A time- and cost-effective method of obtaining a broad experimental data base of actual vortex location and extent is to use flow-field survey techniques (refs. 1 and 2). These techniques not only provide a large data base but can also give an indication of the best locations for inlet placement. The flow-field survey technique allows observance of the vortex behavior off the body, which makes it possible to determine directly the effectiveness of vortex control devices.

As part of a cooperative research program between NASA, McDonnell Douglas Corporation, and Wright Research and Development Center, a flow-field investigation was conducted on a 7.52-percent-scale wind tunnel model of an advanced fighter aircraft design. The purpose of the investigation was to determine the vortex trajectory and area of influence over the wing to determine the possibility of inlet placement in this region. The investigation was conducted in the Langley 16-Foot Transonic Tunnel at Mach numbers of 0.6, 0.9, and 1.2. Angle of attack was varied from $-4°$ to $30°$ and the model was tested at angles of sideslip of $0°$, $5°$, and $-5°$. Over-the-wing flow-field data were obtained at four fuselage stations by the use of six 5-hole conical probes mounted on a survey mechanism. This paper presents the effects of changes in free-stream Mach number, angle of attack, and angle of sideslip on the over-the-wing vortex extent and tracking by use of the computed local total pressure recoveries. Also presented are effects of vortex control devices on the over-the-wing vortex. These vortex control devices included two different apex flaps, wing leading-edge vortex flaps, and small and large wing fences. Only local total pressure recovery data are presented in this report.

Apparatus and Methods

Wind Tunnel

The experiment was conducted in the Langley 16-Foot Transonic Tunnel, which is a single-return atmospheric tunnel with a slotted octagonal test section and continuous air exchange. The wind tunnel has a variable airspeed to a Mach number of 1.30. Test section plenum suction is required for speeds above a Mach number of 1.10. A complete description of this facility and its operating characteristics is in reference 3.

Model and Support System Description

The model was a 7.52-percent-scale simulation of the complete wing and body of an advanced fighter aircraft designed with a cruise capability of Mach 1.8. Figure 1 shows the model installed in the 16-Foot Transonic Tunnel. The model was sting mounted and the sting was mated to the 16-Foot Transonic Tunnel model support system through the knuckle-to-sting-butt arrangement described in reference 3. A $15°$ pitch knuckle was used to achieve angles of attack from $18°$ to $30°$ and a $5°$ yaw knuckle was used to achieve angles of sideslip of $5°$ and $-5°$. Angle of attack of the model was measured with an accelerometer mounted in the model forebody.

Figure 2 shows a top-view sketch of the model which was 60.1 inches long. The wing was swept $71°$ and had a span of 38.0 inches. In addition to the baseline configuration shown in figures 1 and 2, a number of vortex control devices were also tested. Shown in figure 3 are sketches of the vortex flap, the small and large wing fences, and the large and small apex flaps. Figure 4(a) shows the vortex flap deflected on the model. The large and the small apex flaps are shown on the model in figures 4(b) and (c). Both apex flaps had the same centerline of rotation, as shown in figures 3(c) and (d). Figure 4(d) shows the large wing fences mounted on the model. The small wing fences were mounted in the same position. (See fig. 3(b) for a sketch of the wing fences.)

A conical-probe flow survey mechanism was mounted on the top of the left wing of the model. (See figs. 1 and 4(a).) With the survey mechanism mounted on the left wing, the right wing generated far more lift than the left wing and a very large negative rolling moment resulted. To test the model over

the desired angle-of-attack range without overloading the support system in roll, a dummy of the flow-survey mechanism was mounted on the right wing (fig. 4(a)), which effectively eliminated the large negative rolling moment.

As with any form of intrusive measurement device, the probes that were inserted during testing created a disturbance in the flow. It was recognized in doing this test that the survey mechanism itself as well as the cone probes could have been a source of flow disturbance that could have fed forward at the subsonic Mach numbers. In view of this concern, cone-probe influence on vortex flow fields was assessed by using a 3.50-percent-scale wind tunnel model with a scaled simulation of the cone probe and survey hardware used in the current investigation. A nonintrusive laser-sheet flow-visualization technique was used to survey the over-the-wing flow field of the 3.50-percent model. The 3.50-percent model duplicated the forebody and wing of the 7.52-percent model. The cone-probe simulation hardware, shown in figure 5, could be moved axially (forward and aft) and spanwise to investigate cone-probe influence on different portions of the over-the-wing flow field. Testing was conducted in the McDonnell Douglas Research Laboratories Shear Flow Facility (fig. 6(a)) at a Mach number of approximately 0.2. Cone-probe effects were assessed with a flow-visualization technique that is shown in figure 6(b). A high-speed video system and image processing allowed detailed tracking of the vortex-core trajectory and cross-sectional extent.

Analysis of the flow-field visualization data showed that cone probes did not influence the vortex upstream of the probes at low and moderate angles of attack. However, the presence of the probes induced vortex burst at an angle of attack of 26°, which was a lower angle of attack than that at which the vortex burst for the clean wing at the same fuselage station. (See fig. 7.) The cone probes did not influence the vortex trajectory or cross section upstream of the probes at angles of attack below 24°. (See fig. 8.) However, at higher angles of attack, the presence of the rake-induced vortex burst upstream of the cone-probe tips; this would generally increase the region of total pressure loss associated with the vortex. Changes in survey station or probe location within the feeding sheet did not change the angle of attack at which this vortex burst was induced. That is, low-speed wind tunnel testing with a validated vortex visualization and tracking technique showed that cone probes are appropriate for surveying vortex flow fields at moderate angles of attack. However, these probes can induce premature vortex burst at high angles of attack. The data at high angle of attack (above 22°) presented in this paper are supplementary information and should not be used for vortex examination.

The pressure-survey probes used to acquire flow-field data were 5-hole-pressure, 20° half-angle conical probes, 0.250 inch in diameter at the base of the cone. Each probe measured four pressures on the sides of the cone and one pressure at the tip of the cone. The side pressure orifices were located 0.125 inch aft of the cone tip at 90° intervals. A sketch of an individual probe is shown in figure 9(a). Twelve probes (six used during the test and six backups) were individually calibrated by McDonnell Douglas with a procedure discussed in the section "Data Reduction."

The six probes used during the test were mounted in a probe holder 3.90 inches in height and were arranged with the tips 0.68 inch apart. The probes were 2.00 inches long from the probe holder to the cone tip. A sketch of the six probes mounted in the holder is shown in figure 9(b). The probe holder was connected to the survey mechanism that was mounted on the top of the left wing of the model as shown in figure 9(c). The survey mechanism was designed by using the method outlined in reference 4, and it translated and rotated the rake by remote control. The use of the remote control allowed data to be taken over a large survey area with a minimum of model changes. The axial location and rotation angle of the survey mechanism were measured by potentiometers. The probe pressures were measured with an electronic scanning pressure sensor that was mounted in the survey mechanism.

Tests

Data were obtained at Mach numbers of 0.6, 0.9, and 1.2. Model angle of attack varied from $-4°$ to 30°. Data were obtained at 0°, 5°, and $-5°$ of sideslip. Reynolds number per foot varied from 3.2×10^6 at Mach 0.6 to 4.1×10^6 at Mach 1.2. Not all configurations were tested at all angles of attack and Mach numbers; table I gives a summary of the conditions tested for each configuration. Flow-field data were obtained at four fuselage stations and seven rake rotation positions above the left wing. Figure 2 shows the four axial locations at which data were taken and figure 10 shows a sketch of the survey area covered at each fuselage station. The circles represent a conical-probe position. The boundary-layer transition was fixed on the model by 0.1-inch-wide strips of No. 120 Carborundum grit. These strips were located 1.5 inches aft of the forebody nose

and 0.3 inch aft of and parallel to the wing leading edge.

Data Reduction

As previously stated, each of the conical probes was calibrated separately by McDonnell Douglas. This procedure involved mounting each probe on a sting and testing it over an angle-of-attack and angle-of-sideslip range from $-36°$ to $36°$ over a Mach number range such that the probes could be used to measure local Mach numbers up to 3.5. The angle calibration data were extrapolated to values of flow angles from $90°$ to $-90°$. The probe calibration was done by using the method described in reference 4. The calibration data for each probe were input into the data reduction system in the form of six tables. These tables, along with the five measured pressures from each probe, were used to compute the local flow properties of pressure recovery, Mach number, angle of attack, and angle of sideslip at each probe. Although all data quantities were computed, only the total pressure recovery is presented in this paper. A detailed description of the conical-probe data reduction procedure and related equations is presented in the appendix A. The data reduction scheme was an iterating one, with a finite number of iterations used to determine convergence. If no convergence was found, the data for that particular probe at that particular point were not used.

Inaccuracies exist in the 5-hole cone probes, particularly at the higher flow angles as noted in reference 5. The calibration method explained in reference 4 which was used for the probes in the current investigation attempted to correct as much as possible for any known inaccuracies. Although the probes themselves are inherently inaccurate, they can still be used—as they were in the current investigation—for determining the cross-sectional extent and trajectory of a vortex.

Presentation of Results

Results are presented under two main headings: "Baseline Configuration" and "Vortex Control." Even though the model was tested at angles of attack from $-4°$ to $30°$, data are only presented for $\alpha \geq 8°$ because the wing leading-edge vortex did not appear in the survey area below $\alpha = 8°$.

The data are presented as total pressure recovery (total pressure obtained from the probe divided by the free-stream total pressure) contours at each fuselage station. The contours are presented for various Mach numbers and angles of attack. The contouring program used for plotting interpolated but did not extrapolate the data; therefore, some contours appear incomplete because of the lack of data at some conditions. Any contour that did not use all the data at each of the survey points shown in figure 10 has the locations of the data that were used displayed as plus signs. All contour curves were drawn by using a spline curve fit. Some of the pressure recovery data presented were computed at local angles of attack outside the range of the calibrated flow angles. Appendix B gives the pressure recovery and local angle of attack for the data presented in the figures that had a local angle of attack greater than $40°$ or less than $-40°$. The data are presented as tables for each configuration. For each data point that contained at least one local angle of attack outside the range from $40°$ to $-40°$, the local angle of attack and total pressure recoveries are listed for each probe. The data are identified by free-stream Mach number, model angle of attack, rake rotation angle, and survey station. The probes are numbered 1 through 6 as shown in figure 10(a). In addition the figure number is listed on each point where the data are plotted. Figures 11 through 14 present the data for the baseline configuration at an angle of sideslip of $0°$. Figures 15 through 18 present the data for the baseline configuration at an angle of sideslip of $5°$ and figures 19 through 22 at an angle of sideslip of $-5°$.

The vortex control devices were tested only at Mach 0.9; therefore, the data are presented as a function of survey station and angle of attack for each control device. Figure 23 presents the data for the vortex flap; figures 24 and 25 present the data for the large and small wing fences; figure 26 presents the data for the vortex flap with the large wing fence; figures 27 and 28 present the large and small apex flap data.

Baseline Configuration

Mach number. The effect of increasing Mach number on the over-the-wing flow field was essentially the same for all angles of attack of $8°$ and greater. The main effect of increasing the Mach number was on the strength and movement of the primary wing vortex. Comparing figures 13(a), (b), and (c) reveals that as Mach number increased, the vortex core moved more inboard on the wing. The portion of the survey area influenced by the vortex increased as Mach number increased. Figures 11 through 14 show this effect occurred regardless of survey station or angle of attack. The behavior of the over-the-wing flow field was basically the same at all Mach numbers. Therefore, the rest of the discussion is primarily for Mach 0.9, which was considered the representative Mach number for the transonic range.

Axial survey station. Figures 11 through 14 show the over-the-wing flow field at the four axial survey positions. As the flow field was surveyed at increasing fuselage stations down the body, the primary wing vortex moved more outboard on the wing and elongated upward into the survey area. The forebody vortex also changed at the different axial locations. At an angle of attack of 12°, the highest angle where the forebody vortex was still independent of the primary wing vortex, the forebody vortex was drawn more outboard on the wing as it moved aft and was eventually drawn into the primary wing vortex. This behavior was due to the increased influence of the primary wing vortex on the forebody vortex. Because the behavior of the over-the-wing flow field was generally the same for varying angles of attack and Mach numbers at all survey stations, the rest of the discussion is mostly for the surveys done at fuselage station 36.5. (See fig. 2.)

Angle of attack. The largest effect on the transonic over-the-wing flow field was due to increasing the angle of attack. Figure 13(b) shows the total pressure recovery contours for angles of attack from 8° to 30°. A wing leading-edge vortex could be seen in the survey area at an angle of attack of 8°. At an angle of attack of 12°, the extent of the primary wing vortex had grown to cover the bottom outboard half of the survey area and a forebody vortex was in the survey area and was being pulled outboard by the wing leading-edge vortex. By an angle of attack of 14°, the wing vortex covered more than half the survey area, and the independent forebody vortex disappeared as the angle of attack increased. At angles of attack of 18° and 22°, the wing vortex had grown to influence the entire survey region.

On highly swept wings, the adverse pressure gradients associated with the primary wing leading-edge vortex can spawn a secondary wing vortex (ref. 6). At an angle of attack of 14°, an area of low total pressure recovery had appeared outboard of the primary wing vortex core (fig. 13(b)). The appearance of closed contours between the primary wing leading-edge vortex and the outboard bottom part of the survey area is thought to be from a secondary wing vortex. Although this area could not be fully mapped because of limitations in the flow-survey apparatus, the data from reference 6, in addition to flow visualization pictures from reference 7, make a strong case for the existence of a secondary wing vortex in this area.

Angle of sideslip. The effect of positive and negative sideslip on the over-the-wing flow field was determined by testing the model at angles of sideslip of both 5° and −5°. Angle of sideslip had only a small influence on the over-the-wing vortex system. Movement of the wing vortex system and the portion of the survey area affected was influenced by leeward and windward flow. In leeward flow, the primary wing vortex moved slightly outboard in the survey area. The forebody vortex that was well established at angles of attack of 8° and sideslip of 5° had disappeared as an independent vortex at an angle of attack of 12° (fig. 17(b)), having likely merged with the primary wing vortex. At angles of sideslip of −5° and angle of attack of 12°, the forebody vortex was seen only in the inboard corner of the survey area and was no longer visible at angle of attack of 14° (fig. 21(b)). At negative sideslip, the forebody vortex did not merge with the primary wing vortex but instead was swept along the fuselage out of the survey area.

At an angle of sideslip of 5° (fig. 17(b)), the primary wing vortex had encompassed a larger portion of the survey area than at an angle of sideslip of 0° (fig. 13(b)). This expansion would be expected since yawing the model effectively changed the the wing leading-edge sweep. That is, at positive sideslip the surveyed wing had an effective sweep angle of 76°, and at negative sideslip the wing had an effective leading-edge sweep of 66°. As would be expected, the vortex on the wing at negative sideslip stayed more inboard on the wing than either the vortex on the wing at positive sideslip or the wing at an angle of sideslip of 0°. (Compare figs. 21(b), 17(b), and 13(b).)

At Mach 0.9 for the positive sideslip flow field (fig. 17(b)), indications of a secondary wing vortex had already appeared as an outboard low pressure area separate from the core of the primary wing vortex at an angle of attack of 12°. Because of the increased effective leading-edge sweep of the wing, the secondary vortex formed at the lower angle of attack (ref. 6). On the windward wing, there was no evidence of a secondary vortex forming at any angle of attack at either Mach 0.9 (fig. 21(b)) or Mach 1.2 (fig. 21(c)). Reference 7 gives flow-visualization data for a 65° delta wing. At Mach 0.85 the data show visual evidence of a secondary wing vortex that first appeared at an angle of attack of approximately 12° at approximately 80-percent wing chord section. In the present study the effective sweep of the wing at negative sideslip was nearly the same as the wing in reference 7. However, for the present study, the most aft survey station was at approximately the 50-percent wing chord and the secondary vortex might have been seen in a survey area farther aft on

the wing at negative sideslip if the existing hardware could have surveyed there.

The data at an angle of attack of 8° in figure 21(b) exhibited an unusual contour pattern unlike any of the other contours. This uncommon pattern might have been an anomaly of the contour plotting program. The authors cannot determine any other explanation for these unusual patterns.

Vortex Control

A part of this investigation of over-the-wing flow fields was to determine the effectiveness of various vortex control devices. The devices evaluated were a vortex flap and two different wing fences and apex flaps. (See fig. 4.) All these devices were designed to influence the over-the-wing flow field by uncoupling the forebody vortex and the primary wing leading-edge vortex, thereby reducing the overall strength of the vortex system. The second purpose of these devices was to influence the movement of the vortex core to provide advantages in aerodynamic integration. The effectiveness of the vortex control devices was determined by comparing the over-the-wing flow field measured when they were installed with the baseline flow field. Because of time constraints, data with the vortex control devices installed were acquired only at Mach 0.9, which was considered to be representative of the transonic Mach numbers. The flap deflections were scheduled appropriately for the test angles of attack. (See fig. 3 for deflection angles.) Also, the wing fences by themselves were tested only at angles of attack of 18° and greater.

Vortex flap. Figure 23(c) shows the total pressure recovery contours at fuselage station 36.5 for the configuration with vortex flap deflected 30°. At an angle of attack of 8°, no indication of the primary wing vortex was seen in the survey area. In comparison, the vortex was seen in the survey area for the baseline configuration at an angle of attack of 8°. (See fig. 13(b).) The only disturbances in the survey area at an angle of attack of 8° were a small region of pressure loss evident near the middle bottom of the survey area, which was possibly due to separation from the flap hinge line, and a slight indication of a possible forebody vortex far inboard in the survey area. At an angle of attack of 12°, the primary wing vortex had appeared in the survey area but affected a smaller portion of the survey area than for the baseline configuration. The disturbance in the left-hand portion of the survey area was probably still caused by the possible separation from the flap hinge line. Because of the much smaller primary wing vortex, the forebody vortex was not drawn into the survey area at an angle of attack of 12°, unlike the baseline configuration. At an angle of attack of 15°, the forebody vortex was inboard in the survey area independent from the wing leading-edge vortex, which was still only in the outboard portion of the survey area. The vortex flap prevented the wing vortex from being large enough to be seen in the survey area until a higher model angle of attack. The vortex was kept small by using flap deflection angles scheduled with model angle of attack to keep the effective angle of attack of the wing leading edge lower, which is consistent with the expected performance of the vortex flap. The baseline configuration showed that the forebody vortex merged with the primary wing vortex at an angle of attack of 14°. Because of model hardware constraints, only set angles of the vortex flap could be tested. By properly scheduling the vortex flap deflection at each angle of attack, probably even more control of the over-the-wing vortex system could be achieved.

Wing fences. Small and large wing fences were tested at angles of attack of 18° and 26°. (See figs. 24 and 25.) Neither of the wing fences had any appreciable effect on the movement of the primary wing vortex. Also, no evidence was seen of any forebody and wing vortex uncoupling. Essentially the only effects observed in the survey area were a section of lower pressure recovery on the bottom inboard edge, which may have been due to separation from the wing fence, and a slight decrease in the survey area affected by the wing leading-edge vortex as compared to the baseline configuration (fig. 13(b)). The two effects were observed for both the large and small fences.

The large wing fence was tested in conjunction with the vortex flap at angles of attack of 8°, 12°, and 14° (fig. 26). Because of an instrumentation malfunction, only three points were obtained in the outboard half of the survey area. These data were not enough to draw any meaningful contours in this area. From the data obtained in the inboard portion of the survey area, it appeared that the wing fence tended to negate at least in part the uncoupling of the wing vortex and the forebody vortex that had been accomplished by the vortex flap alone.

Apex flaps. Two apex flap designs were tested. The large apex flap had a 71° sweep angle and was tested at angles of attack from −4° to 30°. As with the vortex flap, the apex flap deflections were scheduled with angle of attack. Because of the instrumentation malfunction mentioned in the previous section, the contours in the outboard half

of the survey area could not be plotted. Comparing the inboard contours in figure 27(c) with the baseline data in figure 13(b), the large apex flap was successful in uncoupling the forebody vortex from the wing vortex at fuselage station 36.5. At angles of attack of 12° and 14°, an independent forebody vortex appears to exist, but it is difficult to draw conclusions without the outboard survey area data.

The small apex flap had a 45° sweep angle and was tested only at the higher angles of attack from 18° to 30°. Because of the instrumentation malfunction, too little data were taken to draw any meaningful conclusions.

Inlet Placement

All the vortex control devices showed some success in decreasing the extent of the primary wing vortex in the survey area, with the vortex flap being most effective. However, the over-the-wing flow field—even with the vortex control devices—was still not conducive to the placement of inlets above the wing because of the extent and the trajectory of the vortex. Even with the vortex flap, which was quite effective, the inlet could not be placed so as to avoid vortex ingestion.

The cross-sectional extent and trajectory of the wing leading-edge vortex as mapped by the cone-probe survey data was very consistent with other published data for the flow across a delta wing. Thus, this method of flow-field mapping for vortex extent and trajectory was found to be efficient and useful.

Conclusions

A flow-field investigation of a wind tunnel model of an advanced fighter aircraft design has given the following conclusions:

1. The major contributor to the reduction in the total pressure recovery of the over-the-wing flow field was the primary wing leading-edge vortex.

2. The model forebody generated a separate vortex that coupled with the primary wing vortex at angles of attack above 12° for the baseline configuration at 0° sideslip.

3. The effect of windward and leeward flow on the over-the-wing flow field was the same as would be expected by increasing and decreasing wing leading-edge sweep angle.

4. The vortex flap uncoupled the forebody vortex from the primary wing leading-edge vortex at angles of attack of up to 18°.

5. Even with the use of the vortex control devices, the over-the-wing flow field was still not conducive to inlet integration.

NASA Langley Research Center
Hampton, VA 23665-5225
March 10, 1992

Appendix A

Data Reduction Procedure and Equations for Conical Probes

The data reduction scheme used the local Mach number as the independent quantity with all other flow properties as a function of local Mach number. The computation of the local flow-field properties was accomplished with an iteration scheme based on the convergence of an average ratio of cone-probe side pressure to total pressure. The method and equations of the iteration scheme are detailed in the following explanation. Note that the equations as given are for a single probe and are repeated for each probe. All interpolation and extrapolation was linear.

An average of the four cone-probe side pressures was computed, and this average was then divided by tunnel total pressure to give

$$\text{PSPTCP} = \frac{\text{PSACP}}{\text{PTO}}$$

The quantity PSPTCP was the initial assumption for the iteration. With this quantity along with the rake orientation angle Θ, a value of local Mach number was obtained from a calibration table. If the local Mach number was greater than 1.0, local pressure recovery was computed as follows:

$$\text{PR} = \frac{\text{PTCP}}{\text{PTO}} \frac{\text{PTLCP}}{\text{PTCP}}$$

If the local Mach number was less than or equal to 1.0, local pressure recovery was

$$\text{PR} = \frac{\text{PTCP}}{\text{PTO}}$$

With the use of the local pressure recovery and local Mach number, a value of dynamic pressure was computed as follows:

$$Q_L = \frac{q_L}{\text{PTLCP}} \text{ PR PTO}$$

where

$$\frac{q_L}{\text{PTLCP}} = 0.7 M_2^L \left(1 + 0.2 M_L^2\right)^{-3.5}$$

With this dynamic pressure and the cone-probe side pressures, the following quantities were computed:

$$\text{DPSVQL} = \frac{\text{PSCP3} - \text{PSCP1}}{Q_L}$$

$$\text{DPSHQL} = \frac{\text{PSCP2} - \text{PSCP4}}{Q_L}$$

Cone-probe side pressures measured at orifices 1, 2, 3, and 4 are shown in figure A1. By using these quantities and local Mach number, a value for local angle of attack and a value for local angle of sideslip were obtained from the calibration tables. If the local angle of attack or local sideslip exceeded $\pm 90°$, they were set equal to $\pm 90°$. With the use of the values of local alpha, local angle of sideslip, and local Mach number, pressure correction ratios were obtained from the calibration tables. These values were then used to compute the correction factor as follows:

$$\text{CF} = \text{CFA} + \text{CFS} - 1$$

By using this quantity, pressure recovery, and PSACP/PTO, a new value of PSPTCP was computed as follows:

$$\text{PSPTCP} = \text{PSPTCP} \frac{1}{\text{CF}} \frac{1}{\text{PR}}$$

This new value of PSPTCP was compared with the old value of PSPTCP. If the absolute value of the difference was less than 0.0005, the solution was considered converged. If the difference was

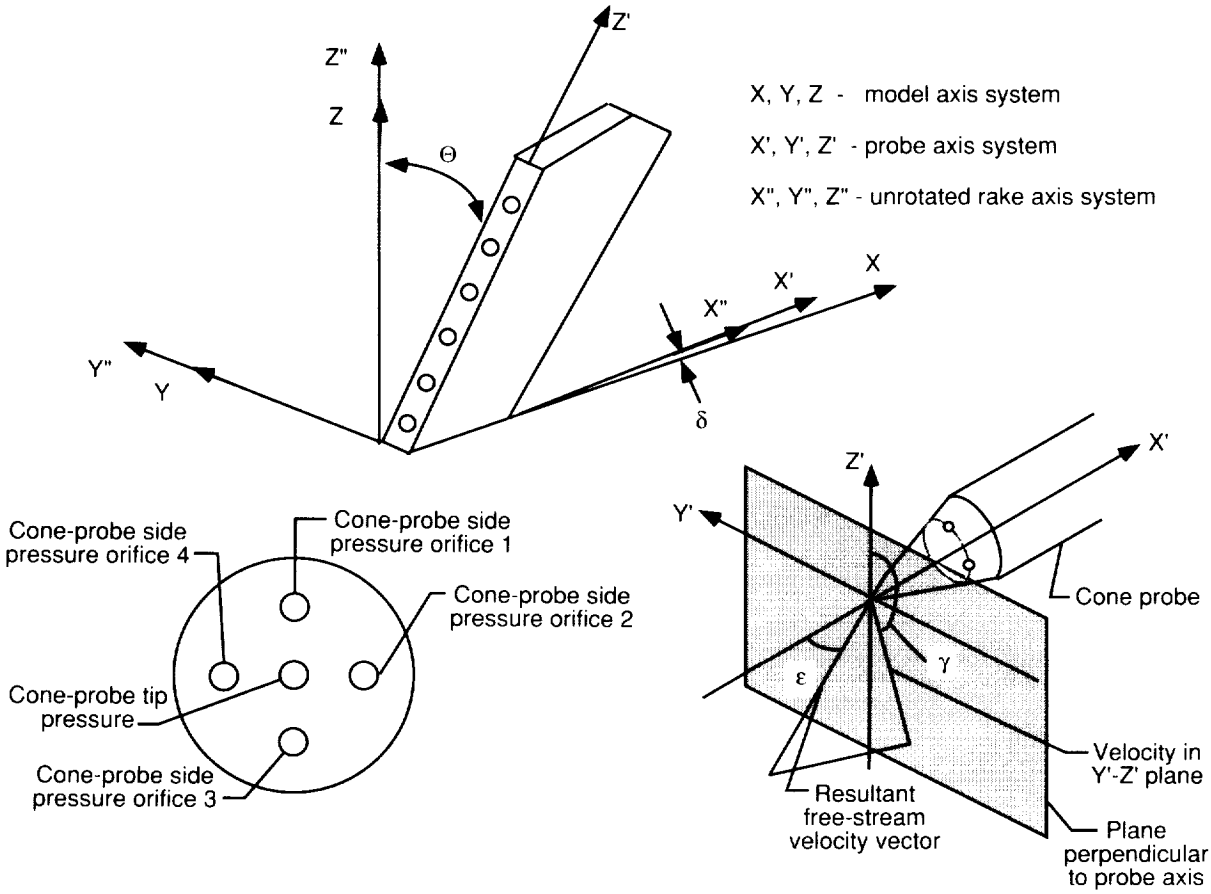

Figure A1. Cone-probe pressures and axis system.

greater than 0.0005, the new value of PSPTCP was taken and the procedure started again. If after 25 iterations the solution had not converged, the value of local Mach number at the 24th iteration was compared with the value at the 25th iteration. If the Mach numbers were within 0.005, the solution was declared converged. If the Mach numbers were not within 0.005, then a new value of PSPTCP was computed by averaging PSPTCP from the 24th and the 25th iterations. The iteration was begun again with this scheme for computing the new PSPTCP. If after another 25 iterations the solution was still not converged, the data for that particular probe at that particular point were not used.

The local flow properties calculated as just presented were in the cone-probe axis system. For convenience of use and analysis, α'_L and Ψ'_L were transferred to the model coordinate system in the following manner. First, the local velocities relative to the probe axis system were calculated as

$$W' = \sqrt{\frac{M_L^2(\sin\alpha'_L)^2[1-(\sin-\Psi'_L)^2]}{1-(\sin\alpha'_L)^2(\sin-\Psi'_L)^2}}$$

$$V' = \sqrt{\frac{M_L^2(\sin\Psi'_L)^2[1-(\sin-\alpha'_L)^2]}{1-(\sin\alpha'_L)^2(\sin-\Psi'_L)^2}}$$

$$U' = \cos\alpha'_L\sqrt{M_L^2-(\mathrm{V}')^2}$$

These equations for velocity vectors did not take into account the sign of the velocity and the following convention was necessary:

$$W' = W' \qquad (\alpha'_L \geq 0)$$

$$W' = -W' \qquad (\alpha'_L < 0)$$

$$V' = V' \qquad (\Psi'_L \geq 0)$$

$$V' = -V' \qquad (\Psi'_L < 0)$$

Before the final transformation to the model axis system, the velocity vectors were obtained along the vertical (Z''), horizontal (Y''), and axial (X'') axes of the stationary rake. This transformation was accomplished by a pure rotation (Θ) about the $X' = X''$ axis as follows (fig. A1):

$$\begin{Bmatrix} U'' \\ V'' \\ W'' \end{Bmatrix} = \begin{Bmatrix} 1 & 0 & 0 \\ 0 & \cos\Theta & -\sin\Theta \\ 0 & \sin\Theta & \cos\Theta \end{Bmatrix} \begin{Bmatrix} U' \\ V' \\ W' \end{Bmatrix}$$

To obtain the velocity components in the model axis system, a transformation was accomplished by a pure rotation (δ) about the $Y' = Y''$ axis as follows (fig. A1):

$$\begin{Bmatrix} U \\ V \\ W \end{Bmatrix} = \begin{Bmatrix} \cos\delta & 0 & \sin\delta \\ 0 & 1 & 0 \\ -\sin\delta & 0 & \cos\delta \end{Bmatrix} \begin{Bmatrix} U'' \\ V'' \\ W'' \end{Bmatrix}$$

The value of δ was dependent on where the survey mechanism was mounted on the model (i.e., over the wing, under the wing, near the body, or far from the body). Note that for the investigation presented in this paper, only the over-the-wing near-the-body survey mechanism position was used. Using these velocity vectors, α_L and β_L were computed in the model coordinate system by the following equations:

$$\alpha_L = \sin^{-1}\left(\frac{W}{\sqrt{M_L^2 - V^2}}\right)$$

$$\beta_L = \sin^{-1}\left(\frac{-V}{\sqrt{M_L^2 - W^2}}\right)$$

Because of inaccuracies in the cone-probe measurement of true total pressure at angle of attack or angle of sideslip, a scheme was devised to correct each cone-probe total pressure measurement. With the local Mach number and the velocity vectors W' and V', two angles (ε and γ) were computed as follows:

$$\varepsilon = 90 - \cos^{-1}\left(\sqrt{\frac{W'^2 + V'^2}{M_L}}\right)$$

The angle γ was defined with respect to the sign of the differences in cone-probe side pressure (DPSHQL and DPSVQL):

$$\gamma = \left| \tan^{-1} \frac{V'}{W'} \right| \qquad (\text{DPSHQL} \geq 0;\ \text{DPSVQL} \leq 0)$$

$$\gamma = 90 + \left| \tan^{-1} \frac{W'}{V'} \right| \qquad (\text{DPSHQL} > 0;\ \text{DPSVQL} > 0)$$

$$\gamma = 180 + \left| \tan^{-1} \frac{V'}{W'} \right| \qquad (\text{DPSHQL} \leq 0;\ \text{DPSVQL} \geq 0)$$

$$\gamma = 270 + \left| \tan^{-1} \frac{W'}{V'} \right| \qquad (\text{DPSHQL} \leq 0;\ \text{DPSVQL} < 0)$$

With these angles and local Mach number, a local pressure recovery correction (TPC) was obtained from the calibration tables and applied to determine the corrected value of pressure recovery PRCOR, as follows:

$$\text{PRCOR} = \text{PR} + \text{TPC}$$

New values of local total pressure, local static pressure, and local dynamic pressure were then computed with PRCOR and the equations previously defined.

Appendix B

Total Pressure Recoveries at $\alpha_L < -40°$ or $\alpha_L > 40°$

This appendix presents the total pressure recovery and local angle of attack for all the probes at any point where at least one probe had a calculated local angle of attack greater than 40° or less than −40°. Blank spots in the table indicate where data were not computed and therefore not plotted. Tables B1, B2, and B3 are for the baseline configuration at $\beta = 0°$, −5°, and 5°, respectively. Table B4 is for the configuration with the vortex flap deflected; table B5, with wing fences; table B6, with large wing fences and vortex flap deflected; and table B7, with apex flaps deflected.

Table B1. Baseline Configuration at $\beta = 0°$

M_∞	α, deg	θ, deg	FS	α_L^1, deg	PR1	α_L^2, deg	PR2	α_L^3, deg	PR3	α_L^4, deg	PR4	α_L^5, deg	PR5	α_L^6, deg	PR6	Figure in text
0.6	12	61	32.8	5	0.999	4	0.999	4	0.998	-3	0.999	17	0.970	89	0.830	11(a)
0.6	12	30	32.8	5	1.000	2	0.999	1	0.997	-3	0.990	19	0.933	73	0.809	11(a)
0.6	12	60	32.8	9	0.984	2	0.975	0	0.949	5	0.917	19	0.783	74	0.634	11(a)
0.6	12	85	32.8	9	0.979	1	0.966	3	0.928	21	0.876	40	0.761			11(a)
0.6	14	75	32.8	3	0.998	0	0.998	4	0.998	15	0.988	45	0.873			11(a)
0.6	14	61	32.8	3	0.999	1	0.998	5	0.994	16	0.971	43	0.836			11(a)
0.6	14	30	32.9	5	0.998	0	0.995	4	0.980	-10	0.938	28	0.823	46	0.661	11(a)
0.6	14	30	32.8	12	0.980	4	0.966	7	0.923	11	0.843	5	0.768	43	0.555	11(a)
0.6	14	85	32.8	13	0.963	3	0.940	5	0.891	34	0.862	50	0.757			11(a)
0.6	18	75	32.8	1	1.000	7	1.000	19	0.984	42	0.924	75	0.740			11(a)
0.6	18	61	32.8	2	0.999	9	0.995	-22	0.965	51	0.873	80	0.702			11(a)
0.6	18	30	32.8	2	0.989	8	0.973	-28	0.892	-25	0.859	48	0.708	52	0.583	11(a)
0.6	18	31	32.8	24	0.931	13	0.882	54	0.801	34	0.774	30	0.693			11(a)
0.6	18	60	32.8	23	0.923	12	0.891	44	0.854	43	0.846	60	0.653			11(a)
0.6	18	85	32.8	19	0.920	7	0.886	15	0.844	40	0.782	65	0.712			11(a)
0.6	22	75	32.8	7	0.995	17	0.987	-39	0.927	-60	0.814					11(a)
0.6	22	60	32.8	9	0.984	22	0.963	-56	0.862	-79	0.742					11(a)
0.6	22	30	32.8	1	0.951	21	0.900	-23	0.823	28	0.791	59	0.586			11(a)
0.6	22	30	32.8	42	0.833	28	0.792	72	0.814	42	0.684	44	0.546			11(a)
0.6	22	60	32.8	38	0.850	26	0.805	67	0.808	56	0.743	86	0.595			11(a)
0.6	22	85	32.8	31	0.858	10	0.820	26	0.837	54	0.659	84	0.639			11(a)
0.9	12	61	32.8	10	0.984	3	0.975	0	0.952	1	0.937	17	0.707	58	0.539	11(b)
0.9	12	85	32.8	10	0.979	2	0.964	7	0.926	6	0.872	38	0.749	76	0.513	11(b)
0.9	14	75	32.8	2	0.998	2	0.997	9	0.994	28	0.953	58	0.744			11(b)
0.9	14	61	32.8	3	0.999	2	0.997	9	0.984	32	0.849	50	0.615			11(b)
0.9	14	30	32.8	6	0.997	1	0.990	3	0.963	1	0.795	23	0.556	43	0.504	11(b)
0.9	14	30	32.8	14	0.978	7	0.963	13	0.919	13	0.858	13	0.668	51	0.494	11(b)
0.9	14	60	32.8	15	0.967	6	0.951	9	0.917	11	0.853	41	0.653	70	0.548	11(b)
0.9	14	85	32.8	15	0.959	4	0.936	5	0.890	19	0.707	55	0.595	83	0.581	11(b)

Table B1. Continued

M_∞	α, deg	θ, deg	FS	α_L^1, deg	PR1	α_L^2, deg	PR2	α_L^3, deg	PR3	α_L^4, deg	PR4	α_L^5, deg	PR5	α_L^6, deg	PR6	Figure in text
0.9	18	75	32.8	4	1.000	-13	0.995	-31	0.946	-51	0.805	77	0.598	44	1.000	11(b)
0.9	18	-59	32.8	2	0.993	13	0.979	-40	0.835	37	0.634			-40	0.746	11(b)
0.9	18	30	32.8	7	0.982	3	0.962	6	0.644	7	0.645	40	0.445	18	0.663	11(b)
0.9	18	30	32.8	28	0.929	19	0.925	39	0.791	24	0.775	44	0.466	48	0.691	11(b)
0.9	18	60	32.8	27	0.918	15	0.908	34	0.836	26	0.819	52	0.577	58	0.731	11(b)
0.9	18	85	32.8	26	0.908	8	0.885	6	0.820	32	0.772	70	0.349			11(b)
0.9	22	-75	32.8	-12	0.985	26	0.960	-45	0.827	69	0.650					11(b)
0.9	22	-60	32.8	-17	0.954	-29	0.856	-42	0.594	54	0.698			41	0.702	11(b)
0.9	22	31	32.8	36	0.863	24	0.947	-43	0.661	26	0.798	28	0.707	50	0.603	11(b)
1.2	12	75	32.8	5	0.952	5	0.878	1	0.871	5	0.918	25	0.860	47	0.821	11(c)
1.2	12	-61	32.8	5	0.990	3	0.972	3	0.925	3	0.922	-27	0.787	43	0.822	11(c)
1.2	12	85	32.8	11	0.977	2	0.988	-3	0.918	6	0.821	58	0.419	75	0.315	11(c)
1.2	14	60	32.8	4	0.982	0	0.945	3	0.906	12	0.883	36	0.441	46	0.618	11(c)
1.2	14	30	32.8	15	0.987	8	1.000	10	0.886	6	0.846	5	0.451	41	0.343	11(c)
1.2	14	60	32.8	15	0.981	6	1.000	7	0.897	7	0.853	34	0.427	40	0.703	11(c)
1.2	14	84	32.8	15	0.975	4	0.977	2	0.873	26	0.638	59	0.389	65	0.438	11(c)
1.2	18	75	32.8	3	0.926	11	0.919	-29	0.827	41	0.735			56	0.598	11(c)
1.2	18	60	32.8	2	0.919	13	0.906	-37	0.574	37	0.379			-42	0.348	11(c)
1.2	18	30	32.8	9	0.926	2	0.909	6	0.476	0	0.434	-49	0.206	22	0.276	11(c)
1.2	22	75	32.8	14	0.900	22	0.901	37	0.681	51	0.563					11(c)
1.2	22	60	32.8	-11	0.842	31	0.596	-31	0.293	-44	0.494					11(c)
1.2	22	-30	32.8	17	0.887	6	0.507	4	0.362	-12	0.512	-52	0.170	9	0.426	11(c)
1.2	22	30	32.8	29	0.968	20	1.000	38	0.562	16	0.657	16	0.643	46	0.387	11(c)
1.2	22	85	32.8	26	0.914	8	0.977	7	0.618	22	0.594	28	0.720	78	0.146	11(c)
0.6	12	31	35.0	4	1.000	1	1.000	1	0.999	-5	0.998	16	0.978	49	0.935	12(a)
0.6	12	60	35.0	7	0.986	2	0.961	14	0.906	2	0.875	13	0.694	51	0.740	12(a)
0.6	12	84	35.0	8	0.968	0	0.963	31	0.879	47	0.772	61	0.639	88	0.701	12(a)
0.6	14	75	35.0	3	1.000	0	1.000	3	1.000	9	0.999	-27	0.959	-86	0.812	12(a)
0.6	14	60	35.0	3	1.000	1	1.000	-4	1.000	-10	0.996	30	0.943	84	0.816	12(a)
0.6	14	31	35.0	3	1.000	3	0.998	8	0.991	16	0.975	35	0.889	-84	0.791	12(a)

Table B1. Continued

M_∞	α, deg	θ, deg	FS	α_L^1, deg	PR1	α_L^2, deg	PR2	α_L^3, deg	PR3	α_L^4, deg	PR4	α_L^5, deg	PR5	α_L^6, deg	PR6	Figure in text
0.6	14	85	35.0	13	0.945	2	0.942	26	0.869	52	0.753	71	0.611			12(a)
0.6	18	-75	35.0	-2	1.000	-7	1.000	16	0.992	-28	0.965	51	0.837			12(a)
0.6	18	60	35.0	3	0.999	9	0.998	19	0.981	-35	0.944	47	0.811			12(a)
0.6	18	30	35.0	2	0.991	-12	0.980	34	0.924	39	0.875	69	0.727	-52	0.663	12(a)
0.6	18	60	35.0	27	0.891	14	0.835	60	0.860	63	0.692	64	0.586			12(a)
0.6	18	86	35.0	21	0.899	9	0.915	35	0.810	57	0.745	67	0.660			12(a)
0.6	22	75	35.0	7	0.997	15	0.992	31	0.959	44	0.889	71	0.737			12(a)
0.6	22	60	35.0	10	0.988	20	0.977	42	0.927	49	0.850	76	0.712			12(a)
0.6	22	30	35.0	11	0.952	30	0.891	47	0.802	-44	0.762	83	0.602	51	0.562	12(a)
0.6	22	30	35.0	48	0.759	31	0.807	58	0.697	45	0.639	31	0.526			12(a)
0.6	22	60	35.0	43	0.816	36	0.805	76	0.774			71	0.575			12(a)
0.6	22	84	35.0	33	0.840	8	0.915	30	0.718	76	0.658	66	0.676			12(a)
0.9	12	60	35.0	4	0.999	2	1.000	0	1.000	6	1.000	21	0.965	83	0.846	12(b)
0.9	12	31	35.0	4	0.999	0	1.000	3	0.999	8	0.992	29	0.903	62	0.800	12(b)
0.9	12	60	35.0	9	0.977	2	0.964	15	0.926	2	0.842	29	0.545	69	0.520	12(b)
0.9	12	86	35.0	10	0.965	6	0.950	14	0.782	35	0.796	57	0.581			12(b)
0.9	14	75	35.0	2	0.998	2	0.999	7	0.998	19	0.983	41	0.854			12(b)
0.9	14	60	35.0	2	1.000	3	1.000	9	0.995	22	0.963	-44	0.777			12(b)
0.9	14	30	35.0	4	0.997	3	0.996	10	0.977	24	0.894	32	0.684	42	0.652	12(b)
0.9	14	31	35.0	12	0.972	1	0.950	1	0.871	6	0.692	10	0.538	47	0.493	12(b)
0.9	14	60	35.0	14	0.957	2	0.938	1	0.910	29	0.750	45	0.500			12(b)
0.9	14	85	35.0	16	0.939	7	0.924	19	0.725	50	0.611	57	0.662			12(b)
0.9	18	75	35.0	-5	1.000	12	0.997	-27	0.966	39	0.886	65	0.693			12(b)
0.9	18	60	35.0	5	0.996	14	0.987	36	0.922	51	0.763					12(b)
0.9	18	30	35.0	1	0.973	14	0.946	24	0.707	14	0.662	46	0.488	42	0.492	12(b)
0.9	18	30	35.0	29	0.900	13	0.953	31	0.715	28	0.535	43	0.486	48	0.644	12(b)
0.9	18	60	35.0	27	0.905	10	0.904	25	0.832	53	0.662	57	0.598	55	0.733	12(b)
0.9	18	85	35.0	23	0.886	0	0.892	23	0.690	50	0.404	51	0.577	50	0.790	12(b)
0.9	22	75	35.0	12	0.991	20	0.970	39	0.895	52	0.772	77	0.575	50	0.809	12(b)
0.9	22	60	35.0	16	0.967	31	0.880	51	0.712	-49	0.706					12(b)

Table B1. Continued

M_∞	α, deg	θ, deg	FS	α_L^1, deg	PR1	α_L^2, deg	PR2	α_L^3, deg	PR3	α_L^4, deg	PR4	α_L^5, deg	PR5	α_L^6, deg	PR6	Figure in text
0.9	22	31	35.0	31	0.899	16	0.803	34	0.696	38	0.577	36	0.667	55	0.534	12(b)
0.9	22	60	35.0	36	0.825	11	0.723	30	0.770	39	0.741	52	0.524	54	0.836	12(b)
0.9	22	85	35.0	25	0.841	4	0.860	22	0.783	40	0.371	45	0.378			12(b)
1.2	12	60	35.0	8	0.989	0	0.988	1	0.897	5	0.617	24	0.325	48	0.666	12(c)
1.2	12	84	35.0	8	0.985	6	0.993	5	0.841	37	0.555	55	0.458	64	0.514	12(c)
1.2	14	75	35.0	1	0.945	1	0.932	5	0.919	11	0.918	32	0.782	50	0.550	12(c)
1.2	14	60	35.0	3	0.946	2	0.943	6	0.917	14	0.905	31	0.826	41	0.795	12(c)
1.2	14	59	35.0	13	0.977	3	1.000	8	0.840	29	0.538	50	0.368	59	0.497	12(c)
1.2	14	85	35.0	11	0.976	6	0.989	1	0.743	40	0.339	56	0.437	50	0.472	12(c)
1.2	18	75	35.0	3	0.926	10	0.918	23	0.876	33	0.875	46	0.526			12(c)
1.2	18	60	35.0	4	0.924	12	0.924	31	0.783	41	0.618	64	0.425	54	0.509	12(c)
1.2	18	30	35.0	6	0.915	5	0.904	7	0.442	5	0.439	45	0.270	31	0.316	12(c)
1.2	18	30	35.0	21	1.000	9	0.948	6	0.541	6	0.522	15	0.389	44	0.354	12(c)
1.2	18	60	35.0	19	0.986	5	0.965	14	0.569	33	0.630	49	0.722	55	0.617	12(c)
1.2	18	85	35.0	17	0.975	4	0.916	20	0.622	29	0.547	61	0.222	64	0.455	12(c)
1.2	22	75	35.0	13	0.917	21	0.905	34	0.761	39	0.779	79	0.359	56	0.530	12(c)
1.2	22	60	35.0	16	0.855	28	0.848	40	0.473	46	0.654	79	0.317			12(c)
1.2	22	30	35.0	7	0.875	1	0.484	0	0.291	16	0.298	57	0.229	36	0.218	12(c)
1.2	22	30	35.0	27	0.858	14	0.956	20	0.534	20	0.718	18	0.717	54	0.480	12(c)
1.2	22	60	35.0	24	0.940	8	0.960	21	0.614	29	0.495	48	0.560	71	0.433	12(c)
1.2	22	86	35.0	21	0.921	4	0.773	22	0.618	33	0.472	49	0.172	65	0.200	12(c)
0.6	12	60	36.5	6	0.973	0	0.948	12	0.860	6	0.733	17	0.747	42	0.832	13(a)
0.6	12	86	36.5	3	0.951	12	0.962	43	0.868	64	0.693	62	0.651	66	0.803	13(a)
0.6	14	75	36.5	3	1.000	0	1.000	3	1.000	7	0.999	18	0.980	73	0.894	13(a)
0.6	14	59	36.5	2	1.000	1	1.000	4	1.000	9	0.998	20	0.974	73	0.902	13(a)
0.6	14	30	36.5	1	1.000	4	0.999	9	0.994	15	0.986	28	0.941	61	0.881	13(a)
0.6	14	60	36.5	14	0.945	11	0.903	46	0.830	39	0.703	38	0.631	82	0.655	13(a)
0.6	14	86	36.5	10	0.913	1	0.846	51	0.803	70	0.684	87	0.565			13(a)
0.6	18	76	36.5	3	1.000	7	1.000	15	1.000	24	1.000	40	0.920			13(a)
0.6	18	60	36.5	4	0.999	9	0.998	18	0.986	27	0.964	38	0.871	86	0.767	13(a)

Table B1. Continued

M_∞	α, deg	θ, deg	FS	α_L^1, deg	PR1	α_L^2, deg	PR2	α_L^3, deg	PR3	α_L^4, deg	PR4	α_L^5, deg	PR5	α_L^6, deg	PR6	Figure in text
0.6	18	30	36.5	-5	0.993	14	0.983	33	0.944	-41	0.889	61	0.781	-84	0.733	13(a)
0.6	18	0	36.5	2	0.950	14	0.911	30	0.836	-30	0.744	-41	0.689	9	0.656	13(a)
0.6	18	30	36.5	25	0.871	6	0.831	16	0.809	31	0.654	15	0.622	41	0.600	13(a)
0.6	18	59	36.5	32	0.878	34	0.851	83	0.756	67	0.654	59	0.554			13(a)
0.6	18	85	36.5	22	0.850	26	0.805	55	0.757	66	0.725	73	0.620			13(a)
0.6	22	76	36.5	7	0.998	14	0.994	28	0.969	-37	0.921	56	0.789			13(a)
0.6	22	61	36.5	10	0.990	19	0.982	38	0.943	-41	0.887	58	0.763			13(a)
0.6	22	31	36.5	16	0.956	34	0.912	50	0.831	63	0.735	82	0.654	47	0.633	13(a)
0.6	22	30	36.5	42	0.772	28	0.780	37	0.725	40	0.637					13(a)
0.6	22	60	36.5	43	0.819	49	0.810					63	0.566			13(a)
0.6	22	86	36.5	23	0.777	27	0.806	64	0.684	66	0.721	65	0.645			13(a)
0.9	12	75	36.5	3	1.000	-1	0.973	6	0.803	-5	0.853	12	0.956	47	0.906	13(b)
0.9	12	61	36.5	4	1.000	1	1.000	0	1.000	5	1.000	-15	0.983	-49	0.916	13(b)
0.9	12	-30	36.5	3	1.000	1	1.000	4	1.000	8	0.997	23	0.959	47	0.903	13(b)
0.9	12	59	36.5	7	0.973	5	0.955	3	0.747	8	0.700	32	0.558	58	0.633	13(b)
0.9	12	84	36.5	8	0.941	22	0.911	29	0.814	48	0.675	61	0.535			13(b)
0.9	14	75	36.5	2	0.999	2	0.999	-6	0.998	-15	0.992	32	0.913	86	0.747	13(b)
0.9	14	60	36.5	2	1.000	3	0.999	-8	0.997	-17	0.984	-34	0.878	-83	0.754	13(b)
0.9	14	-31	36.5	2	0.998	-5	0.997	13	0.983	-27	0.945	38	0.760	-43	0.721	13(b)
0.9	14	30	36.5	8	0.970	-6	0.948	-12	0.832	0	0.603	8	0.597	43	0.543	13(b)
0.9	14	60	36.5	14	0.948	1	0.930	33	0.796	36	0.590	43	0.533			13(b)
0.9	14	85	36.5	11	0.906	-13	0.757	36	0.665	46	0.730	59	0.619			13(b)
0.9	18	76	36.5	5	1.000	-12	0.997	-25	0.973	-35	0.916	54	0.759			13(b)
0.9	18	-61	36.5	-6	0.996	14	0.988	33	0.946	-42	0.842	-65	0.691			13(b)
0.9	18	30	36.5	5	0.972	23	0.905	45	0.687	27	0.649	60	0.496	-48	0.509	13(b)
0.9	18	30	36.5	29	0.881	12	0.879	32	0.612	36	0.511	38	0.478	55	0.457	13(b)
0.9	18	84	36.5	13	0.843	6	0.573	18	0.539	38	0.518	52	0.586	54	0.939	13(b)
0.9	22	-76	36.5	-13	0.990	20	0.973	-37	0.908	-47	0.817	-65	0.640	-60	0.601	13(b)
0.9	22	61	36.5	-18	0.966	28	0.900	-44	0.808	-60	0.683					13(b)
0.9	22	-31	36.5	-8	0.812	14	0.649	13	0.591	-25	0.659	66	0.394	-25	0.550	13(b)

Table B1. Continued

M_∞	α, deg	θ, deg	FS	α_L^1, deg	PR1	α_L^2, deg	PR2	α_L^3, deg	PR3	α_L^4, deg	PR4	α_L^5, deg	PR5	α_L^6, deg	PR6	Figure in text
0.9	22	29	36.5	29	0.854	15	0.766	34	0.557	63	0.408	42	0.478	62	0.534	13(b)
0.9	22	60	36.5	30	0.870	23	0.807	38	0.752			41	0.739	52	0.908	13(b)
1.2	12	86	36.5	2	0.993	16	0.952	4	0.709	44	0.505	52	0.564	49	0.820	13(c)
1.2	14	60	36.5	10	0.989	1	0.996	14	0.754	32	0.544	40	0.401	67	0.399	13(c)
1.2	14	86	36.5	5	0.974	16	0.901	4	0.620	45	0.351	50	0.563	72	0.425	13(c)
1.2	18	-75	36.5	-3	1.000	9	1.000	-20	0.981	-29	1.000	40	0.820	60	0.732	13(c)
1.2	18	-60	36.5	4	1.000	11	1.000	25	0.945	34	0.961	43	0.693	49	0.744	13(c)
1.2	18	29	36.5	2	1.000	10	1.000	24	0.558	12	0.574	44	0.373	28	0.702	13(c)
1.2	18	30	36.5	18	0.953	4	0.969	4	0.461	13	0.352	22	0.399	45	0.288	13(c)
1.2	18	60	36.5	16	0.986	11	0.876	32	0.640			38	0.712	52	0.514	13(c)
1.2	18	86	36.5	11	1.000	5	0.572	25	0.849	70	0.217	48	0.430	49	0.791	13(c)
1.2	22	-75	36.5	10	0.998	19	0.993	32	0.883	36	0.864	58	0.502			13(c)
1.2	22	-60	36.5	16	0.974	25	0.955	42	0.640	42	0.822	61	0.444			13(c)
1.2	22	31	36.5	-1	0.760	9	0.490	-7	0.324	21	0.347	51	0.298	30	0.326	13(c)
1.2	22	0	36.5	23	0.767	10	0.511	7	0.440	4	0.290	7	0.248	9	0.294	13(c)
1.2	22	30	36.5	23	0.944	12	0.591	21	0.521	28	0.618	31	0.183	41	0.352	13(c)
1.2	22	59	36.5	19	0.863	11	0.881	21	0.546	39	0.573	47	0.542	56	0.633	13(c)
1.2	22	85	36.5	13	0.897	25	0.606	29	0.588	44	0.212	29	0.343			13(c)
0.6	12	87	40.5	47	0.819	56	0.710			85	0.688	39	0.878	28	0.949	14(a)
0.6	14	60	40.5	25	0.887	16	0.820	41	0.618	48	0.651	25	0.764	44	0.892	14(a)
0.6	18	-75	40.5	4	0.990	8	0.997	14	0.993	19	0.985	28	0.948	78	0.863	14(a)
0.6	18	-61	40.5	-5	0.997	9	0.998	17	0.991	22	0.981	29	0.940	77	0.888	14(a)
0.6	18	31	40.5	9	0.993	16	0.988	30	0.967	30	0.944	44	0.888	47	0.859	14(a)
0.6	18	-1	40.5	17	0.943	33	0.889	41	0.836	52	0.820	46	0.771	11	0.797	14(a)
0.6	18	59	40.5	38	0.868	47	0.713					43	0.634	88	0.703	14(a)
0.6	18	86	40.5	54	0.766	56	0.744					72	0.640			14(a)
0.6	22	-75	40.5	6	0.965	12	0.993	23	0.979	27	0.957	38	0.883	84	0.783	14(a)
0.6	22	-61	40.5	11	0.991	17	0.987	29	0.967	30	0.943	36	0.868	86	0.804	14(a)
0.6	22	31	40.5	21	0.964	30	0.939	43	0.885	54	0.849	68	0.780	40	0.758	14(a)
0.6	22	1	40.5	27	0.845	29	0.813	36	0.755	47	0.710	48	0.655	5	0.689	14(a)

Table B1. Concluded

M_∞	α, deg	θ, deg	FS	α_L^1, deg	PR1	α_L^2, deg	PR2	α_L^3, deg	PR3	α_L^4, deg	PR4	α_L^5, deg	PR5	α_L^6, deg	PR6	Figure in text
0.6	22	29	40.5	26	0.771	20	0.715	33	0.576			6	0.595	50	0.641	14(a)
0.6	22	60	40.5	55	0.761	74	0.634					52	0.588			14(a)
0.6	22	85	40.5	64	0.697	56	0.740	85	0.685			83	0.607			14(a)
0.9	14	75	40.5	1	0.999	2	0.999	-5	0.999	10	0.998	17	0.978	-59	0.863	14(a)
0.9	14	61	40.5	0	1.000	4	1.000	-8	1.000	12	0.997	-19	0.972	-43	0.933	14(a)
0.9	14	0	40.5	-5	0.986	15	0.975	36	0.930	33	0.833	-40	0.773	-14	0.878	14(a)
0.9	8	86	40.5	-8	0.733	8	0.900	24	0.609	41	0.725	12	0.992	4	0.938	14(a)
0.9	12	85	40.5	37	0.797	40	0.736	90	0.526			49	0.714	49	0.813	14(a)
0.9	14	60	40.5	-1	0.767	9	0.855	28	0.613	67	0.458	46	0.548	55	0.720	14(a)
0.9	14	86	40.5	41	0.732	44	0.733	84	0.617	85	0.535	69	0.566	84	0.662	14(a)
0.9	18	-60	40.5	7	0.999	13	0.996	-25	0.978	-26	0.953	-33	0.875	79	0.813	14(b)
0.9	18	-31	40.5	13	0.979	28	0.948	-43	0.849	47	0.785	54	0.738	-37	0.762	14(b)
0.9	18	28	40.5	24	0.757	9	0.678	12	0.520	29	0.451	21	0.483	43	0.636	14(b)
0.9	22	-75	40.5	-7	0.971	-16	0.980	-30	0.954	-33	0.914	-45	0.811			14(b)
0.9	22	61	40.5	17	0.976	22	0.961	37	0.919	37	0.874	48	0.775	44	0.792	14(b)
0.9	22	31	40.5	31	0.850	39	0.788	44	0.610	68	0.576	-65	0.590	39	0.624	14(b)
0.9	22	-16	40.5	23	0.728	23	0.643	-26	0.671	48	0.488	59	0.539	25	0.589	14(b)
0.9	22	31	40.5	24	0.730	14	0.557	32	0.360			22	0.419	48	0.528	14(b)
0.9	22	59	40.5	44	0.744	51	0.640									14(b)
0.9	22	85	40.5	47	0.359	61	0.429	66	0.642	64	0.602	88	0.372			14(b)
1.2	8	86	40.5	19	0.945	1	0.876	19	0.561	44	0.535	22	0.917	9	0.872	14(c)
1.2	12	86	40.5	15	0.495	38	0.568	43	0.690	39	0.707	41	0.685	35	0.961	14(c)
1.2	14	60	40.5	-5	0.924	5	0.947	23	0.634	45	0.405	37	0.738	35	0.985	14(c)
1.2	14	86	40.5	23	0.456	38	0.540	56	0.437	43	0.666	54	0.465	44	1.000	14(c)
1.2	18	76	40.5	5	0.911	-8	0.914	15	0.885	22	0.894	30	0.822	41	0.693	14(c)
1.2	18	60	40.5	1	0.780	25	0.758	88	0.349	42	0.679	46	0.461	50	0.649	14(c)
1.2	18	86	40.5	25	0.560	44	0.268	63	0.371	57	0.473	42	0.724	59	0.505	14(c)
1.2	22	75	40.5	-8	0.903	-15	0.898	27	0.822	29	0.867	-36	0.726	45	0.839	14(c)
1.2	22	61	40.5	16	0.905	23	0.898	32	0.762	36	0.870	40	0.640	-39	0.768	14(c)
1.2	22	29	40.5	13	0.684	12	0.536	14	0.470	28	0.519	47	0.405	23	0.655	14(c)

Table B2. Baseline Configuration at $\beta = -5°$

M_∞	α, deg	θ, deg	FS	α_L^1, deg	PR1	α_L^2, deg	PR2	α_L^3, deg	PR3	α_L^4, deg	PR4	α_L^5, deg	PR5	α_L^6, deg	PR6	Figure in text
0.6	12	75	32.8	5	0.980	3	0.970	6	0.939	3	0.909	11	0.775	65	0.640	19(a)
0.6	12	85	32.8	4	0.979	3	0.968	8	0.933	2	0.920	24	0.764	77	0.620	19(a)
0.6	14	31	32.8	13	0.972	4	0.958	7	0.920	14	0.868	12	0.776	44	0.597	19(a)
0.6	14	61	32.8	10	0.966	1	0.951	0	0.912	9	0.885	28	0.819	88	0.580	19(a)
0.9	12	60	32.8	8	0.979	1	0.970	3	0.944	4	0.923	1	0.768	43	0.481	19(b)
0.9	12	85	32.8	5	0.978	4	0.966	12	0.928	19	0.936	21	0.768	49	0.489	19(b)
0.9	14	31	32.8	15	0.967	7	0.951	17	0.910	23	0.876	26	0.650	51	0.547	19(b)
0.9	14	85	32.8	9	0.961	3	0.941	14	0.887	24	0.904	32	0.628	53	0.687	19(b)
0.6	12	85	35.0	2	0.969	6	0.963	12	0.885	35	0.787	43	0.655	77	0.708	20(a)
0.6	14	86	35.0	6	0.951	3	0.945	28	0.869	52	0.778	60	0.657			20(a)
0.9	12	85	35.0	3	0.963	10	0.951	16	0.915	30	0.746	38	0.543	68	0.520	20(b)
0.9	14	30	35.0	13	0.959	2	0.938	4	0.890	11	0.823	12	0.547	46	0.459	20(b)
0.9	14	61	35.0	10	0.950	4	0.931	17	0.878	1	0.825	34	0.630	59	0.566	20(b)
0.9	14	85	35.0	8	0.936	14	0.918	15	0.899	40	0.653	44	0.705	60	0.617	20(b)
1.2	12	61	35.0	5	0.973	6	0.993	12	0.884	19	0.861	10	0.405	48	0.303	20(c)
1.2	14	30	35.0	12	0.995	1	0.986	3	0.733	2	0.729	1	0.381	47	0.243	20(c)
1.2	14	85	35.0	6	0.959	8	0.986	5	0.760	19	0.465	44	0.337			20(c)
0.6	12	84	36.5	4	0.958	13	0.971	8	0.917	44	0.734	52	0.665	65	0.793	21(a)
0.6	14	60	36.5	9	0.951	3	0.922	37	0.805	31	0.719	33	0.639	74	0.647	21(a)
0.6	14	85	36.5	1	0.935	17	0.955	4	0.907	53	0.767	65	0.631			21(a)
0.9	8	0	36.5	13	0.829	44	0.830	39	0.968	2	0.988	4	0.840	10	0.783	21(b)
0.9	12	60	36.5	3	0.966	8	0.953	19	0.853	0	0.672	9	0.519	60	0.545	21(b)
0.9	12	85	36.5	3	0.945	21	0.938	10	0.969	36	0.706	51	0.522			21(b)
0.9	14	30	36.5	10	0.956	5	0.931	8	0.861	2	0.741	10	0.519	45	0.468	21(b)
0.9	14	85	36.5	2	0.908	26	0.885	5	0.904	45	0.644	53	0.650			21(b)
1.2	12	1	36.5	10	0.676	52	0.722	36	0.878	3	1.000	7	0.588			21(c)
1.2	14	0	36.5	9	0.641	64	0.656	40	0.795	3	1.000	20	0.202			21(c)
1.2	12	59	36.5	3	0.970	9	1.000	19	0.768	21	0.571	4	0.378	48	0.401	21(c)
1.2	12	84	36.5	2	0.963	14	1.000	15	0.754	6	0.368	40	0.277	67	0.462	21(c)
1.2	14	30	36.5	9	0.972	4	0.911	10	0.685	9	0.791	1	0.336	43	0.334	21(c)
1.2	14	85	36.5	0	0.946	14	0.981	0	0.700	31	0.358	54	0.359			21(c)
0.6	12	84	40.5	6	0.753	21	0.895	35	0.751	69	0.709	38	0.851	35	0.933	22(a)
0.6	14	60	40.5	9	0.951	8	0.977	14	0.786	43	0.659	29	0.740	46	0.851	22(a)
0.6	14	84	40.5	32	0.709	38	0.861	51	0.750	79	0.678	47	0.742	64	0.797	22(a)
0.9	12	60	40.5	14	0.943	25	0.944	22	0.881	7	0.540	32	0.564	42	0.815	22(b)
0.9	12	85	40.5	12	0.641	29	0.747	44	0.602	73	0.506	52	0.602	56	0.786	22(b)
0.9	14	60	40.5	11	0.896	25	0.795	2	0.770	37	0.478	49	0.424	80	0.566	22(b)
0.9	14	85	40.5	32	0.673	37	0.750	63	0.632	83	0.520	88	0.431			22(b)
1.2	12	84	40.5	16	0.884	3	0.562	26	0.394	52	0.323	51	0.438	36	0.847	22(c)
1.2	14	85	40.5	12	0.771	27	0.492	67	0.433	76	0.416	83	0.320	56	0.584	22(c)

Table B3. Baseline Configuration at $\beta = 5°$

M_∞	α, deg	θ, deg	FS	α_L^1, deg	PR1	α_L^2, deg	PR2	α_L^3, deg	PR3	α_L^4, deg	PR4	α_L^5, deg	PR5	α_L^6, deg	PR6	Figure in text
0.6	12	-30	32.8	0	1.000	3	1.000	-5	0.999	-11	0.990	-30	0.912	-74	0.788	15(a)
0.6	12	60	32.8	14	0.985	7	0.974	13	0.940	24	0.910	39	0.708	86	0.622	15(a)
0.6	12	85	32.8	16	0.976	7	0.961	13	0.934	34	0.888	53	0.706			15(a)
0.6	14	75	32.8	1	1.000	-3	1.000	7	1.000	-16	0.992	-38	0.915	-87	0.738	15(a)
0.6	14	-61	32.8	1	1.000	-4	1.000	-9	0.998	17	0.985	-41	0.891			15(a)
0.6	14	31	32.8	13	0.985	6	0.970	12	0.920	16	0.876	15	0.796	41	0.610	15(a)
0.6	14	60	32.8	19	0.967	10	0.946	26	0.898	35	0.886	42	0.730			15(a)
0.6	14	85	32.8	20	0.957	10	0.934	22	0.899	42	0.835	64	0.694			15(a)
0.9	12	-30	32.8	1	1.000	3	1.000	6	0.998	-12	0.977	-25	0.782	42	0.666	15(b)
0.9	12	85	32.8	18	0.973	10	0.956	12	0.930	30	0.835	52	0.628			15(b)
0.9	14	75	32.8	1	0.997	4	0.996	-11	0.993	-23	0.966	-48	0.808			15(b)
0.9	14	60	32.8	-1	0.999	-6	0.998	-13	0.990	-28	0.948	-54	0.744			15(b)
0.9	14	-30	32.8	0	1.000	-5	0.997	-12	0.977	-22	0.874	-29	0.732	-48	0.552	15(b)
0.9	14	30	32.8	15	0.983	9	0.964	17	0.896	18	0.808	23	0.539	55	0.428	15(b)
0.9	14	61	32.8	21	0.965	13	0.947	33	0.908	35	0.851	51	0.558			15(b)
0.9	14	85	32.8	21	0.952	11	0.937	8	0.914	26	0.792	61	0.657			15(b)
1.2	8	85	32.8	9	1.000	5	0.998	3	0.975	2	0.908	12	0.455	42	0.545	15(c)
0.6	12	75	35.0	2	0.999	-1	1.000	-3	1.000	-6	0.999	13	0.990	-40	0.946	16(a)
0.6	12	-61	35.0	-1	1.000	3	1.000	-5	1.000	-7	1.000	15	0.989	-46	0.948	16(a)
0.6	12	-31	35.0	2	1.000	-4	1.000	-7	1.000	-12	0.997	21	0.972	-48	0.931	16(a)
0.6	12	60	35.0	14	0.973	4	0.950	19	0.913	28	0.819	32	0.705	62	0.733	16(a)
0.6	12	85	35.0	17	0.960	8	0.947	47	0.872	55	0.723	74	0.572			16(a)
0.6	14	-75	35.0	1	0.997	3	0.997	-6	0.996	-11	0.994	23	0.965	-76	0.875	16(a)
0.6	14	61	35.0	-2	0.998	-5	0.999	-9	0.997	-14	0.992	26	0.957	-84	0.878	16(a)
0.6	14	-29	35.0	-3	1.000	-7	0.999	-13	0.992	23	0.974	33	0.902	-64	0.849	16(a)
0.6	14	0	35.0	2	0.997	-6	0.992	-19	0.961	28	0.915	42	0.833	-23	0.778	16(a)
0.6	14	60	35.0	20	0.945	10	0.905	46	0.891	39	0.785	48	0.579	87	0.643	16(a)
0.6	14	85	35.0	22	0.936	11	0.940	50	0.830	65	0.720	86	0.561			16(a)
0.9	12	75	35.0	2	0.997	-2	0.997	-4	0.997	-8	0.996	-19	0.969	67	0.873	16(b)
0.9	12	60	35.0	-1	1.000	4	1.000	-6	0.999	-10	0.997	-21	0.963	72	0.873	16(b)

Table B3. Concluded

M_∞	α, deg	θ, deg	FS	α_L^1, deg	PR1	α_L^2, deg	PR2	α_L^3, deg	PR3	α_L^4, deg	PR4	α_L^5, deg	PR5	α_L^6, deg	PR6	Figure in text
0.9	12	-30	35.0	-2	1.000	-5	1.000	-9	0.999	14	0.990	-29	0.919	61	0.832	16(b)
0.9	12	85	35.0	19	0.953	7	0.947	41	0.806	51	0.692	61	0.579			16(b)
0.9	14	61	35.0	2	0.999	6	0.998	-12	0.994	-19	0.981	31	0.903	84	0.772	16(b)
0.9	14	31	35.0	3	1.000	-8	0.998	17	0.983	30	0.949	40	0.797	-44	0.740	16(b)
0.9	14	31	35.0	12	0.977	3	0.950	9	0.818	10	0.582	19	0.623	53	0.525	16(b)
0.9	14	60	35.0	21	0.948	8	0.935	24	0.894	38	0.655	52	0.506			16(b)
0.9	14	85	35.0	27	0.919	1	0.914	47	0.704	52	0.740	70	0.580			16(b)
1.2	12	60	35.0	12	0.990	4	1.000	7	0.853	26	0.643	40	0.452	50	0.753	16(c)
1.2	12	85	35.0	15	0.977	1	0.979	26	0.584	49	0.512	55	0.570	62	0.534	16(c)
1.2	14	75	35.0	0	0.977	-3	0.965	-8	0.940	-15	0.945	-27	0.880	41	0.789	16(c)
1.2	14	60	35.0	17	0.982	8	1.000	36	0.700	40	0.596	54	0.452			16(c)
1.2	14	85	35.0	16	0.985	1	0.984	22	0.631	60	0.322	48	0.626	78	0.405	16(c)
0.6	12	60	36.5	13	0.961	7	0.911	19	0.886	42	0.673	27	0.720	48	0.842	17(a)
0.6	12	85	36.5	17	0.939	31	0.882	68	0.766	89	0.630	58	0.673	63	0.822	17(a)
0.6	14	76	36.5	1	1.000	2	1.000	6	1.000	-10	0.999	19	0.979	60	0.917	17(a)
0.6	14	-60	36.5	-2	1.000	-5	1.000	8	1.000	-13	0.997	21	0.974	-59	0.928	17(a)
0.6	14	31	36.5	-4	1.000	-8	1.000	-14	0.995	-19	0.986	-28	0.945	-49	0.909	17(a)
0.6	14	0	36.5	-2	0.998	-10	0.994	-25	0.967	-30	0.929	-46	0.857	26	0.847	17(a)
0.6	14	60	36.5	25	0.919	24	0.881	44	0.838	58	0.672	38	0.634	68	0.731	17(a)
0.6	14	85	36.5	20	0.904	34	0.879	67	0.773	86	0.646	68	0.630			17(a)
0.9	8	85	36.5	8	0.984	5	0.994	32	0.772	49	0.614	32	0.860	16	0.990	17(b)
0.9	12	60	36.5	0	1.000	-4	1.000	-6	0.999	-9	0.998	17	0.979	43	0.934	17(b)
0.9	12	-30	36.5	-2	1.000	-6	1.000	-10	0.999	-14	0.994	21	0.957	-43	0.918	17(b)
0.9	12	60	36.5	15	0.962	5	0.891	21	0.780	38	0.615	43	0.539	57	0.690	17(b)
0.9	12	86	36.5	22	0.925	35	0.712	63	0.784	71	0.624	78	0.505	82	0.671	17(b)
0.9	14	60	36.5	2	1.000	-6	1.000	-11	0.997	-17	0.990	-26	0.941	73	0.860	17(b)
0.9	14	30	36.5	-4	1.000	-9	0.998	18	0.986	-26	0.964	-31	0.888	56	0.834	17(b)
0.9	14	0	36.5	1	0.995	10	0.982	32	0.883	-30	0.740	-42	0.675	-13	0.736	17(b)
0.9	14	31	36.5	9	0.971	4	0.944	-1	0.742	8	0.581	15	0.602	40	0.647	17(b)
0.9	14	60	36.5	21	0.938	9	0.895	36	0.808	42	0.620	53	0.465			17(b)
0.9	14	71	36.5	21	0.916	10	0.801	51	0.808	67	0.613	62	0.502			17(b)
1.2	8	85	36.5	6	0.983	-5	0.985	26	0.715	46	0.461	36	0.709	21	0.955	17(c)
1.2	12	61	36.5	11	0.972	2	1.000	17	0.746	32	0.437	42	0.506	39	0.967	17(c)
1.2	12	85	36.5	11	1.000	0	0.612	39	0.496	38	0.725	58	0.486	51	0.705	17(c)
1.2	14	60	36.5	16	0.990	10	0.953	43	0.713	58	0.381	55	0.309	46	0.828	17(c)
1.2	14	86	36.5	11	0.983	2	0.530	30	0.364	48	0.528	42	0.703	59	0.600	17(c)
0.6	12	86	40.5	50	0.813	70	0.664			71	0.738	36	0.904	30	0.928	18(a)
0.6	14	60	40.5	26	0.893	27	0.712	36	0.709	42	0.691	20	0.826	39	0.914	18(a)
0.6	14	86	40.5	51	0.799	68	0.683					46	0.815	49	0.861	18(a)
0.9	8	85	40.5	16	0.810	24	0.669	45	0.627	31	0.911	11	0.994	9	0.886	18(b)
0.9	14	75	40.5	1	0.998	-3	0.998	-7	0.997	-10	0.996	-15	0.982	-56	0.820	18(b)
1.2	12	84	40.5	42	0.669	37	0.746	70	0.547			38	0.787	40	0.709	18(c)
1.2	14	60	40.5	2	0.932	8	0.862	33	0.450	43	0.499	28	0.968	34	0.883	18(c)
1.2	14	85	40.5	45	0.539	41	0.624	65	0.600	74	0.473	41	0.731	42	0.751	18(c)

Table B4. Configuration With Vortex Flap Deflected

M_∞	α, deg	θ, deg	FS	α_L^1, deg	PR1	α_L^2, deg	PR2	α_L^3, deg	PR3	α_L^4, deg	PR4	α_L^5, deg	PR5	α_L^6, deg	PR6	Figure in text
0.9	15	−75	32.8	−2	0.917	20	0.689	−13	0.791	−3	0.994	−18	0.971	−88	0.705	23(a)
0.9	15	−60	32.8	11	0.997	13	0.984	8	0.996	0	1.000	−18	0.963	82	0.652	23(a)
0.9	15	60	32.8	12	0.974	3	0.964	1	0.935	−5	0.900	5	0.650	41	0.437	23(a)
0.9	15	86	32.8	11	0.961	−1	0.947	−9	0.910	−14	0.899	6	0.637	57	0.426	23(a)
0.9	18	75	32.8	−1	0.998	−19	0.952	−49	0.727	−49	0.666	−54	0.638			23(a)
0.9	18	61	32.8	7	0.995	5	0.960	5	0.737	6	0.710	−33	0.674	82	0.665	23(a)
0.9	18	59	32.8	19	0.953	7	0.937	9	0.897	6	0.872	15	0.635	43	0.711	23(a)
0.9	18	71	32.8	19	0.947	6	0.928	3	0.882	2	0.863	18	0.659	41	0.727	23(a)
0.9	18	81	32.8	19	0.942	4	0.921	−1	0.867	−10	0.858	22	0.695	41	0.721	23(a)
0.9	22	75	32.8	21	0.859	−36	0.711	57	0.623	45	0.743	−58	0.576	44	0.682	23(a)
0.9	22	61	32.8	11	0.941	3	0.899	9	0.750	34	0.663	61	0.576	76	0.652	23(a)
0.9	22	30	32.8	33	0.909	23	0.900	51	0.780	28	0.640	19	0.723	27	0.765	23(a)
0.9	15	75	35.0	−2	0.950	25	0.732	−14	0.836	2	0.960	12	0.981	−53	0.889	23(b)
0.9	15	60	35.0	9	0.997	13	0.950	7	0.935	3	1.000	13	0.986	62	0.893	23(b)
0.9	15	30	35.0	7	1.000	5	1.000	4	1.000	2	0.998	−20	0.957	55	0.845	23(b)
0.9	15	60	35.0	11	0.964	−3	0.948	16	0.901	13	0.790	2	0.512	64	0.507	23(b)
0.9	15	85	35.0	11	0.951	4	0.928	43	0.592	13	0.683	43	0.463	72	0.557	23(b)
0.9	18	75	35.0	−2	0.999	14	0.986	−46	0.846	57	0.708					23(b)
0.9	18	60	35.0	3	0.997	−3	0.971	−6	0.792	21	0.708	−57	0.584			23(b)
0.9	18	60	35.0	20	0.932	3	0.909	−4	0.854	17	0.626	29	0.729	66	0.524	23(b)
0.9	18	85	35.0	20	0.924	2	0.894	40	0.460	32	0.727	36	0.717	65	0.562	23(b)
0.9	22	75	35.0	−14	0.933	29	0.845	57	0.662	83	0.551					23(b)
0.9	22	30	35.0	33	0.888	18	0.967	37	0.665	22	0.721	25	0.644	41	0.577	23(b)
0.9	22	59	35.0	31	0.871	8	0.875	18	0.794	24	0.818	32	0.760	48	0.714	23(b)
0.9	22	85	35.0	30	0.853	0	0.788	43	0.503	30	0.734	38	0.743	57	0.557	23(b)
0.9	15	30	36.5	6	1.000	3	1.000	0	1.000	−4	0.999	17	0.976	42	0.927	23(c)
0.9	15	60	36.5	11	0.957	6	0.928	−44	0.634	8	0.615	15	0.494	53	0.653	23(c)
0.9	15	85	36.5	7	0.958	1	0.960	67	0.668	41	0.514	54	0.495	61	0.706	23(c)
0.9	18	−76	36.5	−1	1.000	−12	0.994	−38	0.907	51	0.775	88	0.642			23(c)
0.9	18	60	36.5	2	0.998	−5	0.986	−11	0.888	−25	0.753	−67	0.581			23(c)
0.9	18	31	36.5	7	0.995	0	0.987	5	0.957	10	0.778	−33	0.660	42	0.541	23(c)
0.9	18	30	36.5	17	0.951	1	0.926	4	0.860	14	0.627	14	0.663	45	0.486	23(c)
0.9	18	85	36.5	18	0.942	10	0.875	77	0.535	42	0.705	47	0.618			23(c)
0.9	22	−75	36.5	12	0.960	24	0.906	−48	0.773	−84	0.601					23(c)
0.9	22	29	36.5	7	0.946	11	0.850	−13	0.483	−18	0.480	−40	0.474	27	0.458	23(c)
0.9	22	30	36.5	30	0.887	16	0.956	35	0.697	23	0.701	29	0.540	83	0.445	23(c)
0.9	22	59	36.5	33	0.833	5	0.526	31	0.693	29	0.780	44	0.559			23(c)
0.9	22	85	36.5	26	0.889	17	0.791	41	0.712	36	0.734	56	0.542			23(c)
0.9	12	−75	40.5	3	1.000	1	0.996	6	0.979	−18	0.957	−27	0.884	−50	0.728	23(d)

Table B4. Concluded

M_∞	α, deg	θ, deg	FS	α_L^1, deg	PR1	α_L^2, deg	PR2	α_L^3, deg	PR3	α_L^4, deg	PR4	α_L^5, deg	PR5	α_L^6, deg	PR6	Figure in text
0.9	15	30	40.5	3	0.975	-14	0.907	45	0.666	-35	0.588	-28	0.900	3	0.965	23(d)
0.9	15	87	40.5	-16	0.973	4	0.968	70	0.731	57	0.644	43	0.749	39	0.881	23(d)
0.9	18	75	40.5	1	0.999	8	0.995	19	0.968	-33	0.899	52	0.762			23(d)
0.9	18	60	40.5	1	0.999	-7	0.990	14	0.958	21	0.919	42	0.744			23(d)
0.9	18	0	40.5	4	0.946	25	0.785	49	0.652	24	0.670	22	0.582	5	0.546	23(d)
0.9	18	30	40.5	31	0.686	13	0.654	19	0.627	10	0.599	15	0.596	48	0.505	23(d)
0.9	18	60	40.5	20	0.947	25	0.777	80	0.631	43	0.598	40	0.563			23(d)
0.9	18	86	40.5	2	0.969	1	0.963	37	0.663	71	0.588	59	0.575			23(d)
0.9	22	75	40.5	10	0.972	18	0.958	33	0.906	39	0.845	60	0.698			23(d)
0.9	22	61	40.5	11	0.983	20	0.958	34	0.910	36	0.857	51	0.725			23(d)
0.9	22	30	40.5	21	0.887	39	0.732	-44	0.570	56	0.552	65	0.581	50	0.494	23(d)
0.9	22	30	40.5	46	0.650	25	0.618	31	0.613	39	0.498	28	0.557	70	0.439	23(d)
0.9	22	60	40.5	26	0.899	32	0.634	84	0.549	64	0.610	44	0.626			23(d)
0.9	22	86	40.5	21	0.740	4	0.872	6	0.387	56	0.462	65	0.511			23(d)

Table B5. Configuration With Wing Fences

M_∞	α, deg	θ, deg	FS	α_L^1, deg	PR1	α_L^2, deg	PR2	α_L^3, deg	PR3	α_L^4, deg	PR4	α_L^5, deg	PR5	α_L^6, deg	PR6	Figure in text
0.9	18	75	32.8	6	0.917	19	0.778	20	0.790	-34	0.864	-58	0.683			25(a)
0.9	18	60	32.8	6	0.998	0	1.000	16	0.989	44	0.841	73	0.606			25(a)
0.9	18	-29	32.8	6	0.992	2	0.987	-8	0.884	5	0.542	-33	0.417	49	0.406	25(a)
0.9	18	60	32.8	27	0.914	13	0.894	22	0.790	27	0.675	48	0.390			25(a)
0.9	18	75	35.0	-5	0.937	19	0.843	-17	0.747	-30	0.771	-47	0.690			25(b)
0.9	18	61	35.0	3	1.000	1	0.992	-15	0.983	30	0.940	46	0.768			25(b)
0.9	18	30	35.0	2	0.991	7	0.981	25	0.900	38	0.570	-61	0.493	48	0.560	25(b)
0.9	18	60	35.0	31	0.874	7	0.849	38	0.672			56	0.465			25(b)
0.9	18	86	35.0	26	0.884	6	0.905	34	0.788			66	0.567			25(b)
0.9	18	-75	36.5	6	0.928	22	0.879	31	0.829	-27	0.741	40	0.678			25(c)
0.9	18	60	36.5	0	0.998	4	0.988	-13	0.921	-24	0.908	-38	0.782	-86	0.619	25(c)
0.9	18	31	36.5	-1	0.991	11	0.983	24	0.915	-40	0.785	56	0.711	-43	0.650	25(c)
0.9	18	31	36.5	21	0.885	10	0.858	7	0.538	14	0.477	32	0.330	50	0.485	25(c)
0.9	18	60	36.5	32	0.871	26	0.769	86	0.478			63	0.371			25(c)
0.9	18	86	36.5	16	0.851	25	0.570	74	0.435	81	0.501	63	0.559			25(c)
0.9	18	75	40.5	-5	0.944	10	0.967	-25	0.915	33	0.811	43	0.742			25(d)
0.9	18	38	40.5	11	0.791	3	0.530	18	0.442	51	0.393	29	0.559	49	0.537	25(d)
0.9	18	60	40.5	31	0.777	38	0.712	88	0.426			46	0.510			25(d)
0.9	18	85	40.5	65	0.456	58	0.536	78	0.585							25(d)

Table B6. Configuration With Large Wing Fences and Vortex Flap Deflected

M_∞	α, deg	θ, deg	FS	α_L^1, deg	PR1	α_L^2, deg	PR2	α_L^3, deg	PR3	α_L^4, deg	PR4	α_L^5, deg	PR5	α_L^6, deg	PR6	Figure in text
0.9	14	85	40.5							43	0.712					26(d)

Table B7. Configuration With Apex Flaps Deflected

M_∞	α, deg	θ, deg	FS	α_L^1, deg	PR1	α_L^2, deg	PR2	α_L^3, deg	PR3	α_L^4, deg	PR4	α_L^5, deg	PR5	α_L^6, deg	PR6	Figure in text
0.9	18	85	36.5							45	0.204					27(c)
0.9	22	84	36.5							73	0.221					27(c)
0.9	18	30	32.8							2	0.985					28(a)
0.9	18	60	32.8							2	1.000					28(a)
0.9	18	85	32.8							2	1.000					28(a)
0.9	22	30	32.8							3	0.967					28(a)
0.9	22	60	32.8							2	1.000					28(a)
0.9	22	85	32.8							2	1.000					28(a)
0.9	18	75	35.0	21	1.000	21	0.980	20	0.833	27	0.635	60	0.283	57	0.223	28(b)
0.9	18	0	35.0	12	0.995	11	0.984	9	0.905	13	0.935	9	0.919	43	0.259	28(b)
0.9	18	60	35.0							2	1.000					28(b)
0.9	18	85	35.0							3	1.000					28(b)
0.9	22	30	35.0							2	1.000					28(b)
0.9	22	61	35.0							3	1.000					28(b)
0.9	22	86	35.0							68	0.222					28(b)
0.9	18	60	36.5							2	1.000					28(c)
0.9	18	85	36.5							64	0.252					28(c)
0.9	22	61	36.5							63	0.291					28(c)
0.9	22	86	36.5							63	0.292					28(c)
0.9	22	55	40.5	12	0.753	13	0.853	11	0.900	16	0.901	28	0.784	40	0.773	28(d)
0.9	18	60	40.5							18	0.365					28(d)
0.9	18	86	40.5							13	0.562					28(d)

References

1. Reubush, David E.; and Bare, E. Ann: *Investigation of a Supersonic Cruise Fighter Model Flow Field.* NASA TM-86361, 1985.

2. Yaros, Steven F.: *Theoretical and Experimental Flow Fields for a Supersonic Cruise Fighter Forebody.* NASA TM-86450, 1985.

3. Staff of the Propulsion Aerodynamics Branch: *A User's Guide to the Langley 16-Foot Transonic Tunnel Complex—Revision 1.* NASA TM-102750, 1990. (Supersedes NASA TM-83186, 1981.)

4. Doane, P. M.: *Design and Calibration of an Automated Cone Probe Rake for Mach Numbers From 1.60 to 4.65.* MDC A1052, McDonnell Douglas Corp., Dec. 9, 1971.

5. Verhaagen, N.; and Van Ransbeeck, P.: Experimental and Numerical Investigation of the Flow in the Core of a Leading Edge Vortex. AIAA-90-0384, Jan. 1990.

6. Kulfan, R. M.: Wing Geometry Effects on Leading-Edge Vortices. AIAA-79-1872, Aug. 1979.

7. Bütefisch, K. A.: Flow Field Visualization Study on a 65° Delta Wing. *ICAS Proceedings, 1988—16th Congress of the International Council of the Aeronautical Sciences,* 1988, pp. 1845 1851.

Table I. Configuration Matrixes Tested

Configuration[a]	Mach	Configuration tested at α, deg, of									
		−4	0	4	8	12	14	18	22	26	30
B	0.6	√	√	√	√	√	√	√	√	√	√
	.9	√	√	√	√	√	√	√	√	√	√
	1.2	√	√	√	√	√	√	√	√	√	(b)
B+5	0.6	√	√	√	√	√	√				
	.9	√	√	√	√	√	√				
	1.2	√	√	√	√						
B 5	0.6	√	√	√	√	√	√				
	.9	√	√	√	√	√	√				
	1.2	√	√	√	√	√	√				
VF	0.9	√	√	√	√	√	(c)	√	√	√	√
LWF	0.9							√		√	
SWF	0.9							√	√	√	√
LWF+VF	0.9				√	√	√				
LAF	0.9	√	√	√	√	√	√	√	√	√	√
SAF	0.9							√	√	√	√

[a]The configuration designations are defined as follows:

B: Baseline at $\beta = 0°$
B+5: Baseline at $\beta = 5°$
B 5: Baseline at $\beta = -5°$
VF: Vortex flap
LWF: Large wing fence
SWF: Small wing fence
LAF: Large apex flap
SAF: Small apex flap

[b]At fuselage station 40.5, no data at $\alpha = 30°$.

[c]$\alpha = 15°$.

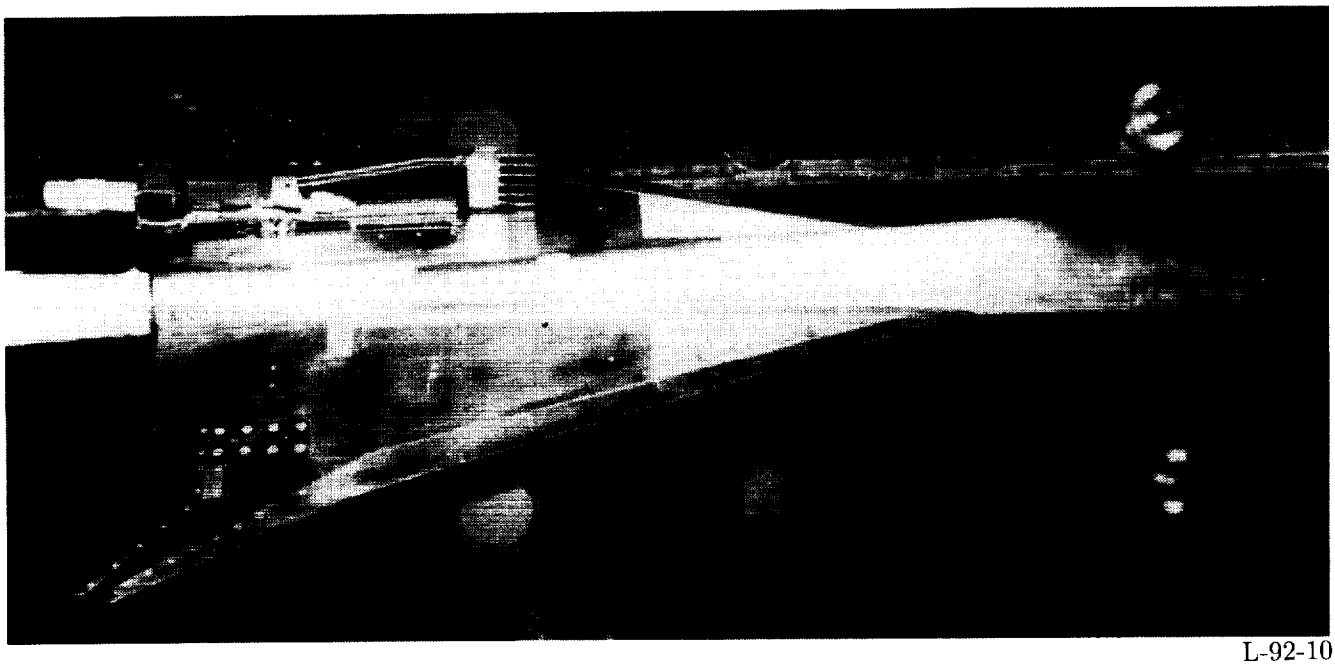

L-92-10

Figure 1. Top view of model installed in 16-Foot Transonic Tunnel.

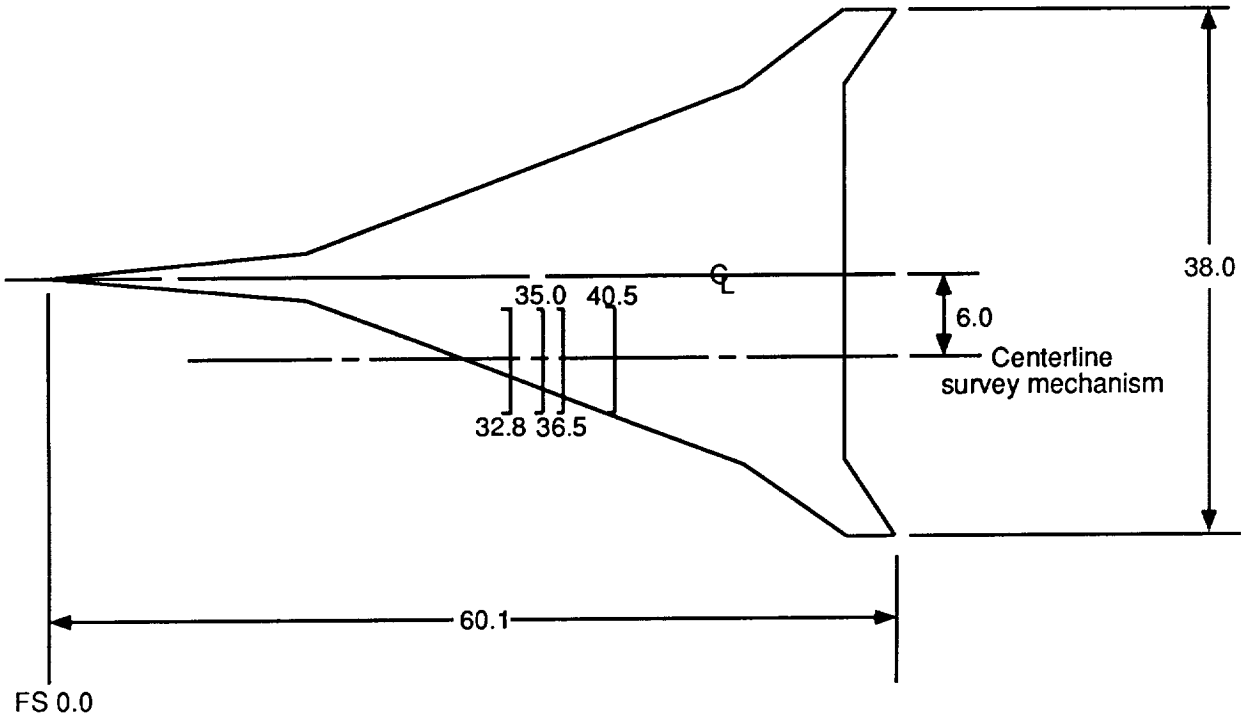

Figure 2. Top-view sketch of the model showing flow-field survey stations. Linear dimensions are in inches.

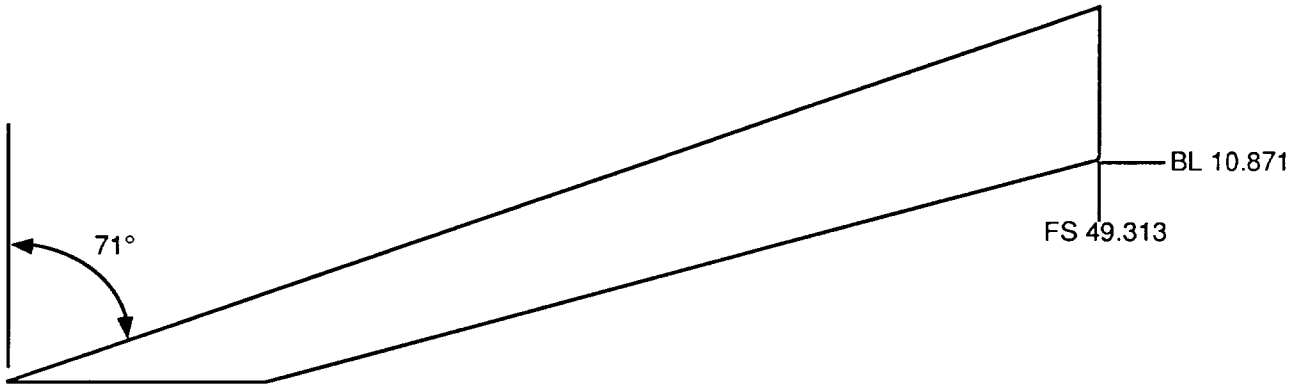

Flap deflection angle, deg	α, deg
30	-4 to 14
45	18 to 30

(a) Vortex flap.

Figure 3. Sketches of vortex control devices. Linear dimensions are in inches.

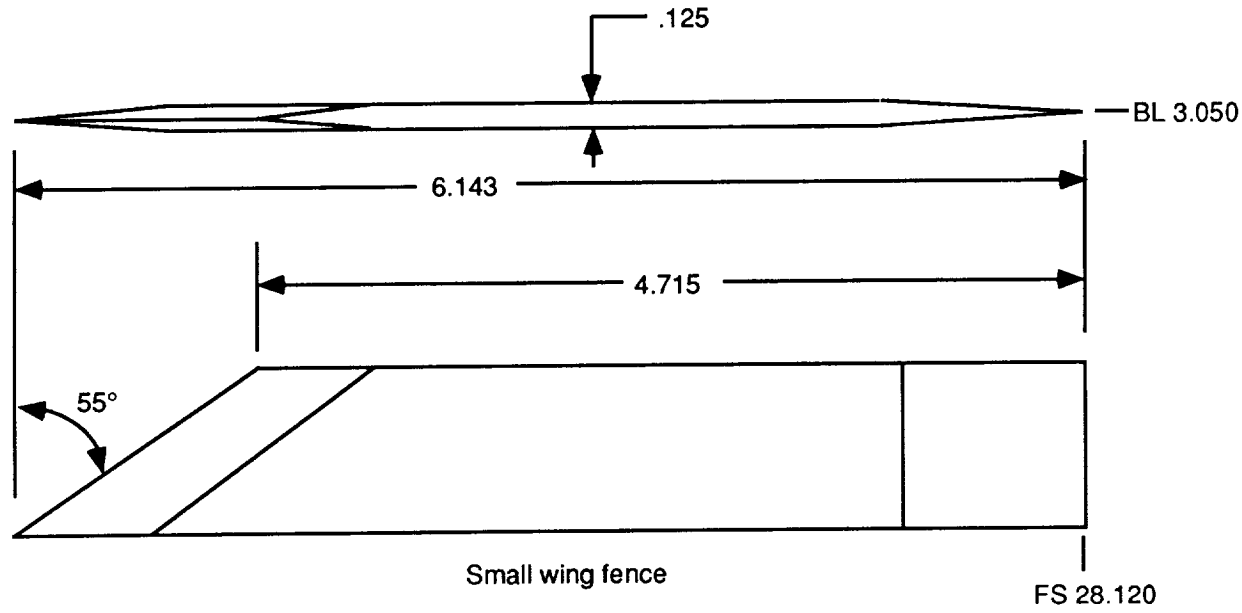

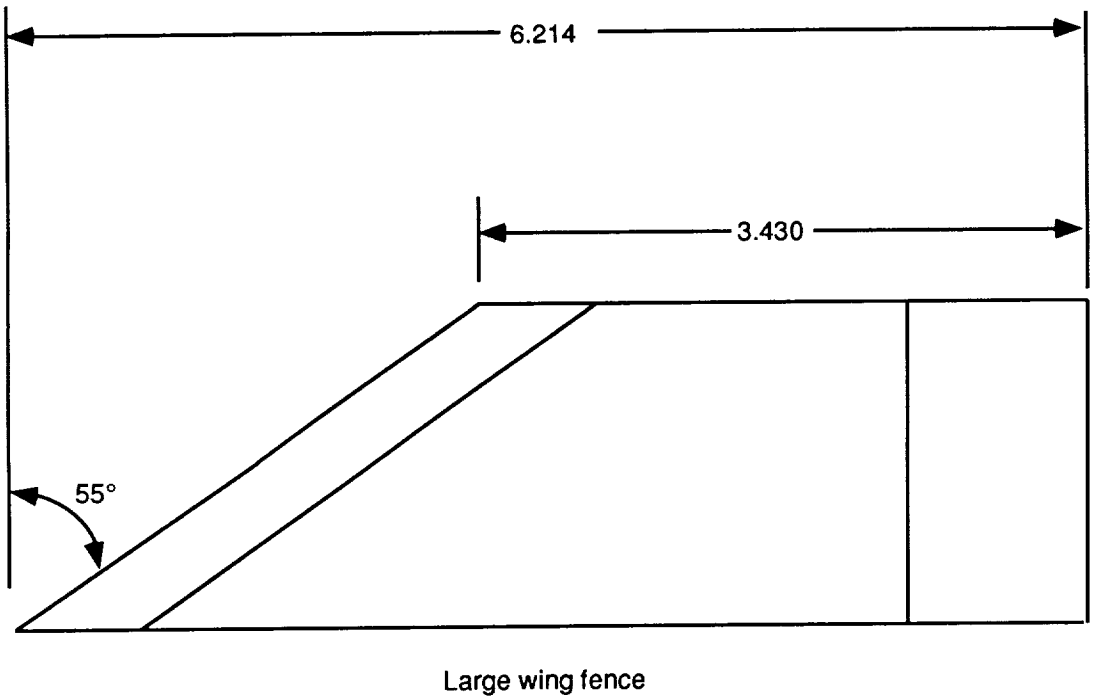

(b) Wing fences.

Figure 3. Continued.

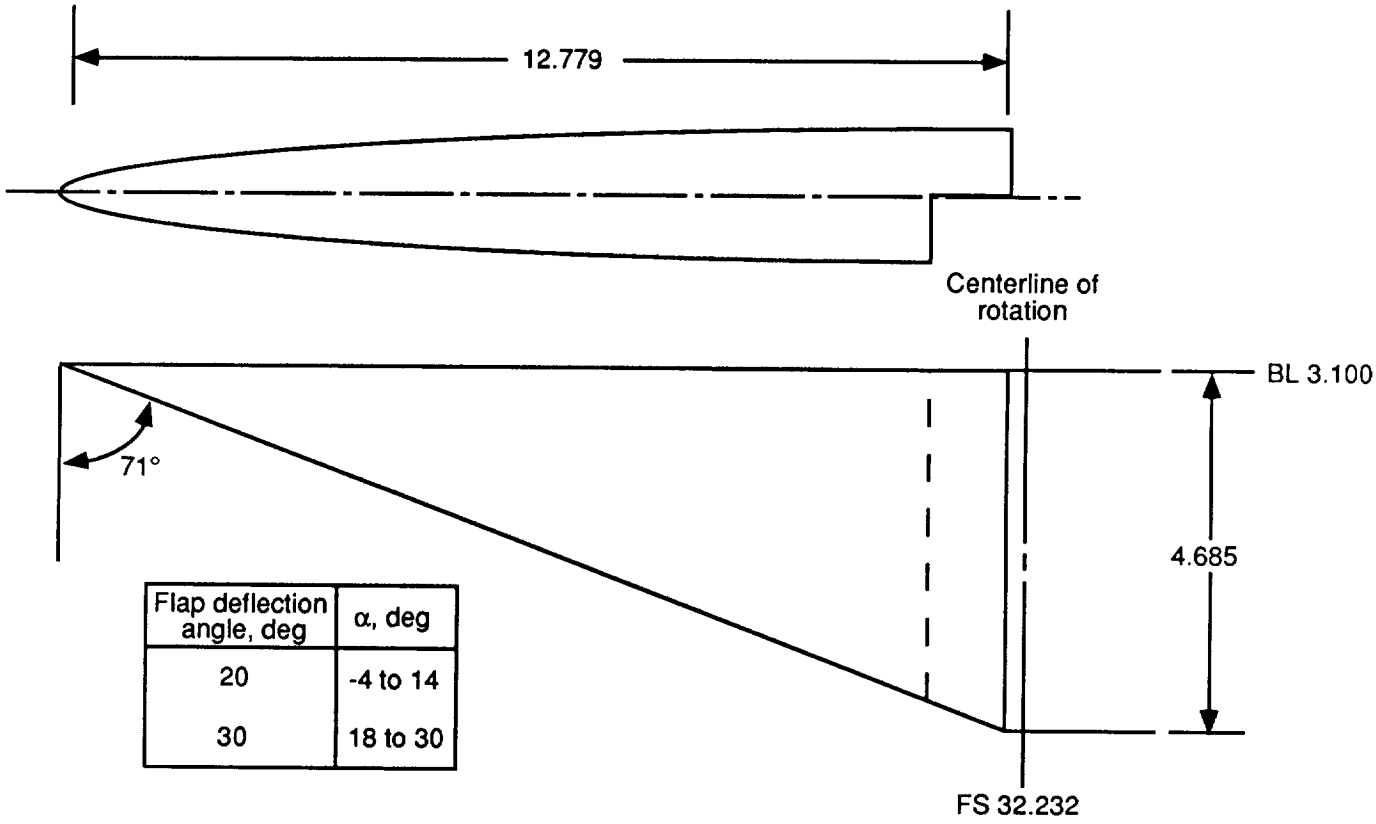

Flap deflection angle, deg	α, deg
20	-4 to 14
30	18 to 30

(c) Large apex flap.

Figure 3. Continued.

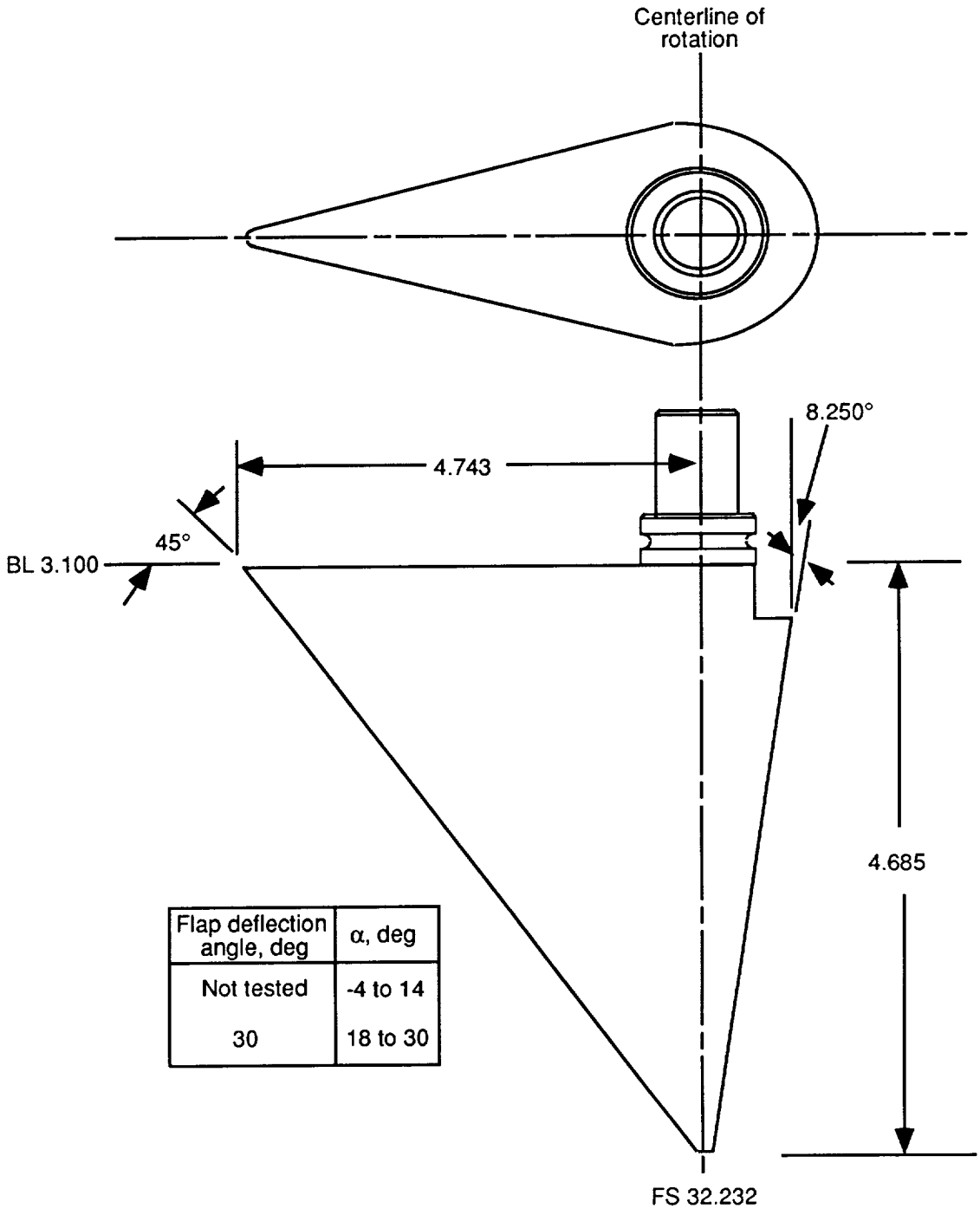

(d) Small apex flap.

Figure 3. Concluded.

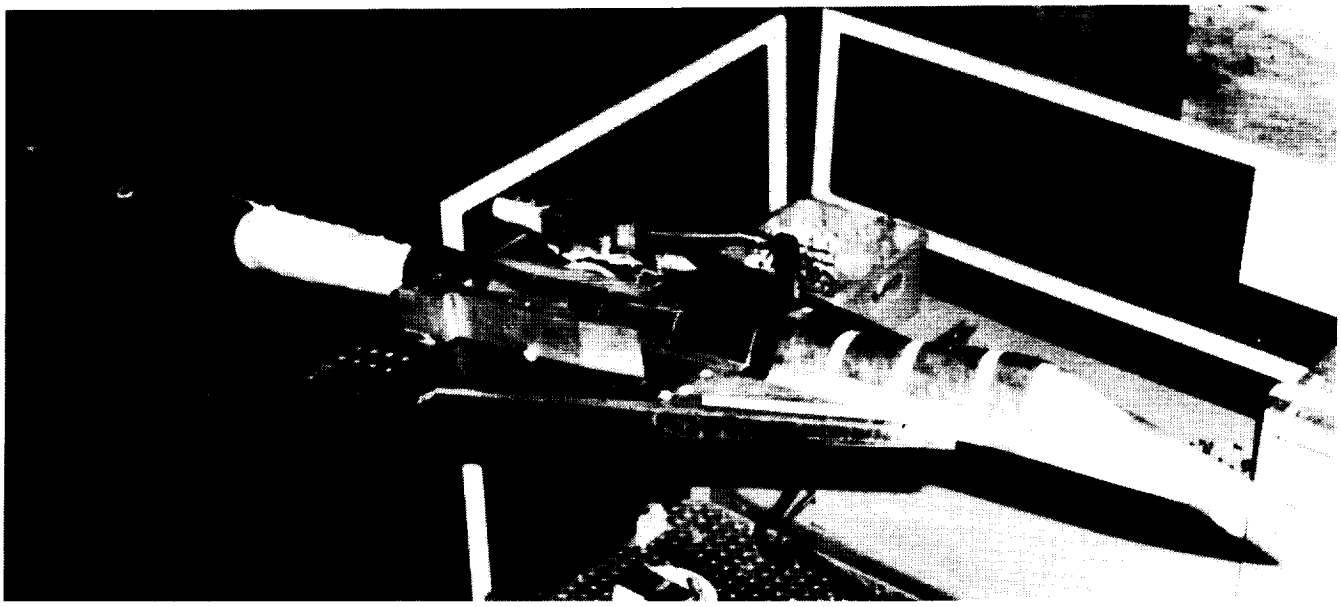

(a) Vortex flap.

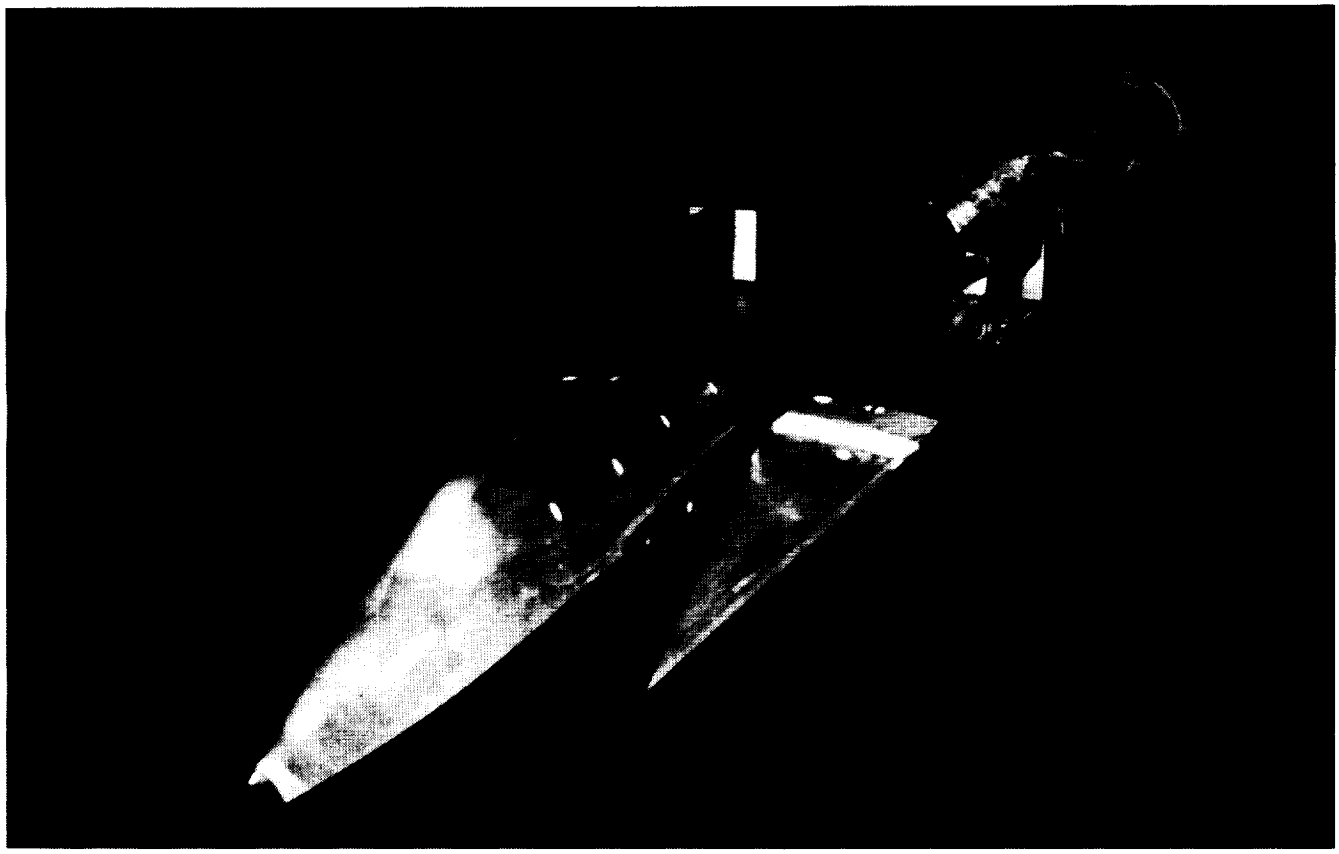

(b) Large apex flap.

L-92-11

Figure 4. Model with vortex control devices installed.

(c) Small apex flap.

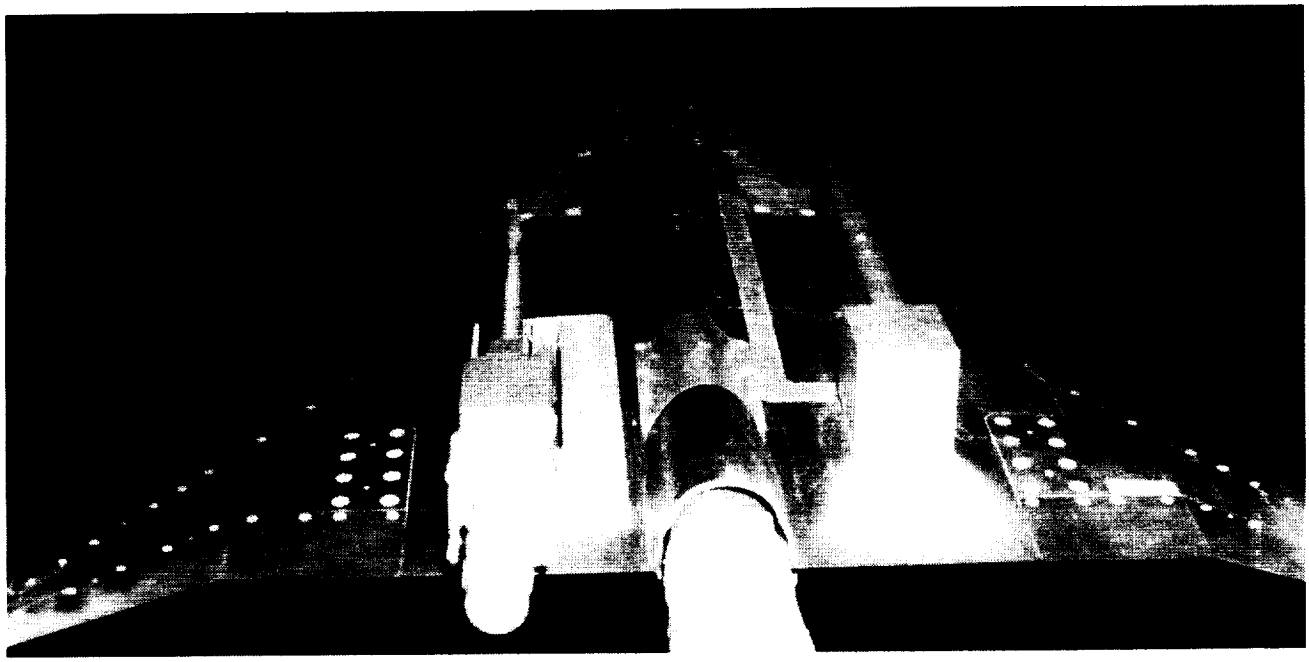

(d) Large wing fence.

L-92-12

Figure 4. Concluded.

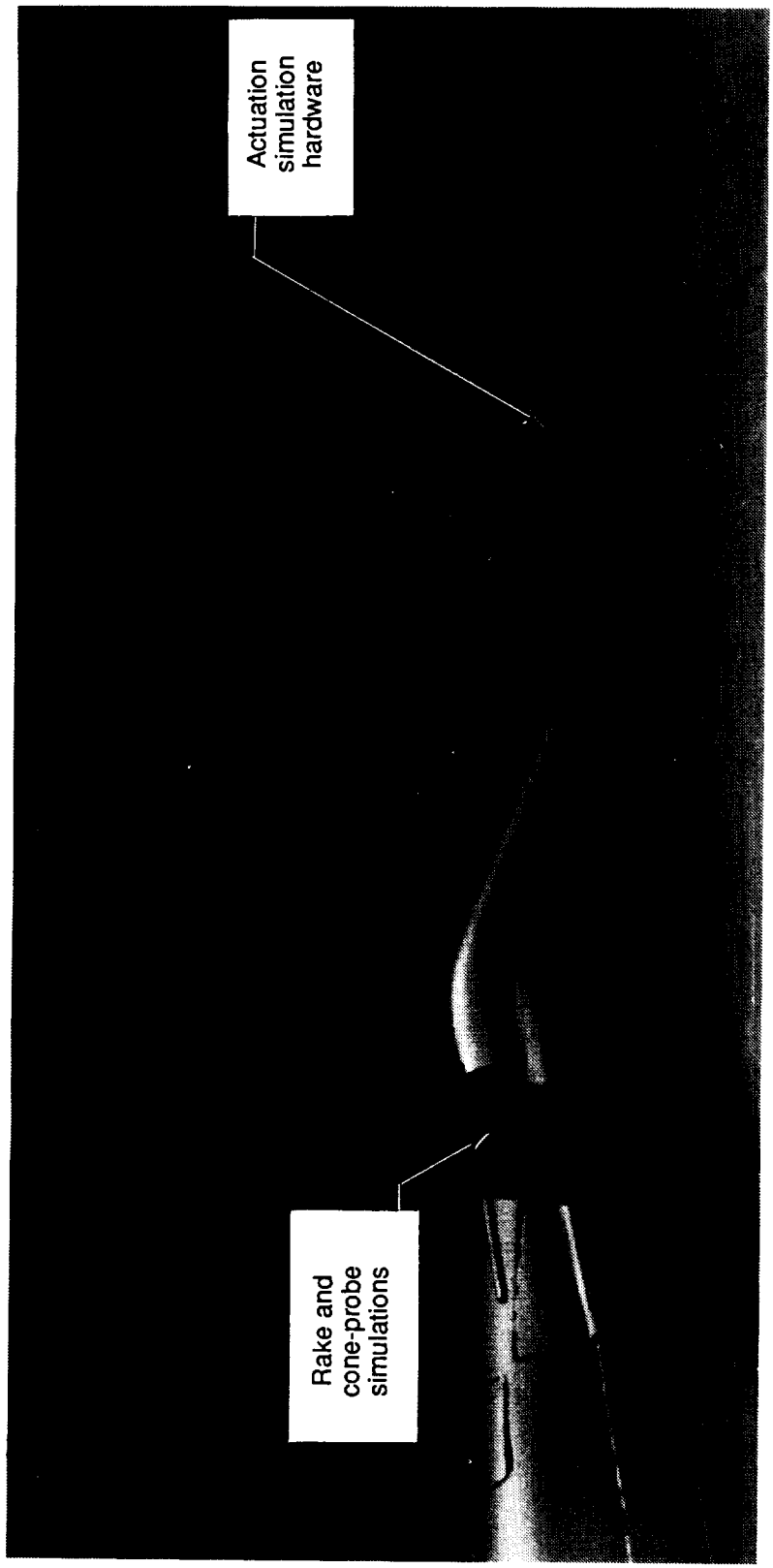

L-92-13

(a) Simulation hardware.

Figure 5. Flow-field survey simulation hardware.

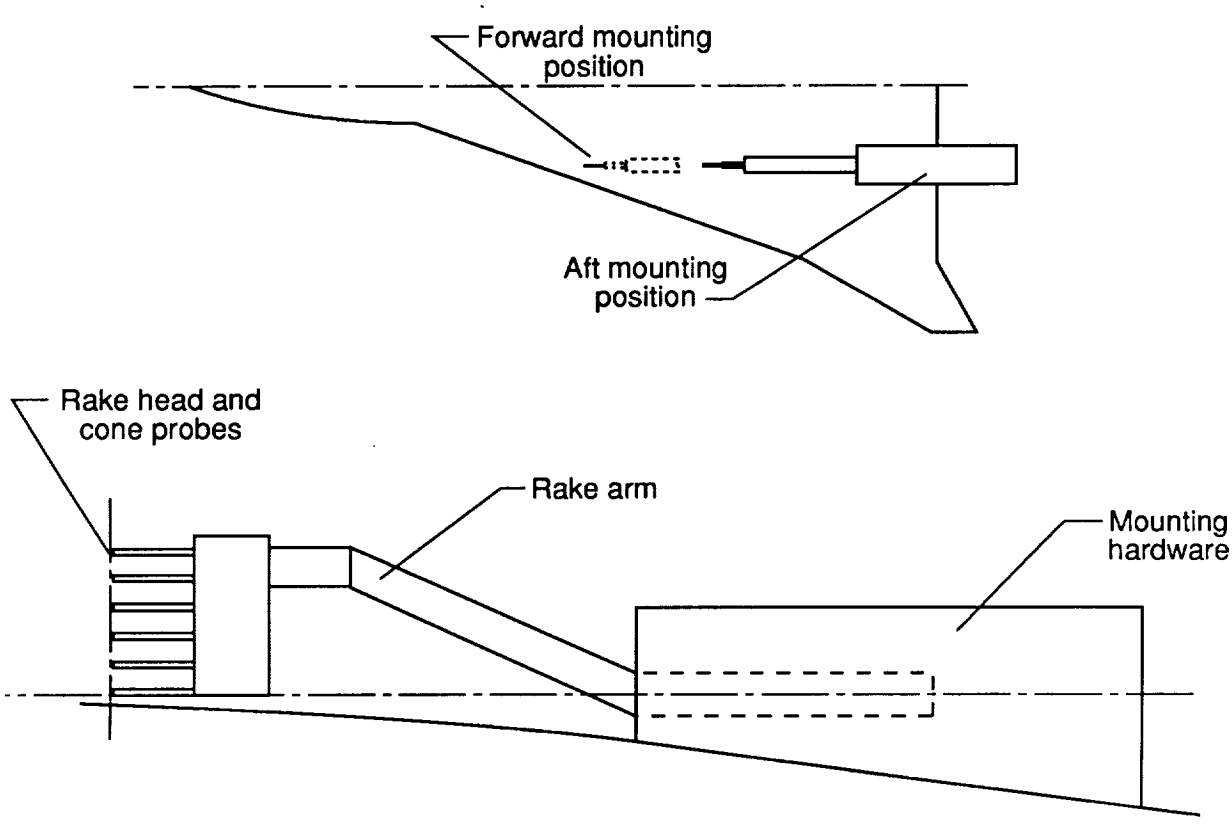

(b) Sketch of simulation hardware.

Figure 5. Concluded.

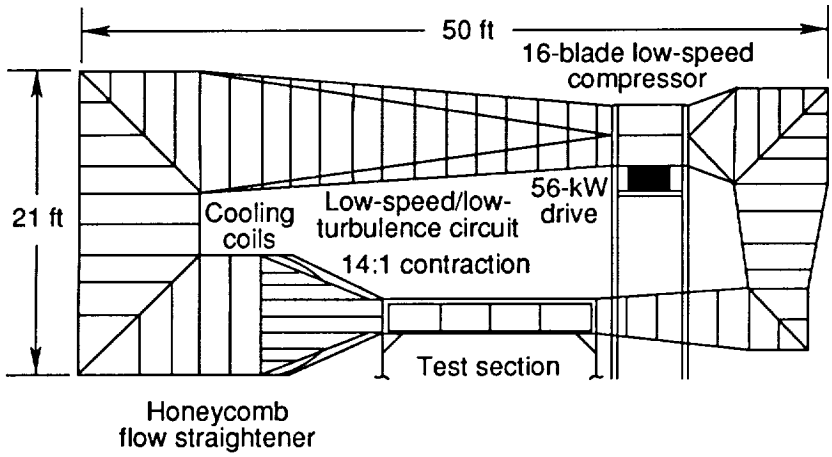

- 3- by 3-ft test section
- 1 to 250 ft/sec
- Re = 1×10^6
- Turbulence less than 0.1%
- Polyethylene glycol mist "smoke seeding"

(a) Wind tunnel.

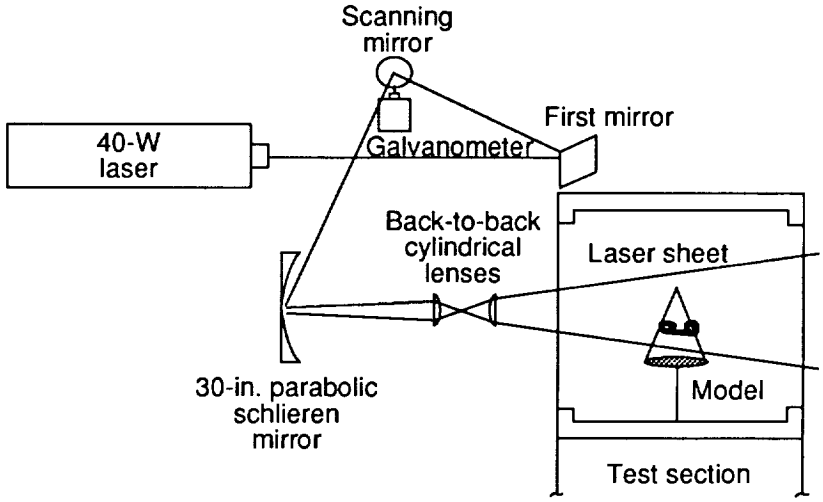

- 2- by 200-mm laser sheet
- 40-W laser
- 6000-pulse/sec rate
- Electro-optical system
  - Spin physics high-speed video
  - McDonnell Douglas image processing digitizer

(b) Imaging system.

Figure 6. Sketch of the McDonnell Douglas Research Laboratories Shear Flow Facility.

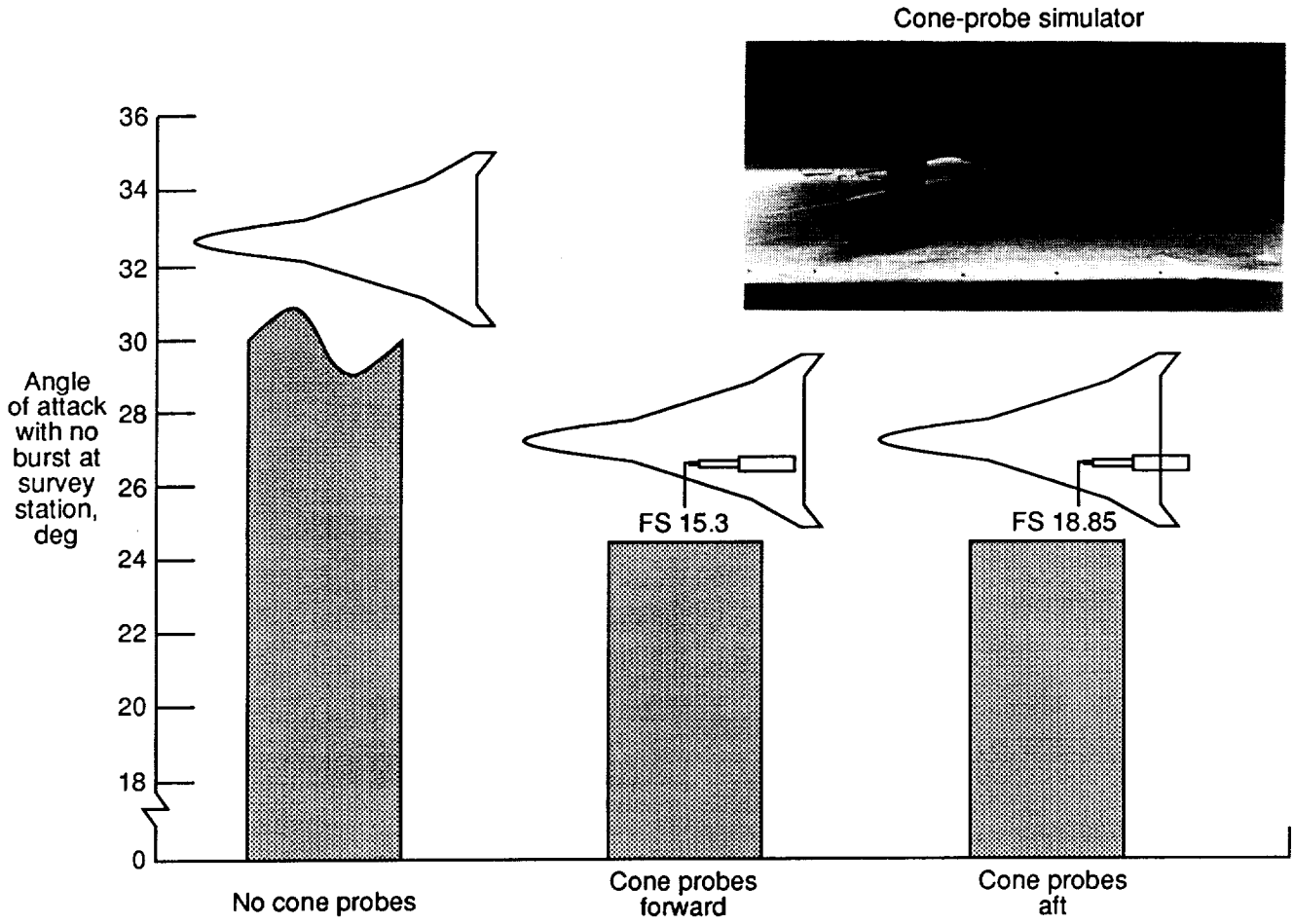

Figure 7. Effect of survey mechanism and cone-probe simulation on the angle of attack of vortex burst.

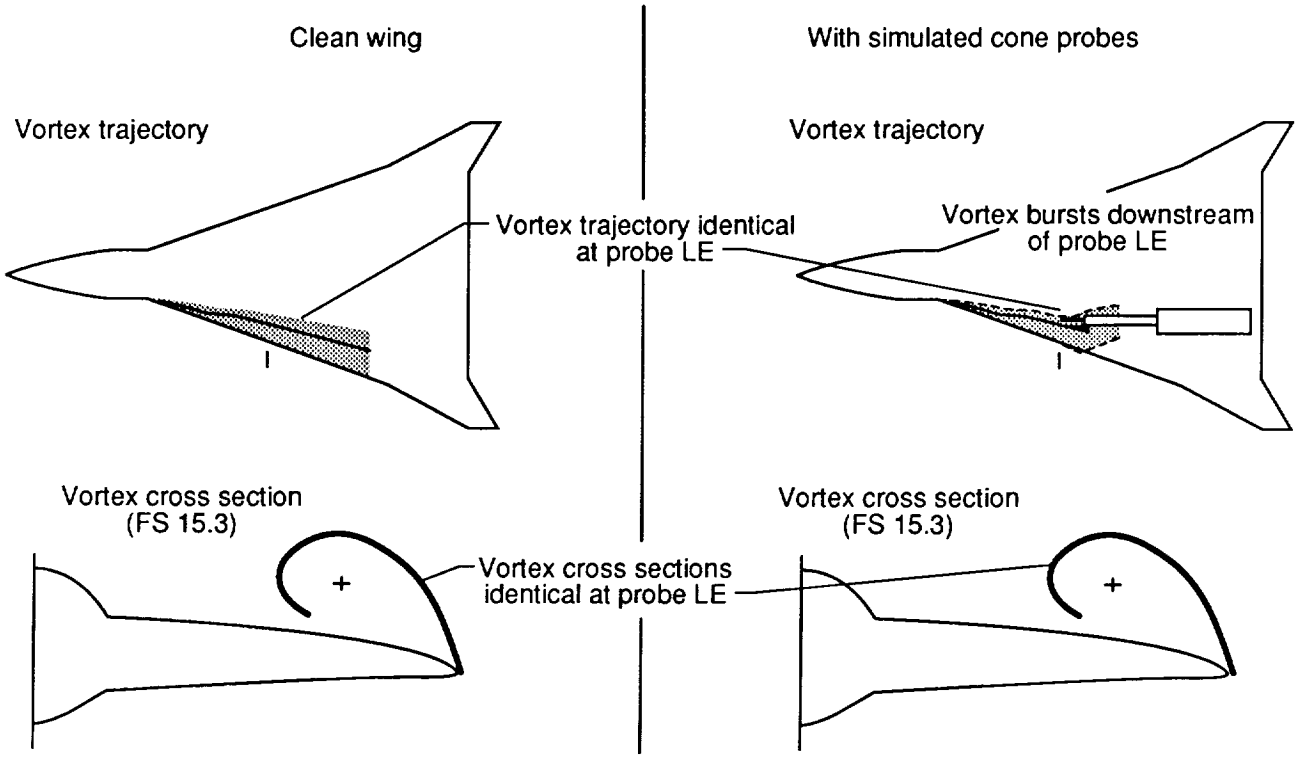

Figure 8. Effect of survey mechanism and cone-probe simulation on vortex trajectory and cross section. Angle of attack, 18°; angle of sideslip, 0°; Re per foot, 600 000.

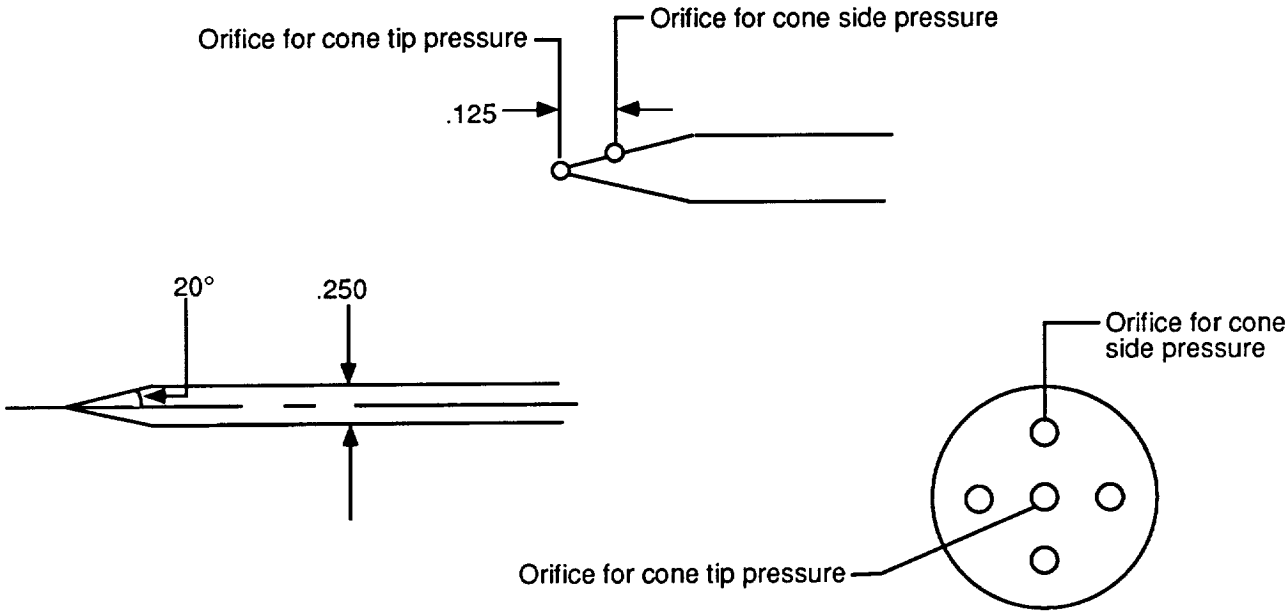

(a) Sketch of cone probe.

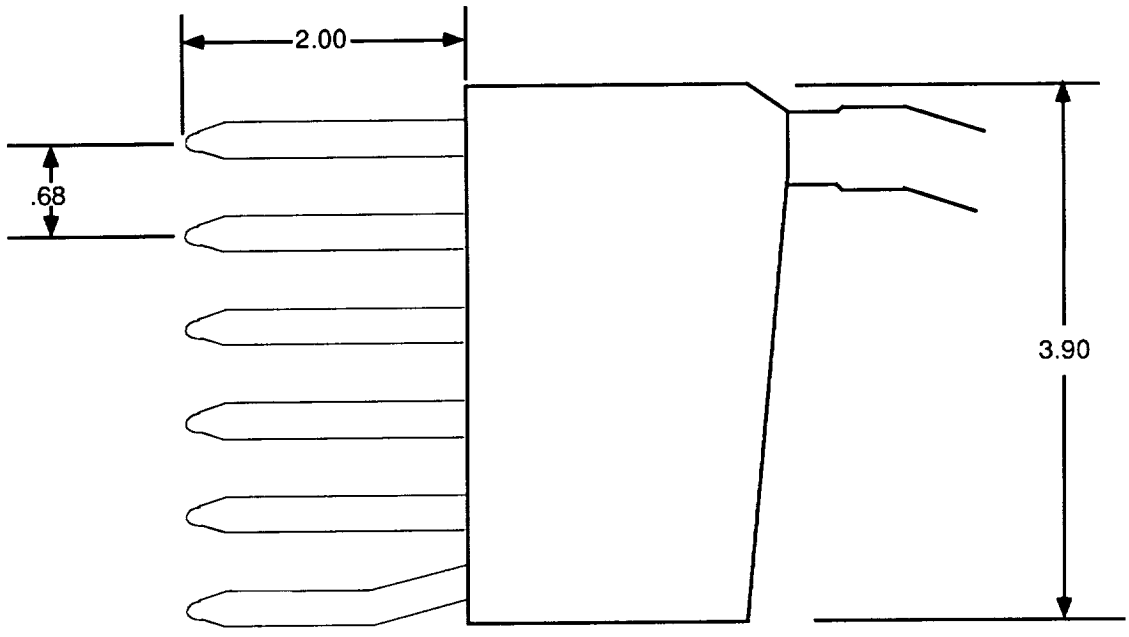

(b) Sketch of cone probes in rake.

Figure 9. Sketch of cone probe and survey mechanism. Dimensions are in inches.

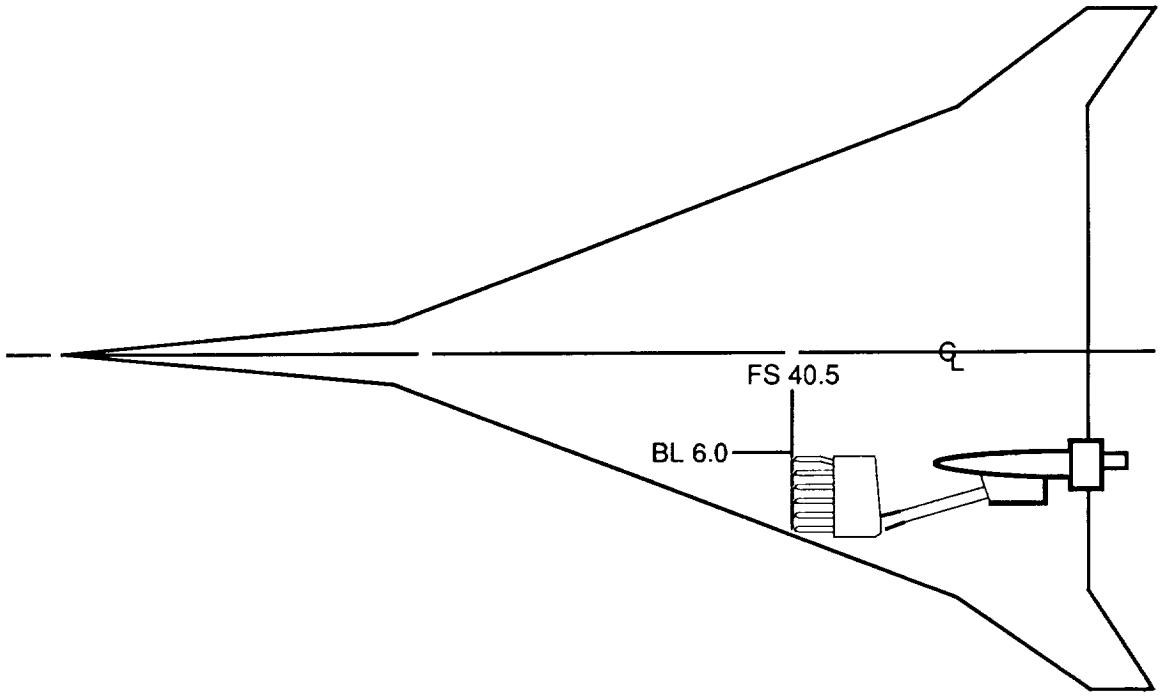

(c) Sketch of rake and survey mechanism mounted on model.

Figure 9. Concluded.

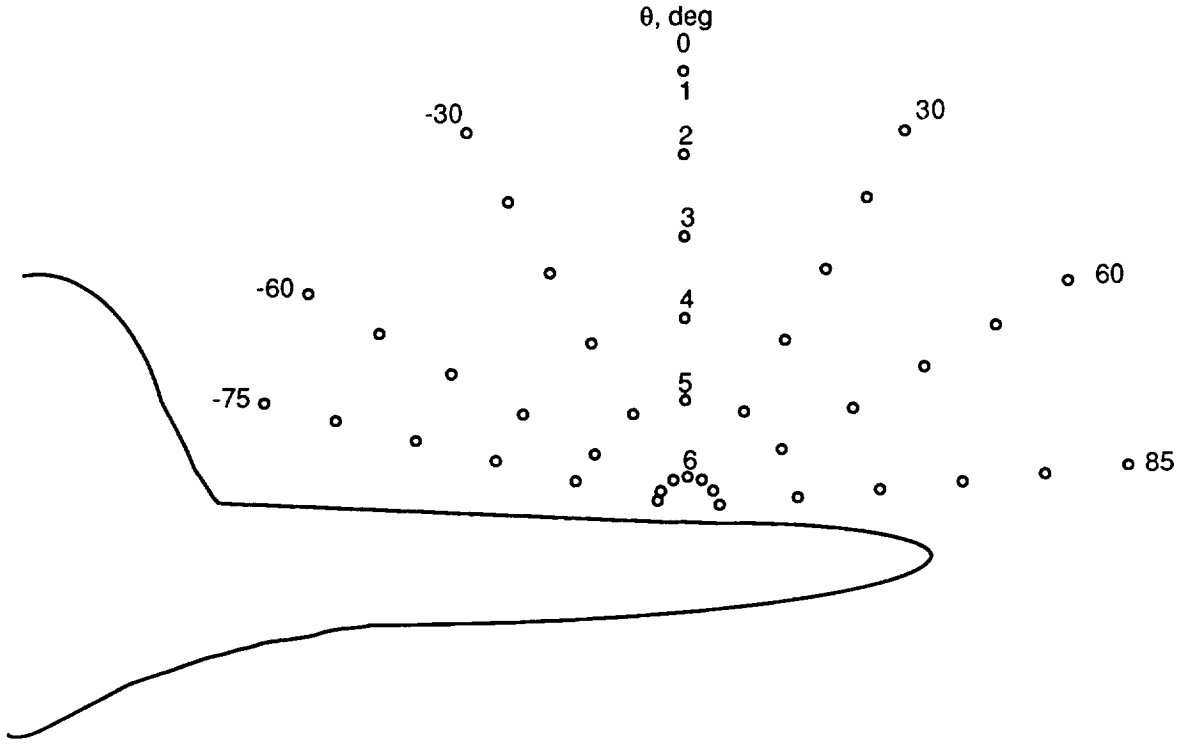

(a) FS 32.8.

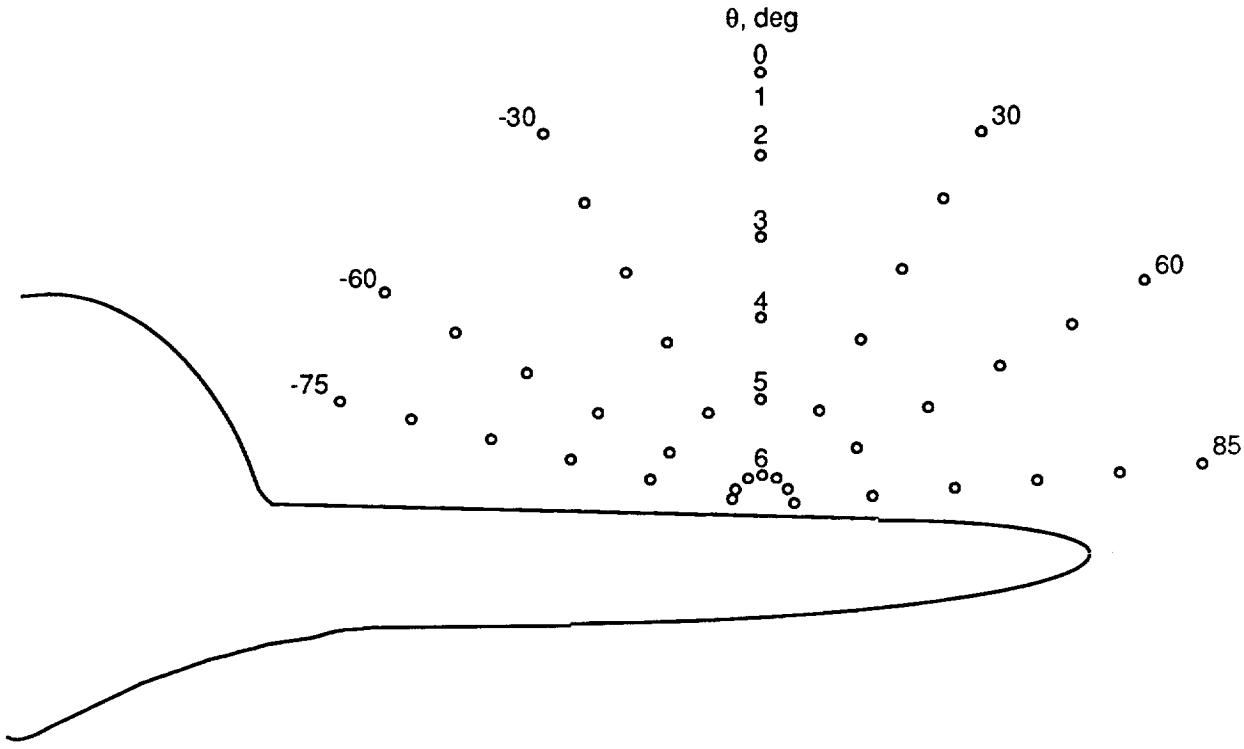

(b) FS 35.0.

Figure 10. Sketches showing the flow-field survey points and probe numbering scheme.

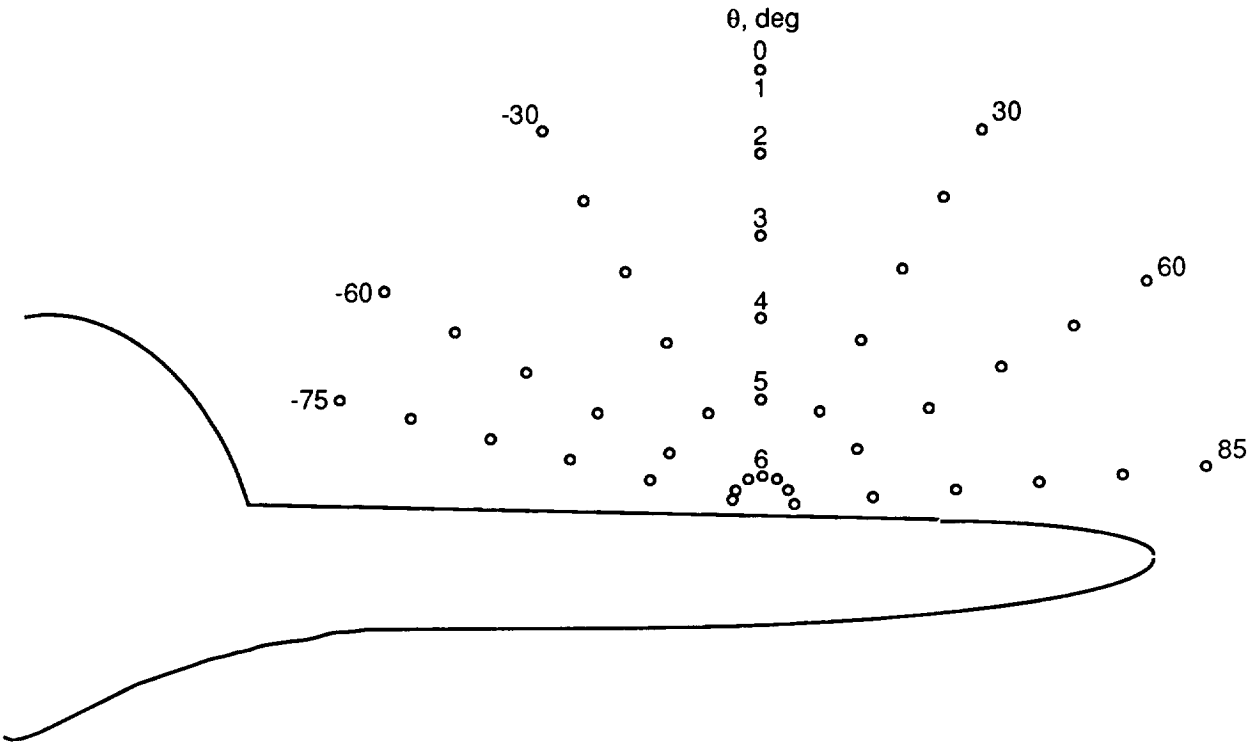

(c) FS 36.5.

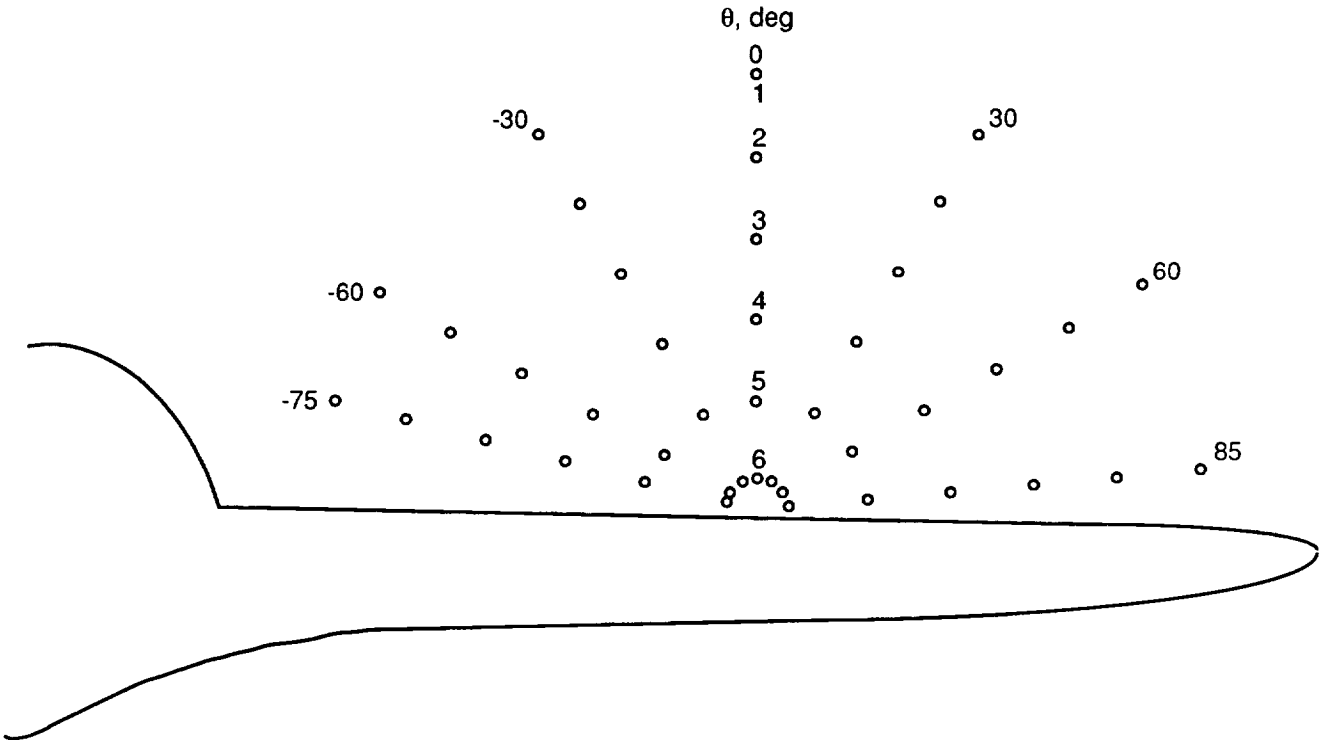

(d) FS 40.5.

Figure 10. Concluded.

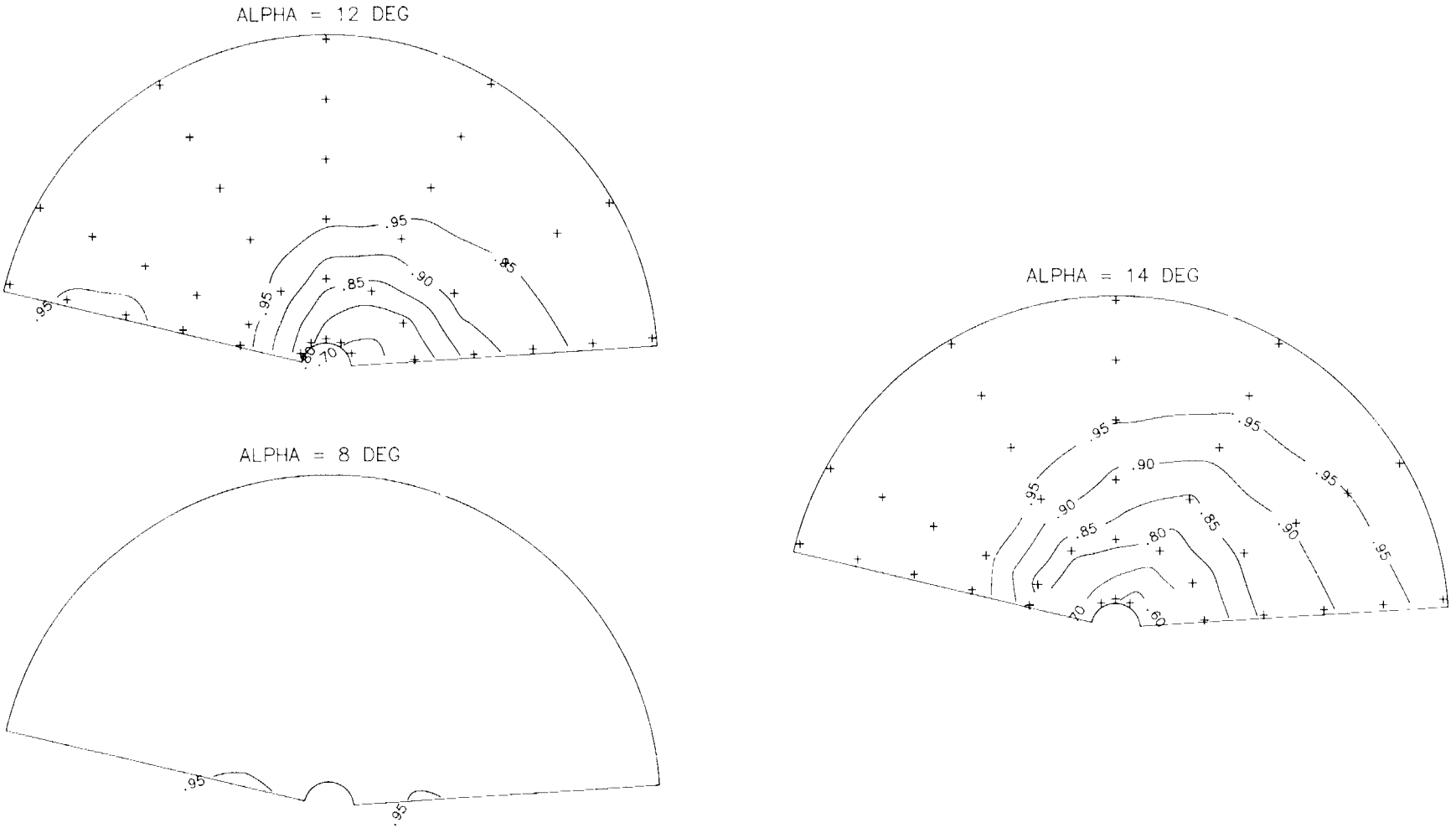

(a) Mach = 0.6.

Figure 11. Total pressure recovery contours for baseline configuration at $\beta = 0°$ and at fuselage station 32.8.

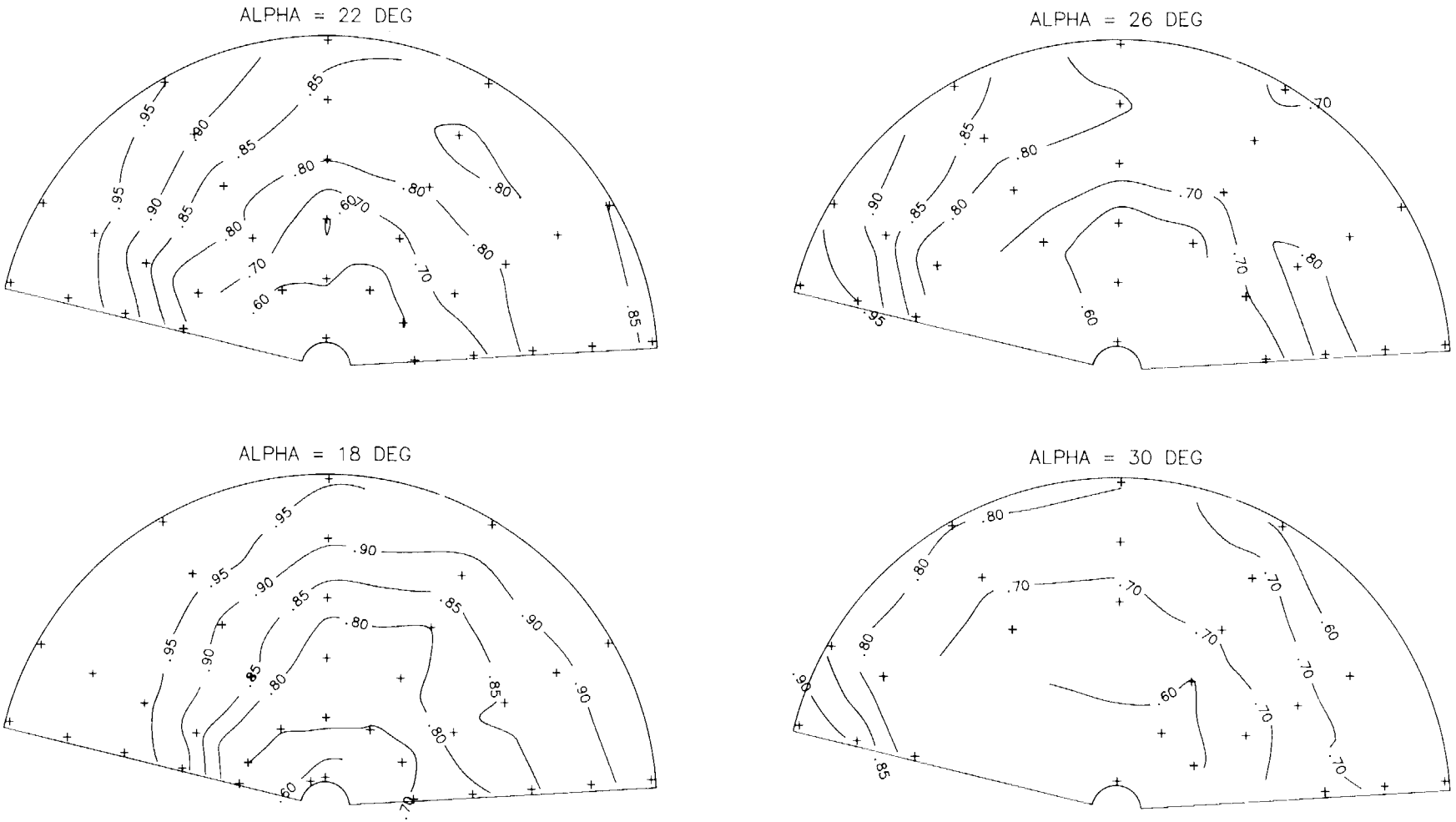

(a) Concluded.

Figure 11. Continued.

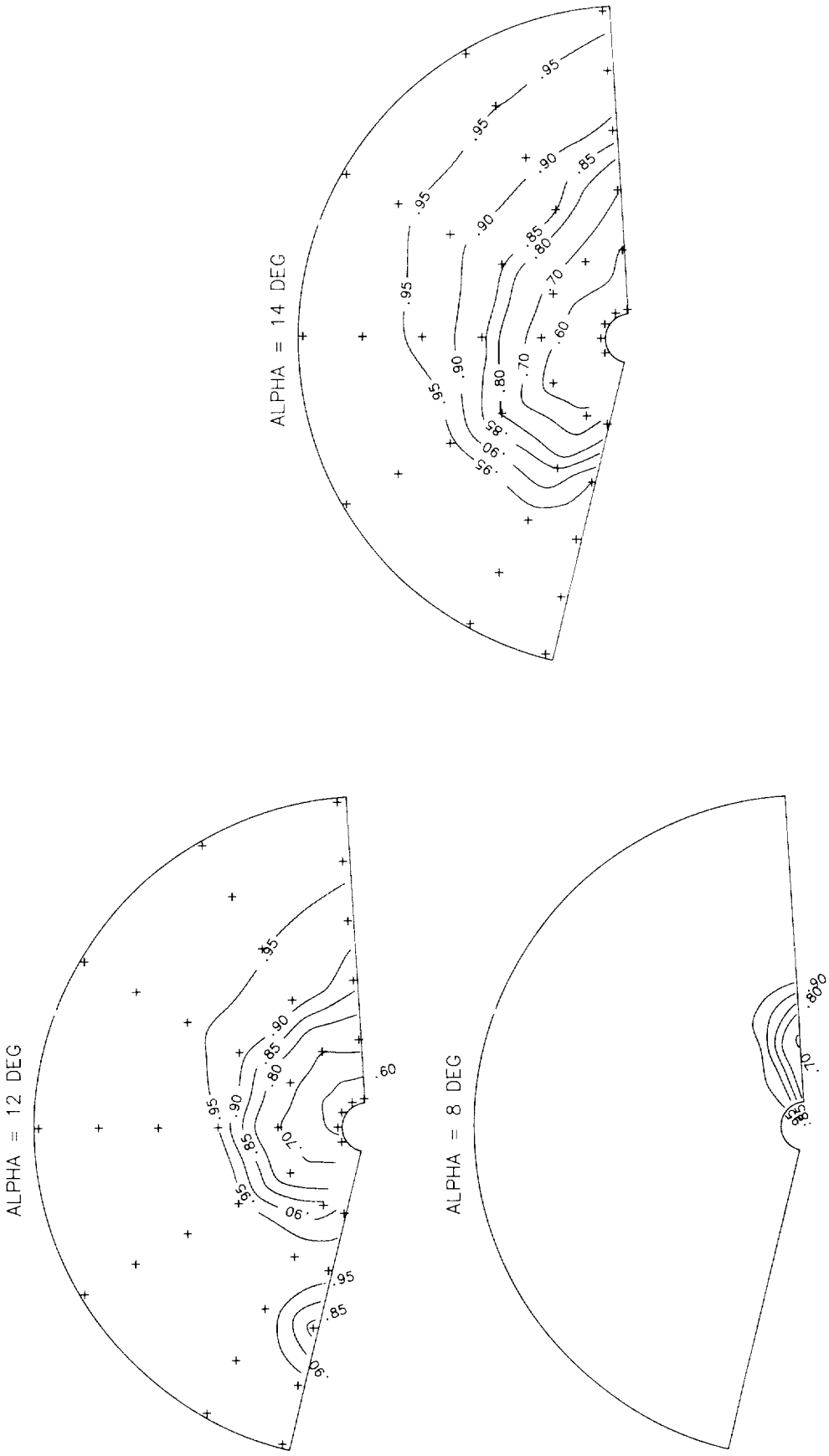

(b) Mach = 0.9.

Figure 11. Continued.

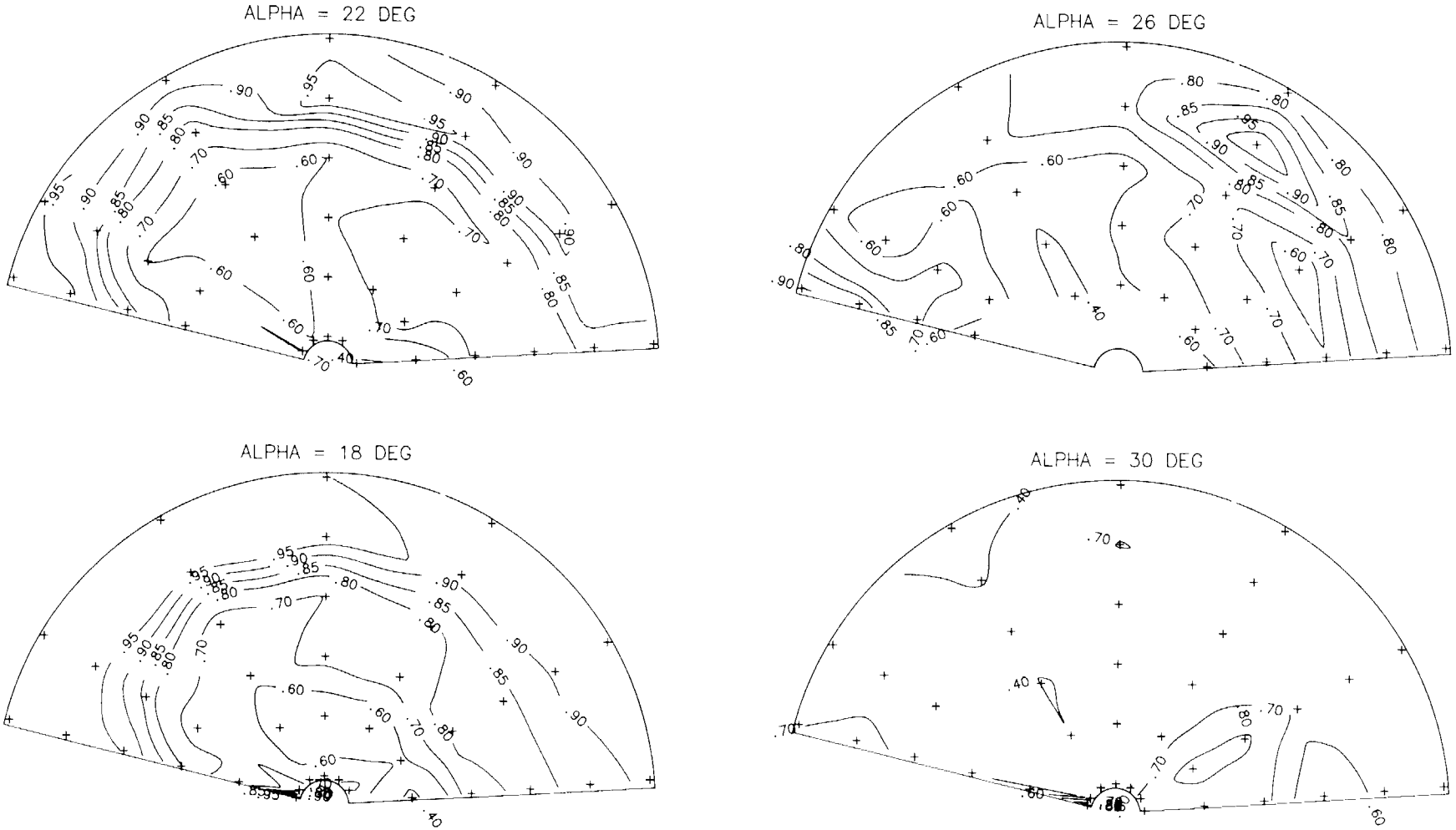

(b) Concluded.

Figure 11. Continued.

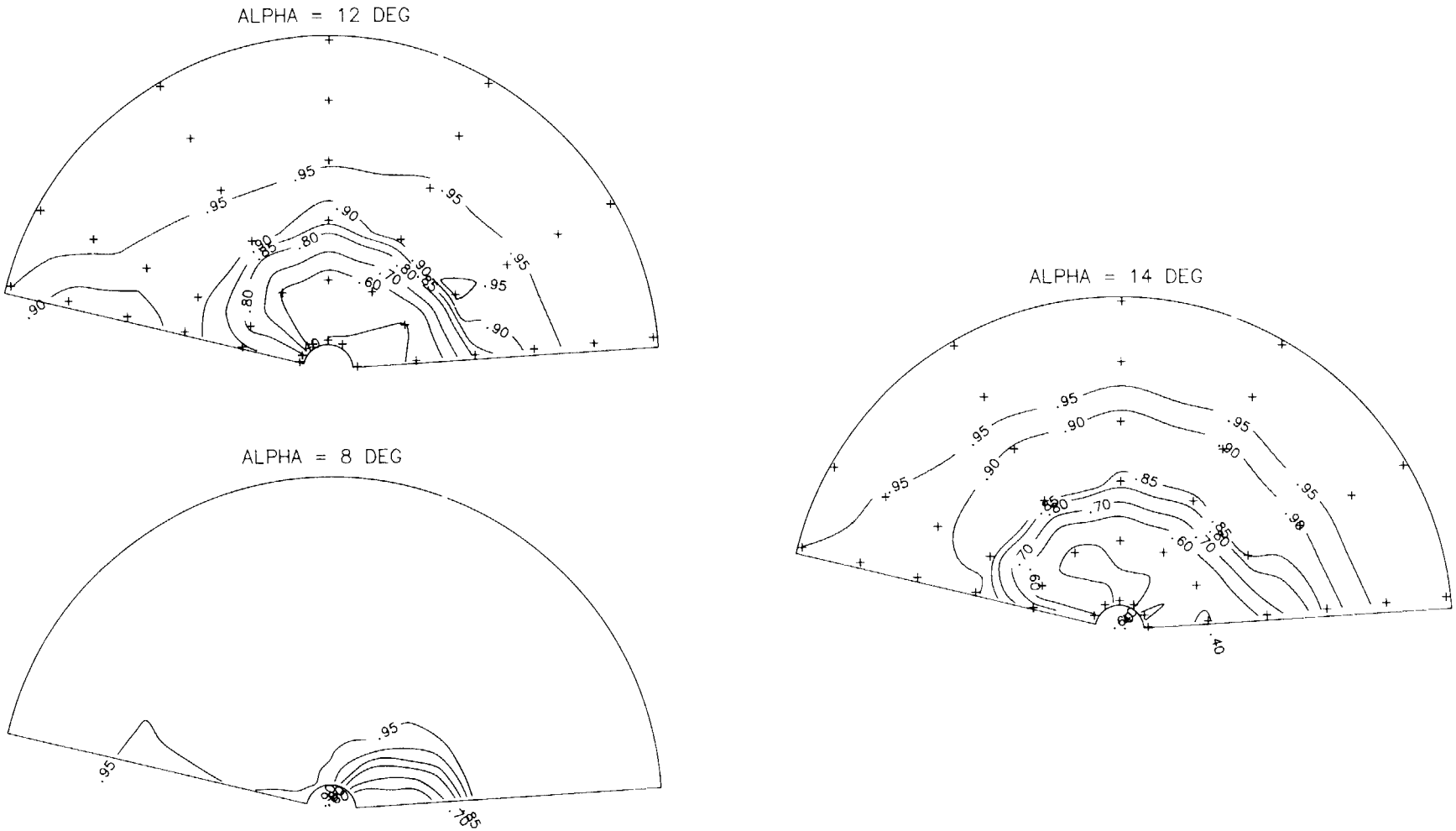

(c) Mach = 1.2.

Figure 11. Continued.

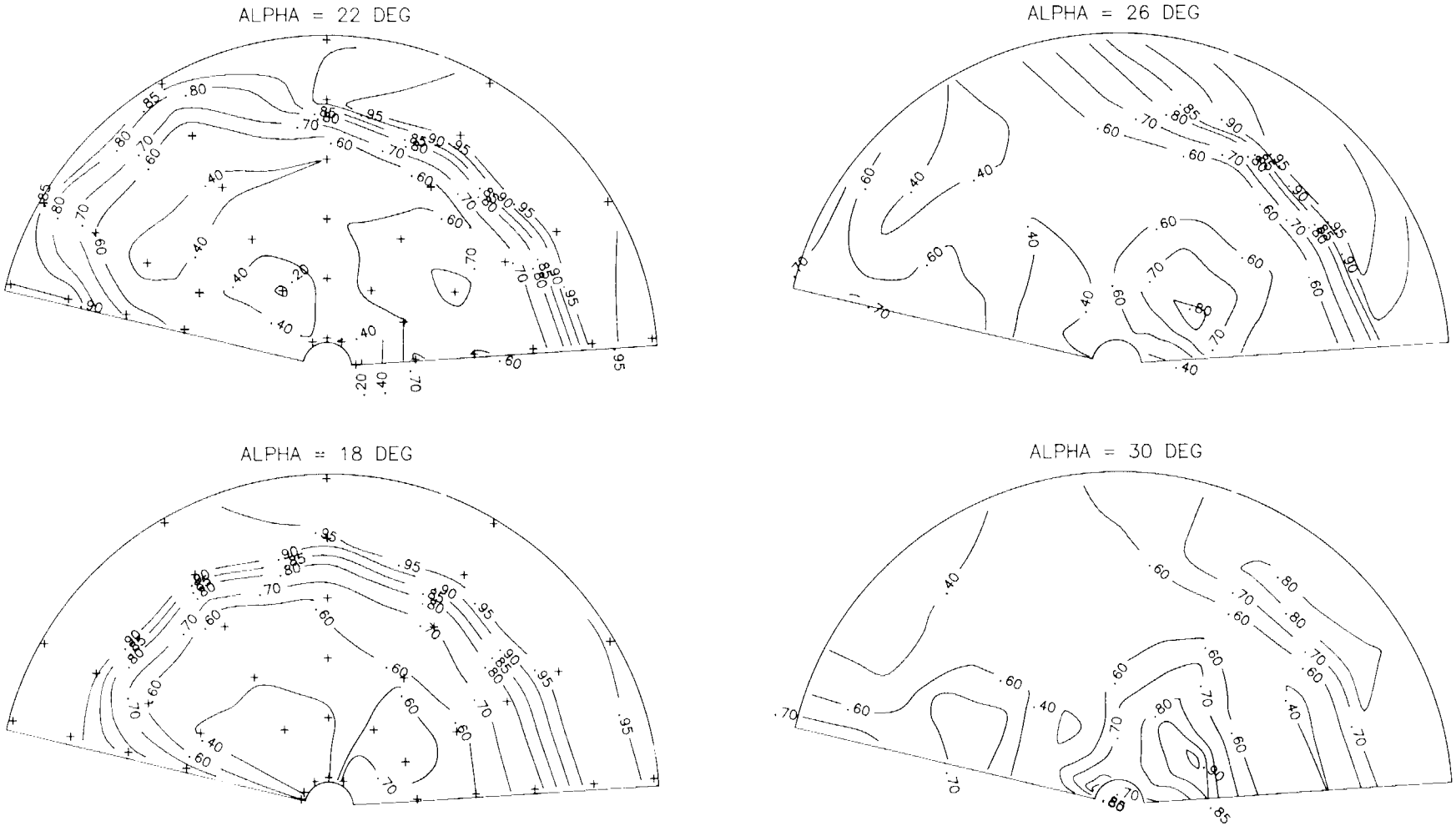

(c) Concluded.

Figure 11. Concluded.

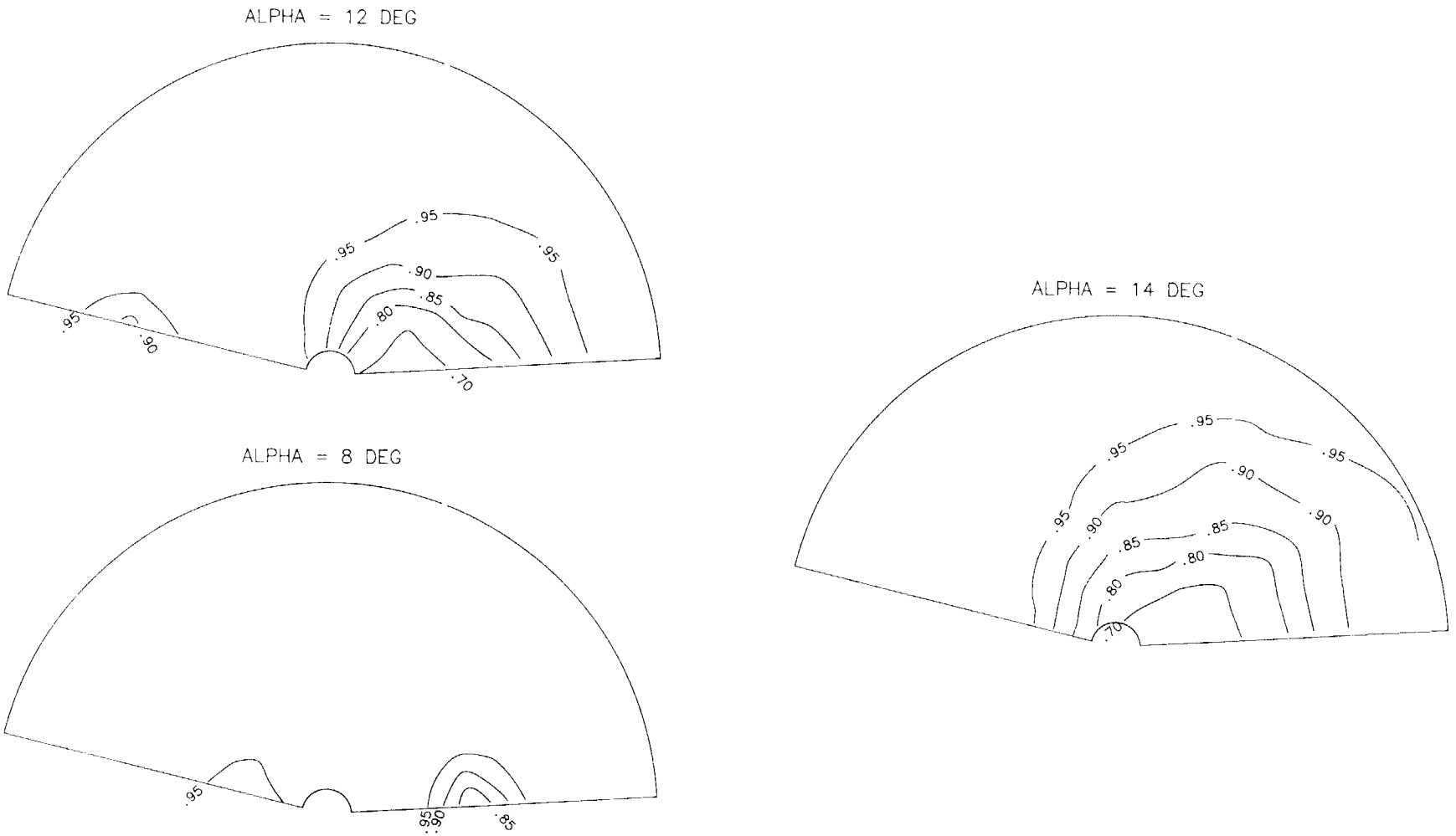

(a) Mach = 0.6.

Figure 12. Total pressure recovery contours for baseline configuration at $\beta = 0°$ and at fuselage station 35.0.

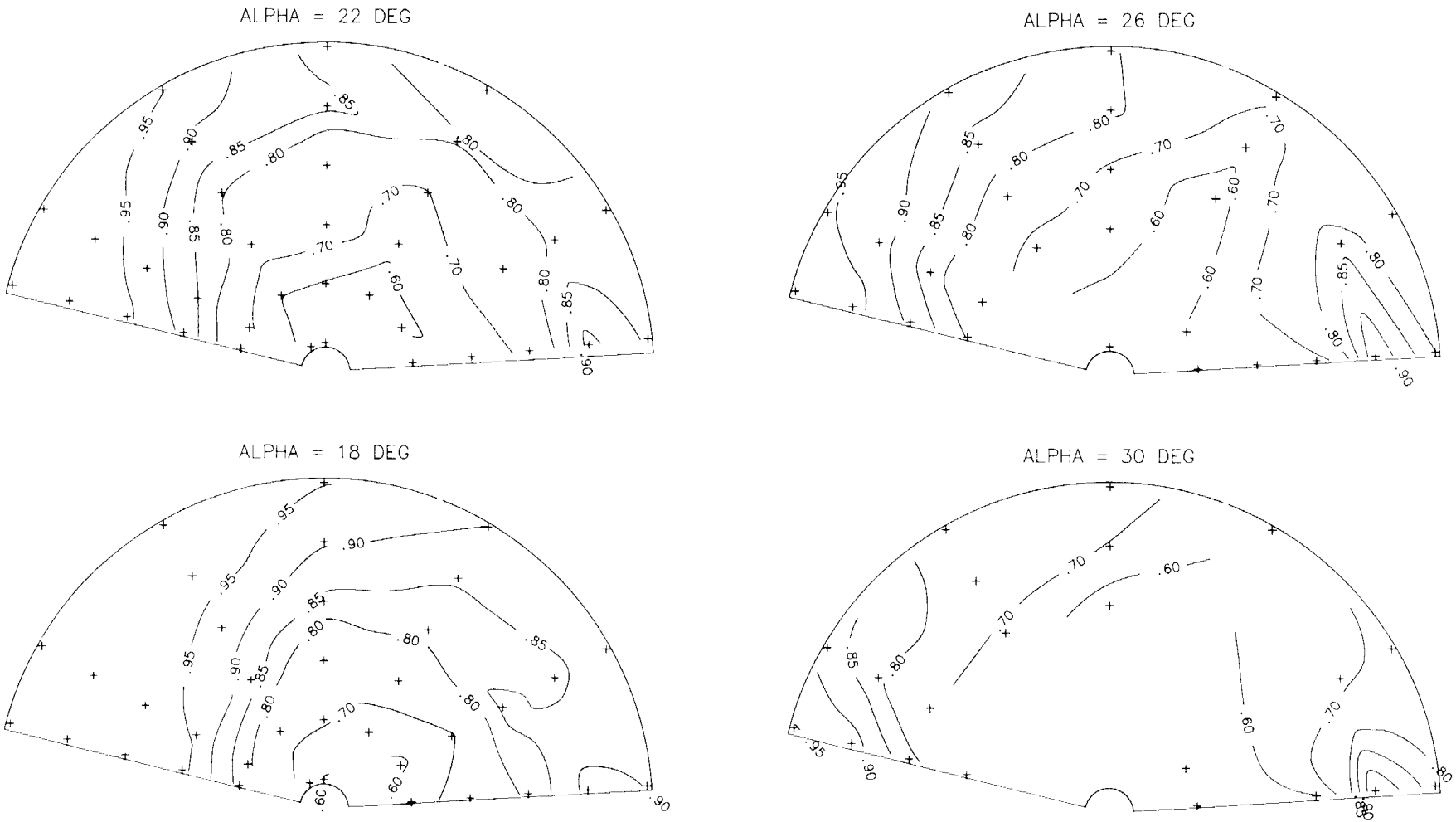

(a) Concluded.

Figure 12. Continued.

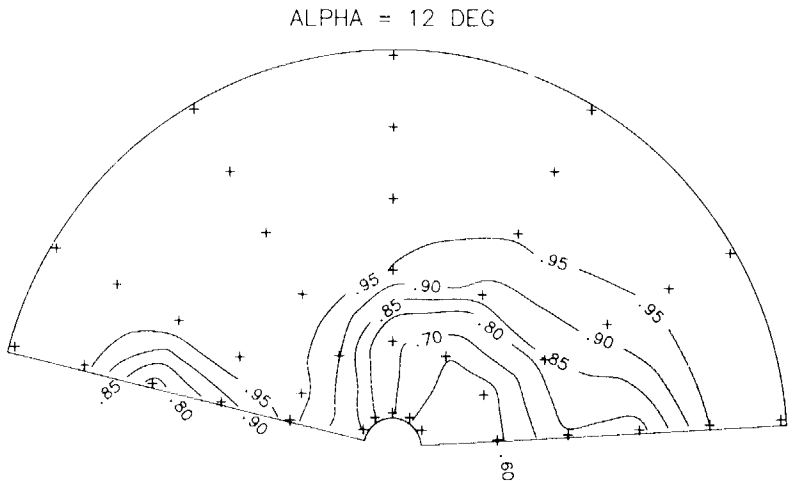

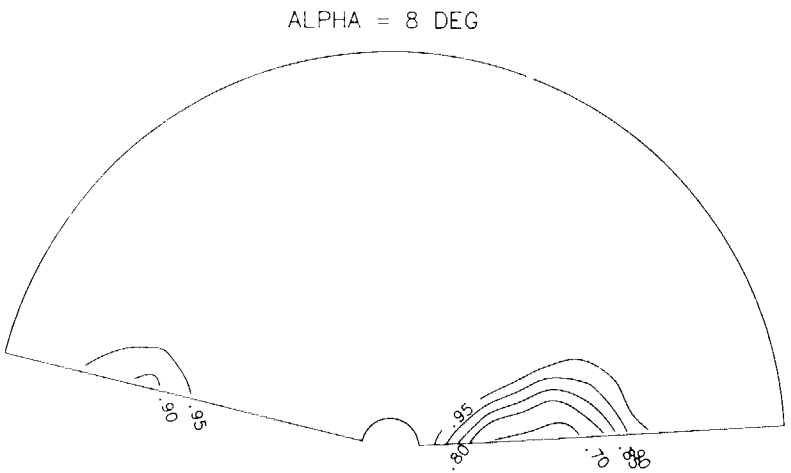

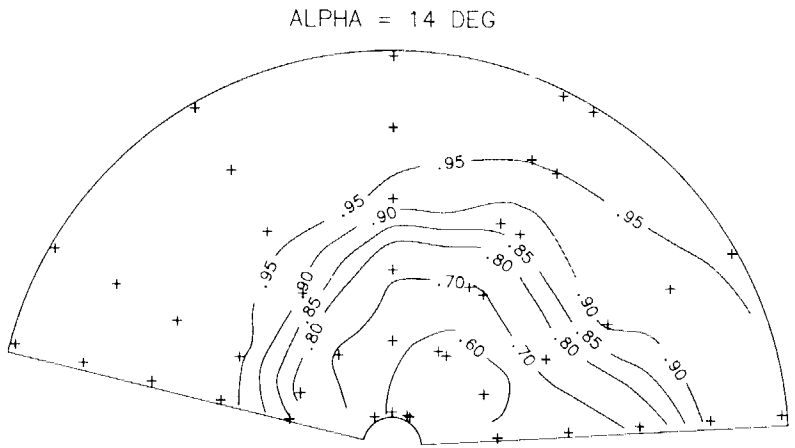

(b) Mach = 0.9.

Figure 12. Continued.

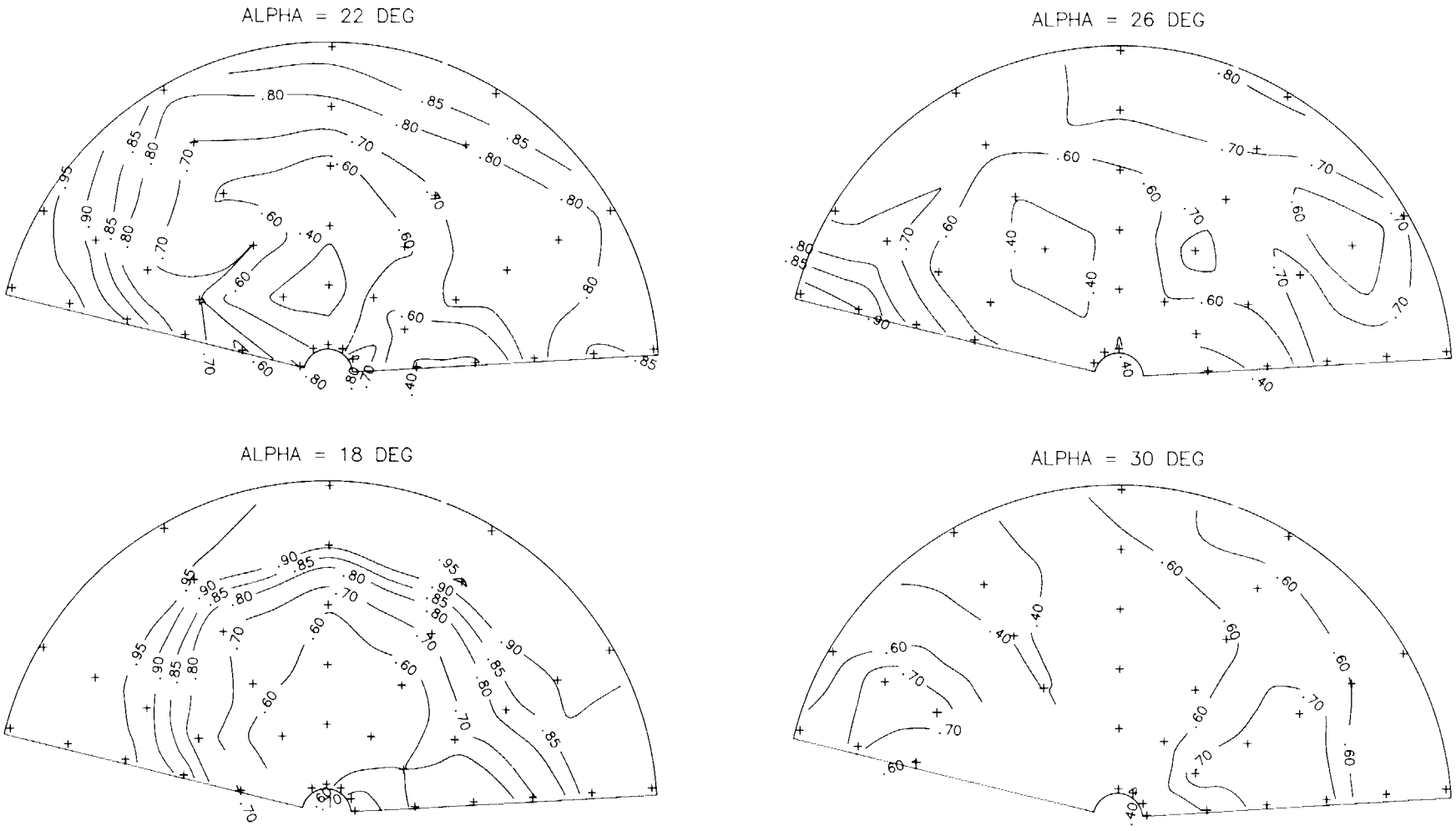

(b) Concluded.

Figure 12. Continued.

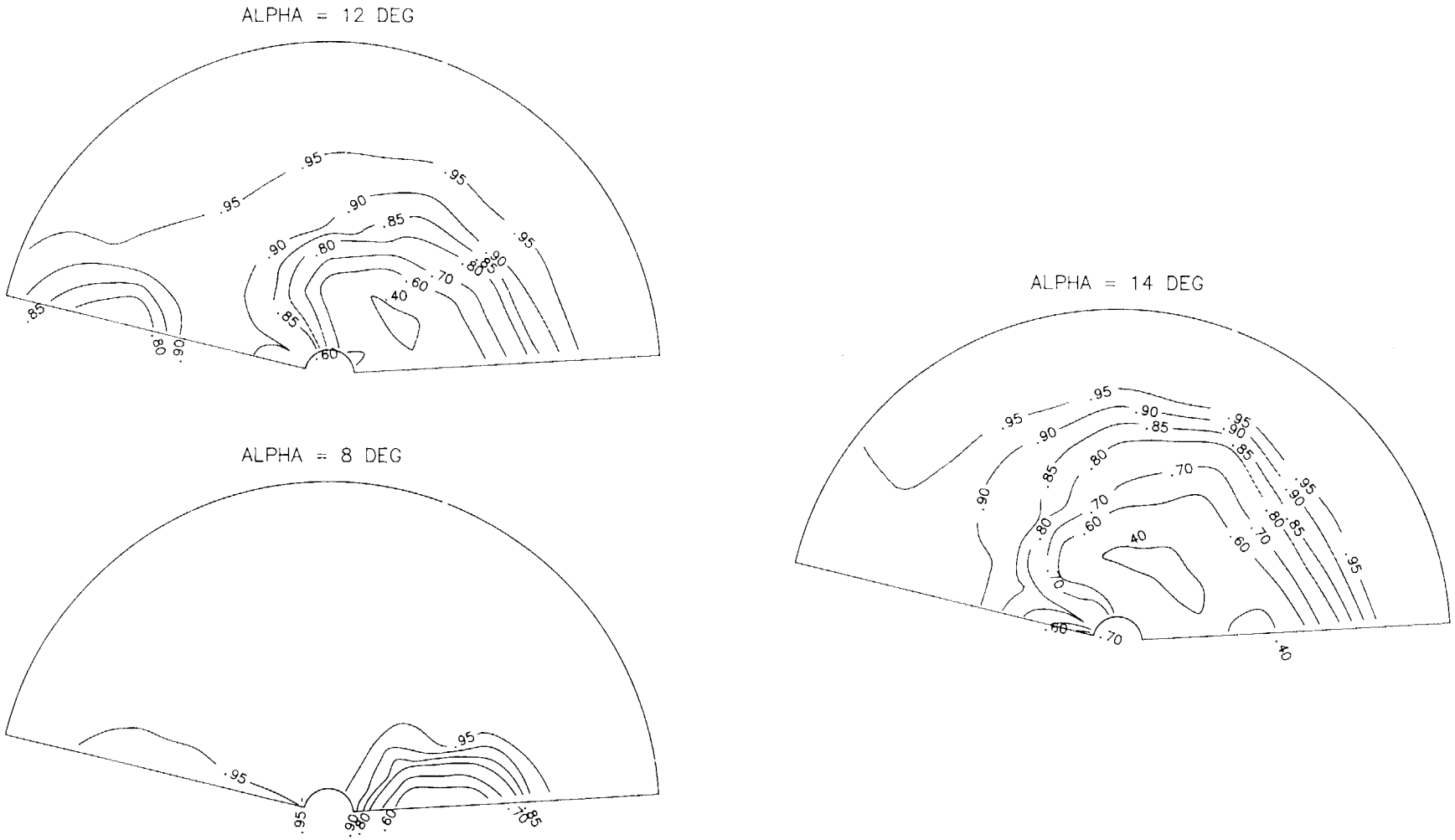

(c) Mach = 1.2.

Figure 12. Continued.

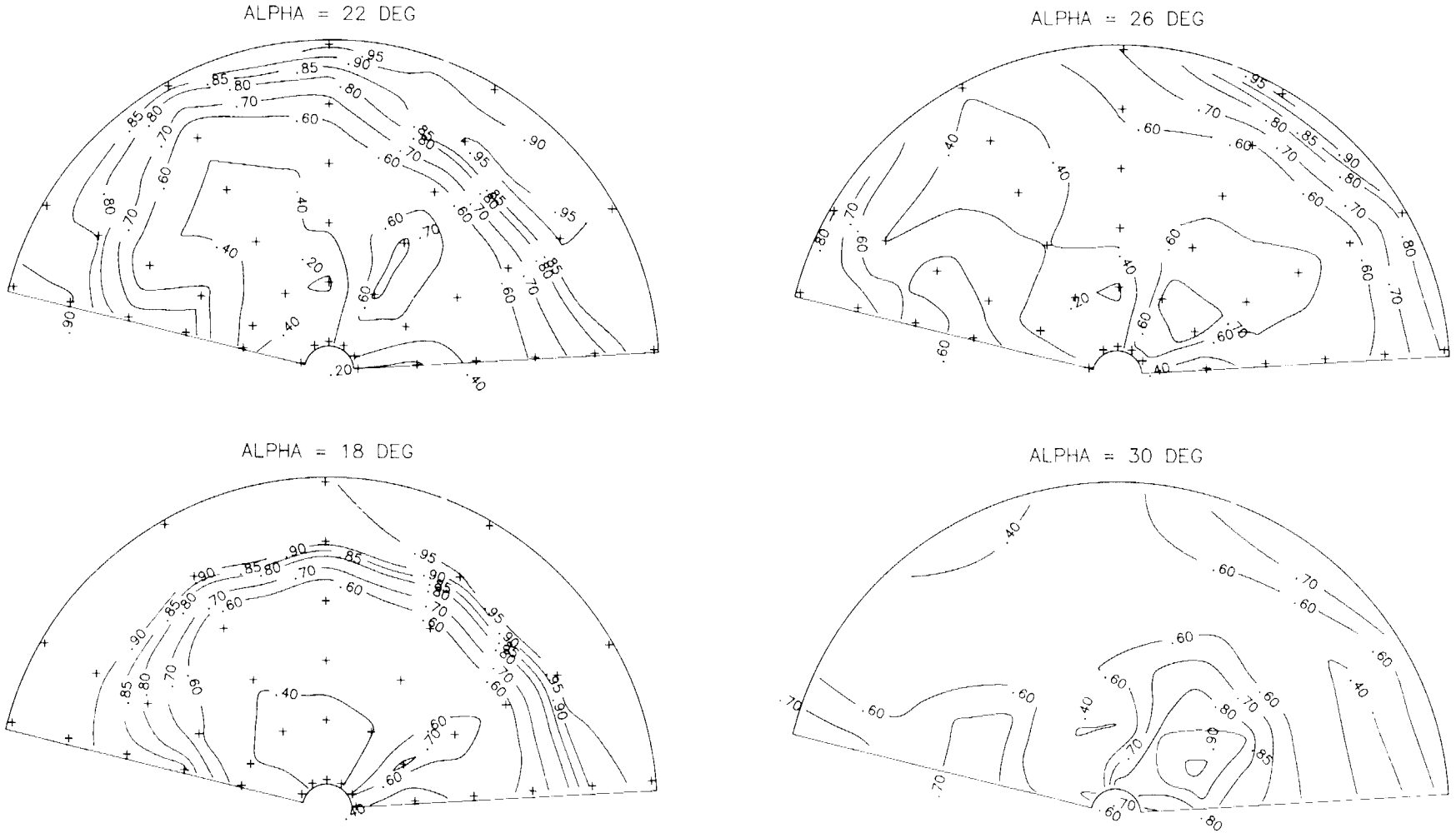

(c) Concluded.

Figure 12. Concluded.

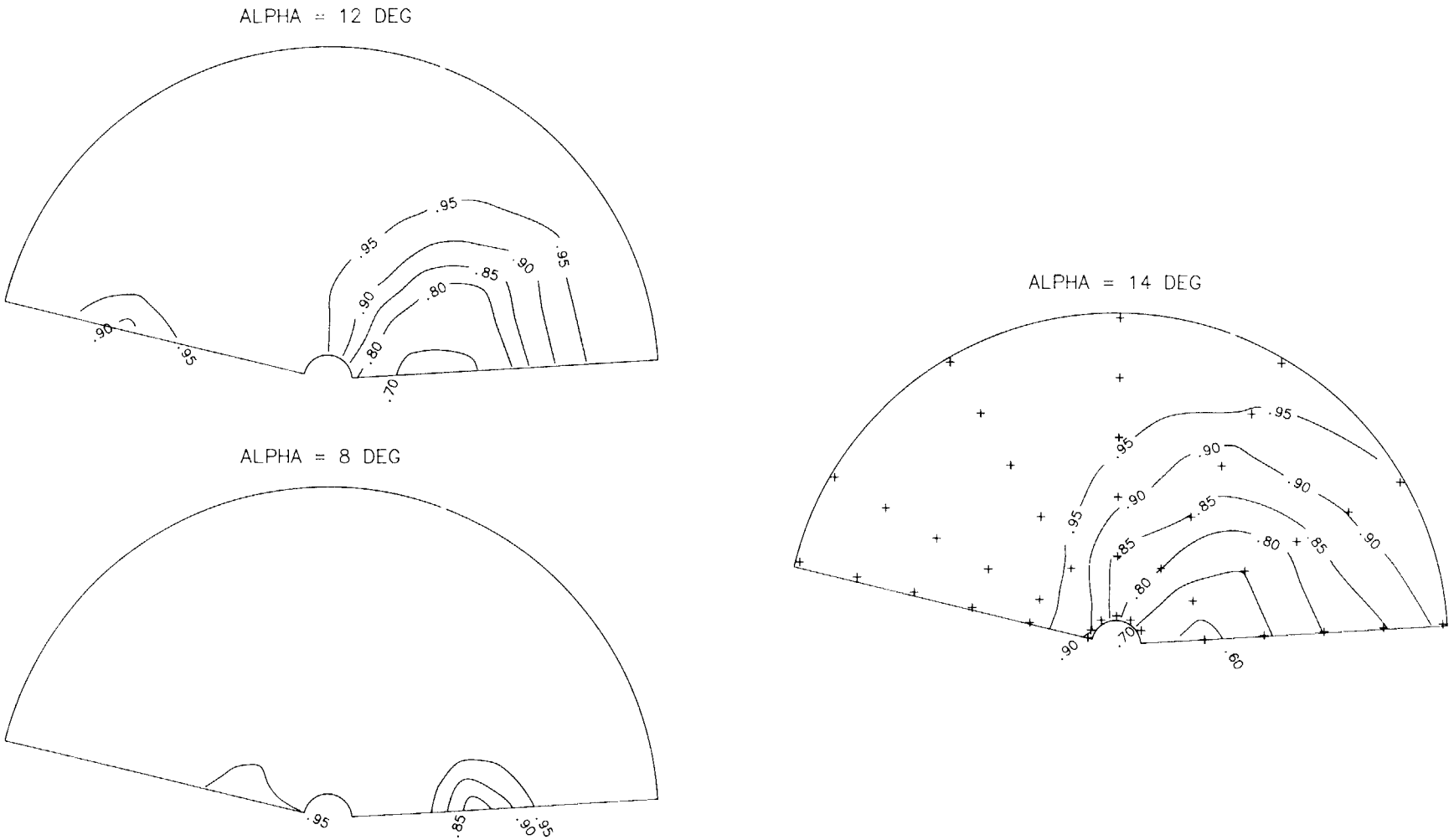

(a) Mach = 0.6.

Figure 13. Total pressure recovery contours for baseline configuration at $\beta = 0°$ and at fuselage station 36.5.

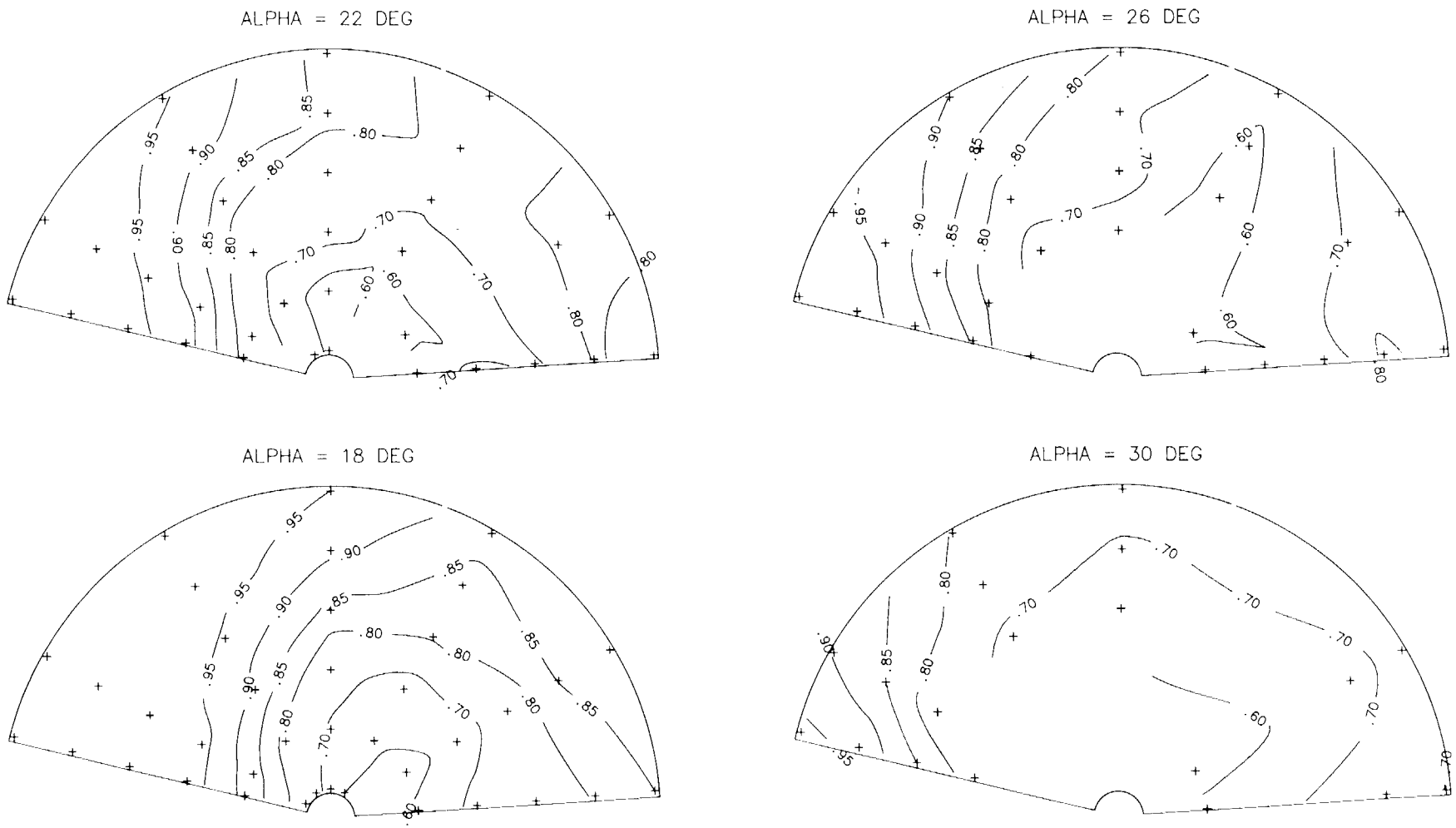

(a) Concluded.

Figure 13. Continued.

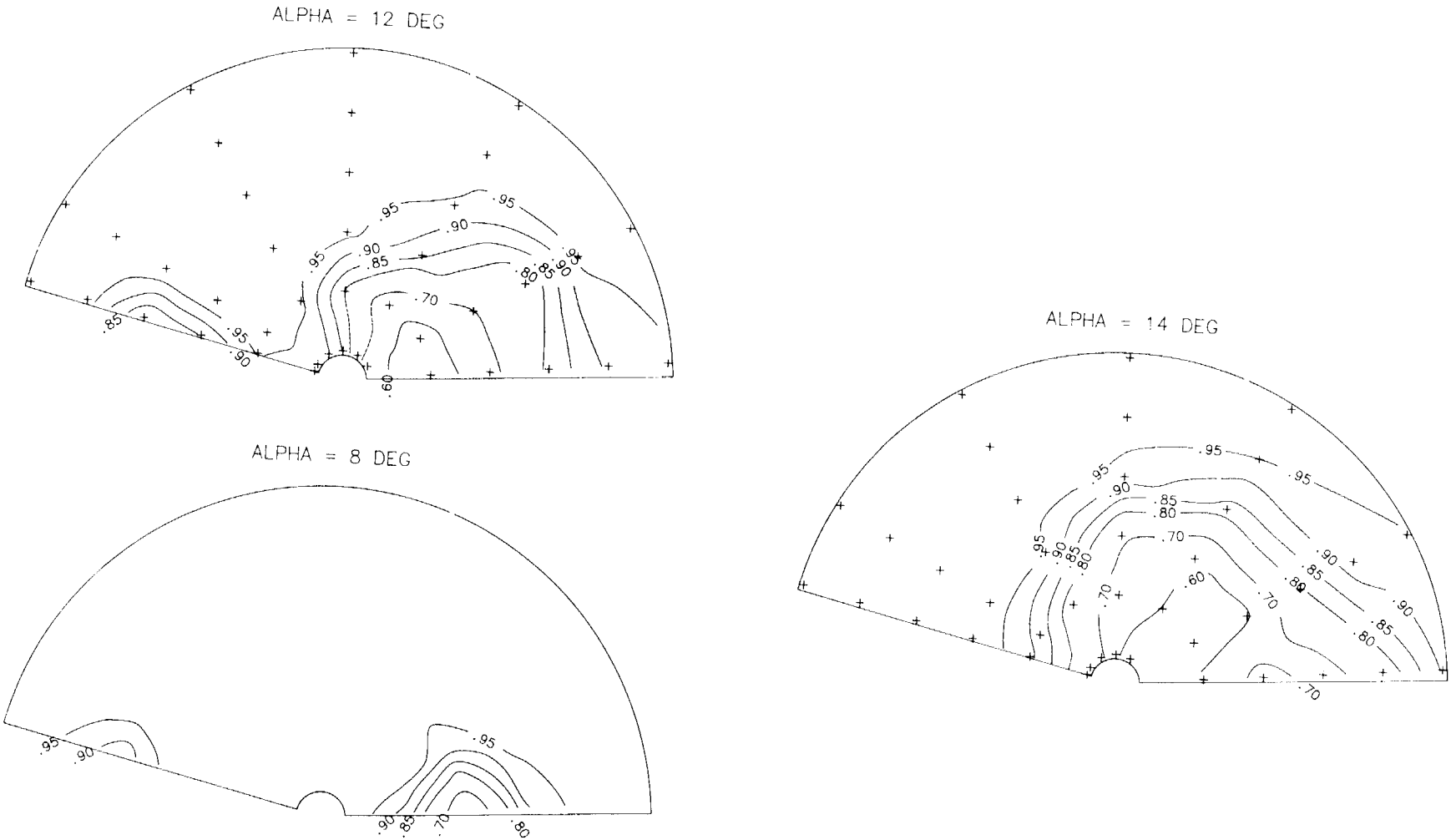

(b) Mach = 0.9.

Figure 13. Continued.

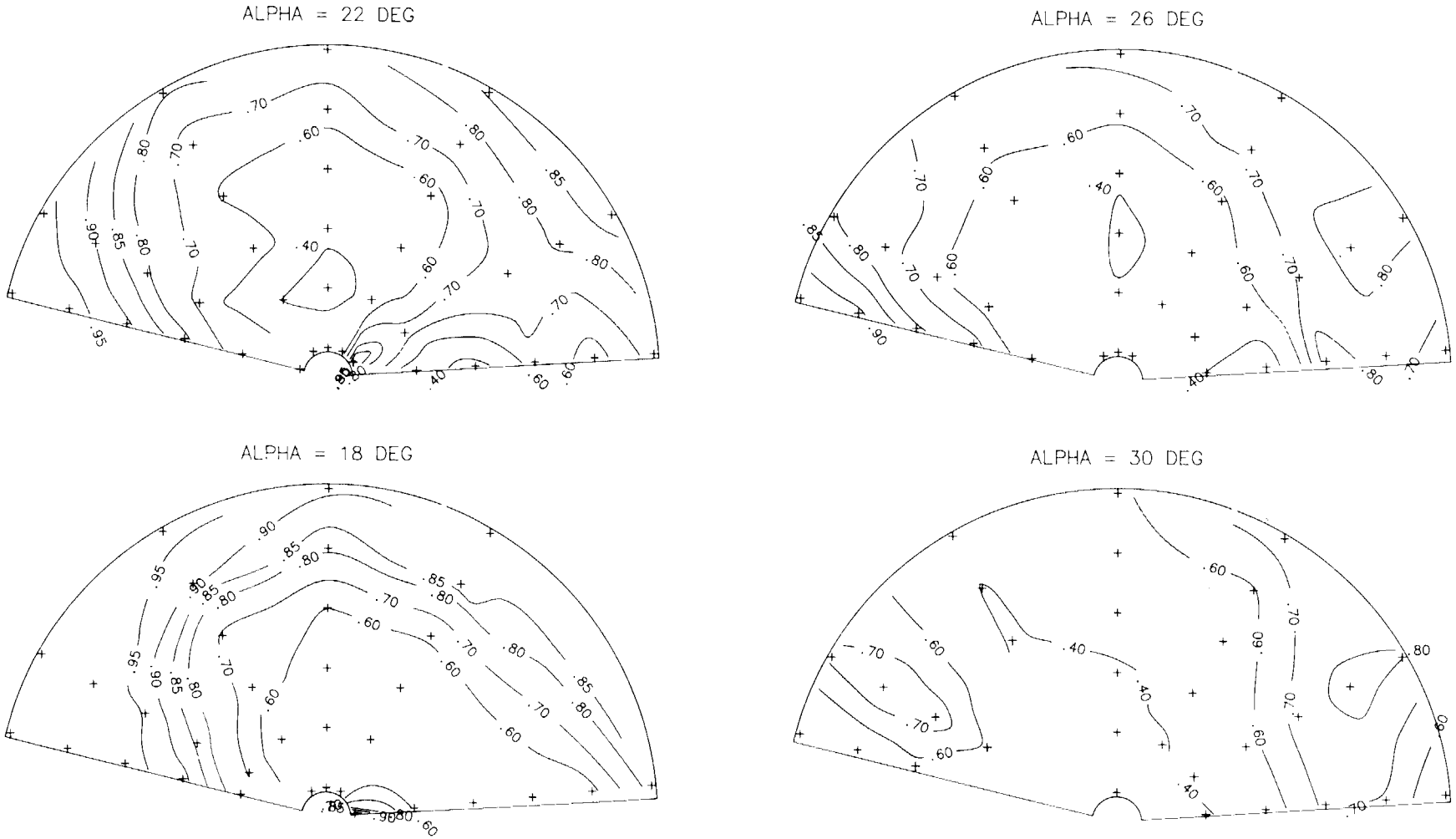

(b) Concluded.

Figure 13. Continued.

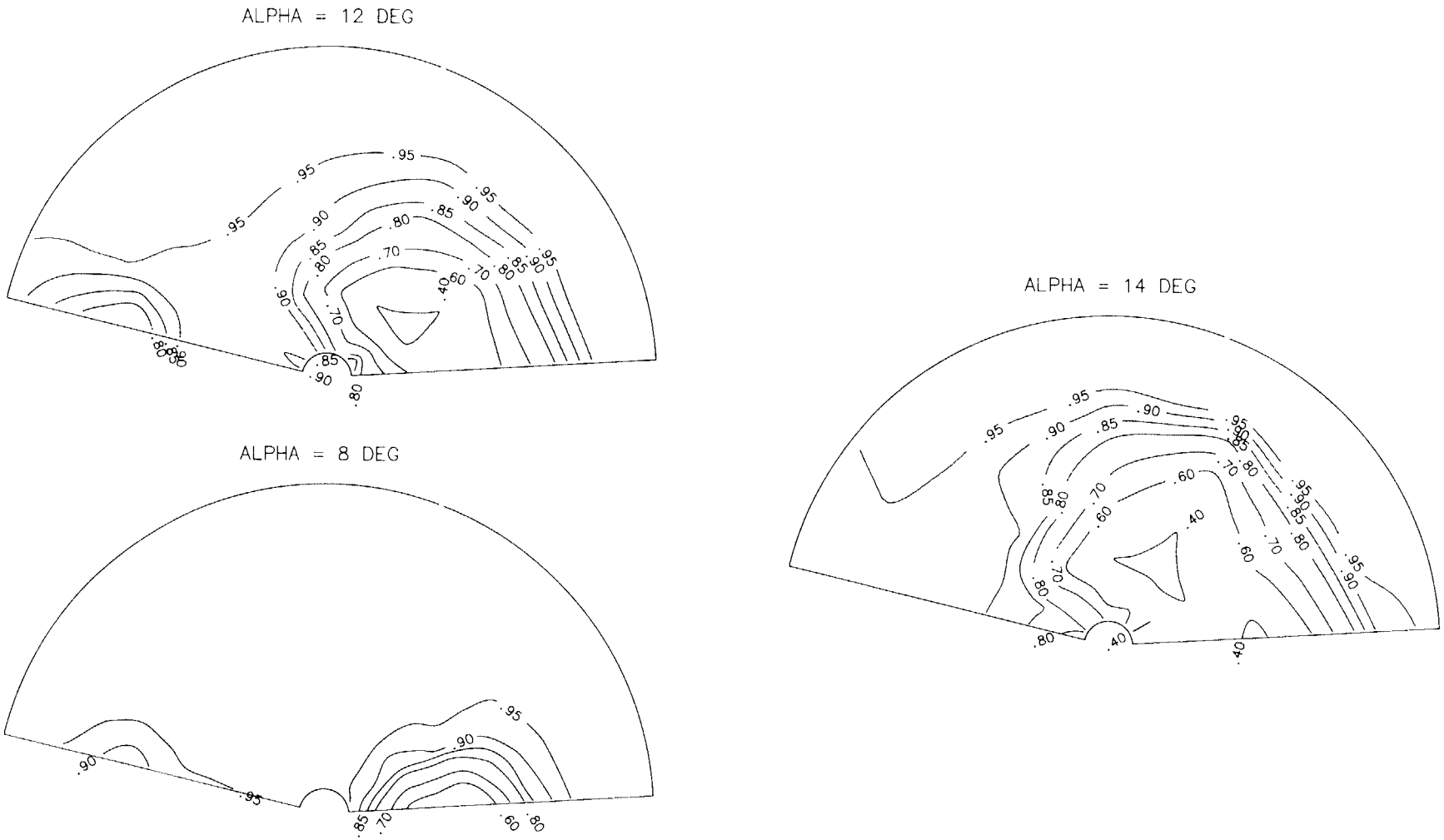

(c) Mach = 1.2.

Figure 13. Continued.

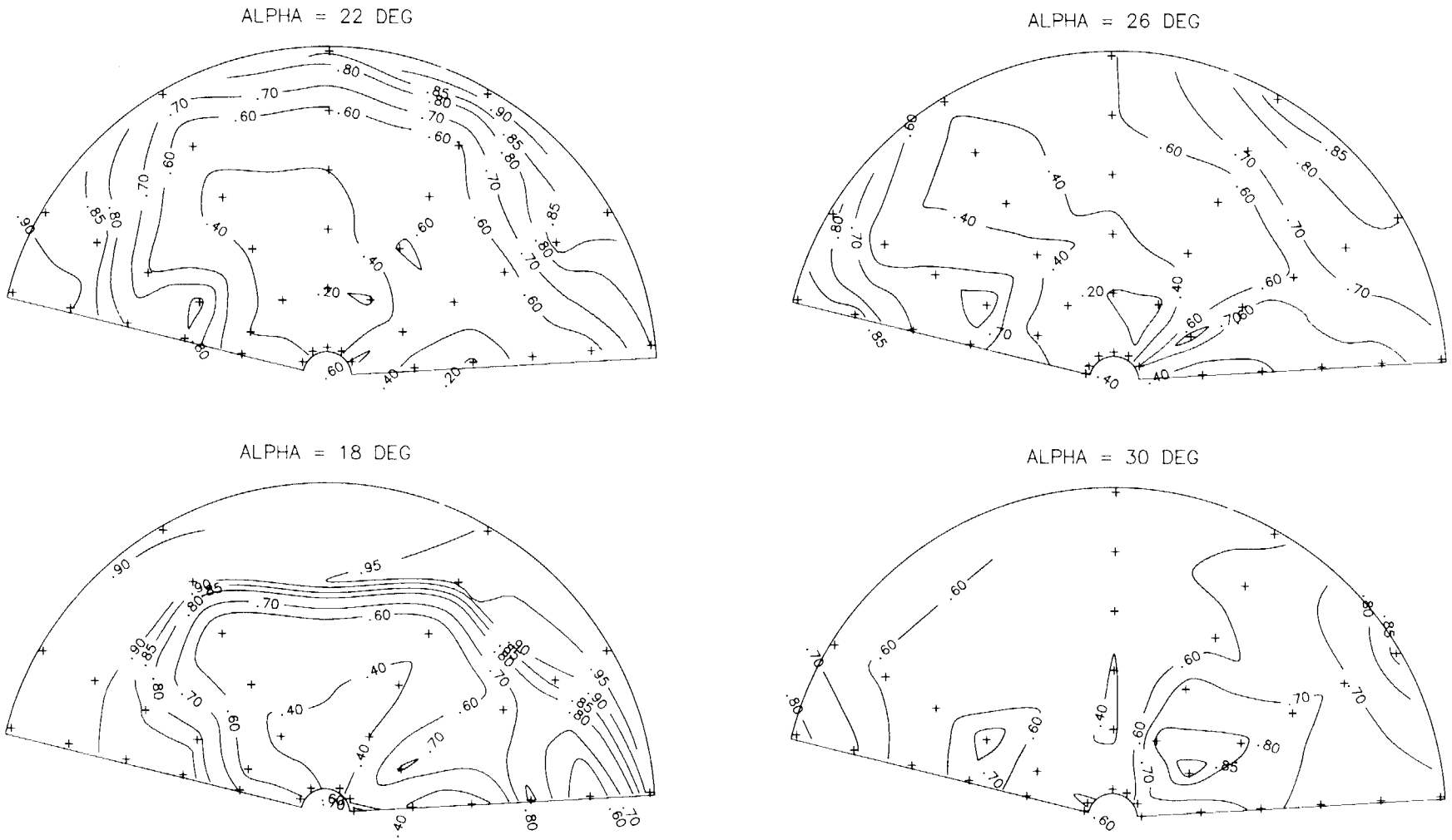

(c) Concluded.

Figure 13. Concluded.

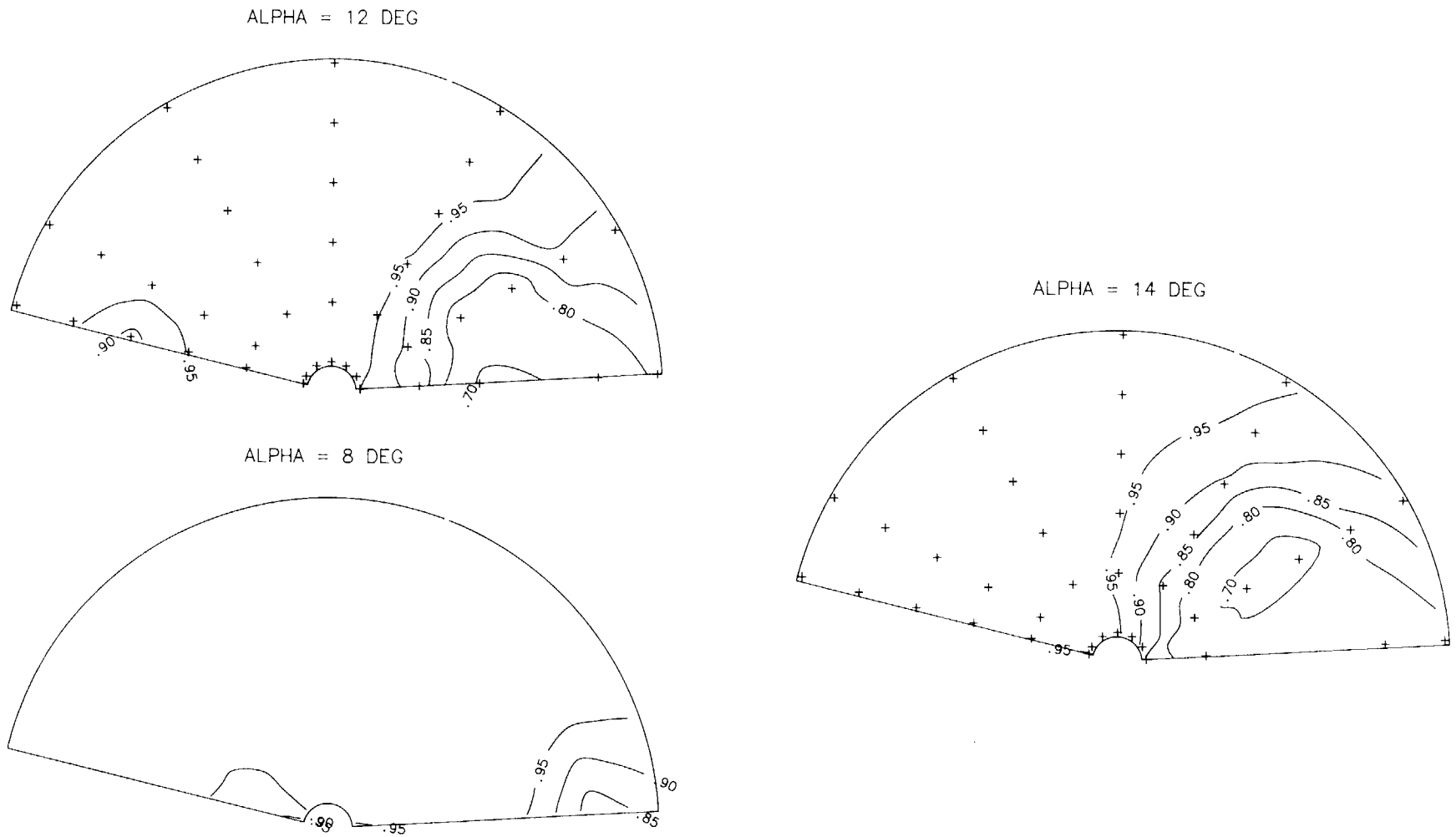

(a) Mach = 0.6.

Figure 14. Total pressure recovery contours for baseline configuration at $\beta = 0°$ and at fuselage station 40.5.

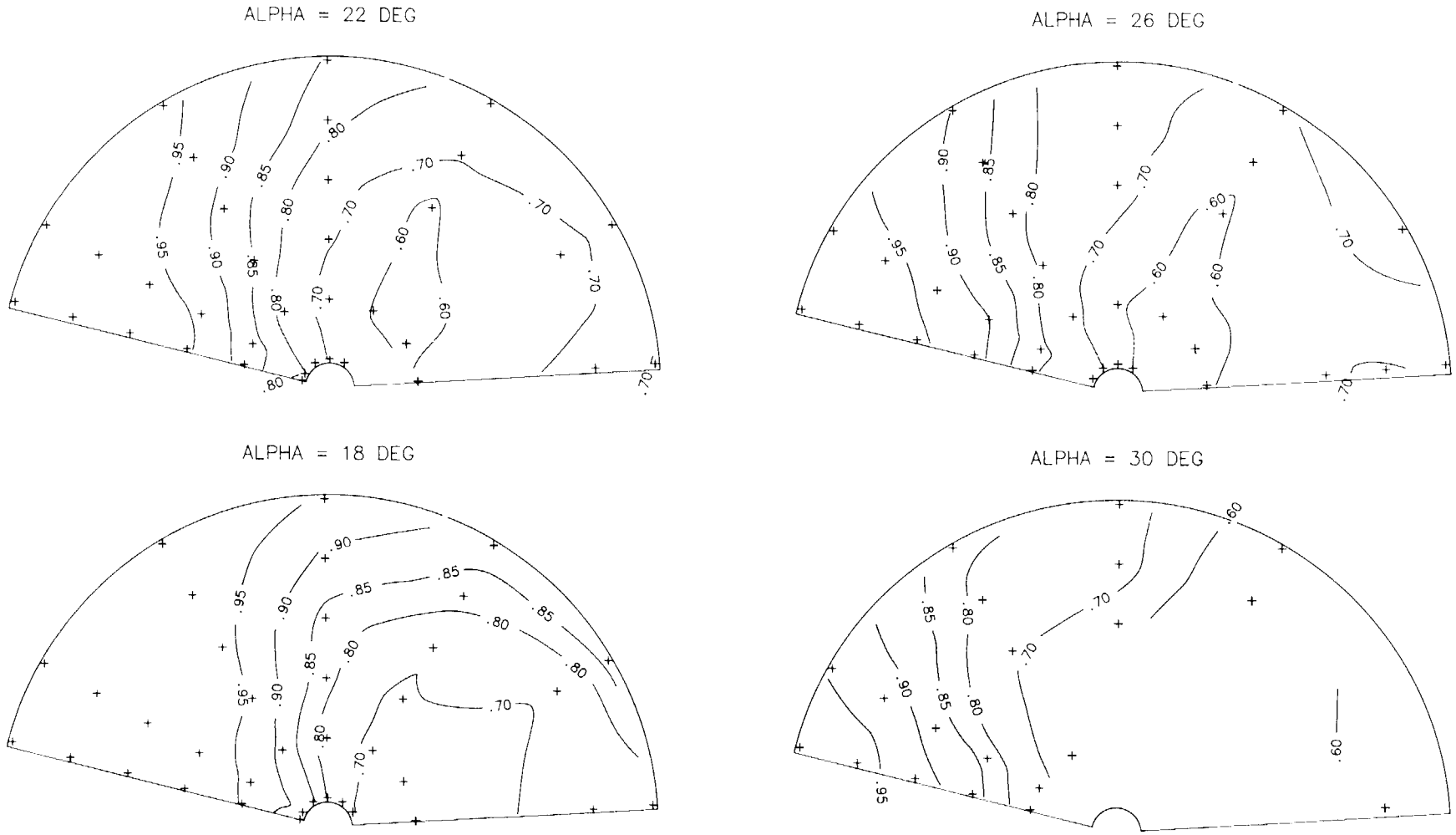

(a) Concluded.

Figure 14. Continued.

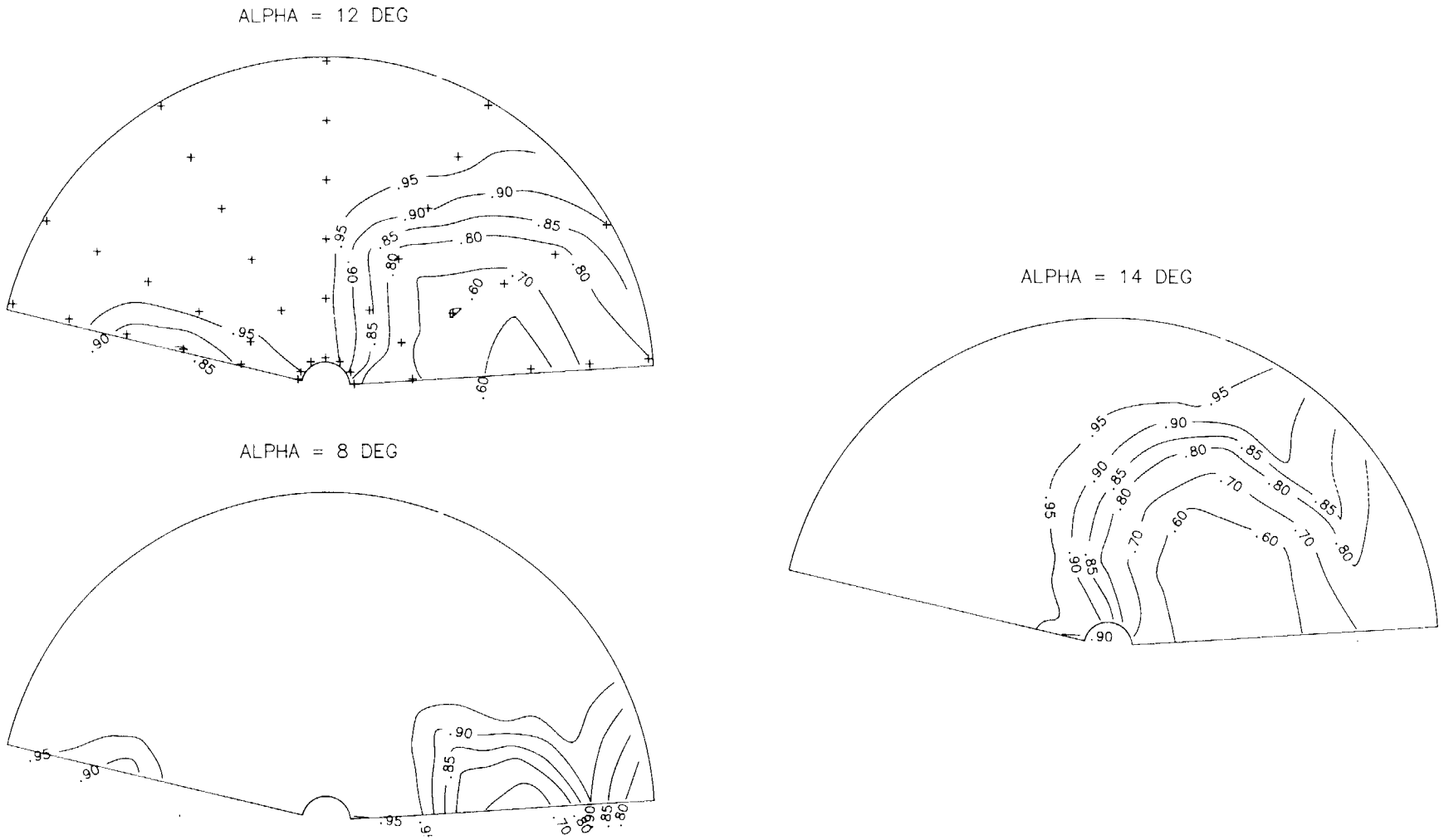

(b) Mach = 0.9.

Figure 14. Continued.

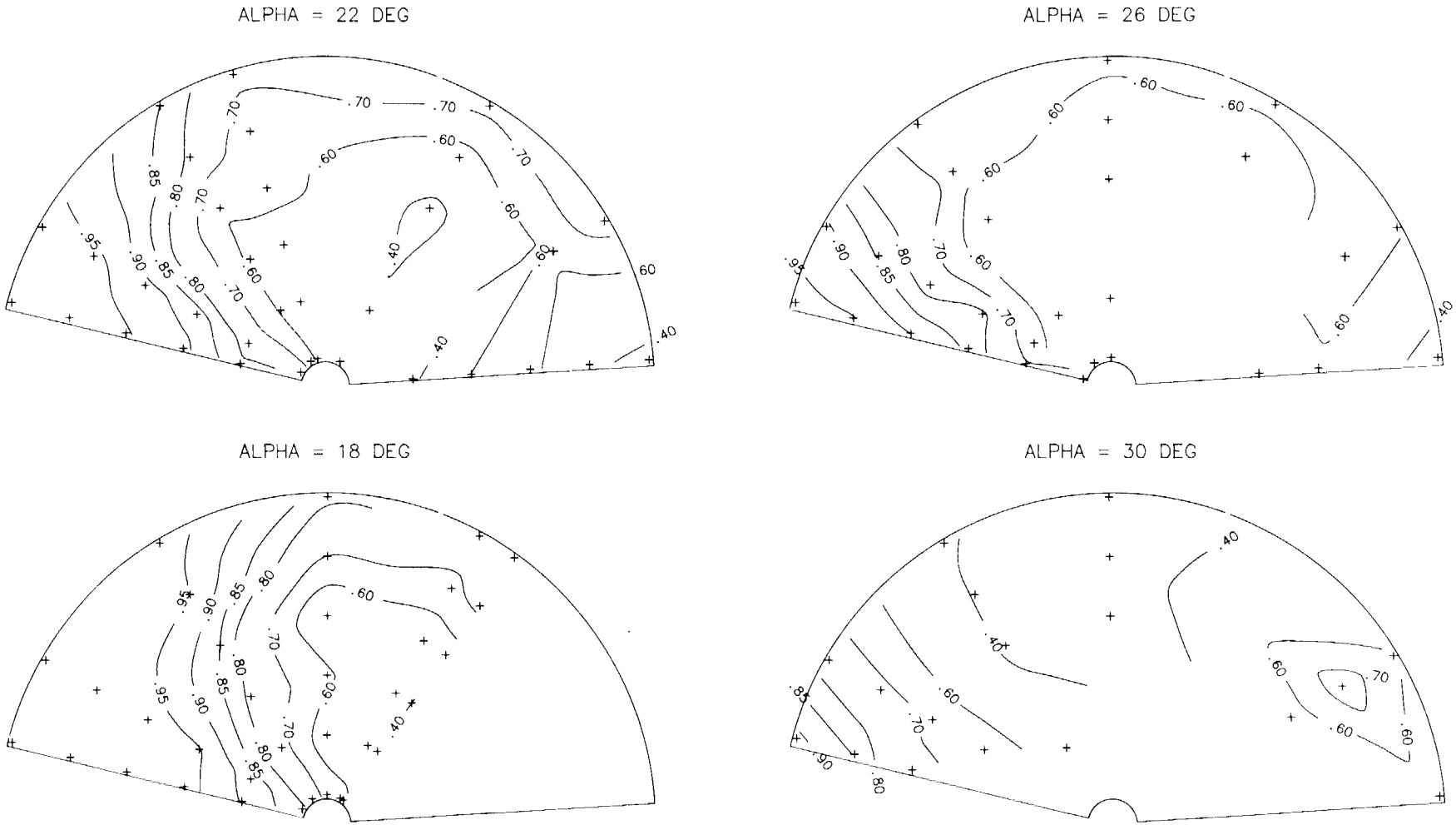

(b) Concluded.

Figure 14. Continued.

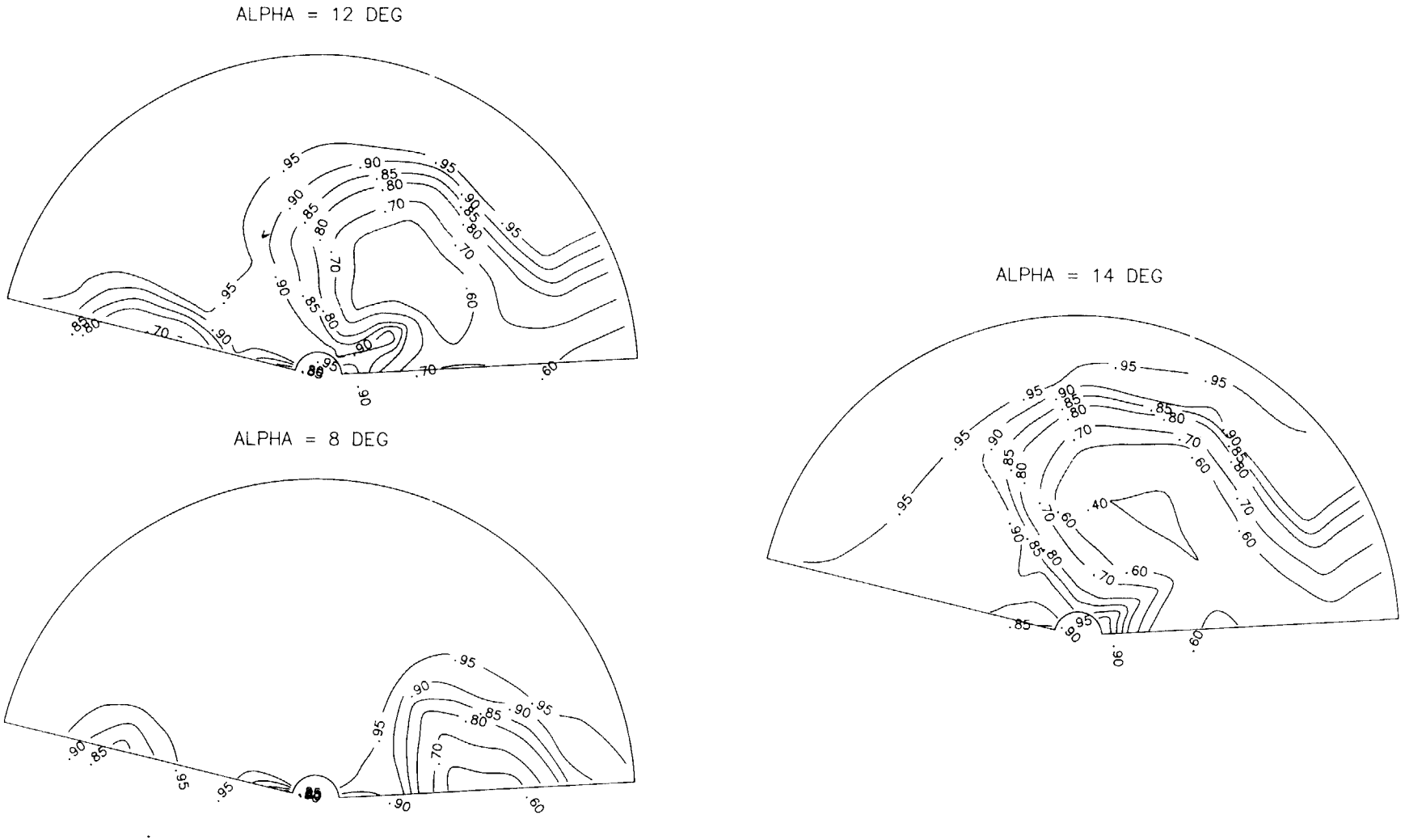

(c) Mach = 1.2.

Figure 14. Continued.

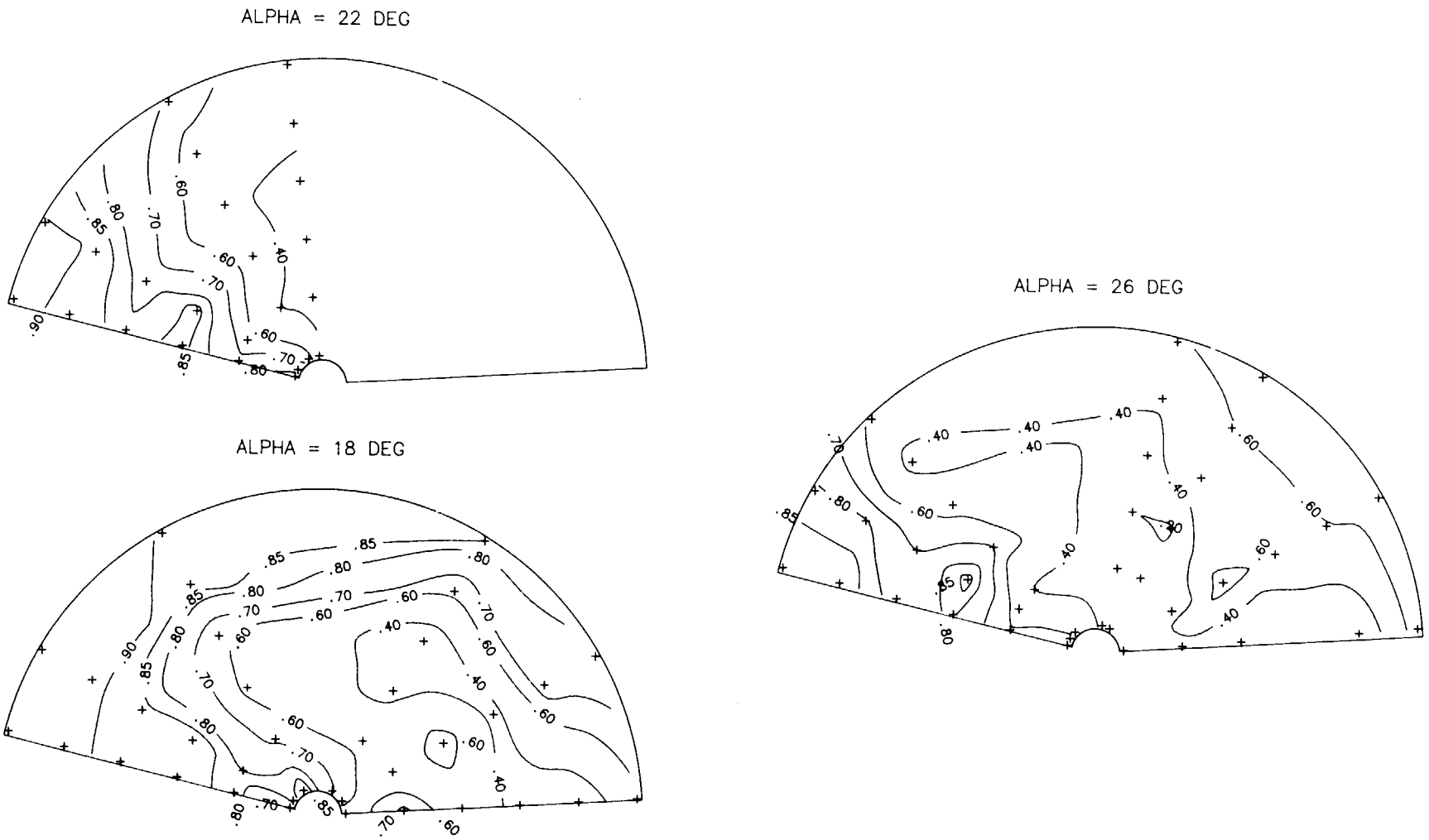

(c) Concluded.

Figure 14. Concluded.

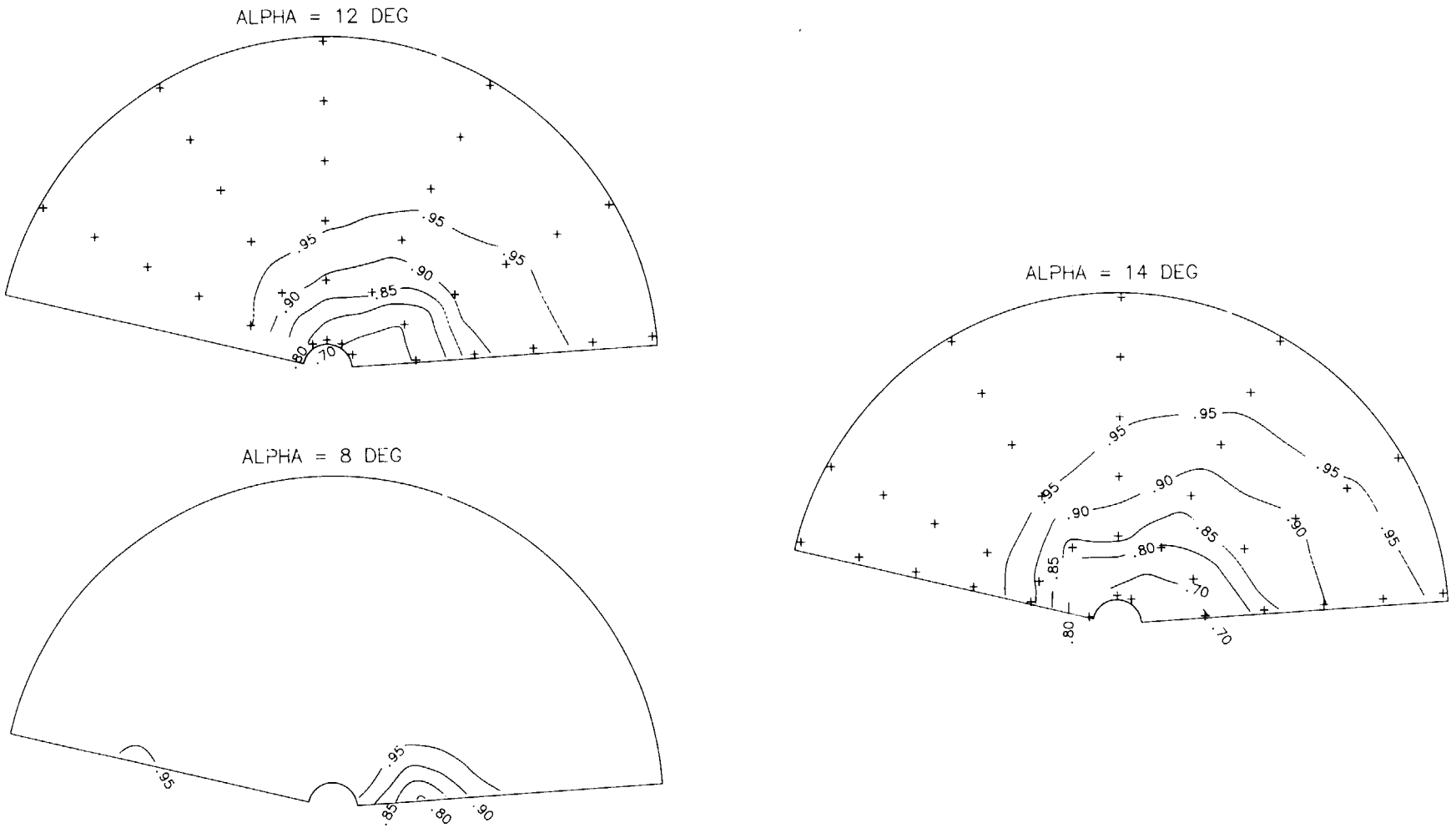

(a) Mach = 0.6.

Figure 15. Total pressure recovery contours for baseline configuration at $\beta = 5°$ and at fuselage station 32.8.

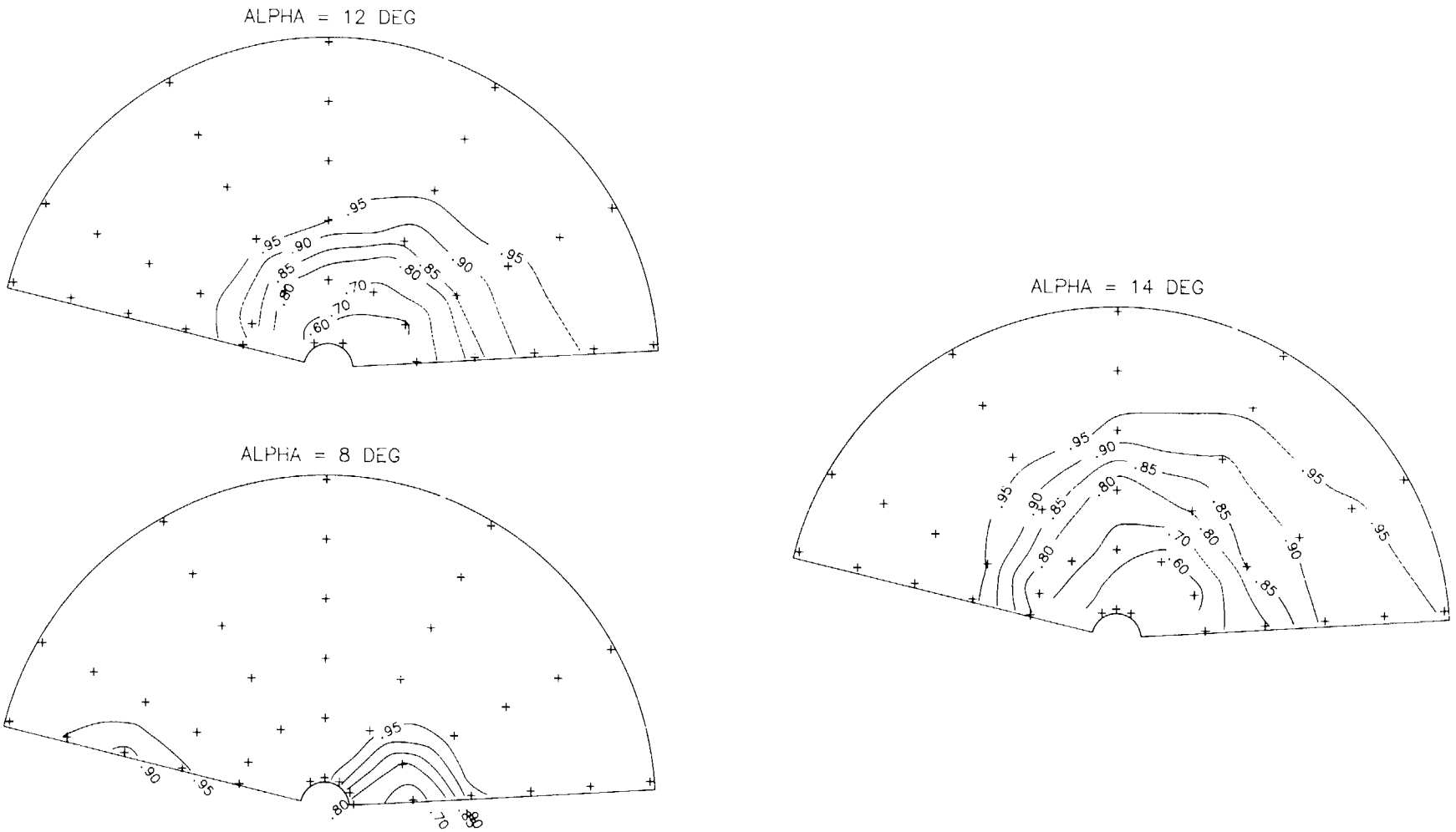

(b) Mach = 0.9.

Figure 15. Continued.

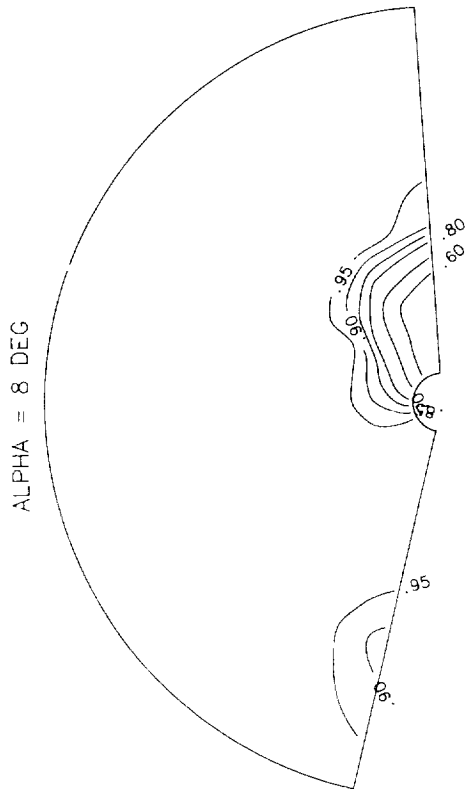

(c) Mach = 1.2.

Figure 15. Concluded.

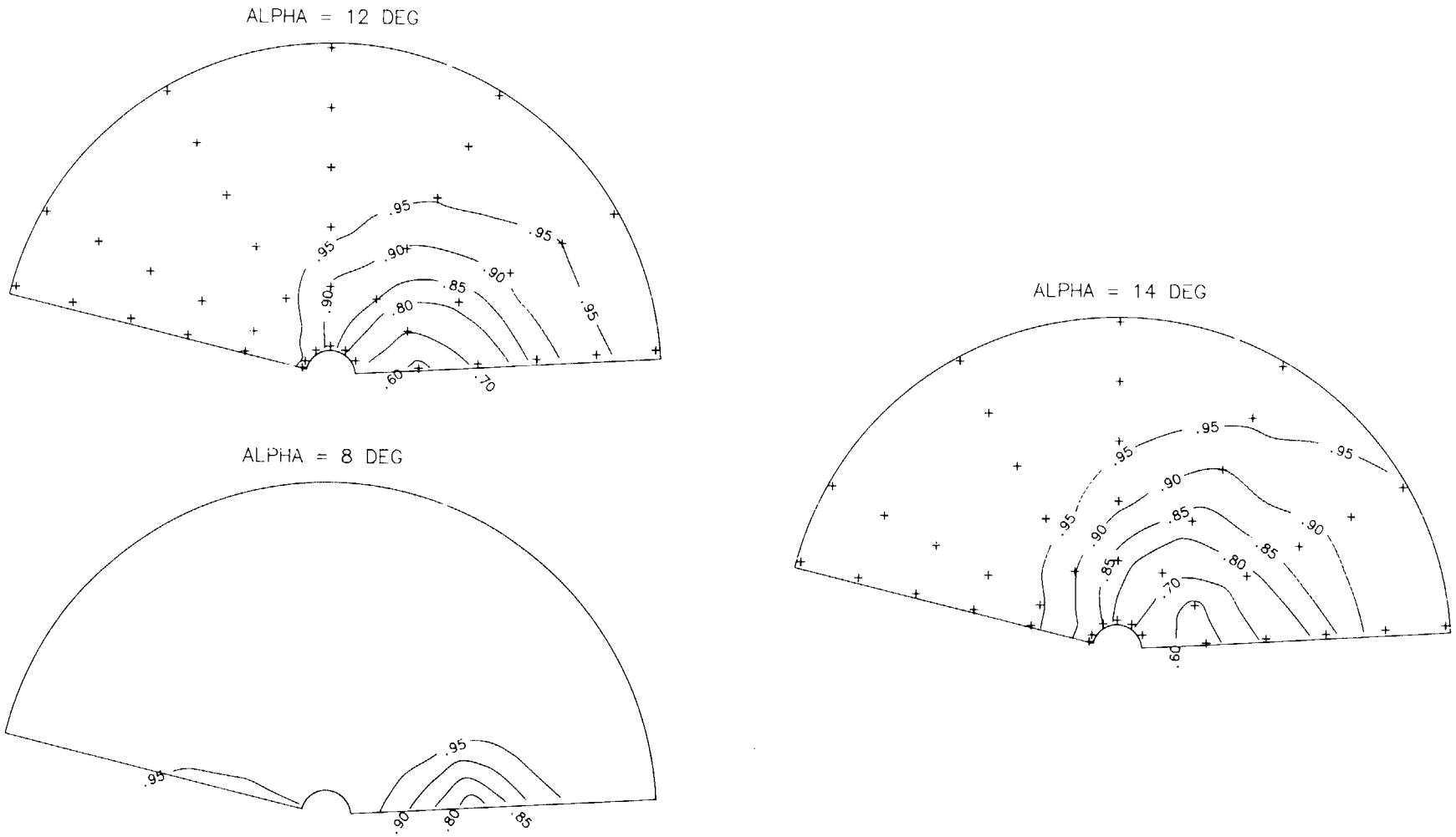

(a) Mach = 0.6.

Figure 16. Total pressure recovery contours for baseline configuration at $\beta = 5°$ and at fuselage station 35.0.

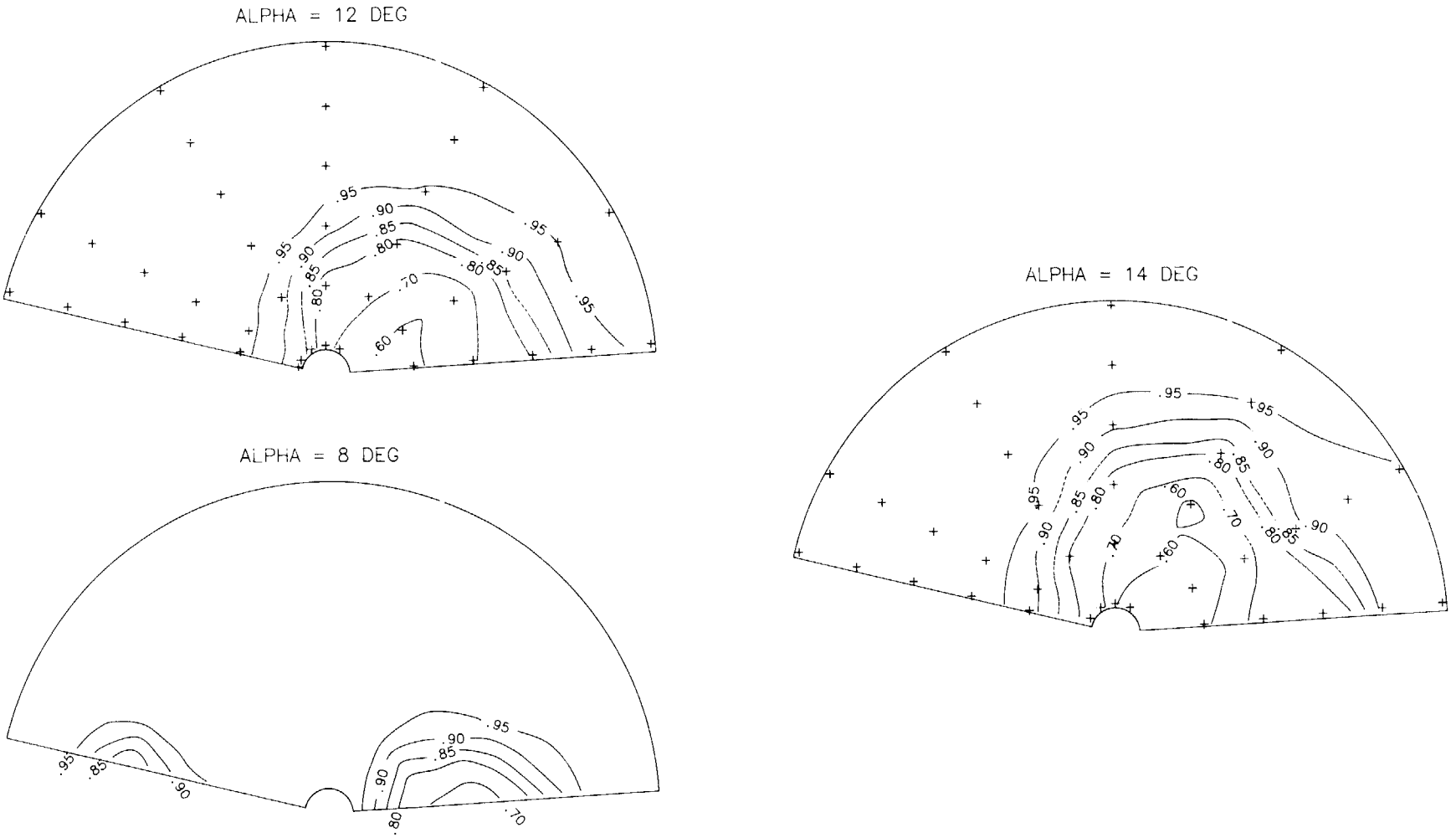

(b) Mach = 0.9.

Figure 16. Continued.

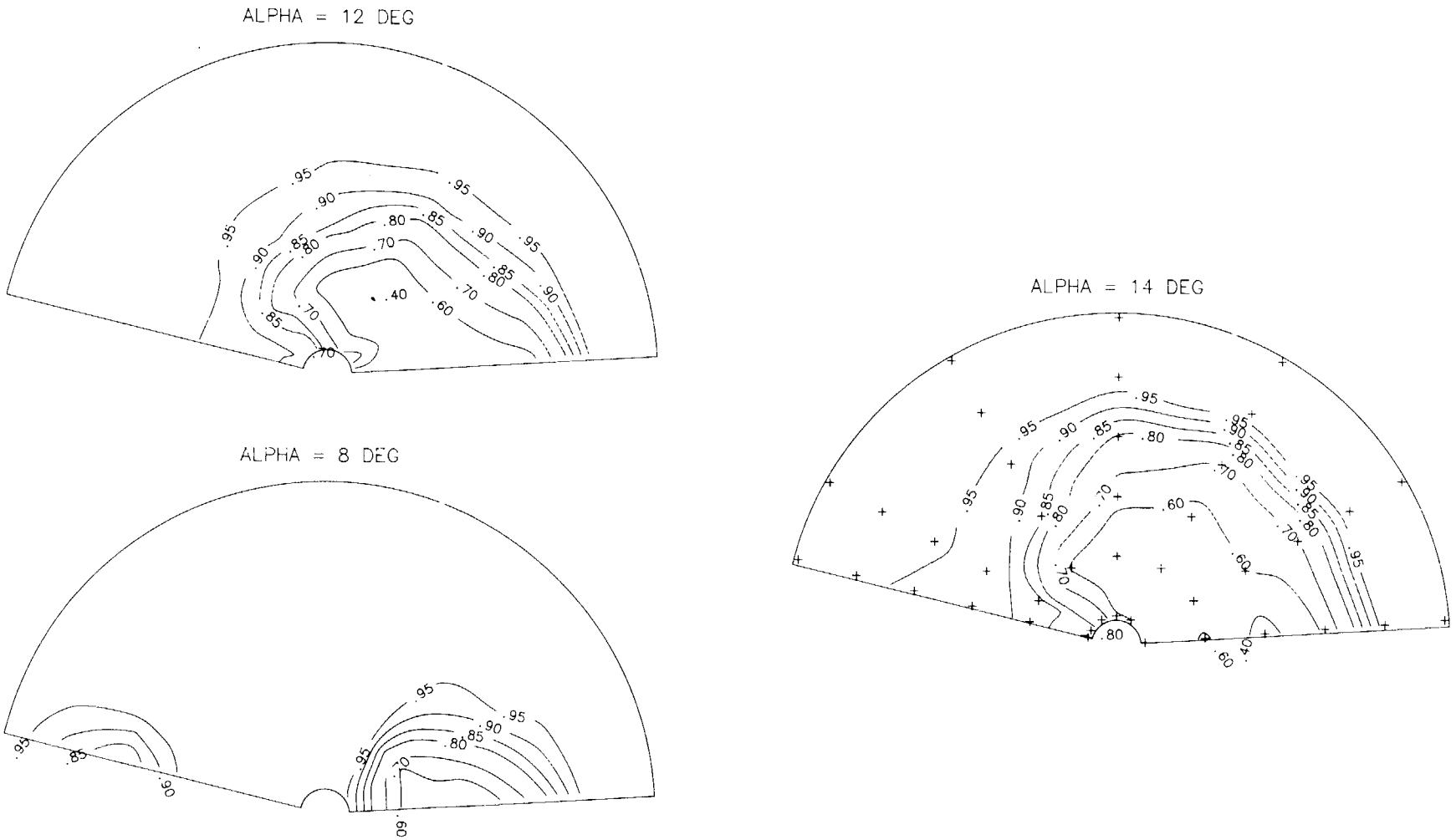

(c) Mach = 1.2.

Figure 16. Concluded.

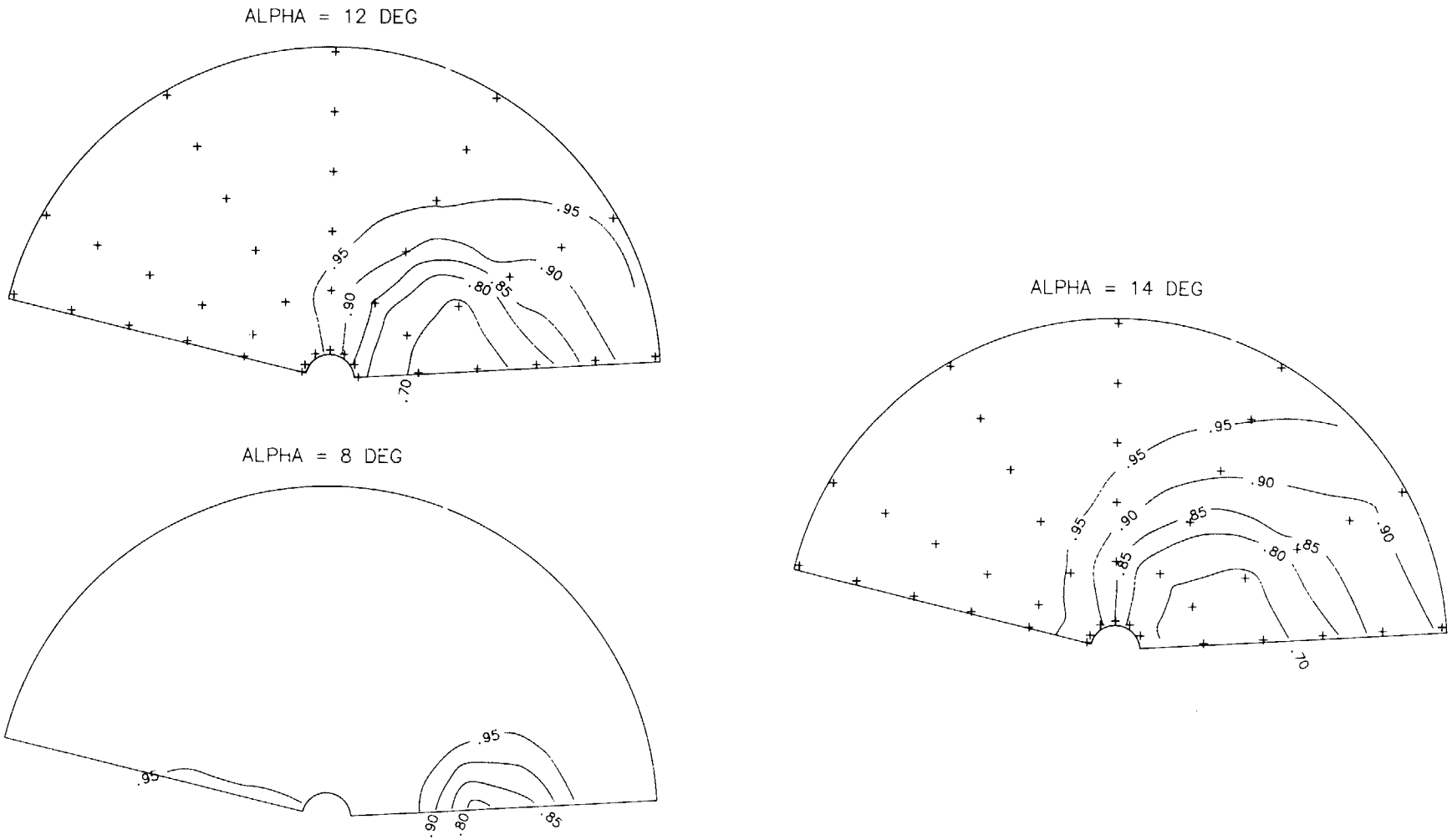

(a) Mach = 0.6.

Figure 17. Total pressure recovery contours for baseline configuration at $\beta = 5°$ and at fuselage station 36.5.

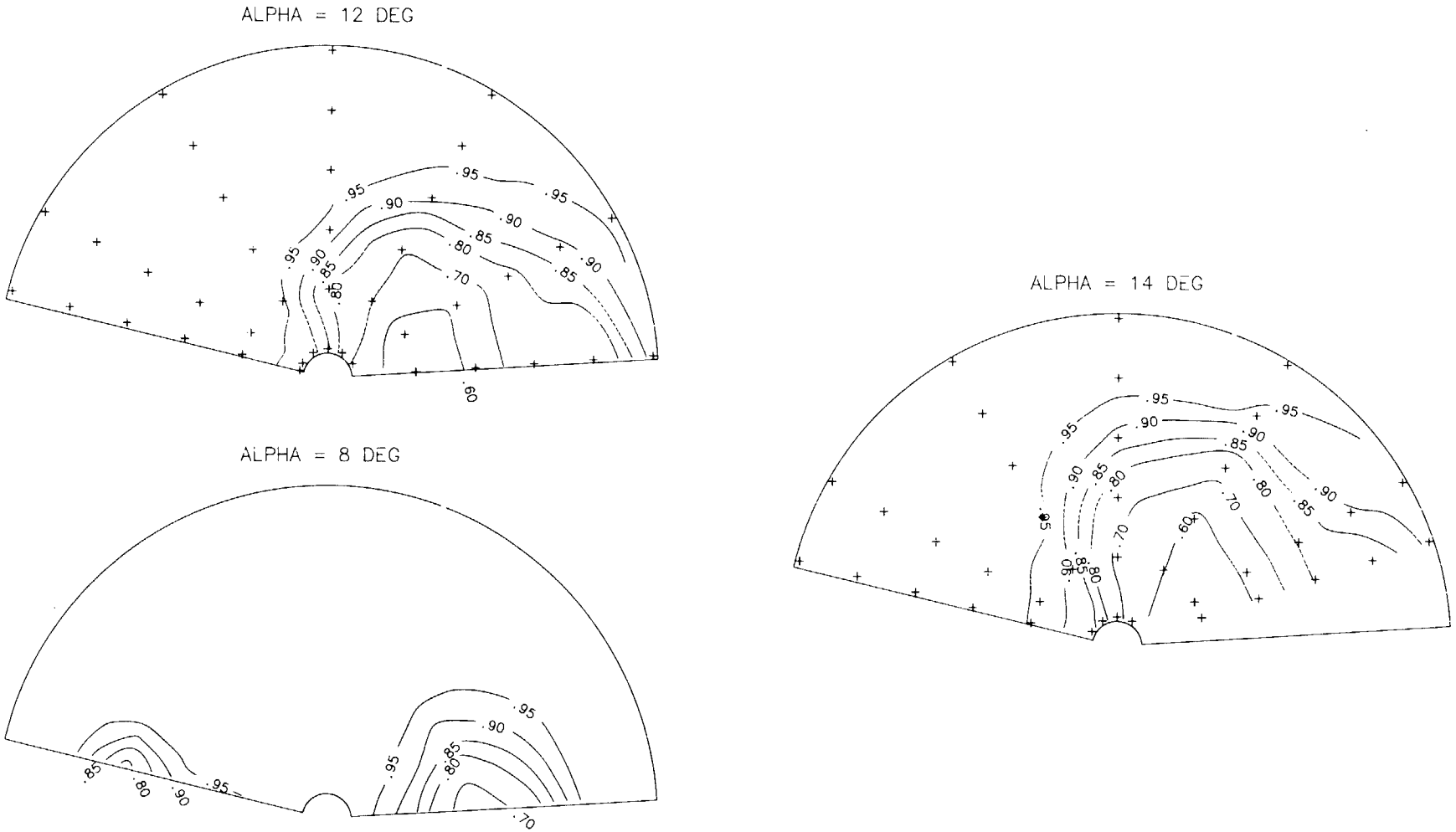

(b) Mach = 0.9.

Figure 17. Continued.

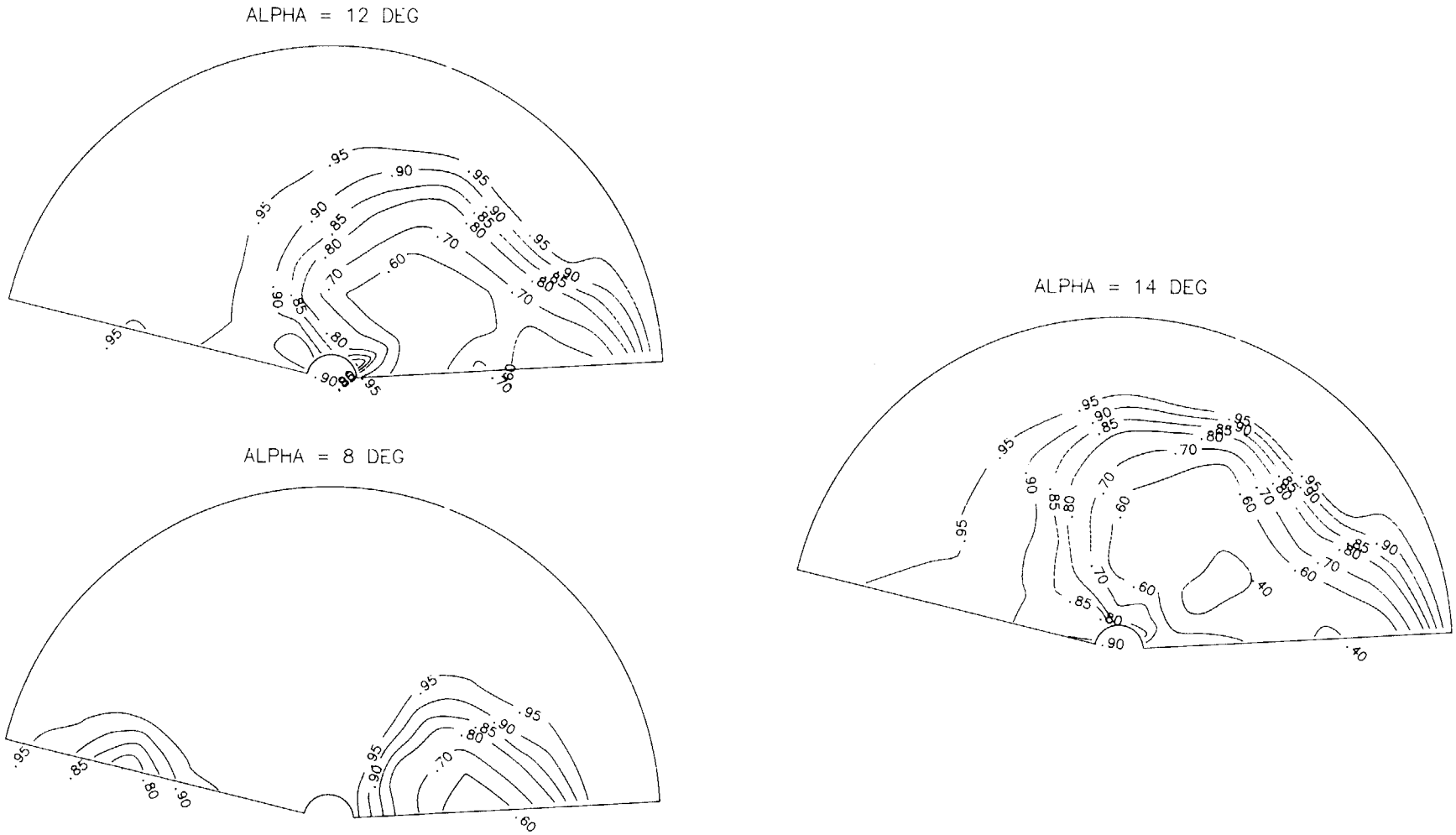

(c) Mach = 1.2.

Figure 17. Concluded.

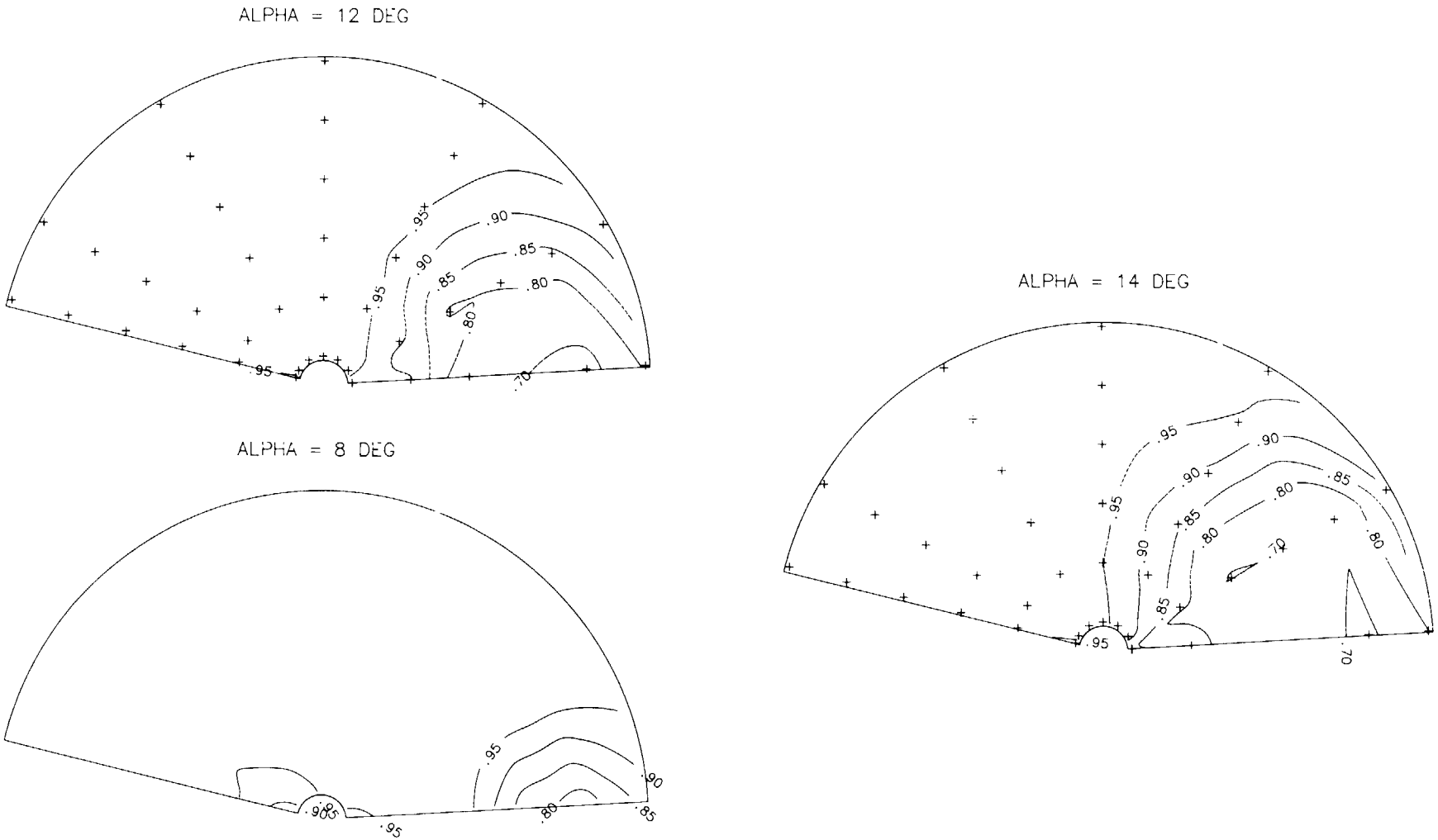

(a) Mach = 0.6.

Figure 18. Total pressure recovery contours for baseline configuration at $\beta = 5°$ and at fuselage station 40.5.

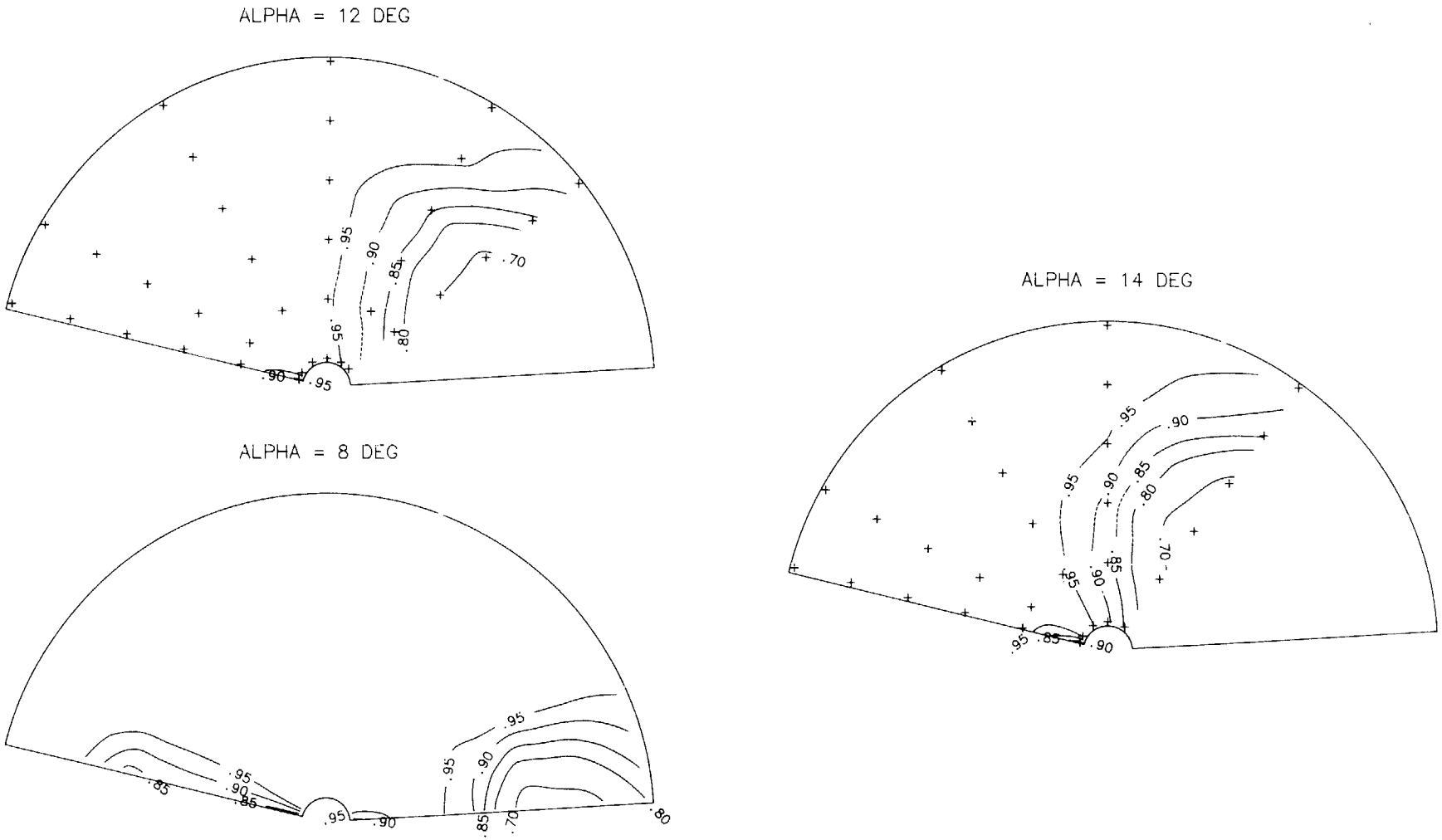

(b) Mach = 0.9.

Figure 18. Continued.

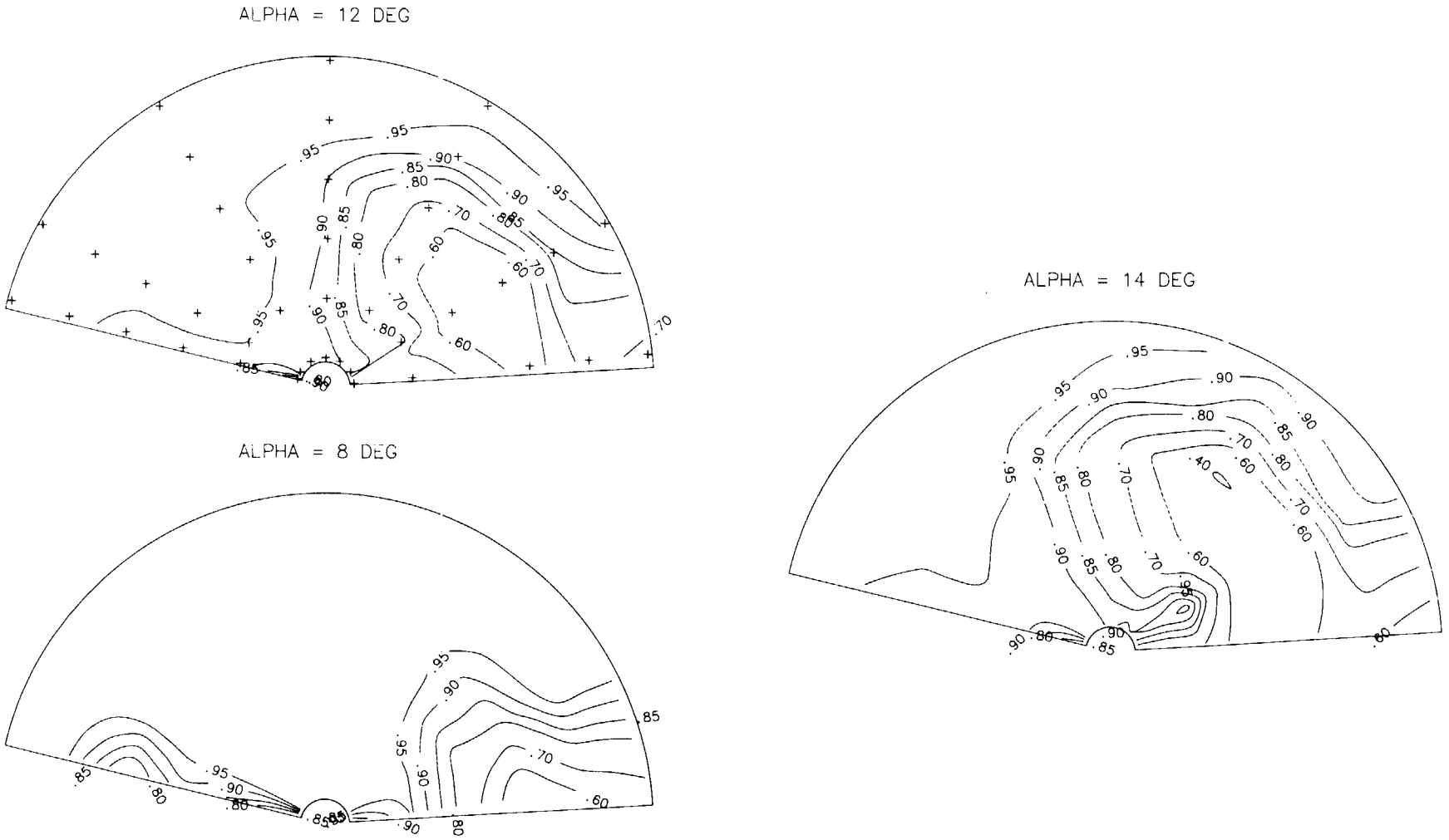

(c) Mach = 1.2.

Figure 18. Concluded.

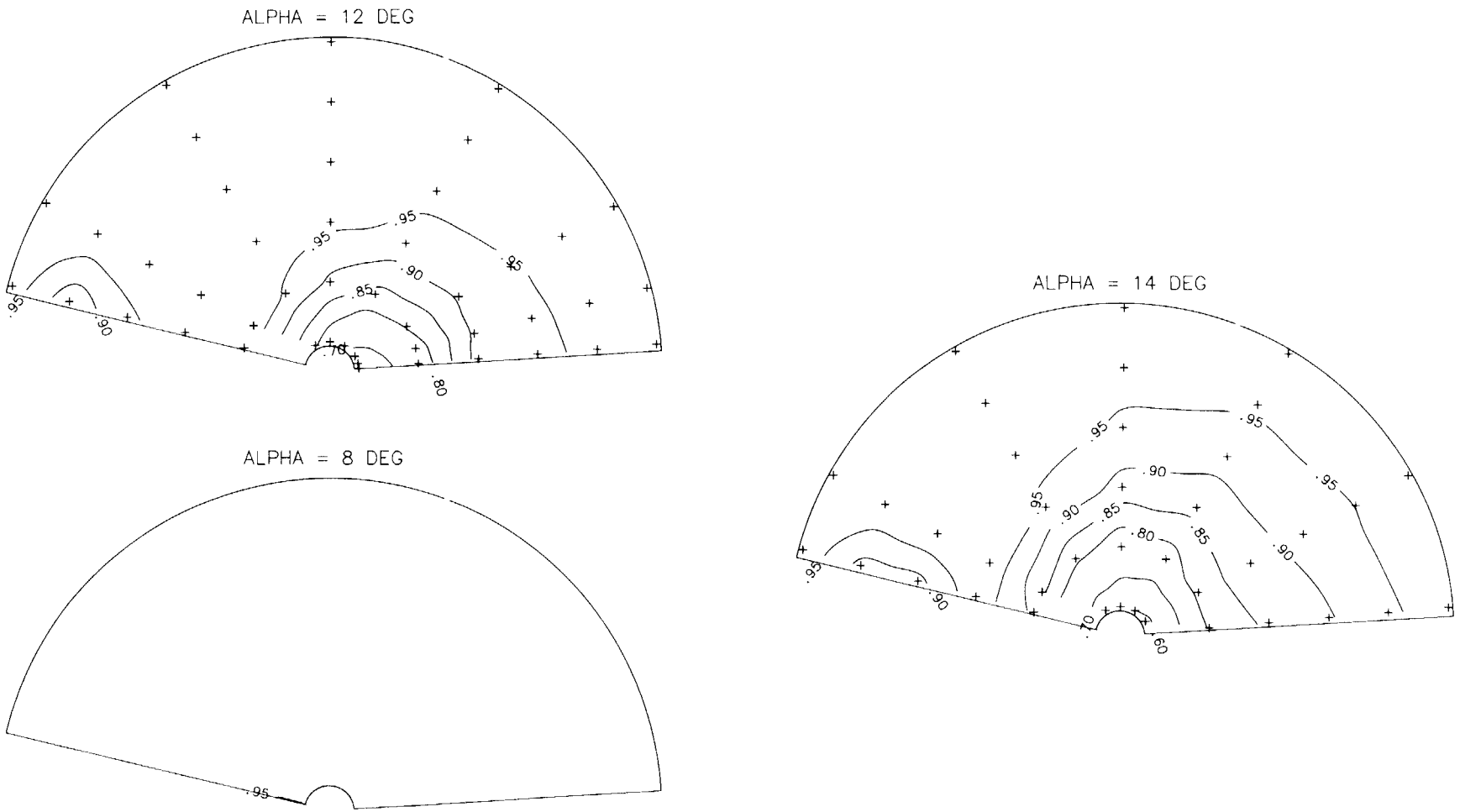

(a) Mach = 0.6.

Figure 19. Total pressure recovery contours for baseline configuration at $\beta = -5°$ and at fuselage station 32.8.

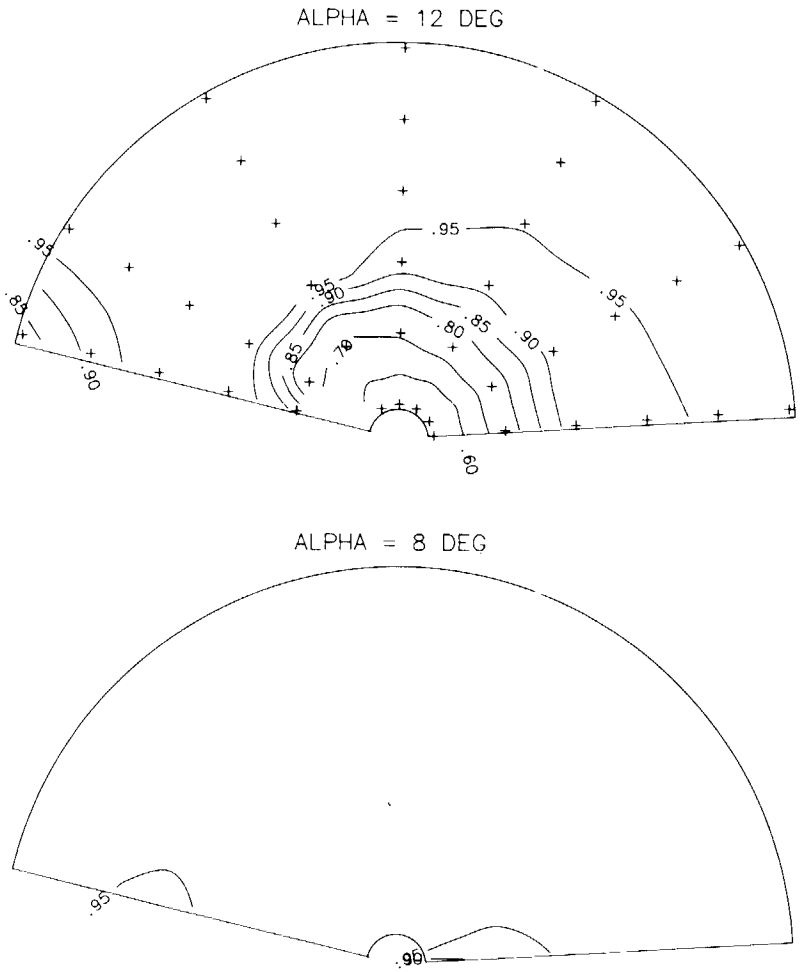

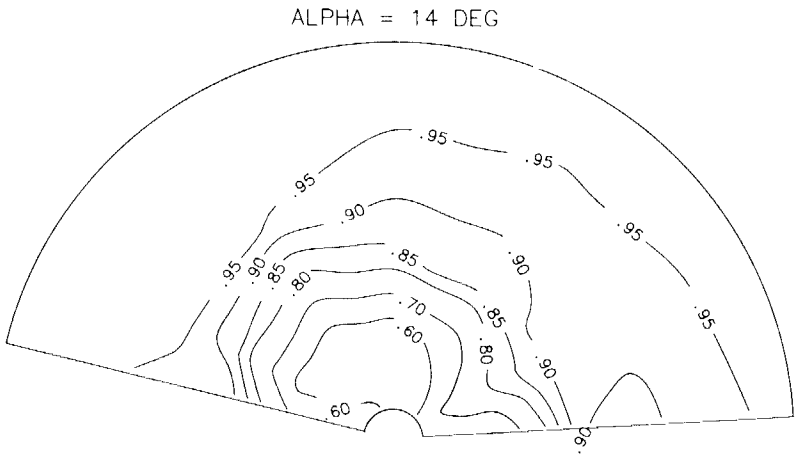

(b) Mach = 0.9.

Figure 19. Continued.

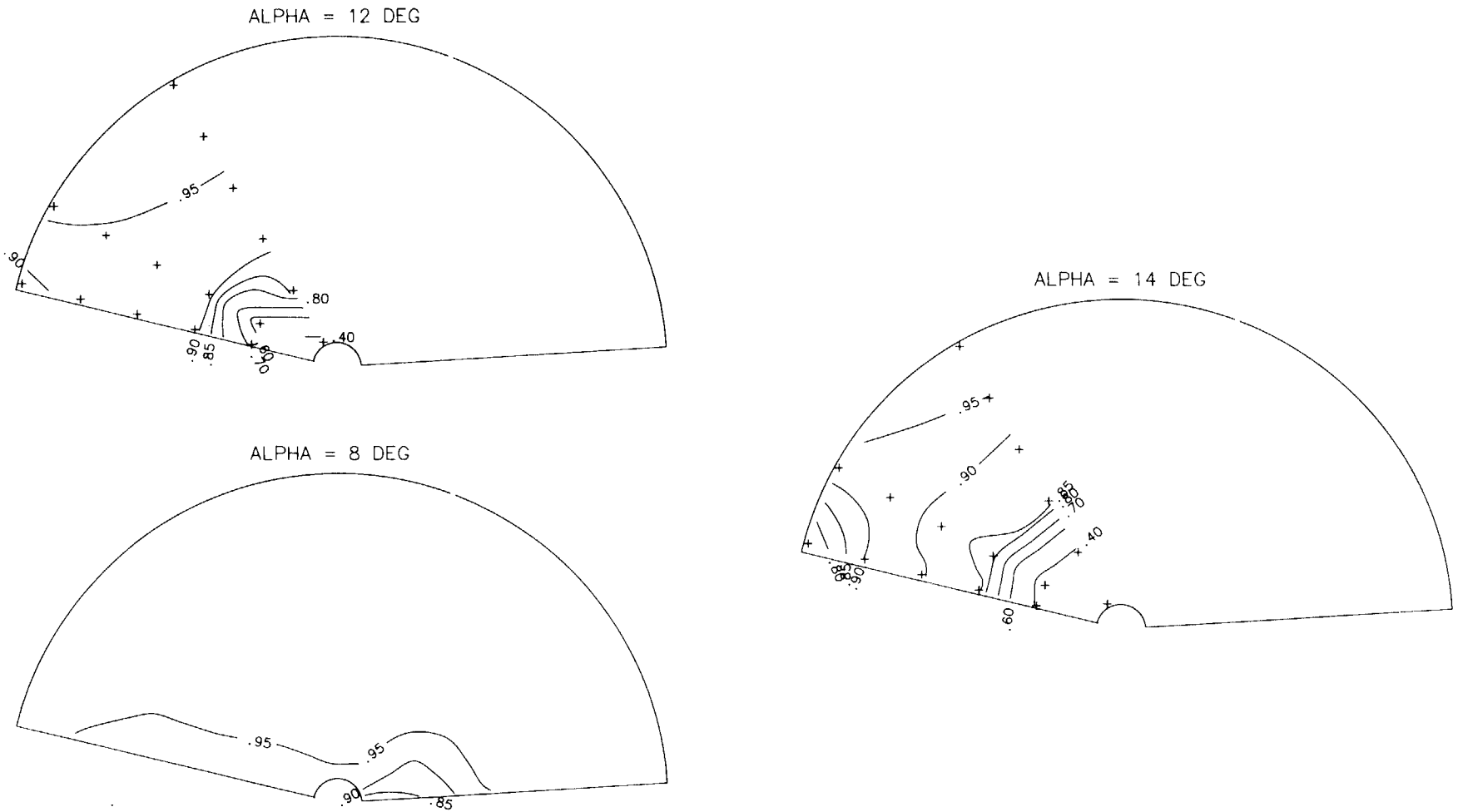

(c) Mach = 1.2.

Figure 19. Concluded.

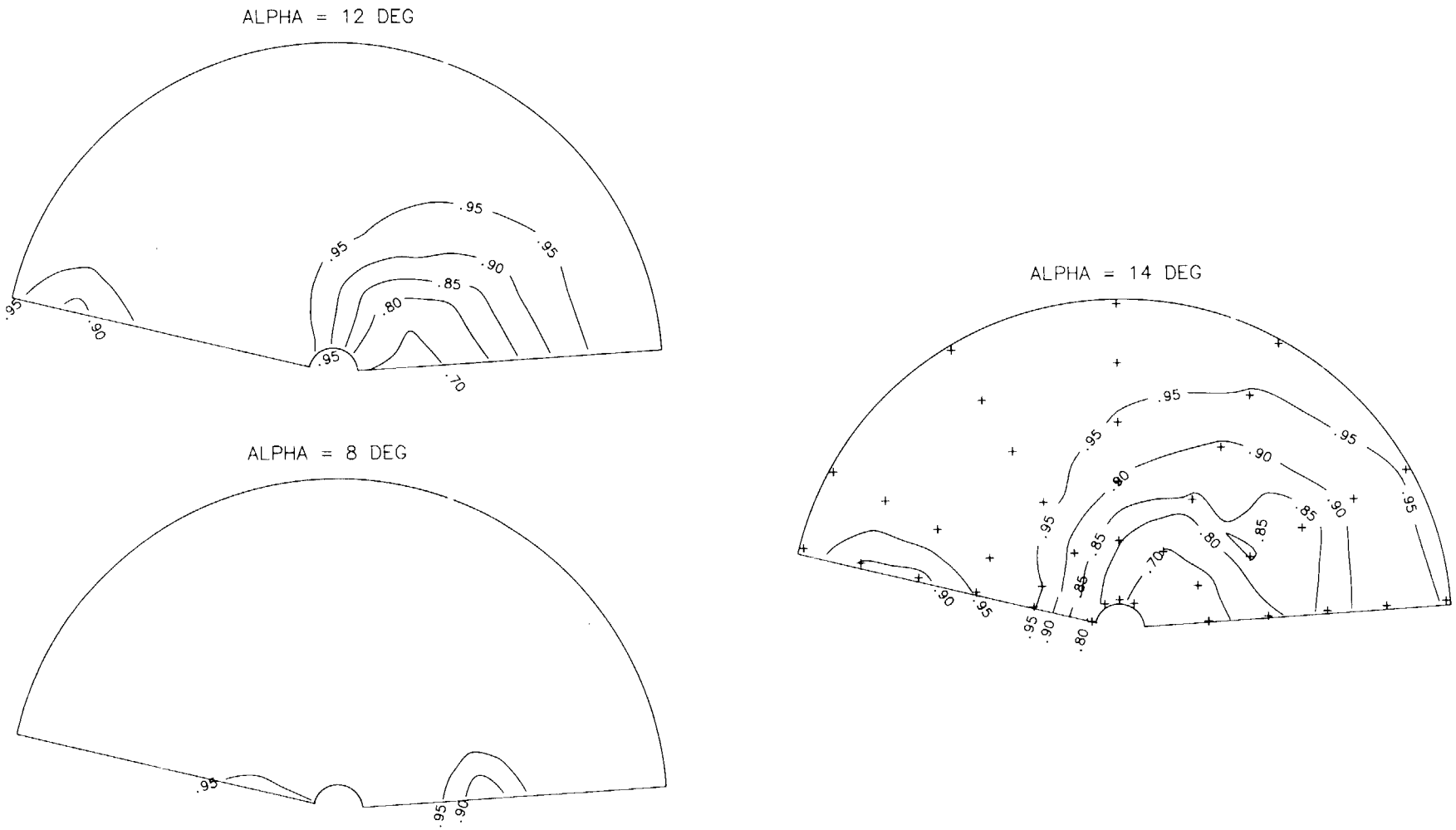

(a) Mach = 0.6.

Figure 20. Total pressure recovery contours for baseline configuration at $\beta = -5°$ and at fuselage station 35.0.

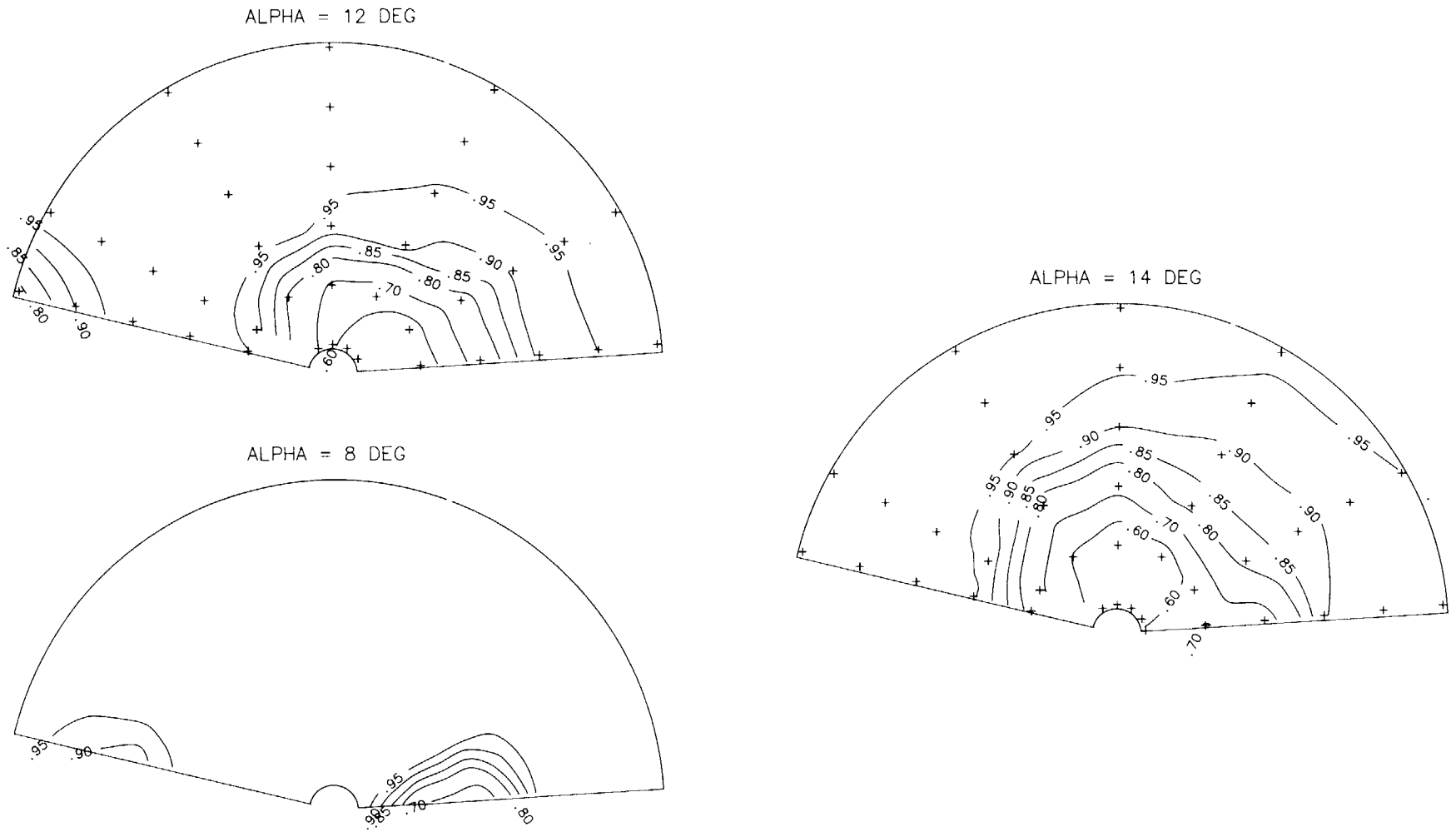

(b) Mach = 0.9.

Figure 20. Continued.

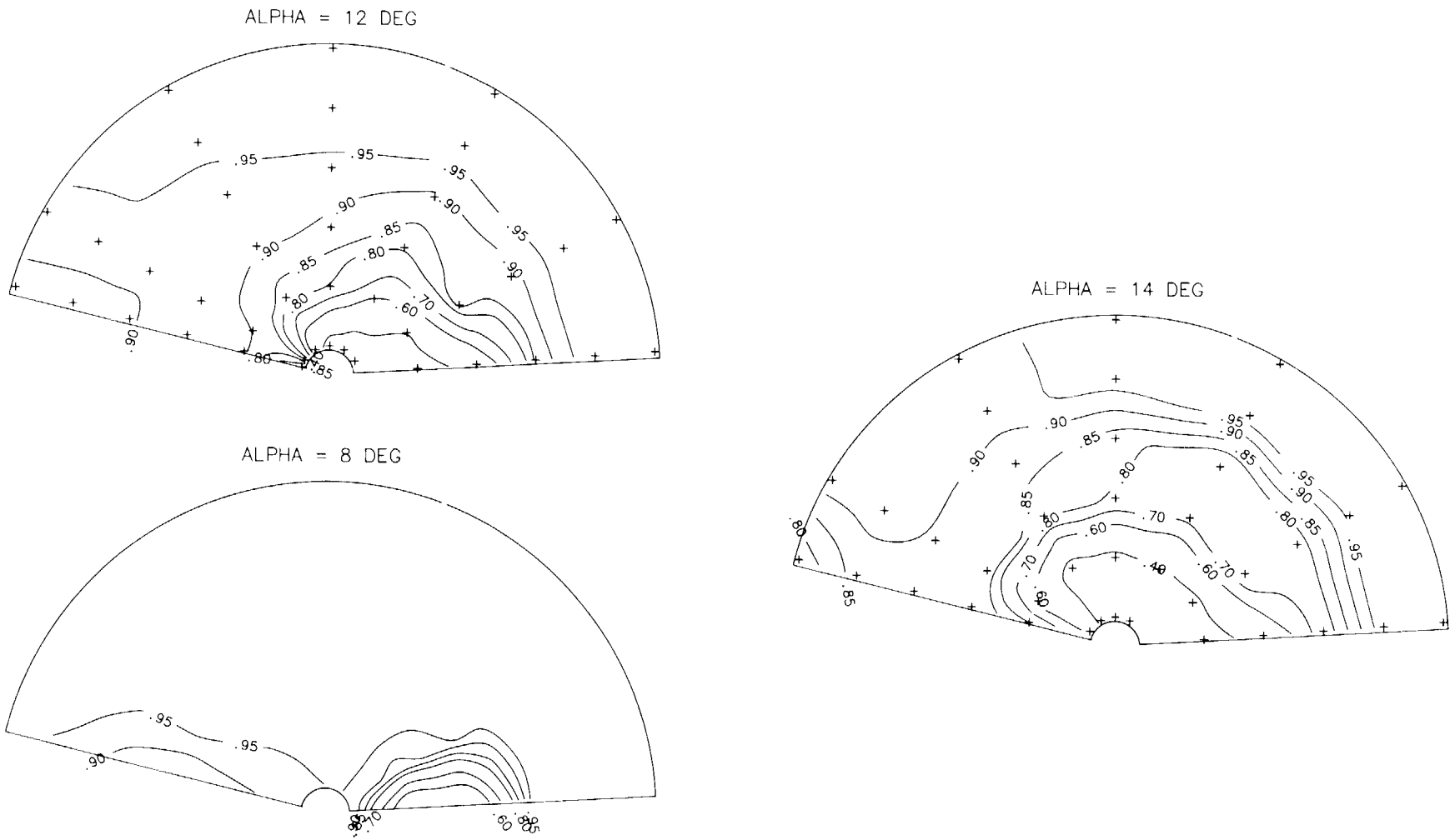

(c) Mach = 1.2.

Figure 20. Concluded.

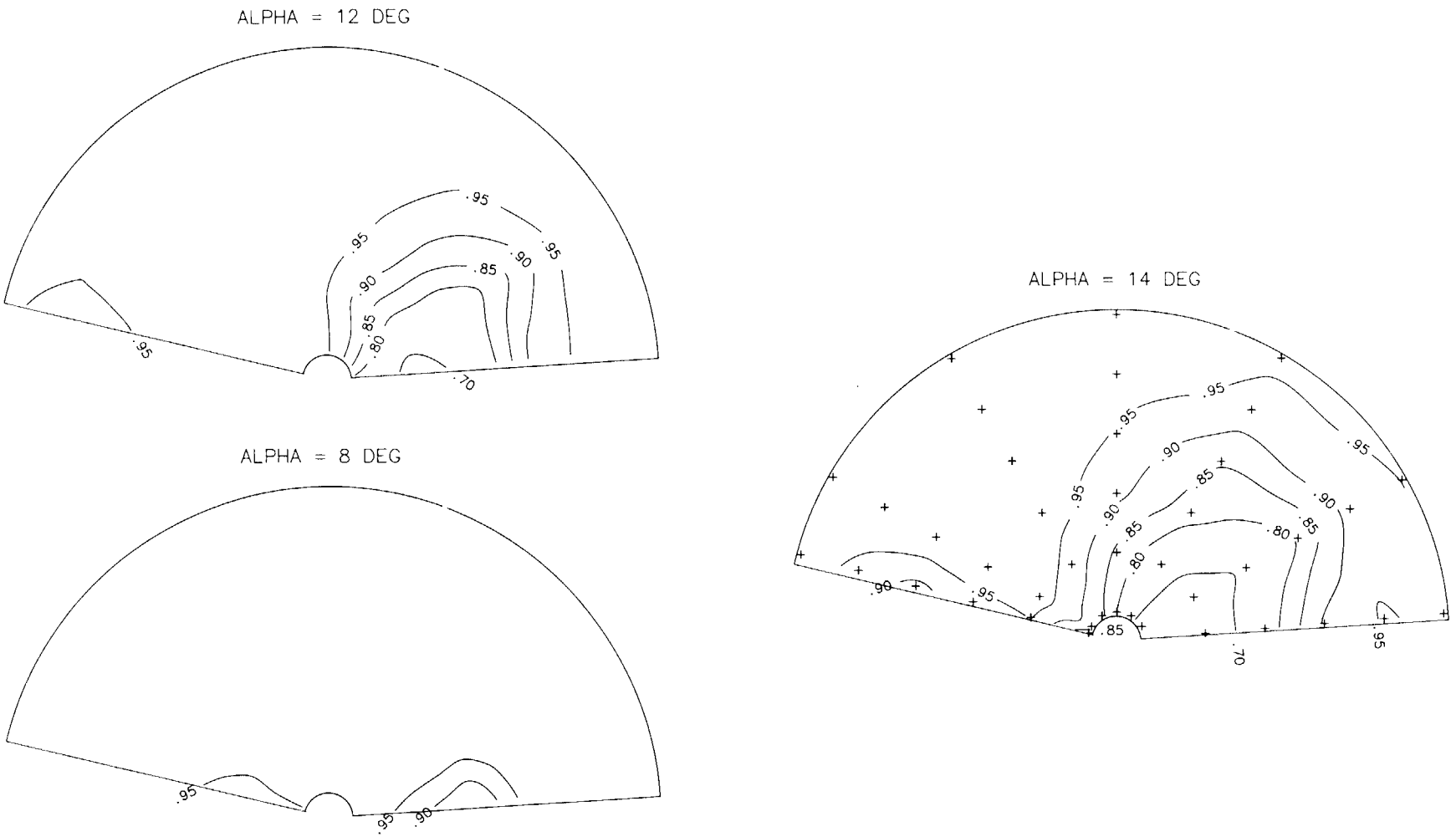

(a) Mach = 0.6.

Figure 21. Total pressure recovery contours for baseline configuration at $\beta = -5°$ and at fuselage station 36.5.

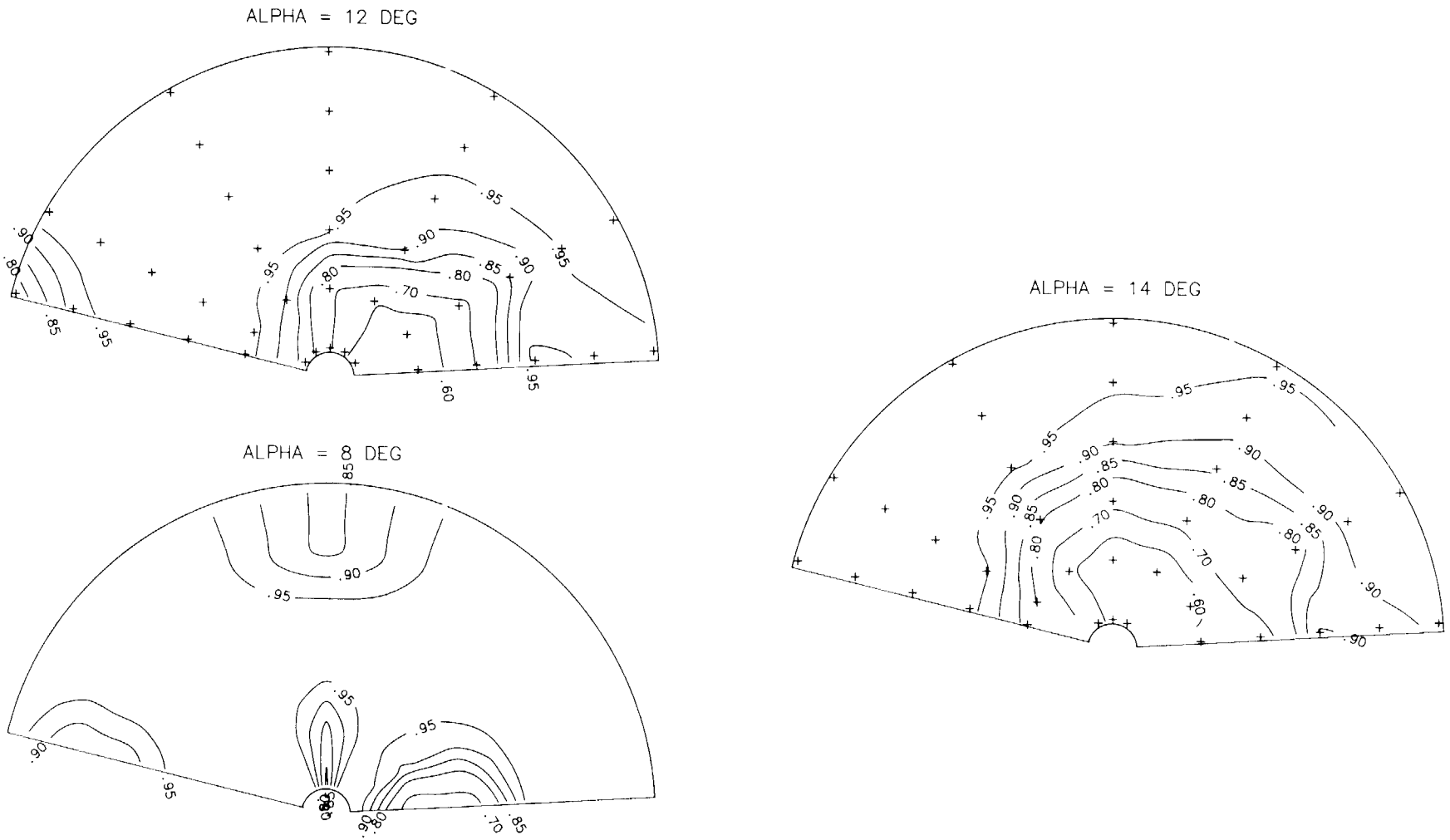

(b) Mach = 0.9.

Figure 21. Continued.

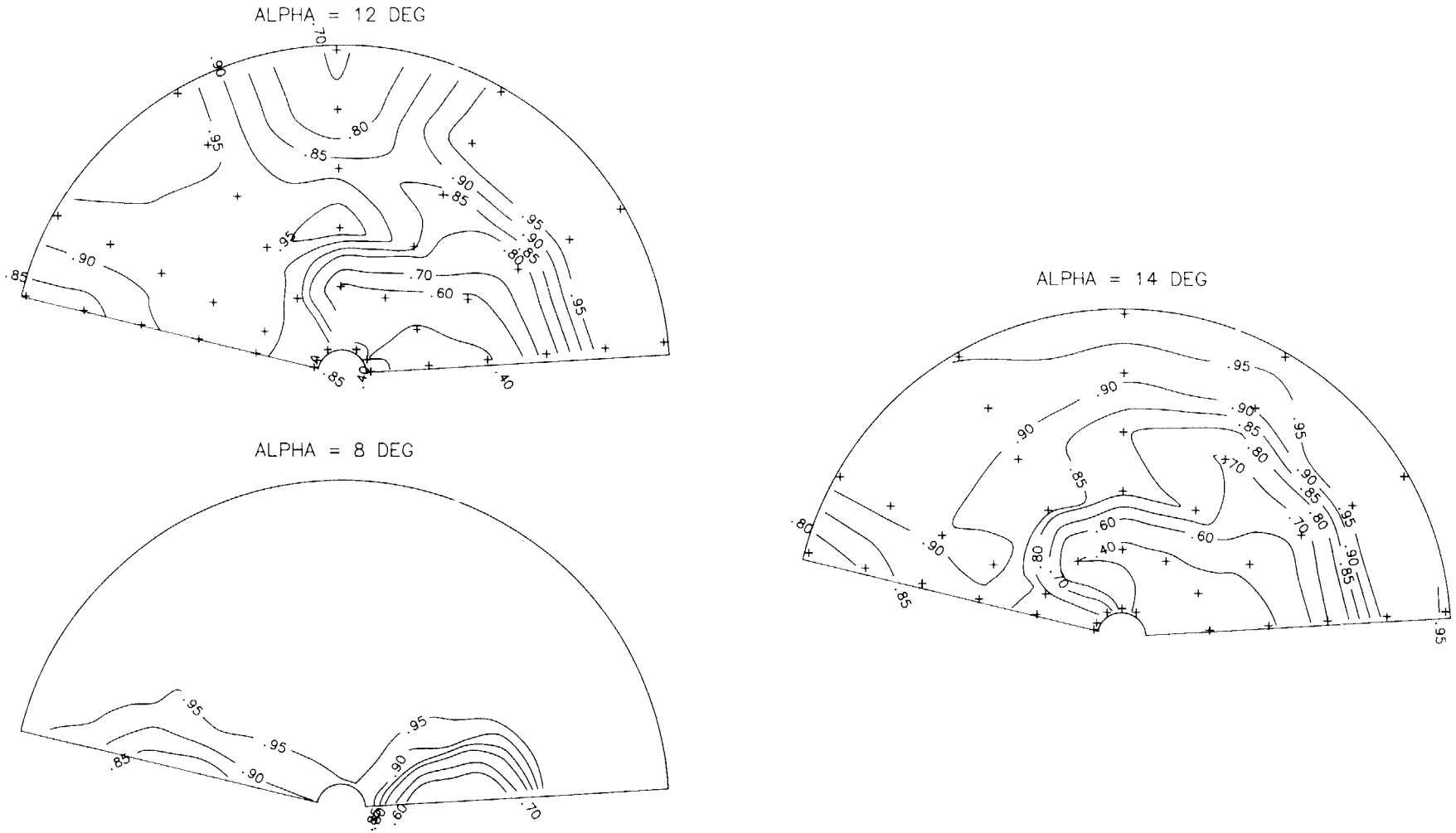

(c) Mach = 1.2.

Figure 21. Concluded.

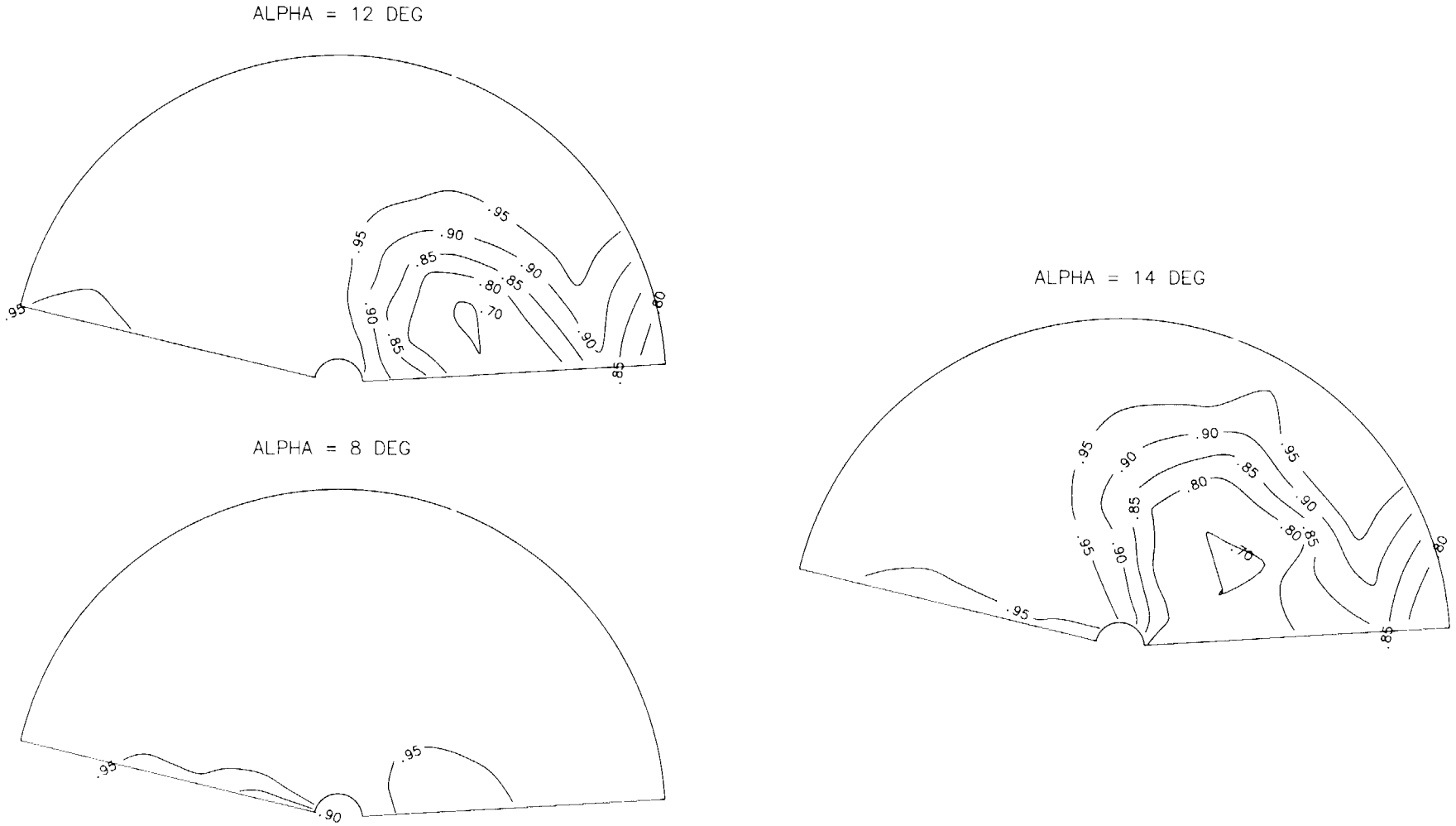

ALPHA = 8 DEG

ALPHA = 14 DEG

(a) Mach = 0.6.

Figure 22. Total pressure recovery contours for baseline configuration at $\beta = -5°$ and at fuselage station 40.5.

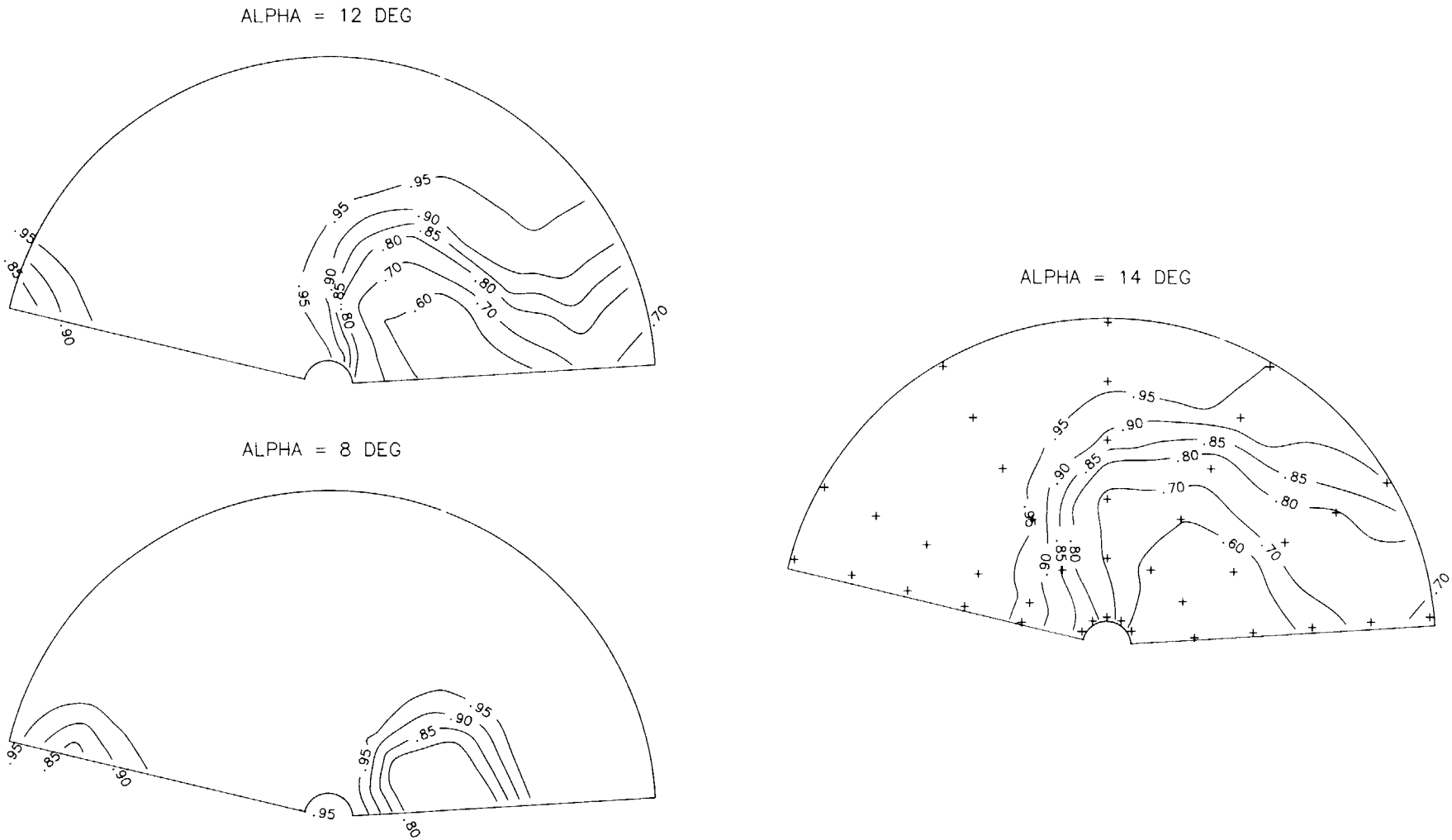

(b) Mach = 0.9.

Figure 22. Continued.

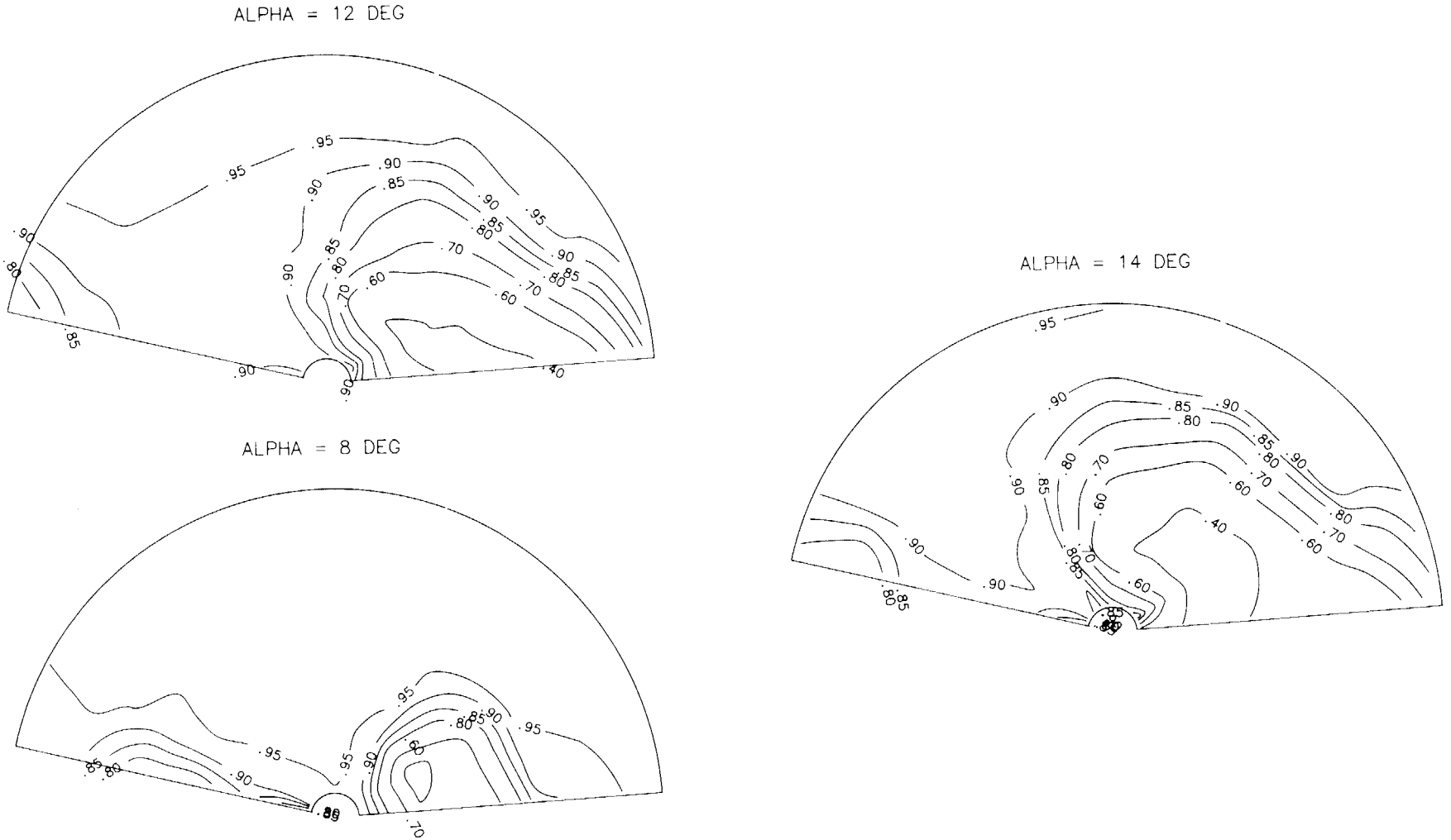

(c) Mach = 1.2.

Figure 22. Concluded.

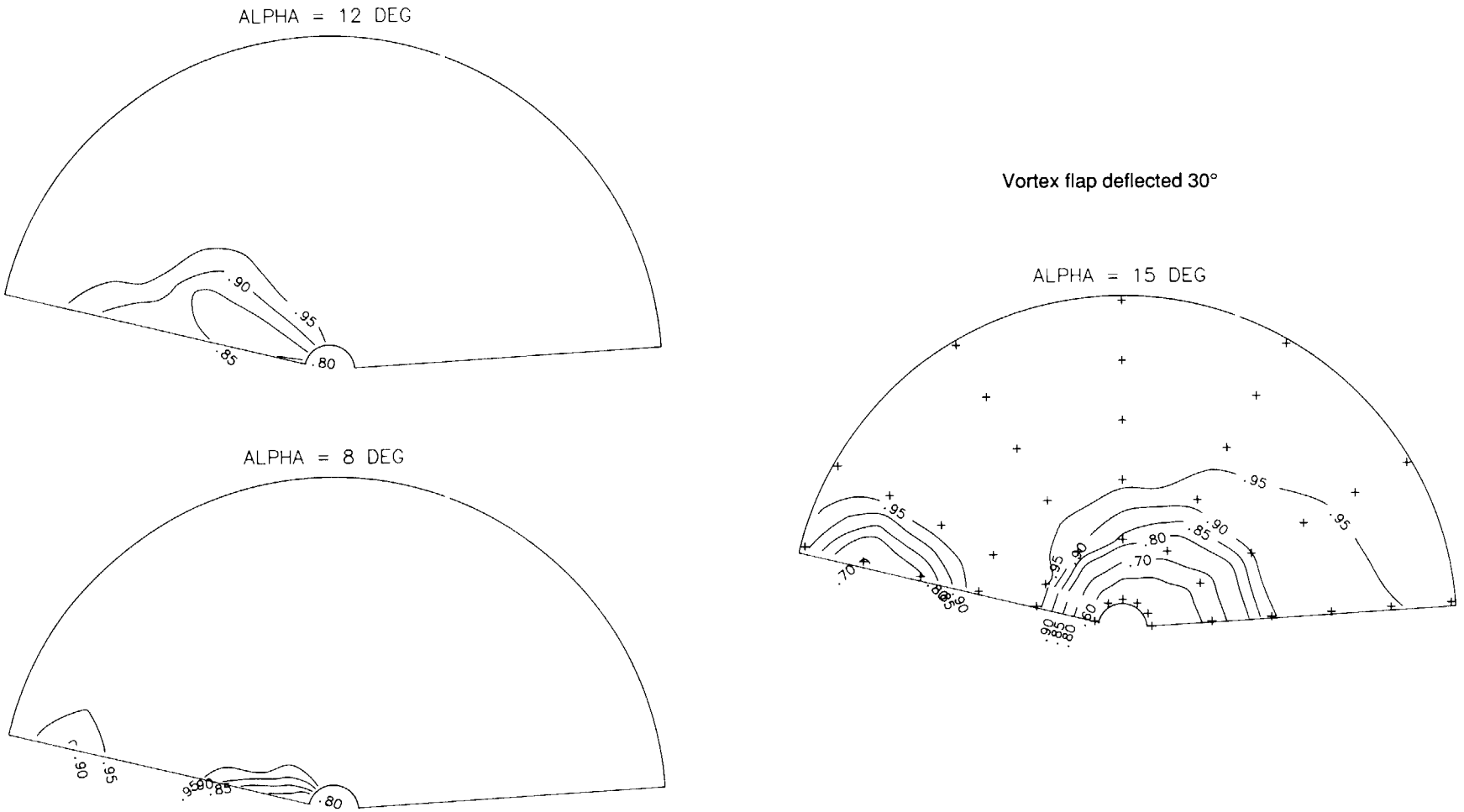

(a) Fuselage station 32.8.

Figure 23. Total pressure recovery contours for configuration with vortex flap deflected at Mach 0.9.

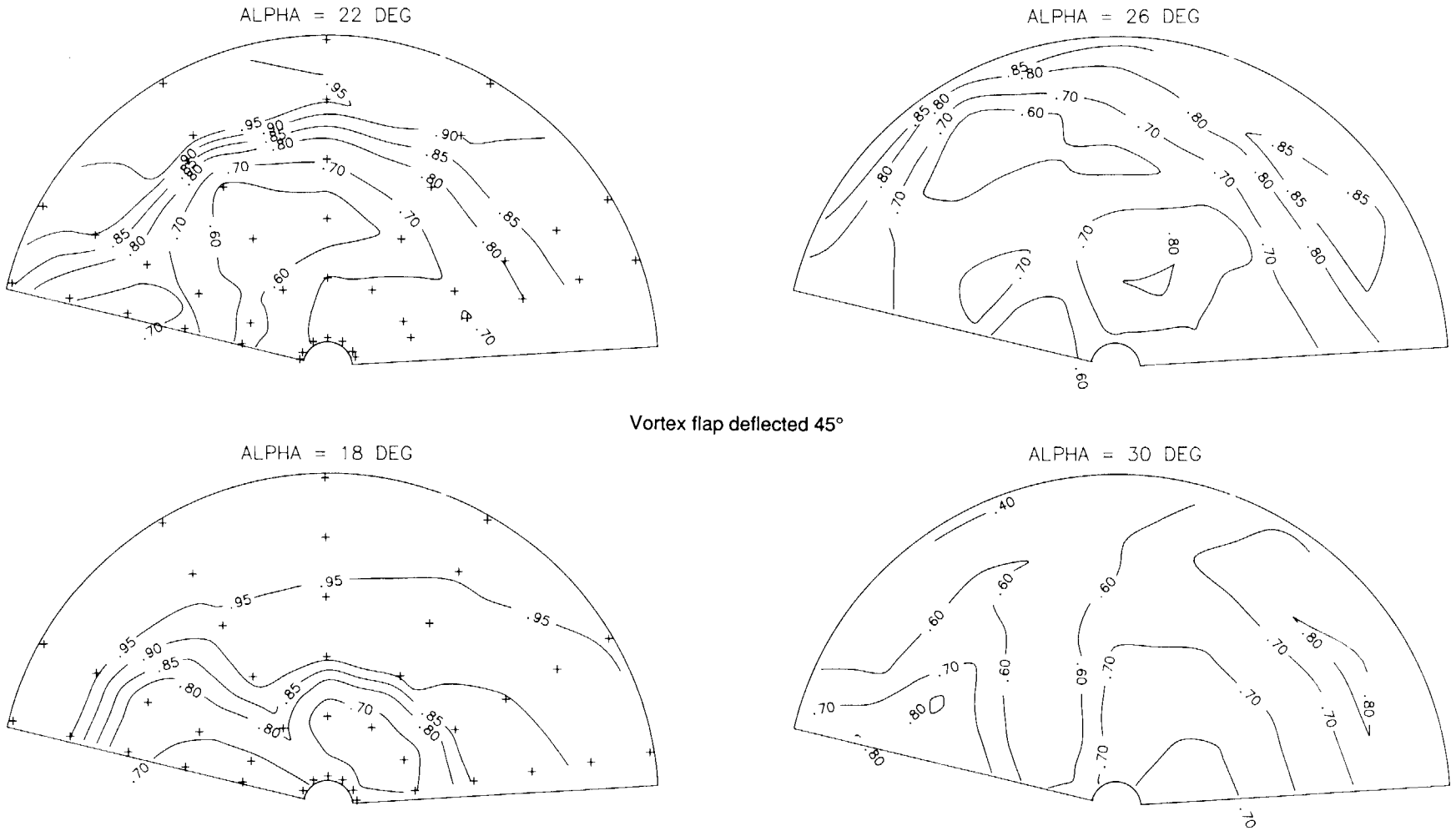

(a) Concluded.

Figure 23. Continued.

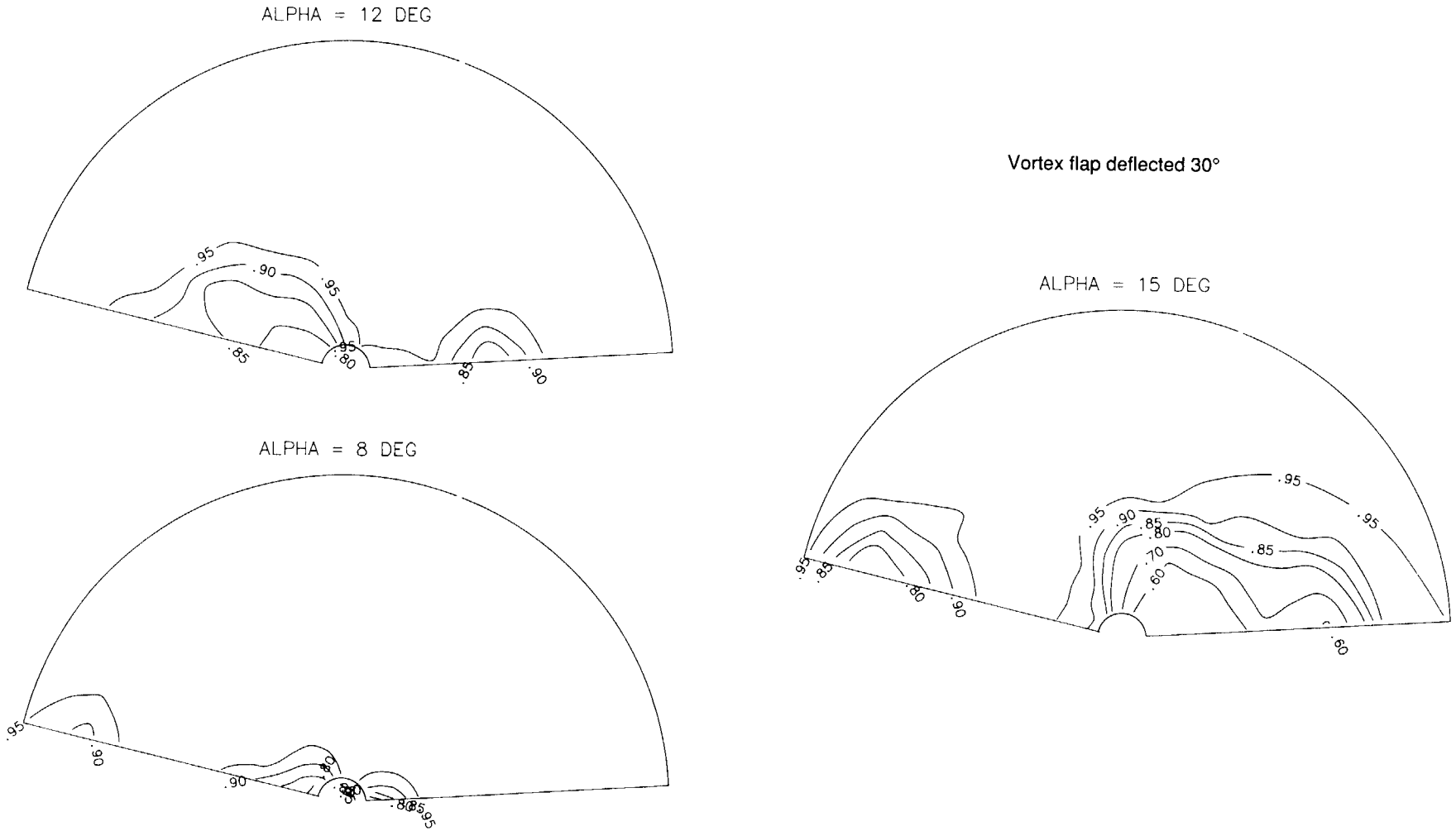

(b) Fuselage station 35.0.

Figure 23. Continued.

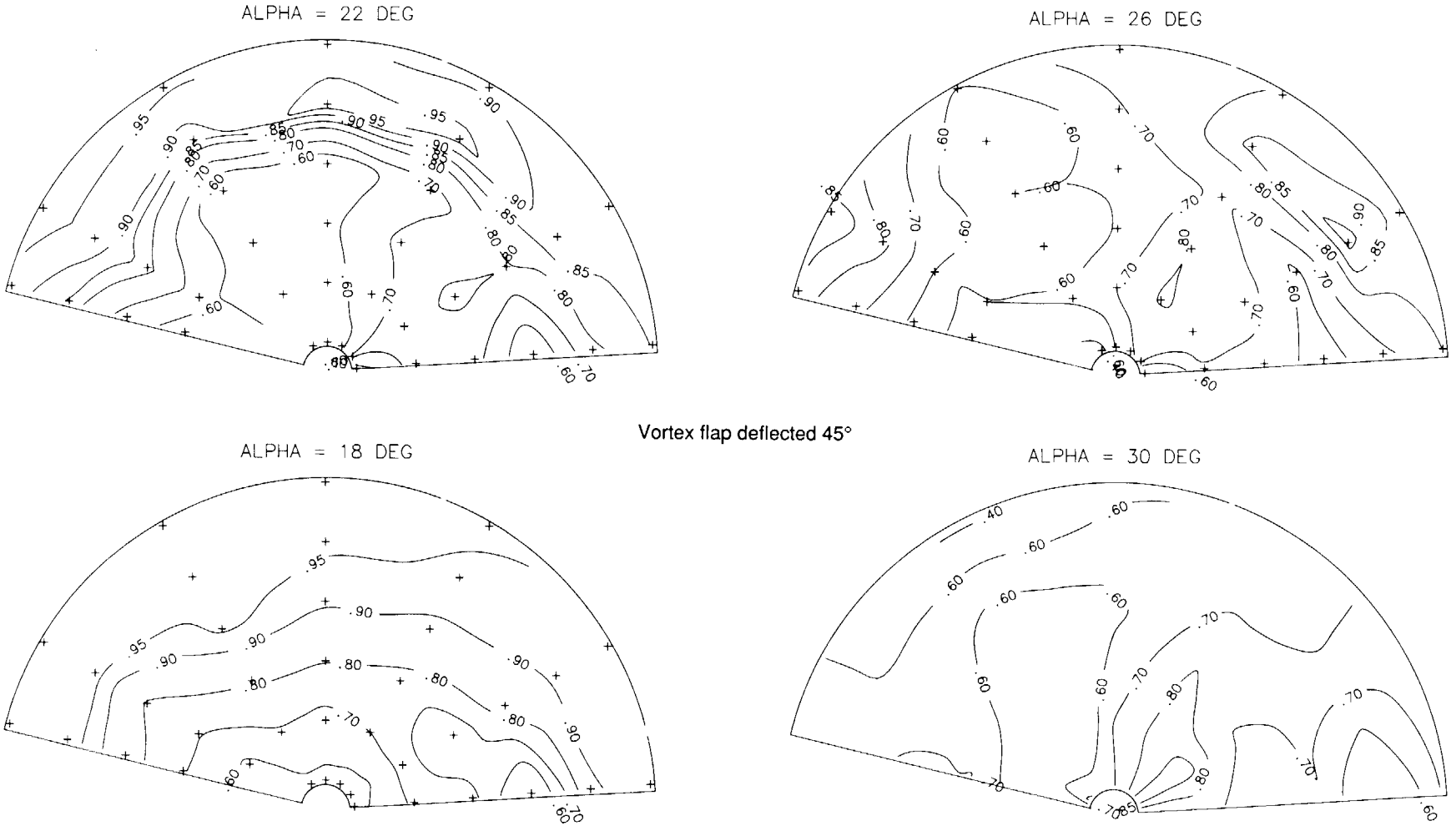

(b) Concluded.

Figure 23. Continued.

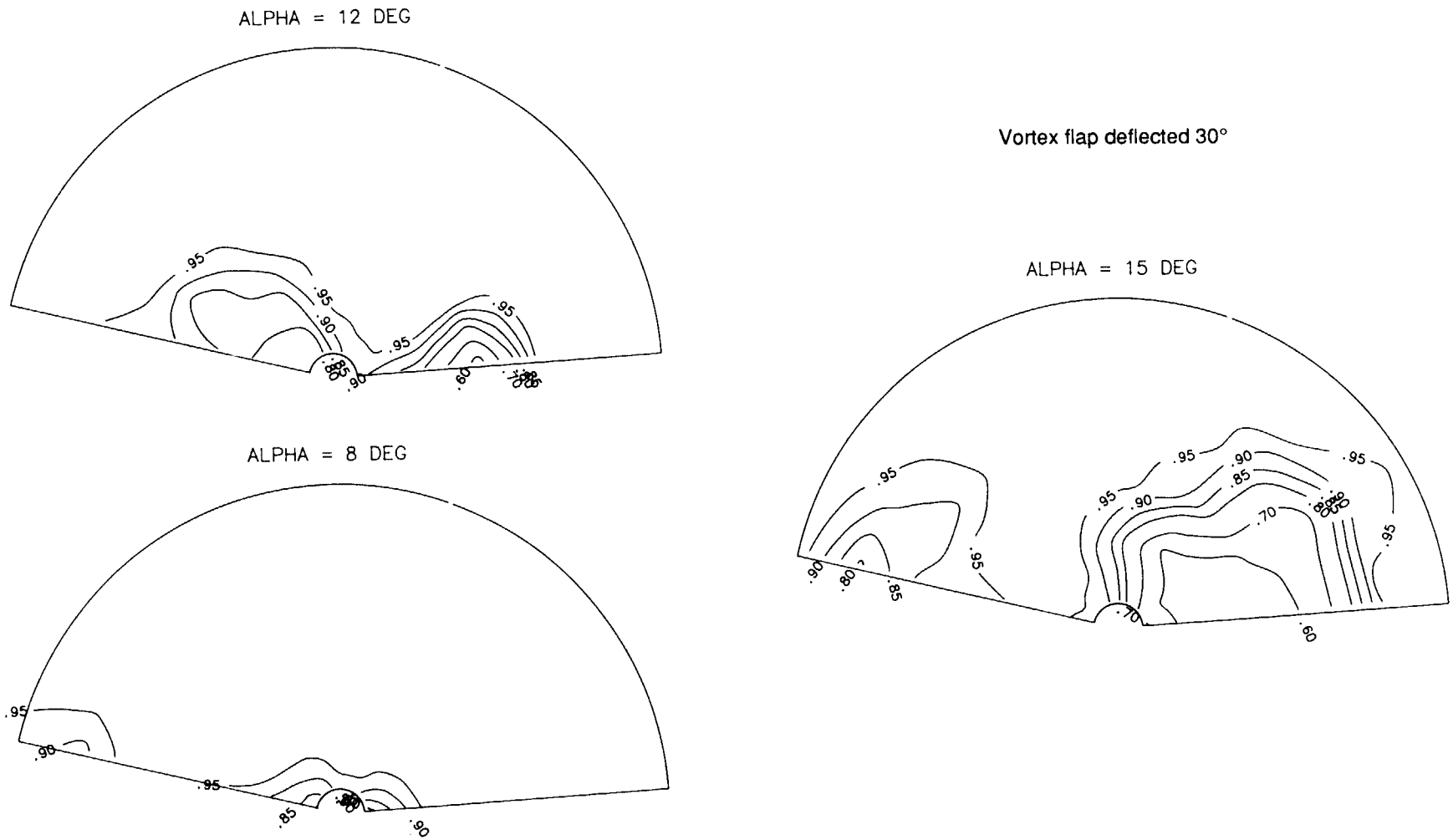

(c) Fuselage station 36.5.

Figure 23. Continued.

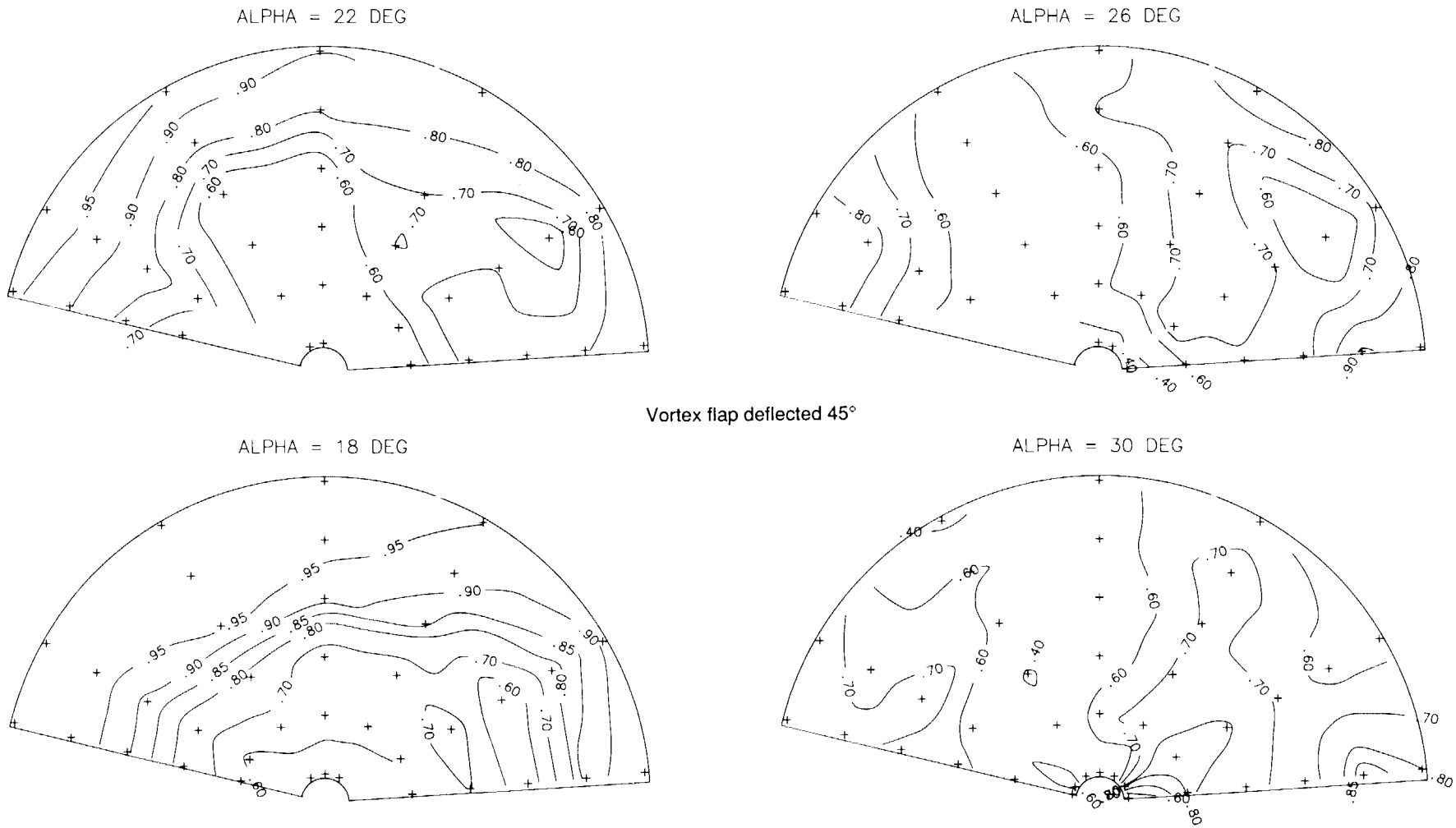

(c) Concluded.

Figure 23. Continued.

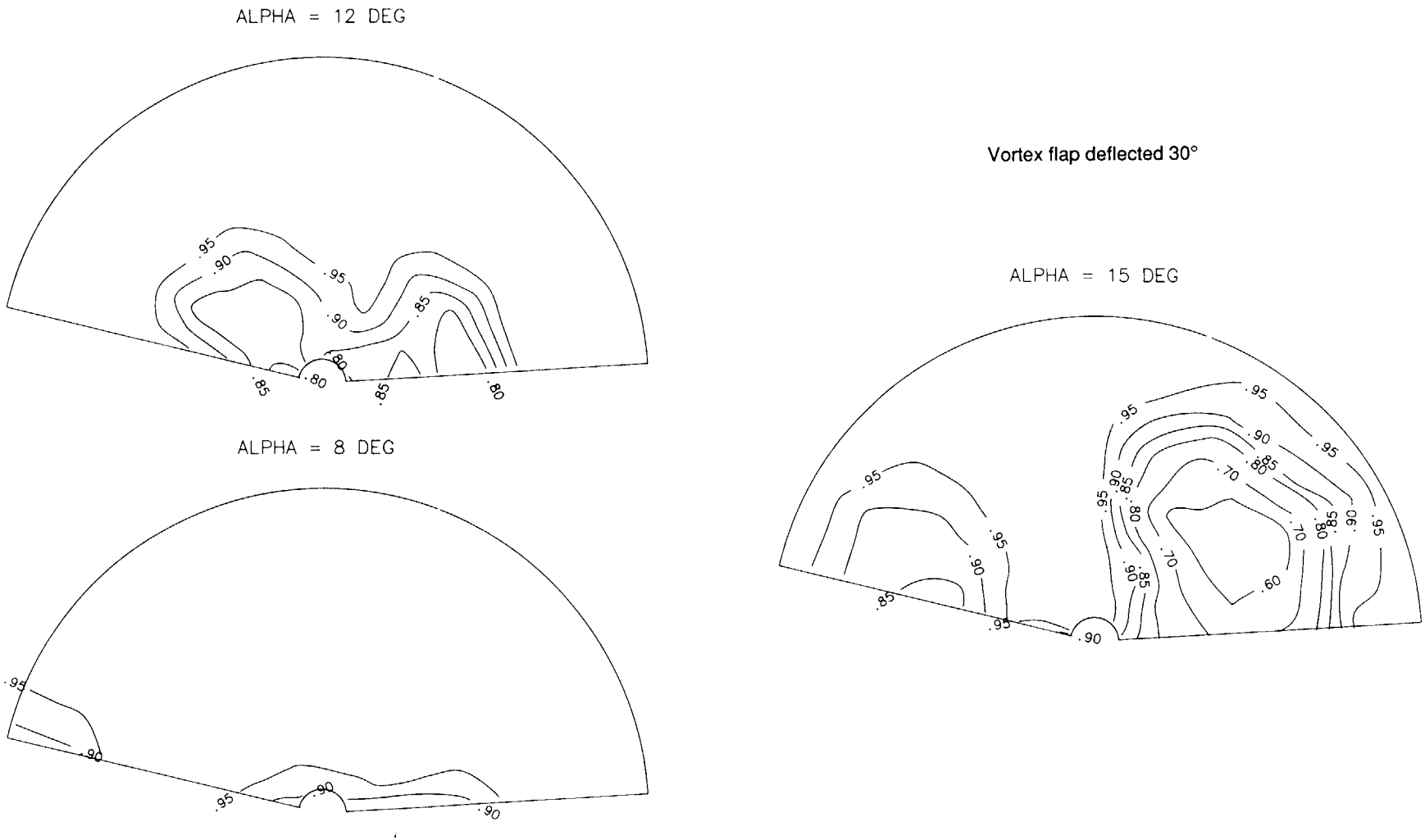

(d) Fuselage station 40.5.

Figure 23. Continued.

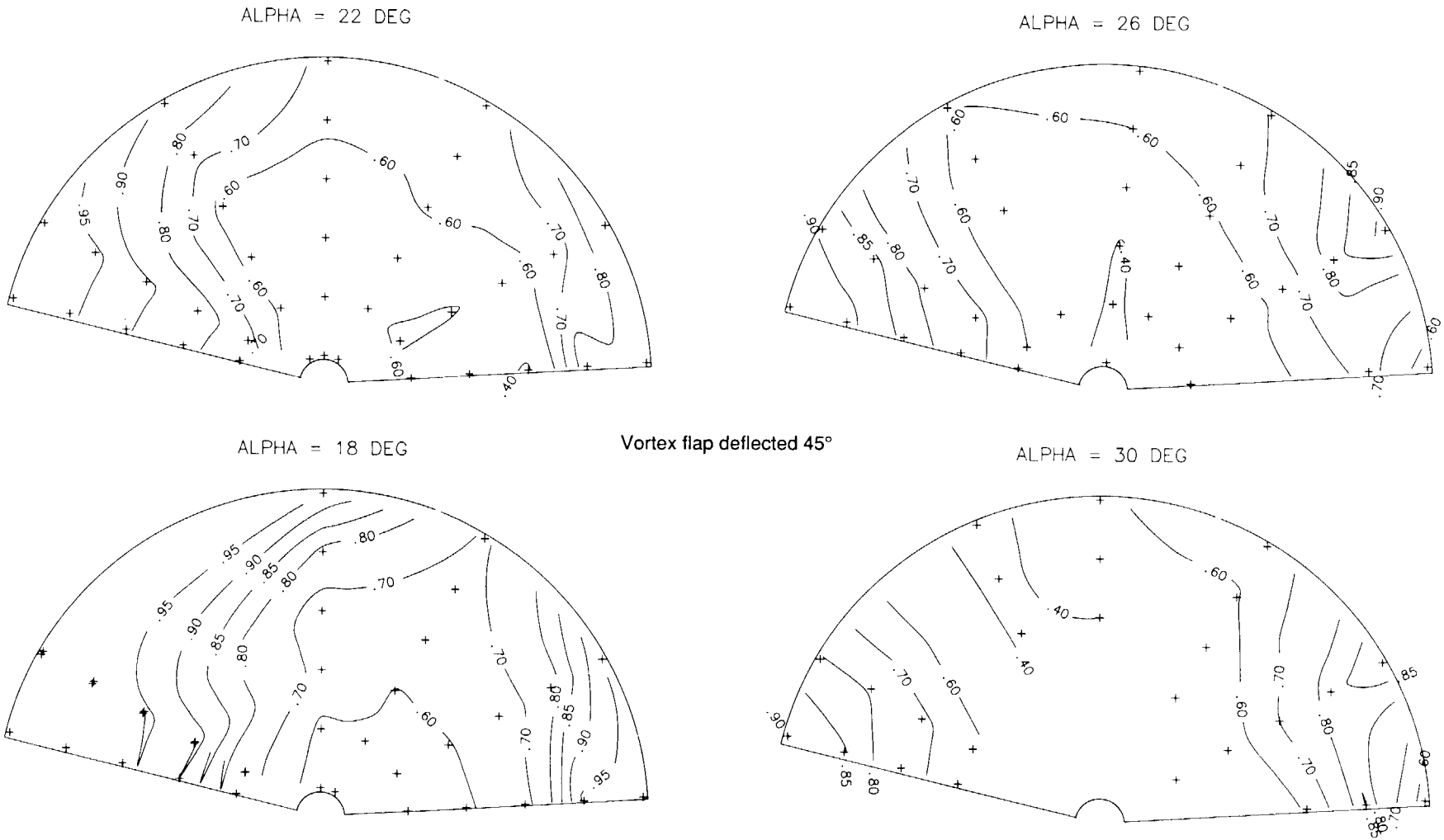

(d) Concluded.

Figure 23. Concluded.

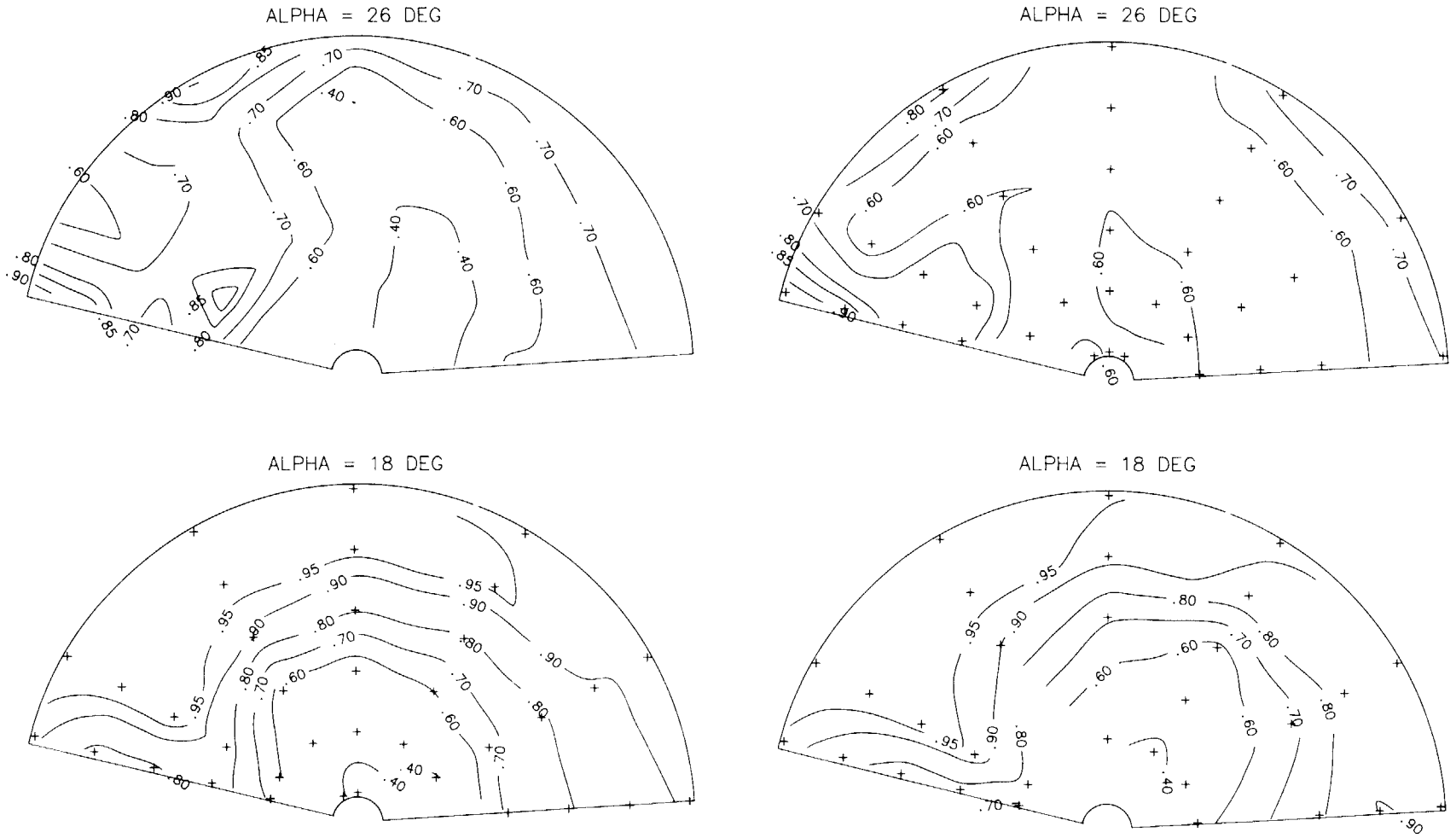

(a) Fuselage station 32.8.

(b) Fuselage station 35.0.

Figure 24. Total pressure recovery contours for configuration with large wing fences at Mach 0.9.

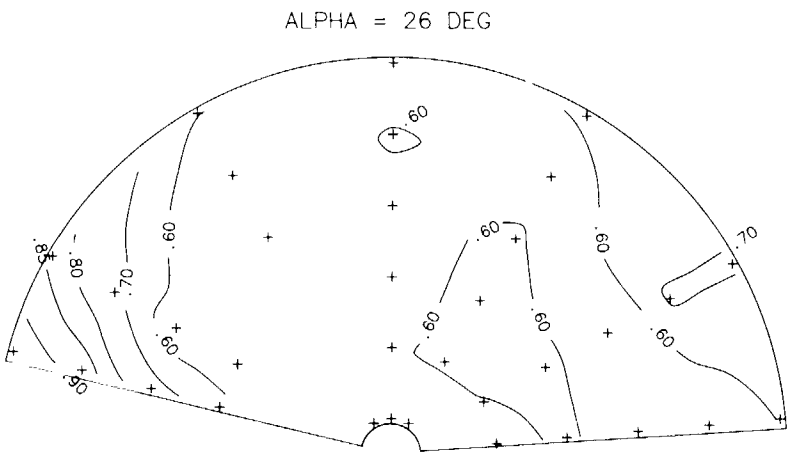

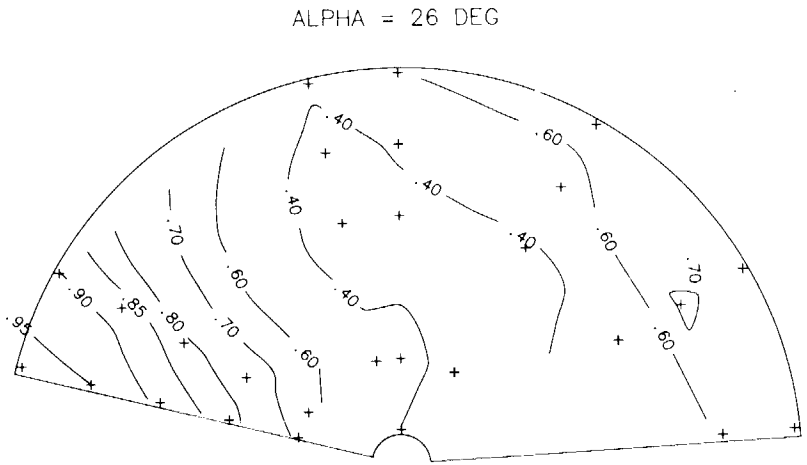

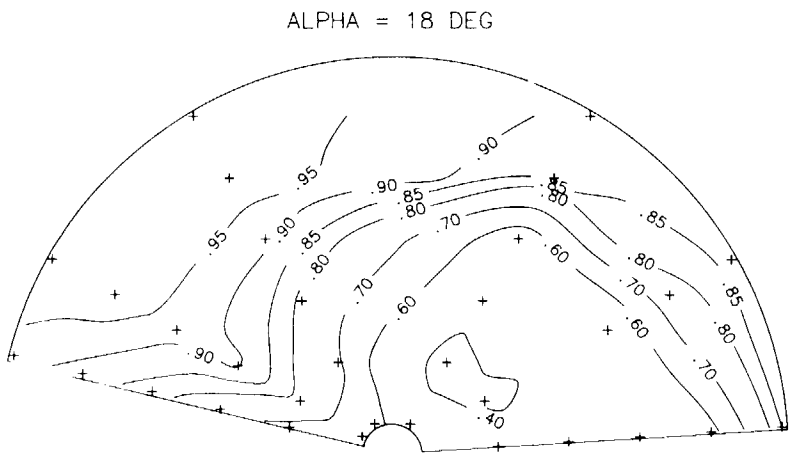

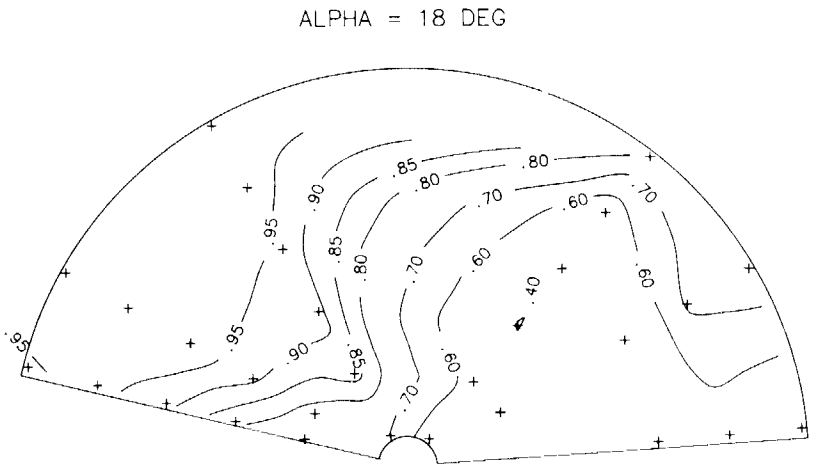

(c) Fuselage station 36.5.

(d) Fuselage station 40.5.

Figure 24. Concluded.

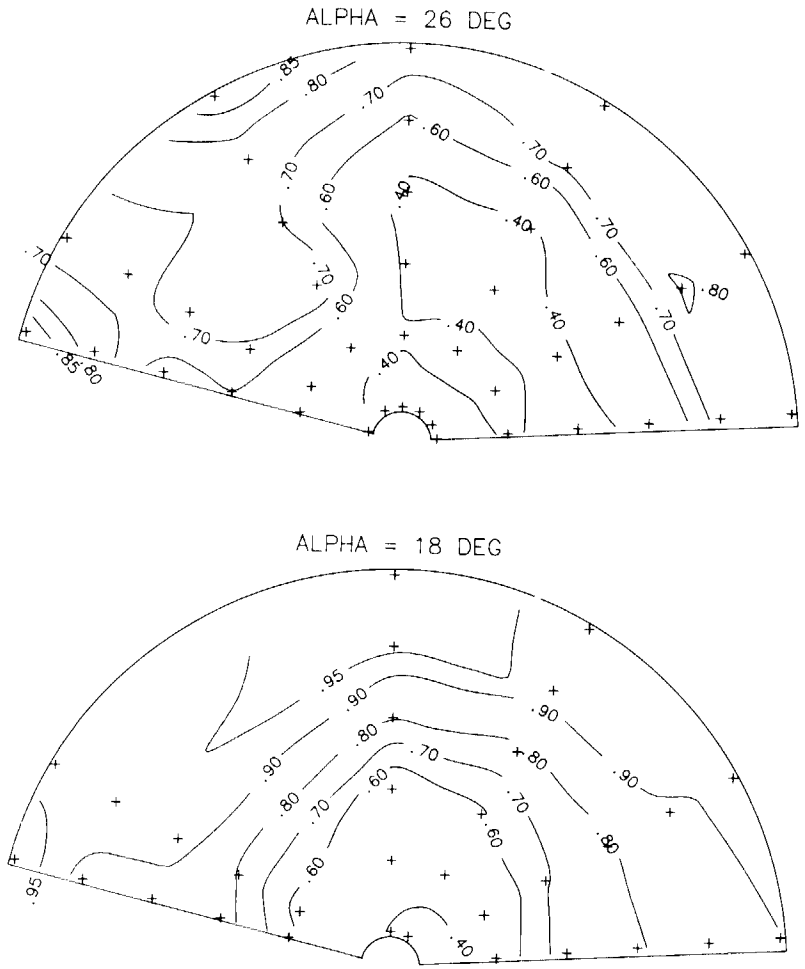

(a) Fuselage station 32.8.

Figure 25. Total pressure recovery contours for configuration with small wing fences at Mach 0.9.

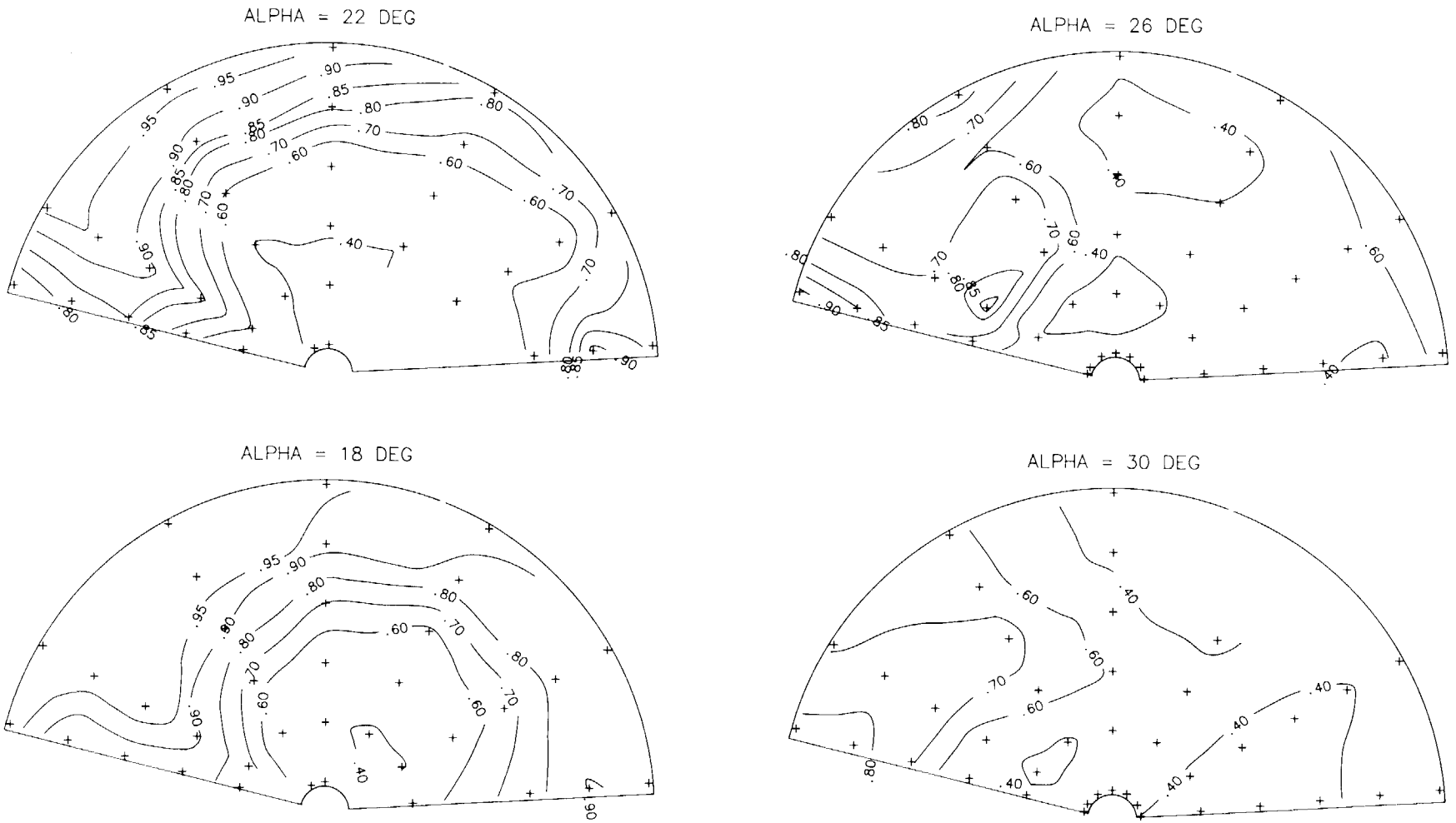

(b) Fuselage station 35.0.

Figure 25. Continued.

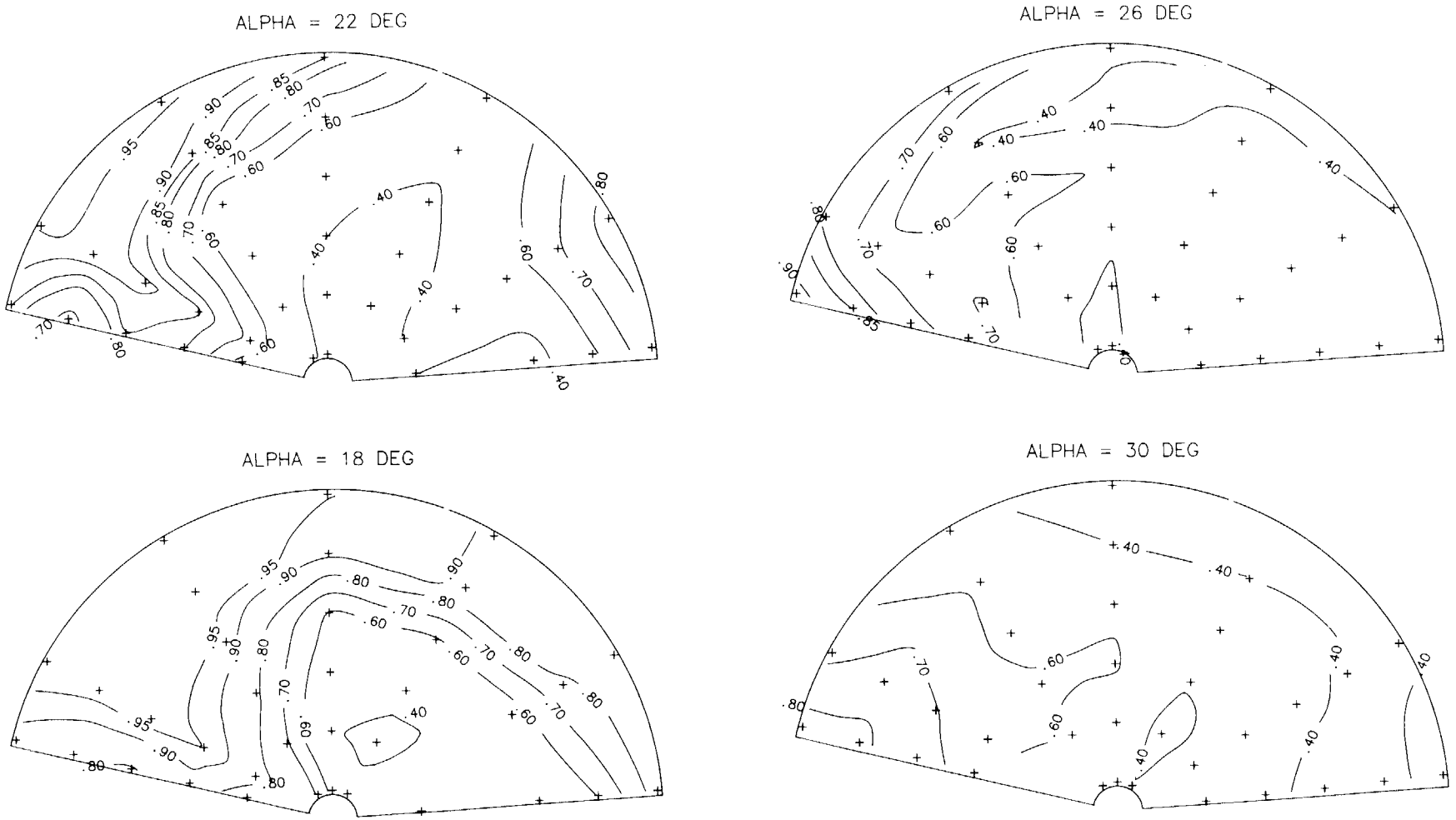

(c) Fuselage station 36.5.

Figure 25. Continued.

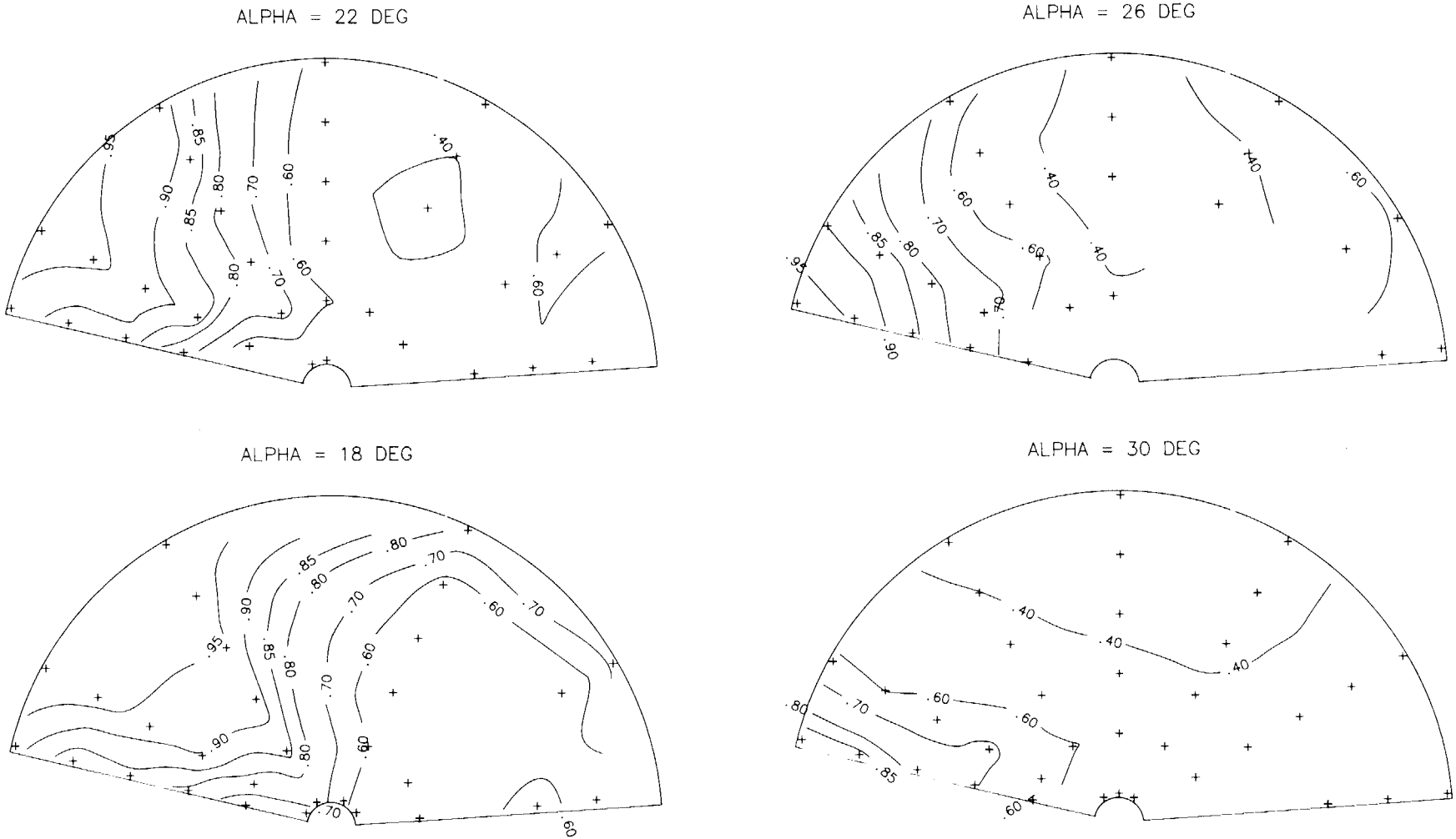

(d) Fuselage station 40.5.

Figure 25. Concluded.

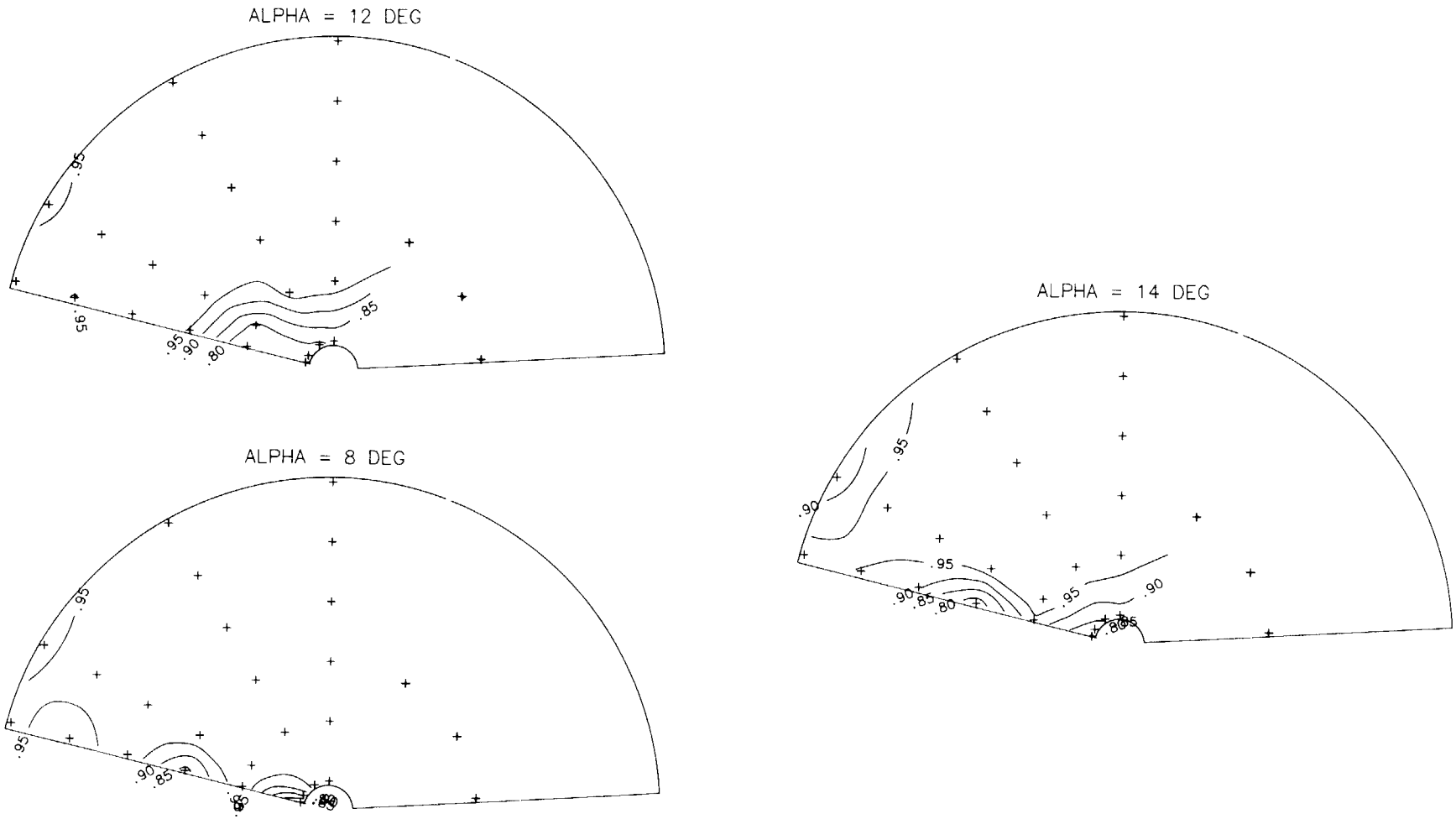

(a) Fuselage station 32.8.

Figure 26. Total pressure recovery contours for configuration with large wing fences and vortex flap deflected 30° at Mach 0.9.

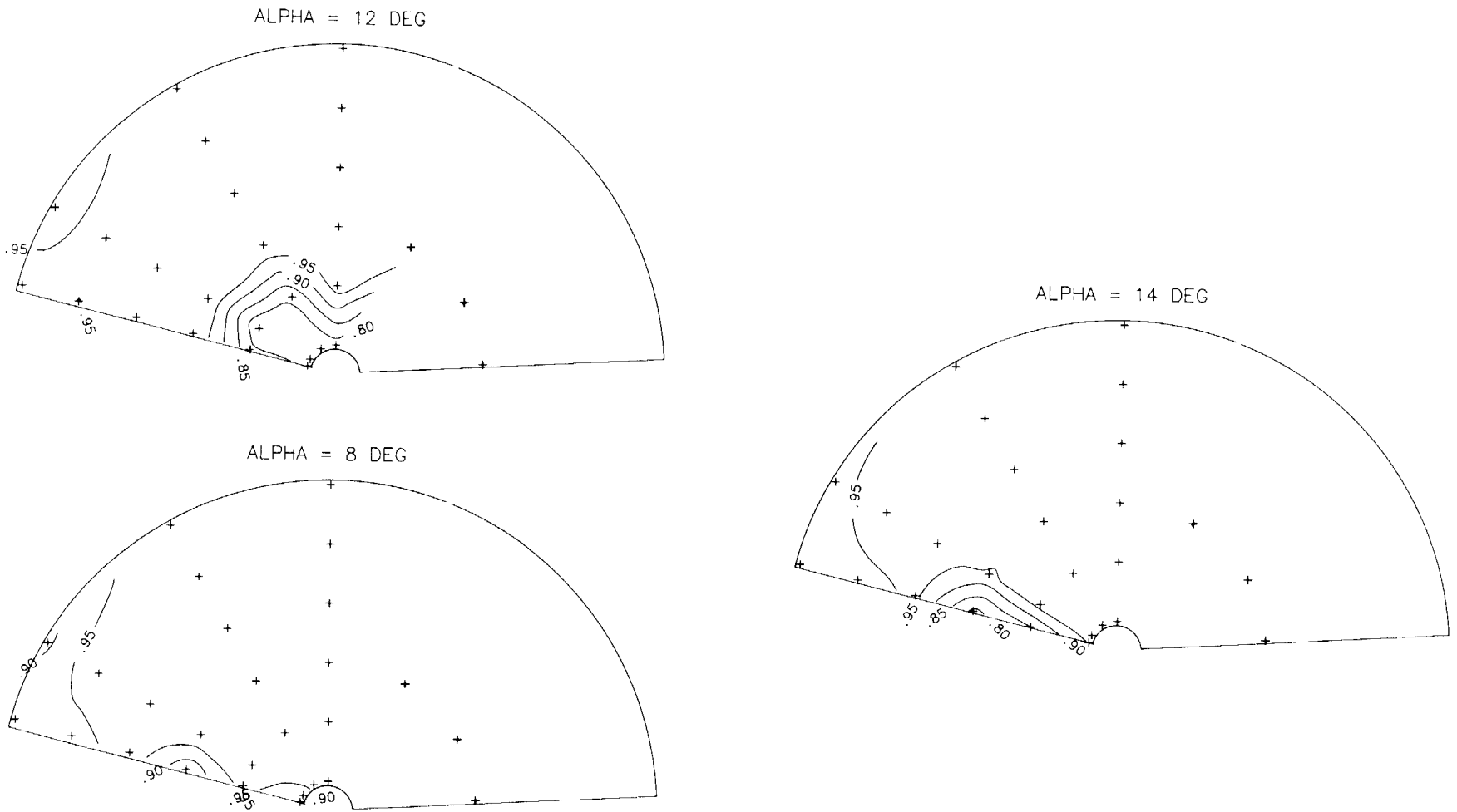

(b) Fuselage station 35.0.

Figure 26. Continued.

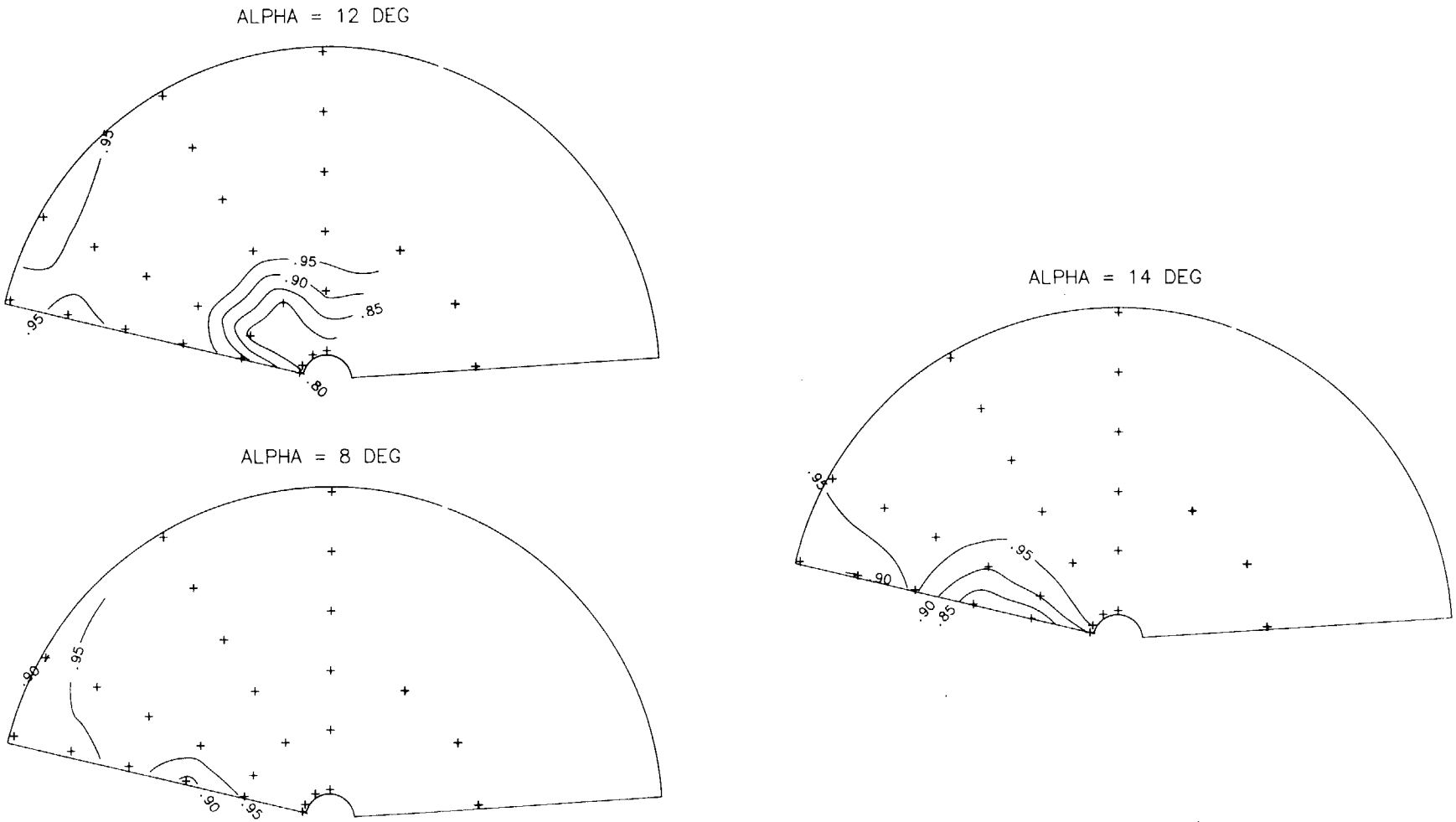

(c) Fuselage station 36.5.

Figure 26. Continued.

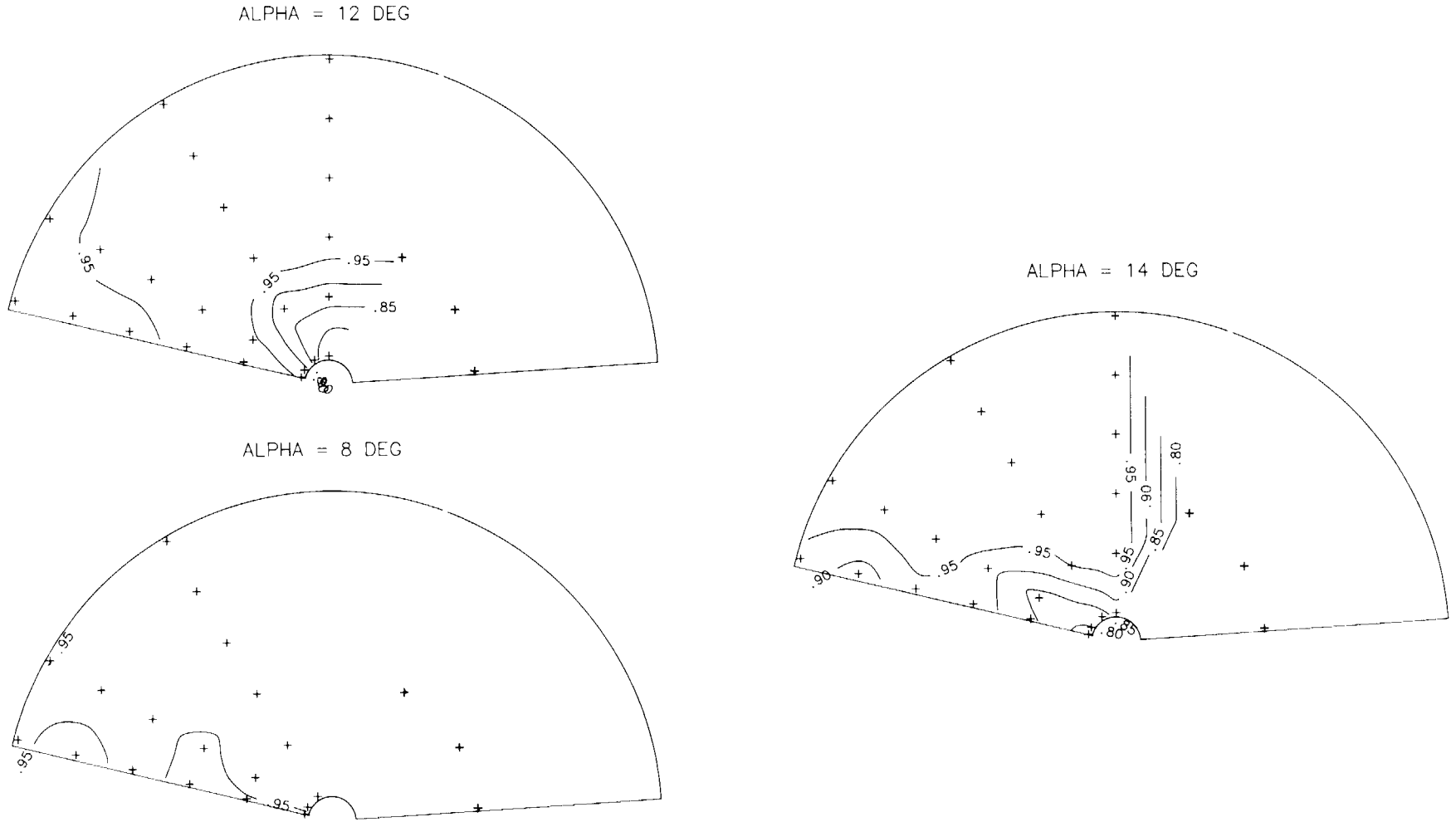

(d) Fuselage station 40.5.

Figure 26. Concluded.

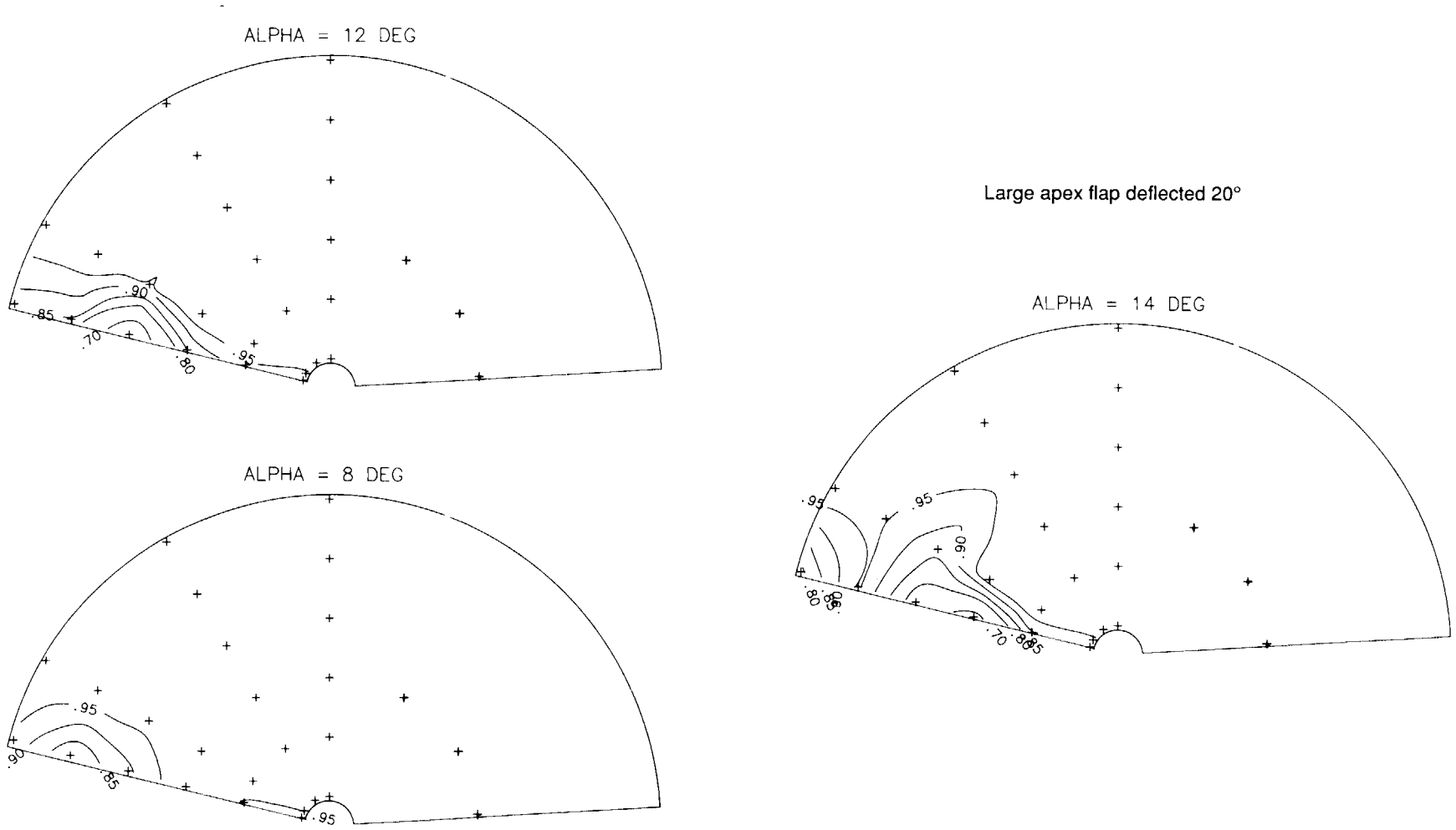

(a) Fuselage station 32.8.

Figure 27. Total pressure recovery contours for configuration with large apex flap at Mach 0.9.

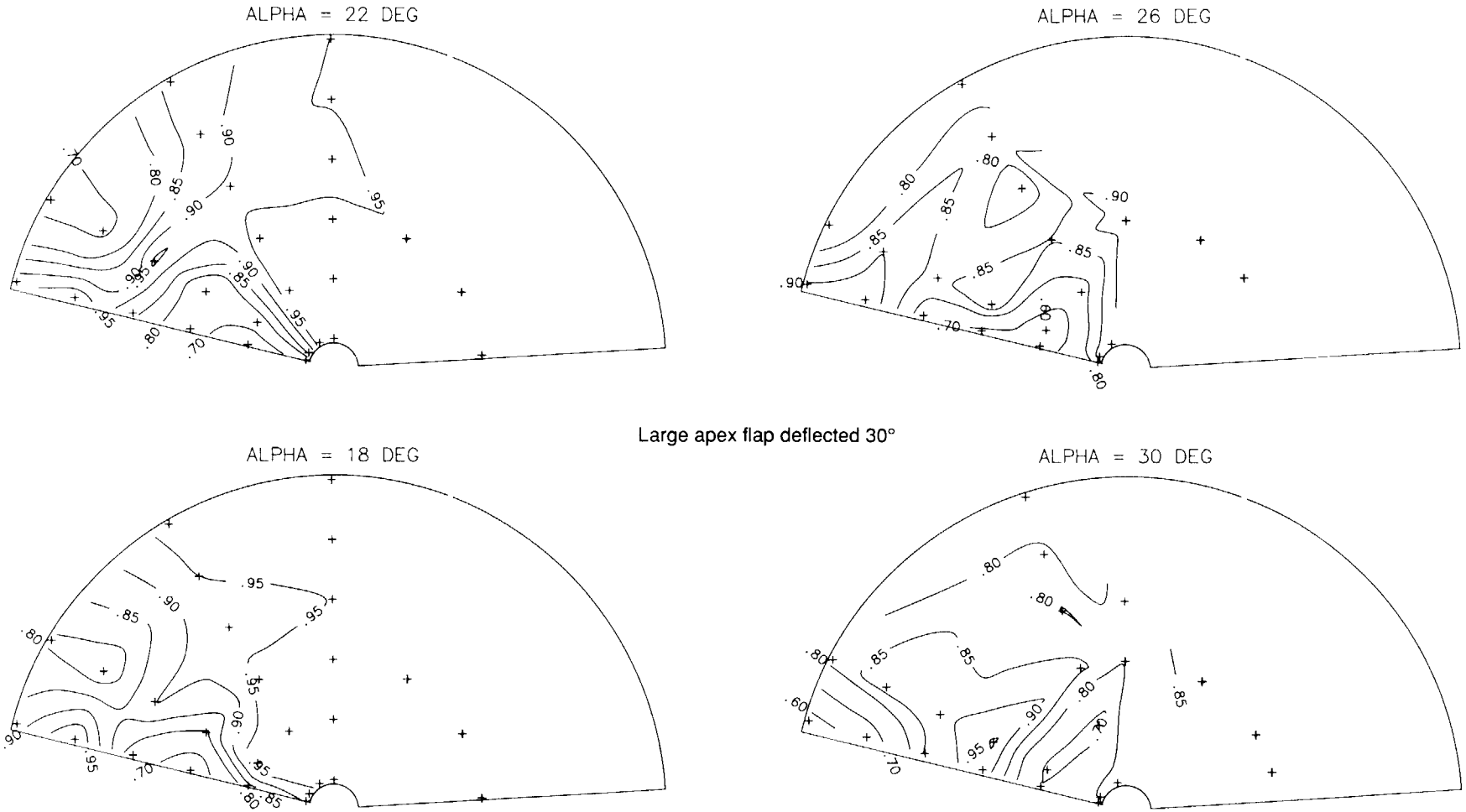

(a) Concluded.

Figure 27. Continued.

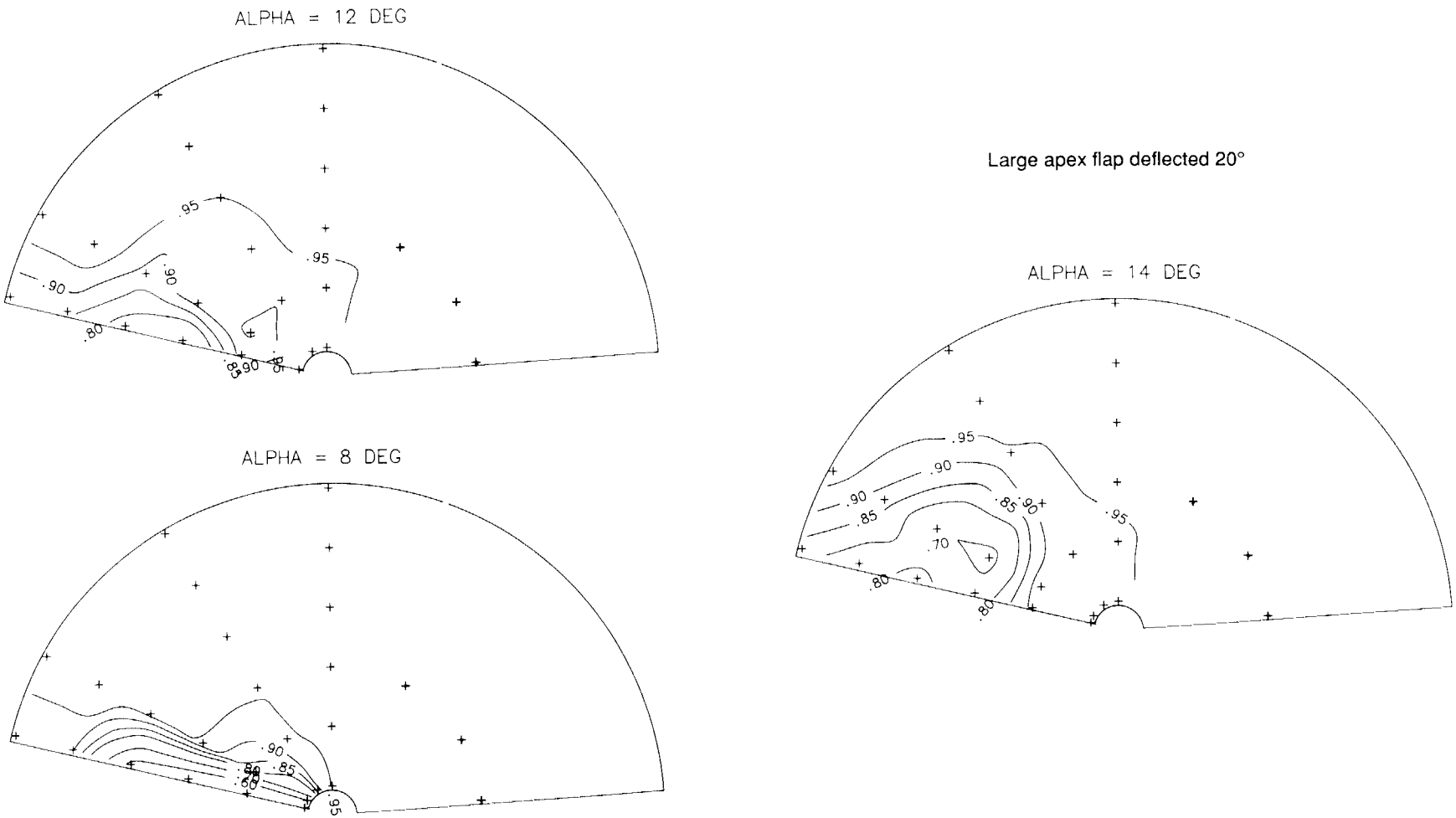

(b) Fuselage station 35.0.

Figure 27. Continued.

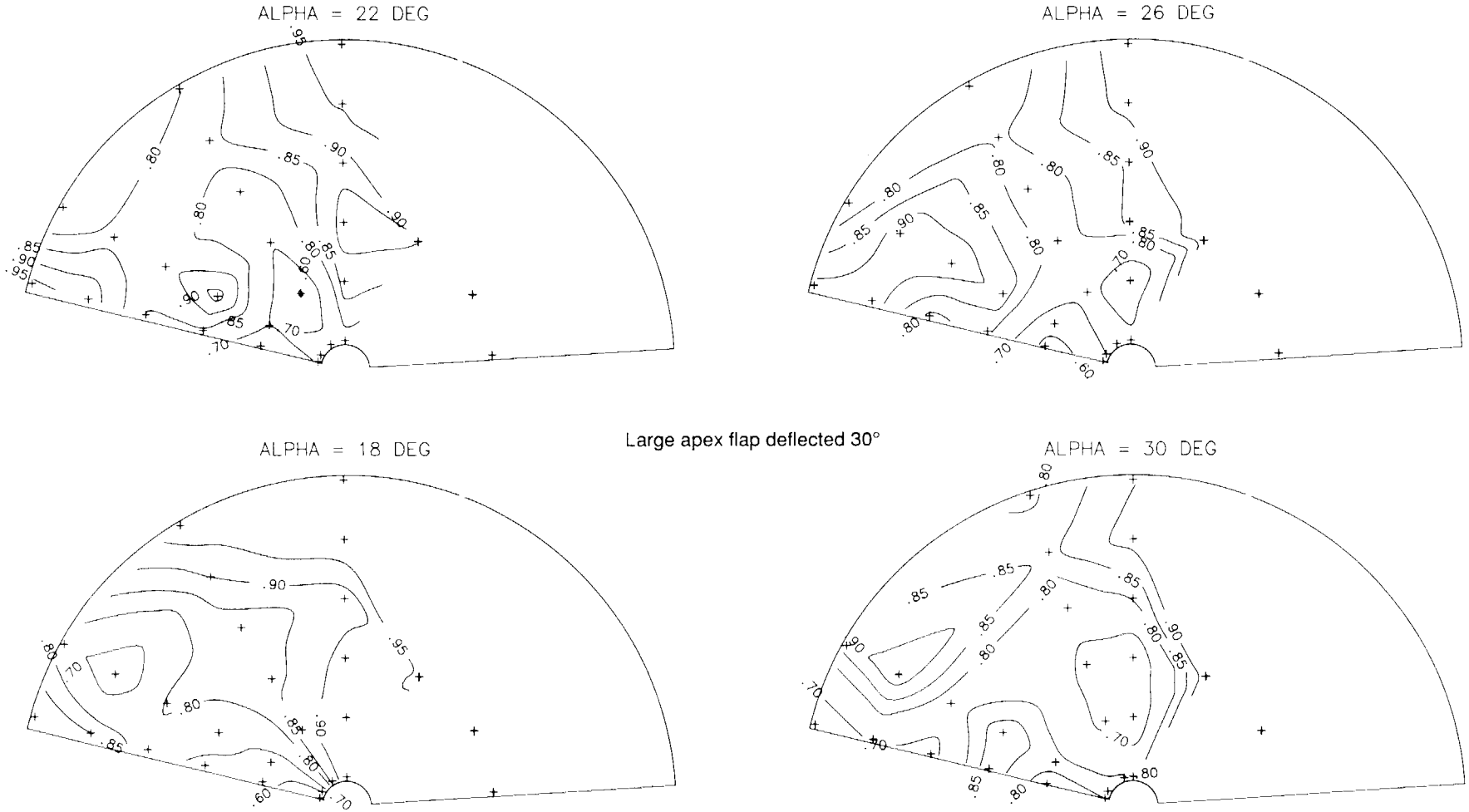

(b) Concluded.

Figure 27. Continued.

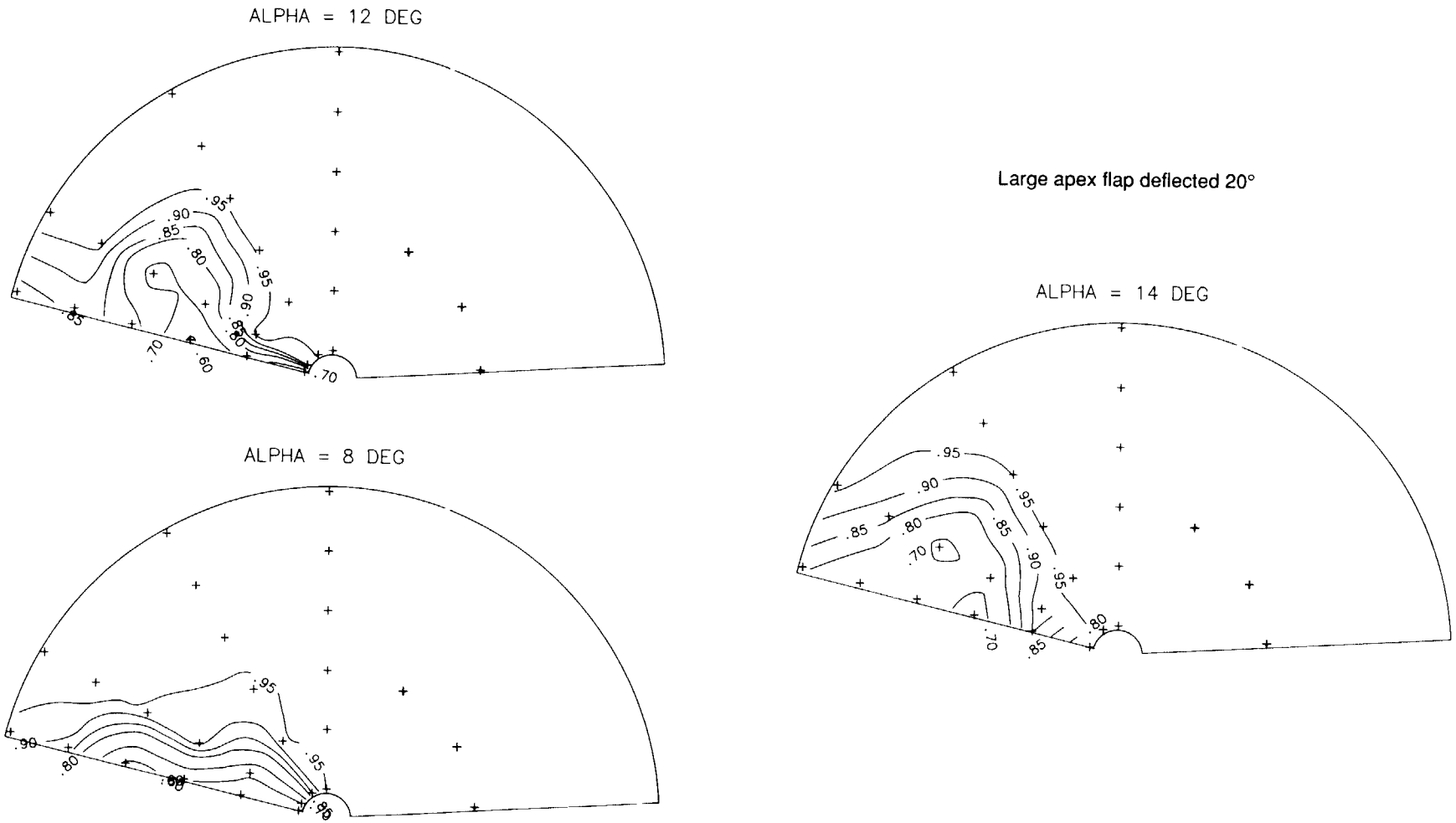

(c) Axial survey station 36.5.

Figure 27. Continued.

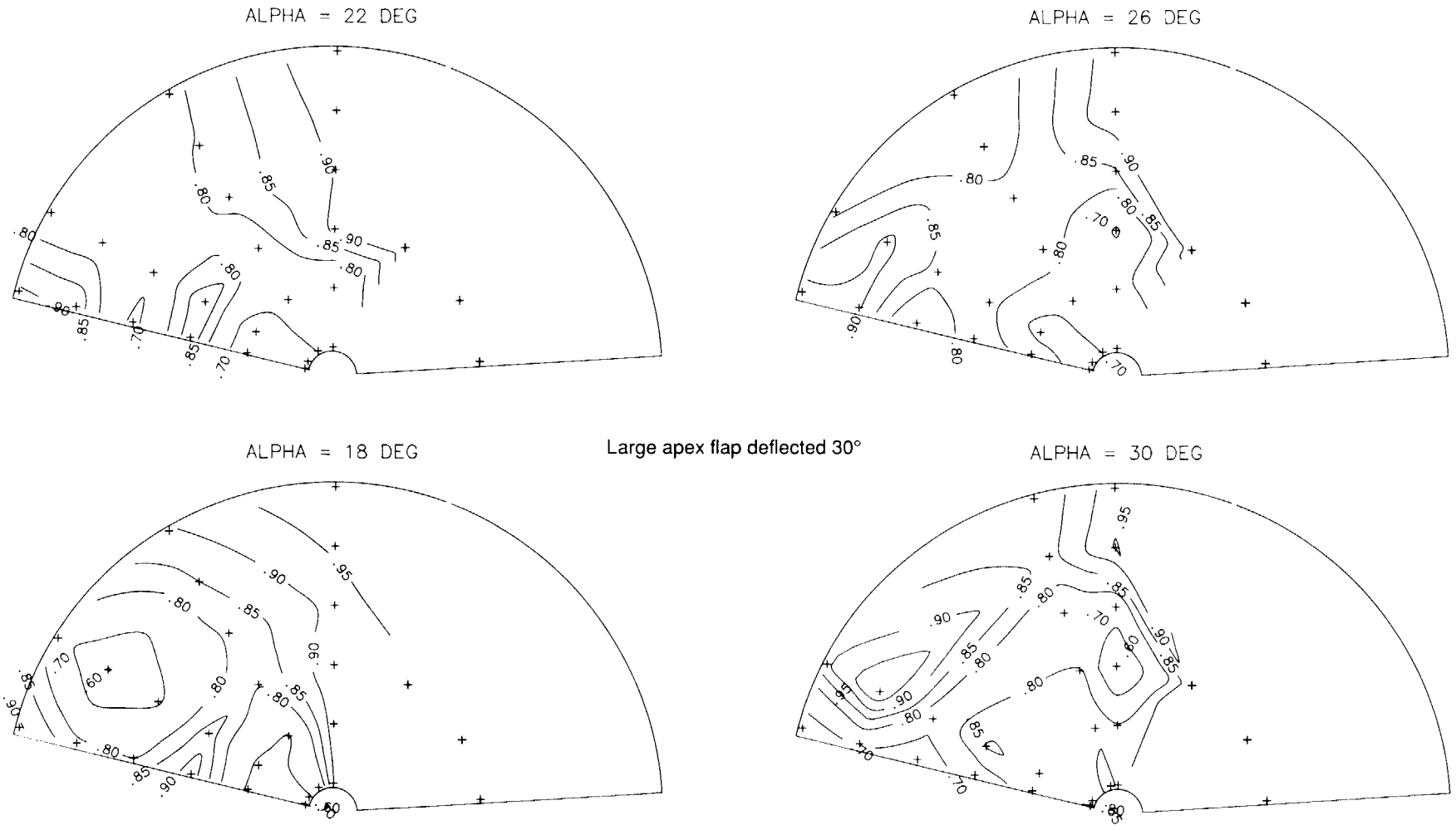

(c) Concluded.

Figure 27. Continued.

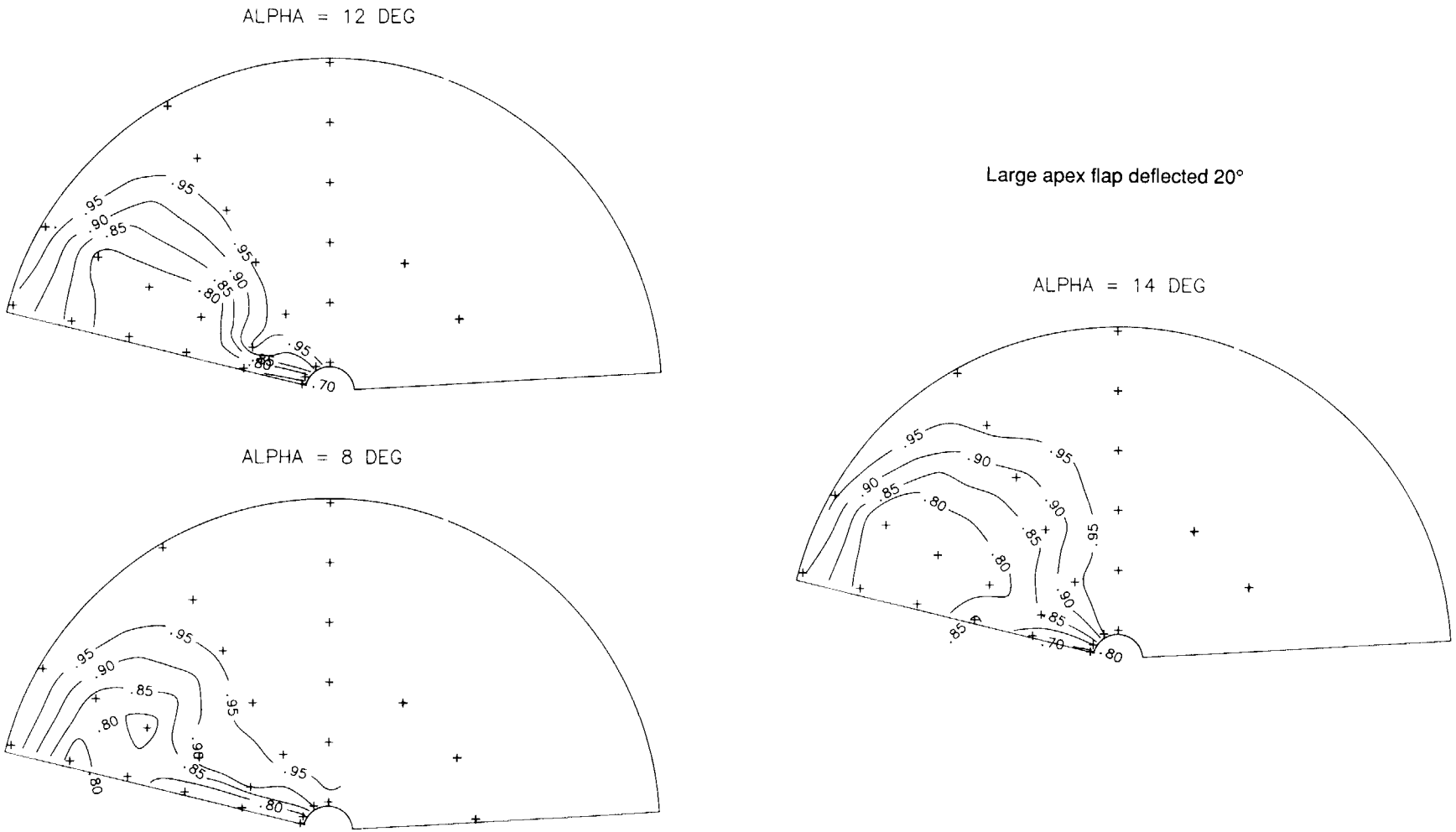

(d) Fuselage station 40.5.

Figure 27. Continued.

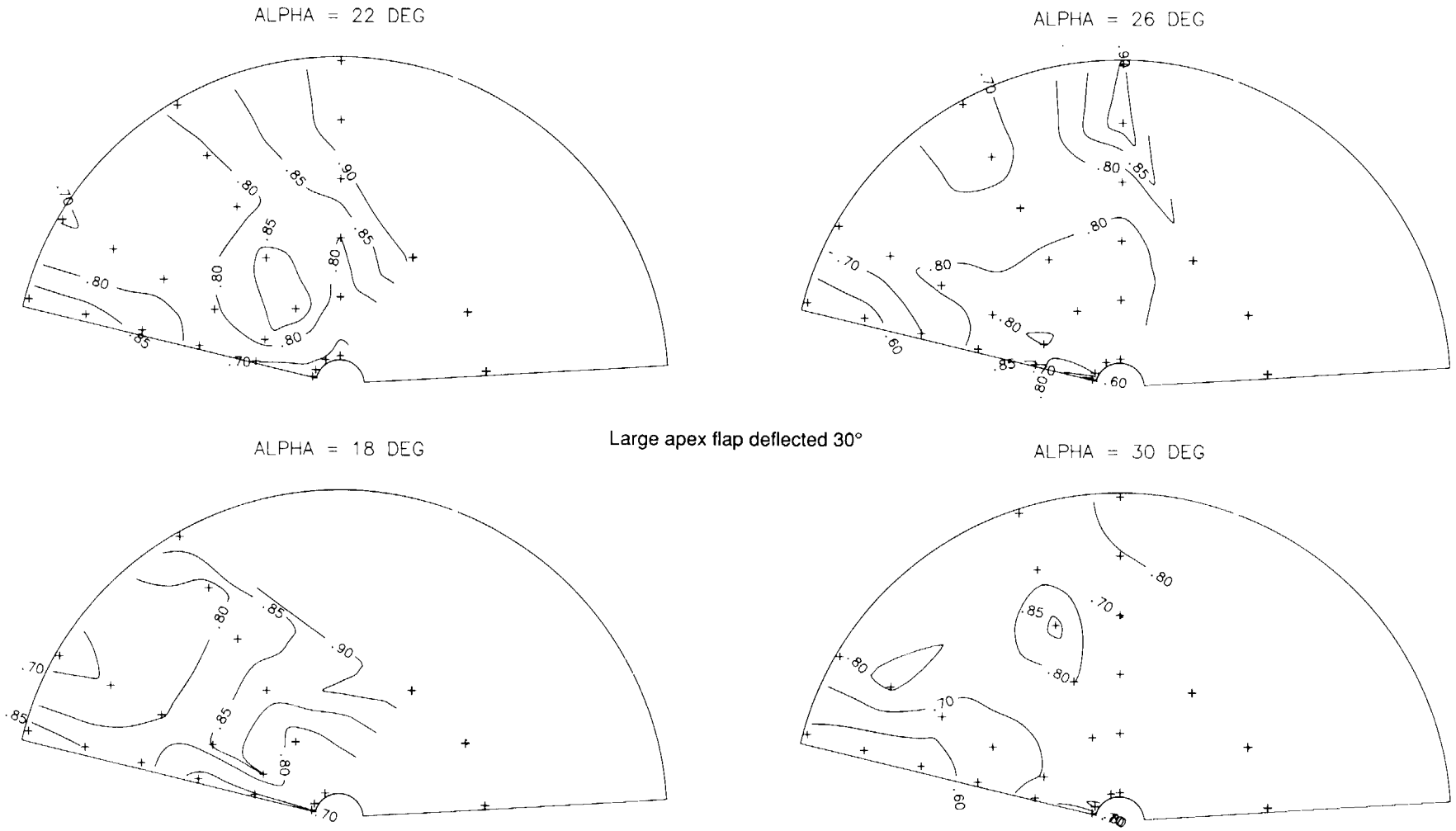

(d) Concluded.

Figure 27. Concluded.

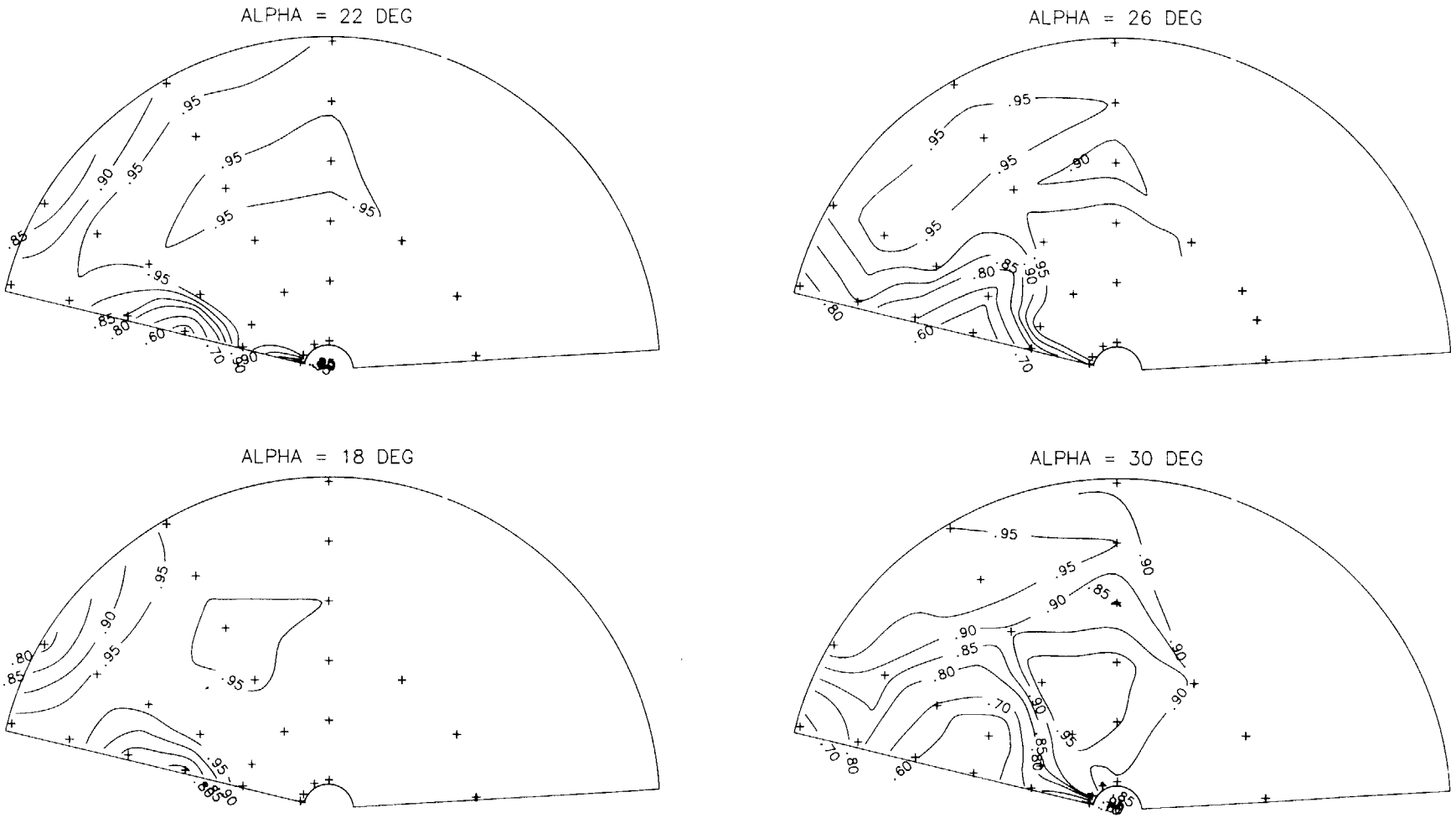

(a) Fuselage station 32.8.

Figure 28. Total pressure recovery contours for configuration with small apex flap deflected 30° at Mach 0.9.

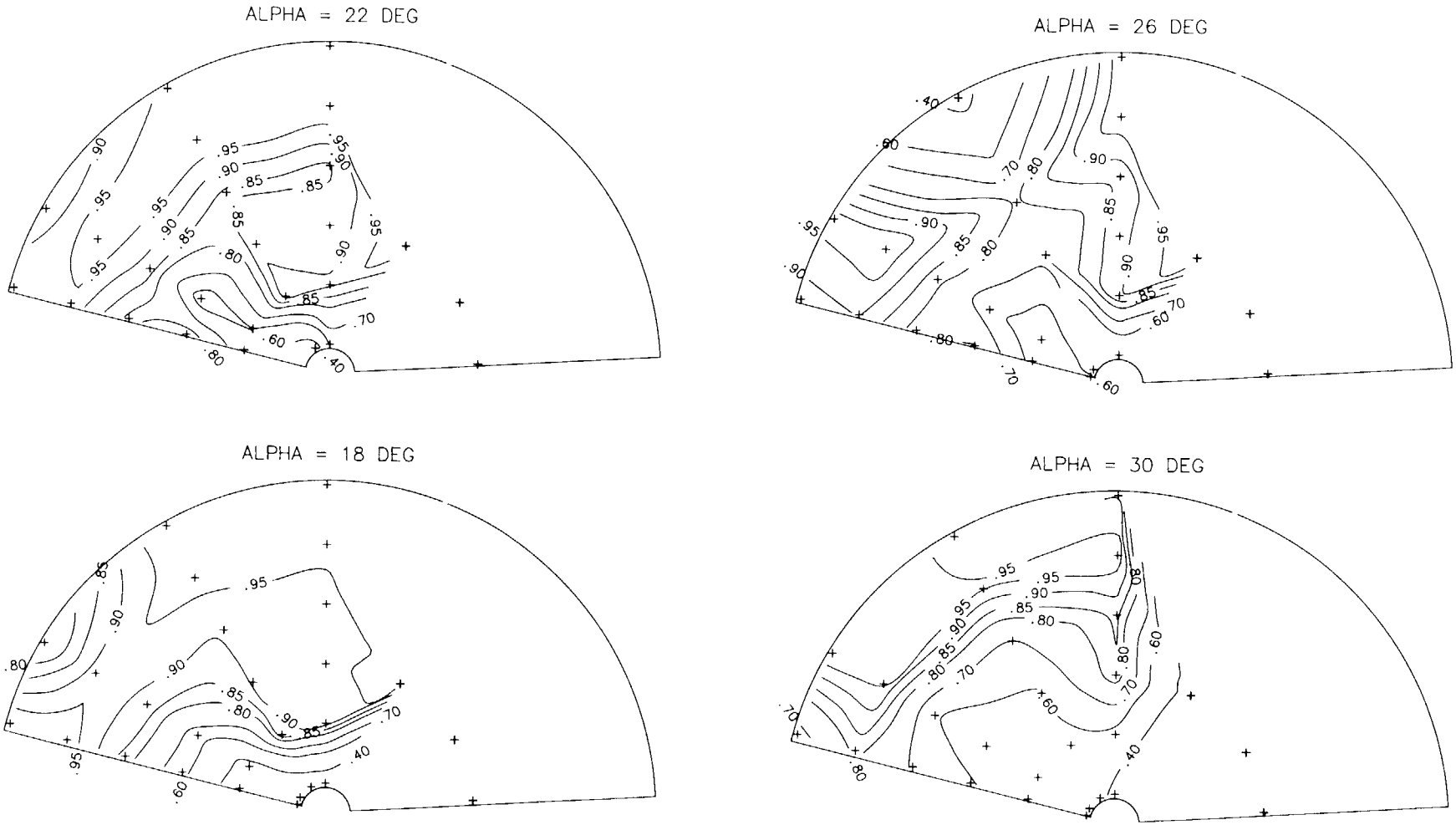

(b) Fuselage station 35.0.

Figure 28. Continued.

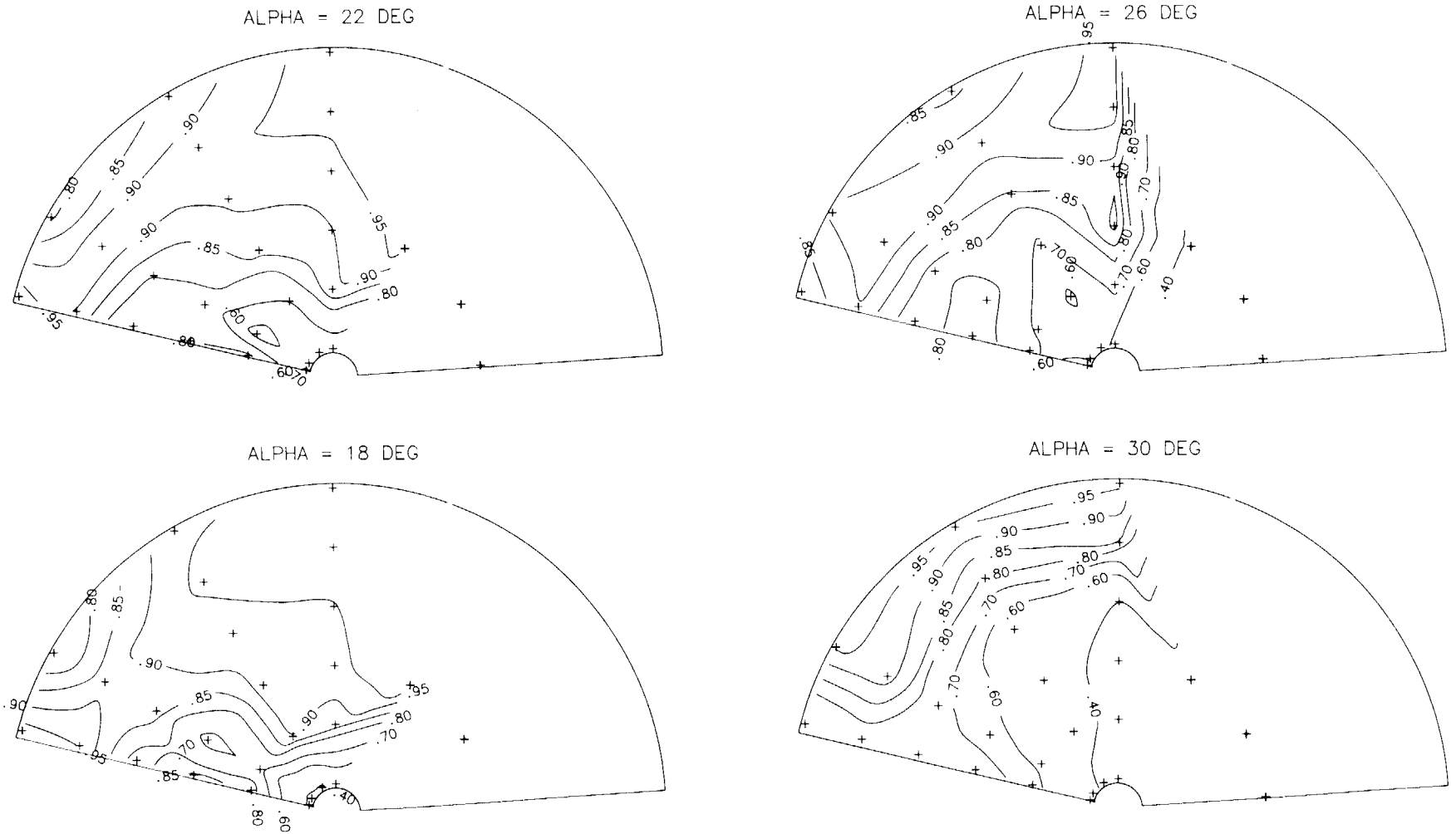

(c) Fuselage station 36.5.

Figure 28. Continued.

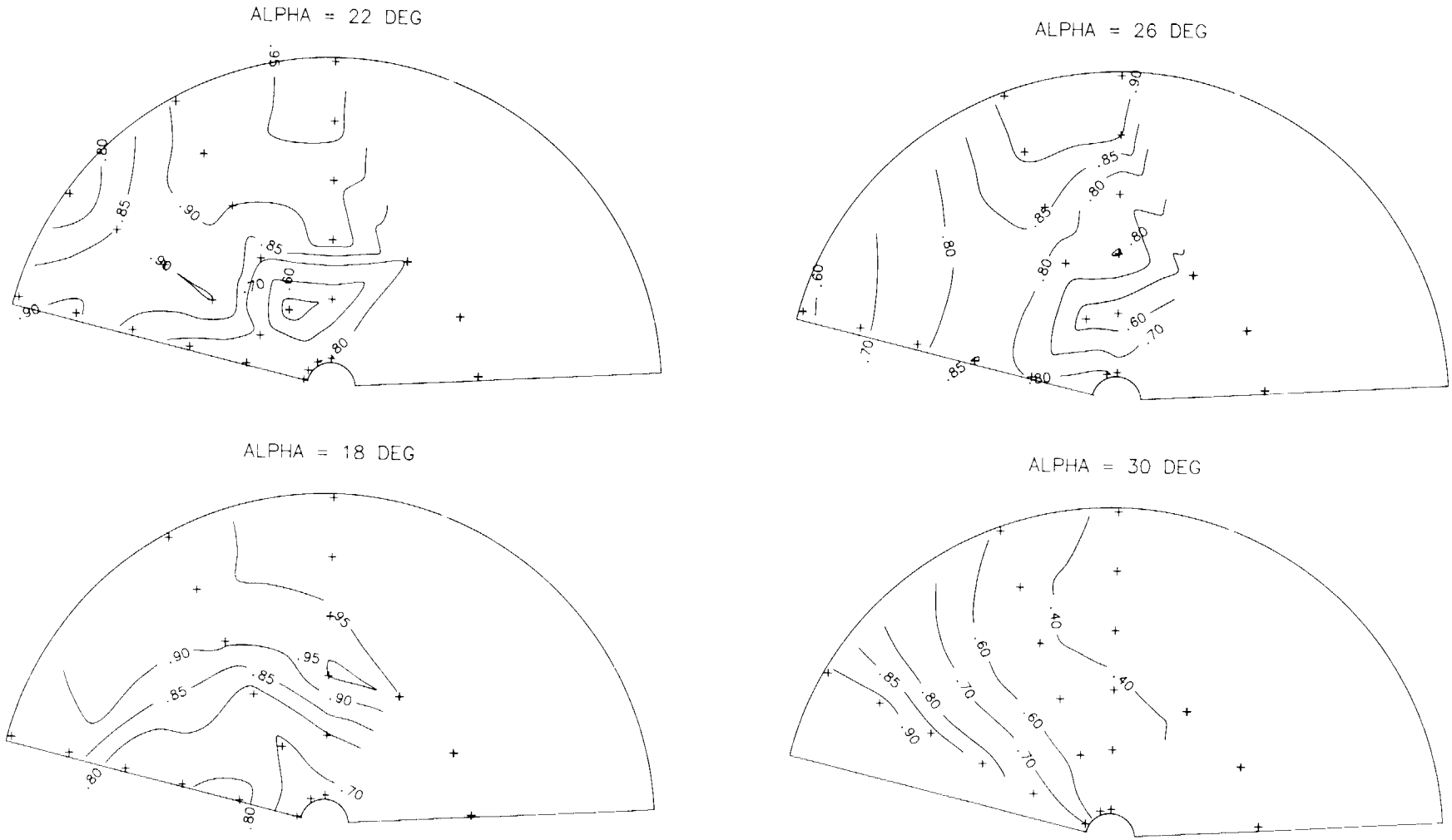

(d) Fuselage station 40.5.

Figure 28. Concluded.

REPORT DOCUMENTATION PAGE

Form Approved
OMB No. 0704-0188

1. AGENCY USE ONLY *(Leave blank)*	2. REPORT DATE	3. REPORT TYPE AND DATES COVERED
	April 1992	Technical Memorandum

4. TITLE AND SUBTITLE
Flow Field Over the Wing of a Delta-Wing Fighter Model With Vortex Control Devices at Mach 0.6 to 1.2

5. FUNDING NUMBERS
WU 505-68-91-06

6. AUTHOR(S)
E. Ann Bare, David E. Reubush, and Raymond C. Haddad

7. PERFORMING ORGANIZATION NAME(S) AND ADDRESS(ES)
NASA Langley Research Center
Hampton, VA 23665-5225

8. PERFORMING ORGANIZATION REPORT NUMBER
L-16834

9. SPONSORING/MONITORING AGENCY NAME(S) AND ADDRESS(ES)
National Aeronautics and Space Administration
Washington, DC 20546-0001

10. SPONSORING/MONITORING AGENCY REPORT NUMBER
NASA TM-4296

11. SUPPLEMENTARY NOTES
Bare and Reubush: Langley Research Center, Hampton, VA; Haddad: McDonnell Douglas Corporation, St. Louis, MO.

12a. DISTRIBUTION/AVAILABILITY STATEMENT
Unclassified Unlimited

Subject Category 02

12b. DISTRIBUTION CODE

13. ABSTRACT *(Maximum 200 words)*

As part of a cooperative research program between NASA, McDonnell Douglas Corporation, and Wright Research and Development Center, a flow-field investigation was conducted on a 7.52-percent-scale wind tunnel model of an advanced fighter aircraft design. The investigation was conducted in the Langley 16-Foot Transonic Tunnel at Mach numbers of 0.6, 0.9, and 1.2. Angle of attack was varied from $-4°$ to $30°$ and the model was tested at angles of sideslip of $0°$, $5°$, and $-5°$. Data for over-the-wing flow field were obtained at four axial survey stations by the use of six 5-hole conical probes mounted on a survey mechanism. The wing leading-edge primary vortex exerted the greatest influence in terms of total pressure loss on the over-the-wing flow field in the area surveyed. A number of vortex control devices were also investigated. They included two different apex flaps, wing leading-edge vortex flaps, and small and large wing fences. The vortex flap and both apex flaps were beneficial in controlling the wing leading-edge primary vortex.

14. SUBJECT TERMS	15. NUMBER OF PAGES
Flow-field data; Cone probes; Delta wing; Fighter aircraft; Vortex control	124
	16. PRICE CODE A06

17. SECURITY CLASSIFICATION OF REPORT	18. SECURITY CLASSIFICATION OF THIS PAGE	19. SECURITY CLASSIFICATION OF ABSTRACT	20. LIMITATION OF ABSTRACT
Unclassified	Unclassified		

NSN 7540-01-280-5500

Standard Form 298(Rev. 2-89)
Prescribed by ANSI Std. Z39-18
298-102

NASA-Langley, 1992